PIEZOELECTRIC ENERGY HARVESTER FOR TYRES

Bridging the research gap between materials and application

Carmela Mangone

PIEZOELECTRIC ENERGY HARVESTER FOR TYRES

Bridging the research gap between materials and application

Carmela Mangone

PIEZOELECTRIC ENERGY HARVESTER FOR TYRES

Bridging the research gap between materials and application

DISSERTATION

to obtain
the degree of doctor at the University of Twente,
on the authority of the rector magnificus,
Prof. Dr. Ir. T. A. Veldkamp,
on account of the decision of the Doctorate Board
to be publicly defended
on Thursday 22 February 2024 at 14.45 hours

by

Carmela Mangone

This dissertation has been approved by:

Promotor
  Prof. Dr. A. Blume

Co-promotor
  Dr. W. Kaewsakul

Graduation Committee:

Chair / secretary: Prof. Dr. Ir. B. H.F.J.M. Koopman
Dean, University of Twente, Engineering Technology ET

Promotor: Prof. Dr. A. Blume
University of Twente, ET, Elastomer Technology and Engineering

Co-promotor: Dr. W. Kaewsakul
University of Twente, ET, Elastomer Technology and Engineering

Committee Members: Prof. Dr. Ir. H. Askes
University of Twente, ET, Computational Mechanics of Multiscale Materials

Prof. Dr. Ir. E. van der Heide
University of Twente, ET, Skin Tribology

Prof. Dr. Ir. S. van der Zwaag
TU Delft

Prof. Dr. M.L. Susoff
Hochschule Osnabrück University of Applied Sciences

Dr. H. Westenberg
Orion Engineered Carbons GmbH

Dr. Ir. K. Bandzierz
Apollo Tyres

TABLE OF CONTENTS

Chapter 1

Introduction

1.1.   Background and motivation

Autonomous driving has significantly transformed modern transportation systems and is expected to bring numerous benefits, for instance, reducing accidents and optimising fuel consumption [1]. To further improve autonomous driving capabilities, an increasing number of sensors are being integrated into vehicles to ensure safe environmental perception. Among the essential components required to boost autonomous driving, smart tyres play a crucial role [2,3]. These tyres can be equipped with sensors, providing real-time information to the driver, including tread wear, load detection, temperature and heat build-up, and pressure of the running tyres.

Current research in this field primarily focuses on addressing challenges related to automatic operations and the limited capacity of batteries used in sensors. One of the initial sensors introduced into tyres for continuous tyre pressure monitoring is the Tyre Pressure Monitoring System (TPMS) [4-6]. In the United States, the Tread Act (2000) mandated the inclusion of this sensor in all light vehicle tyres sold from 2007. The European Union also later adopted the requirement of a TPMS in vehicles in 2009 through regulation no. 661/2009. A TPMS sensor can be installed either inside the tyre tread and on the wheel rim (as shown in Figure 1) [3].

The TPMS system consists of a pressure sensor, circuitry, and a battery. The circuitry includes a controller and a transmitter responsible for monitoring and sending signals to the central system of the vehicle, which then notifies the driver of under or over-inflated tyres. The battery serves as a power supply for the sensor. However, the battery has a limited lifespan, leading to additional maintenance costs for replacing the depleted batteries. Moreover, the use of batteries containing toxic chemicals, e.g. lithium/thionyl chloride batteries is not environmentally friendly [7]. Therefore, it is crucial and desirable to explore alternative solutions for powering TPMS without relying on batteries.

Piezoelectric materials have gained recognition as promising energy harvesting technologies with the potential to replace batteries as power sources for sensors in tyres [8-10]. The piezoelectric effect is a phenomenon where mechanical energy applied to a piezoelectric material during dynamic deformations (such as shear, tension, compression) is converted into electrical energy [11,12]. Upon externally applied mechanical forces, electrical charges accumulate on both surfaces of the piezoelectric material. By applying electrodes to these surfaces, the flow of electrical current can be induced and utilised in car tyres.

Figure 1   A TPMS device installed (a, b) at the lateral side of the rim and on the inner liner (c) [7].

When a vehicle is in motion, various effects occur within the rotating tyres, including the deformations of the tread and sidewall in the contact patch area, and the changes in the tyre components due to periodic acceleration [13]. These factors provide an opportunity to produce electrical energy by incorporating a piezoelectric material into the tyre.

Figure 2 illustrates an energy harvester material mounted onto the inner liner of a tyre, which is subjected to the load exerted by a car. The inner liner is a thin layer positioned on the inner surface of the tyre to improve air retention and maintain tyre pressure.

Figure 2 demonstrates that the contact patch area of the tyre experiences tension during driving, while the regions just before and after the contact patch undergo compression. Consequently, during the cyclic rotation of the tyre, the inner liner is exposed to a certain range of strains and frequencies, which depend on vibrations resulting from tyre-road interactions and gravitational effects.

The goal of this project is to develop a piezoelectric energy harvester capable of generating electrical energy to power a TPMS device. The principal concept of the research is to explore the integration of a piezoelectric energy harvester as an additional component within the tyre structure. This integration would enable continuous electrical energy generation during driving to power the TPMS, thereby overcoming the disadvantages associated with using batteries.
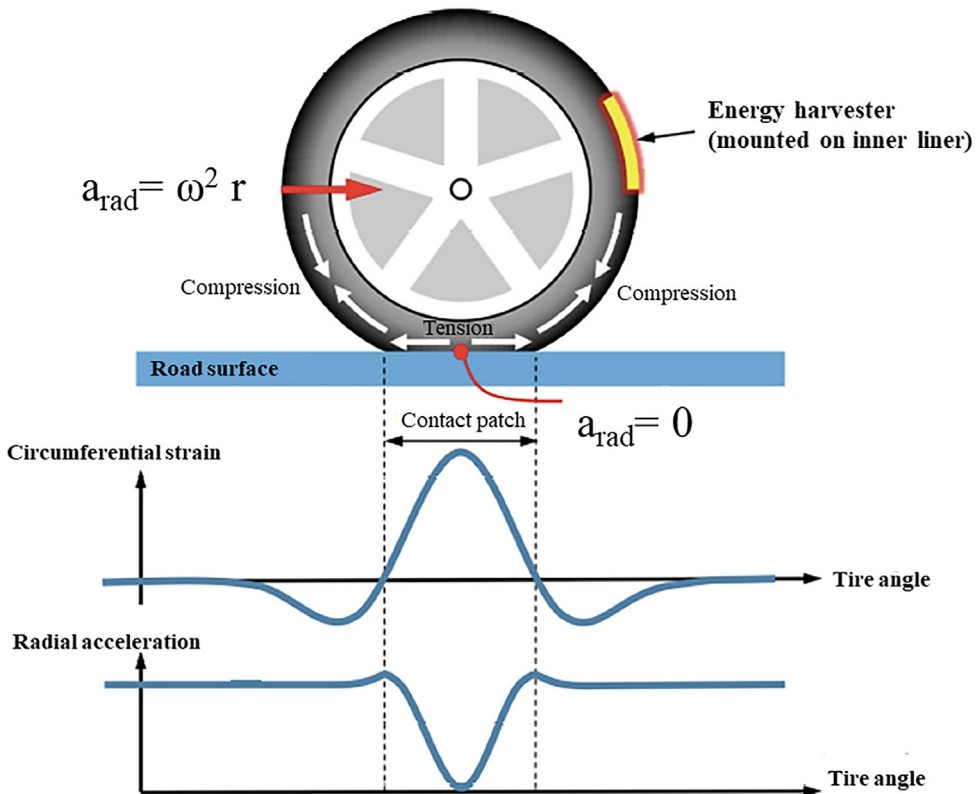
Figure 2 Variations in the circumferential strain and radial acceleration in a tyre rolling on a road surface [3].

There are two categories of piezoelectric materials: ceramics and polymers, each having different coefficients that determine their ability to generate electrical energy. Ceramics generally offer higher piezoelectric coefficients, producing larger amounts

of electrical energy per unit of mechanical work compared to piezoelectric polymers. However, ceramics are rigid, brittle, and relatively heavy, making them unsuitable for tyre applications. On the other hand, piezoelectric polymers offer better flexibility but possess lower piezoelectric coefficients, resulting in inferior electrical energy generation compared to piezoelectric ceramics. Given the promising characteristics and limitations of piezoelectric materials, the objective of this project is to identify an adequate material capable of generating sufficient energy to power a TPMS.

1.2.   Objectives of the research project

The primary objectives of this project are as follows:

➢   Designing a suitable prototype of a piezoelectric device capable of generating sufficient electrical energy to power a TPMS;

➢   Developing approaches to endure strong adhesion and flexibility between the piezoelectric energy harvester components;

➢   Identifying crucial parameters affecting the piezoelectric and conductive performance of the selected materials used in the energy generating system;

➢   Verifying the capability of the developed piezoelectric device to power a TPMS.

1.3.   Outline of the thesis

This thesis comprises of ten chapters, starting from **Chapter 2** providing a literature review on piezoelectricity effect and the key materials used for piezoelectric systems in tyres. **Chapter 3** presents the development of an experimental setup to validate piezoelectric energy harvesters in tyres. Dynamic mechanical analysis was used as a foundation to simulate vibrations and dynamic responses in a rolling tyre, while monitoring the electrical properties of elastomers under varying dynamic strains, frequencies, and temperatures. **Chapter 4** focuses on the design of a piezoelectric energy harvester consisting of the piezoelectric polymer PolyVinyliDene diFluoride (PVDF) between two layers of an electrically conductive elastomer. The chemical adhesion between these components and its impact on output power of the piezoelectric energy harvesters were investigated. **Chapter 5** examines the conductive component of the piezoelectric energy harvester, which is an elastomeric electrode. The influential factors affecting the dynamic electrical conductivity of elastomeric electrodes are identified using Design of Experiments (DoEs) as a pre-screening method, followed by a modelling study. **Chapter 6** continues the investigation of the electrically conductive elastomers by comparing the impact of the two categories of carbon blacks: conventional and conductive carbon blacks. For

Chapter 7, the use of ferroelectric composites based on modified natural rubber: Epoxidised Natural Rubber (ENR), and synthetic rubber: acryloNitrile Butadiene Rubber (NBR) filled with varying amounts of the lead-free ferroelectric ceramic, $K_{0.5}Na_{0.5}NbO_3$ (KNN), was investigated. In this chapter, the effect of rubber types on processability, curing behaviour, contact poling process, mechanical and electrical properties of ferroelectric composites was analysed. In **Chapter 8** the effect of KNN amounts on the processability, curing behaviour, mechanical and electrical properties of ferroelectric composites was investigated. In this chapter, also chemical model study was carried out in order to analyse the interactions between KNN and the rubbers. In **Chapter 9**, the ferroelectric composites were sandwiched between two layers of an electrically conductive elastomer to form energy harvesters. The effect of contact poling and the output power from these harvesters under rolling tyre conditions were analysed. Finally, **Chapter 10** summarises the main findings and provides viewpoints for further research.

1

1.4.   References

[1]   T. Sharma, A. Chehri, P. Fortier, Communication trends, research challenges in autonomous driving and different paradigms of object detection, Smart Innov. Syst. Technol. 359 (2023) 57–66.
https://doi.org/10.1007/978-981-99-3424-9_6/COVER.

[2]   Z. Yang, S. Zhou, J. Zu, D. Inman, High-performance piezoelectric energy harvesters and their applications, Joule. 2 (2018) 642–697.
https://doi.org/10.1016/j.joule.2018.03.011.

[3]   C.R. Bowen, M.H. Arafa, Energy harvesting technologies for tire pressure monitoring systems, Adv. Energy Mater. 5 (2015) 1–17.
https://doi.org/10.1002/aenm.201401787.

[4]   A.E. Kubba, K. Jiang, A comprehensive study on technologies of tyre monitoring systems and possible energy solutions, Sensors. 14 (2014) 10306–10345.
https://doi.org/10.3390/s140610306.

[5]   B. Wu, Y. Fang, L. Deng, Summary of energy collection application in vehicle tire pressure monitoring system, in: ACM Int. Conf. Proceeding Ser., Association for Computing Machinery, Shenzhen, 2019: pp. 1–6.
https://doi.org/10.1145/3351917.3351918.

[6]   T. Lange, M. Löhndorf, Intelligent low-power management and concepts for battery-less direct tire tressure monitoring (TPMS), in: Adv. Microsystems Automot. Appl., Springer, Berlin, Heidelberg, 2007: pp. 237–249.
https://doi.org/https://doi.org/10.1007/978-3-540-71325-8_19.

[7]   R. Matsuzaki, A. Todoroki, Wireless monitoring of automobile tires for intelligent tires, Sensors. 8 (2008) 8123–8138. https://doi.org/10.3390/s8128123.

[8]   L. Liu, X. Guo, W. Liu, C. Lee, Recent progress in the energy harvesting technology from self-powered sensors to self-sustained IoT, and new applications, Nanomaterials. 11 (2021) 1–40. https://doi.org/10.3390/nano11112975.

[9]   K. Uchino, The development of piezoelectric materials and the new perspective, in: Adv. Piezoelectric Mater. Sci. Technol., Woodhead Publishing in Materials, 2010: pp. 1–92. https://doi.org/10.1533/9781845699758.1.

[10]   S. Mishra, L. Unnikrishnan, S.K. Nayak, S. Mohanty, advances in piezoelectric polymer composites for energy harvesting applications, Macromol. Mater. Eng. 304 (2019) 1–25. https://doi.org/10.1002/MAME.201800463.

[11]   M. Safaei, H.A. Sodano, S.R. Anton, A review of energy harvesting using piezoelectric materials: State-of-the-art a decade later (2008-2018), Smart Mater. Struct. 28 (2019) 1–62. https://doi.org/10.1088/1361-665X/AB36E4.

[12]   J. Yvonnet, Piezoelectricity, in: Solid Mech. Its Appl., Springer Verlag, 2019: pp. 91–102. https://doi.org/10.1007/978-3-030-18383-7_5.

[13]   J. Lee, S. Kim, J. Oh, B. Choi, A self-powering system based on tire deformation during driving, Int. J. Automot. Technol. 13 (2012) 963–969.
https://doi.org/10.1007/s12239-012-0098-0.

Chapter 2

Literature study

Chapter 2

2.1.   Introduction

Over the last few decades, the concept of using piezoelectric material as energy harvesters to convert mechanical energy into electrical energy has emerged. However, the origin of piezoelectricity dates back more than a century ago [1,2]. Piezoelectricity was discovered by the French brothers Pierre and Jacques Curie in 1880 [3,4]. They found that certain single crystals, such as quartz and Rochelle salt, produced surface charges when subjected to mechanical load. This phenomenon was later called the direct piezoelectric effect, which refers to the generation of electrical charges from applied stress. In 1881, Gabriel Lippmann mathematically deduced that these crystals also exhibited a mechanical deformation when an electrical potential was applied across the material [5]. This is known as the converse piezoelectric effect and was experimentally proven by the Curie brothers a year later.

During World War II, researchers in the United States, Japan and the Soviet Union synthesised a novel piezoelectric polycrystalline ceramic with an extraordinary dielectric constant in laboratories [6]. Dielectric constant quantifies the ability of a material to store electrical charges when applied by an electrical field. It is also known as relative permittivity where the term "relative" emphasize that it is dimensionless and expressed relative to that a vacuum. This ceramic material, known as Barium Titanate $BaTiO_3$ (BT) is still used today. It exhibits a dielectric constant up to 100 times higher than the crystals commonly used in that period. BT was obtained by mixing TiO_2 and BaO in different proportions, followed by high temperature treatments. In 1946, scientists discovered that the application of an electrical field during a process known as the poling process made this polycrystalline material piezoelectric [7]. This discovery marked the beginning of intense research into piezoelectric materials and their various applications.

Lead Zirconate Titanate (PZT) was discovered by Jaffe in 1954 through the mixing of $PbZrO_3$ and $PbTiO_3$ [8]. The phase diagram of PZT is characterized by a boundary, known as the Morphotropic Phase Boundary (MPB), which exists between a tetragonal and rhombohedral phase at a zirconate content of 52%. At this composition, PZT showed distinct piezoelectric properties. The patent of Jaffe had a significant effect on the further development of piezoelectric sensors, establishing two important notions for superior piezoelectric properties of ceramic: lead (Pb)-included ceramics and MPB compositions.

In 1969, the piezoelectricity of the polymer PolyVinyDene diFluoride (PVDF) was discovered after applying a high electrical field to it. PVDF has a glass transition of -35°C and typically exhibits 55% crystallinity [9,10]. This polymer was

mechanically stretched to orient the molecular chains and then poled under tension. Although PVDF demonstrates lower piezoelectric properties compared to ceramic materials like PZT and barium (BT), this discovery was also very important for the development of flexible piezoelectric materials.

In this chapter, the mechanisms of the piezoelectric and ferroelectric effects are described, providing a comprehensive understanding of these phenomena. It also includes a survey of different categories of piezoelectric materials and their applications as energy harvesters in tyres. Furthermore, the key findings of electrical conduction and their implications pertaining to the present research are summarised.

2

2.2. Dielectric materials: Mechanism

One of the crucial concepts for the understanding of piezoelectric material is the relationship between dielectric, piezoelectric, pyroelectric and ferroelectric materials [11]. In Figure 1 the different classes of dielectric materials are reported.
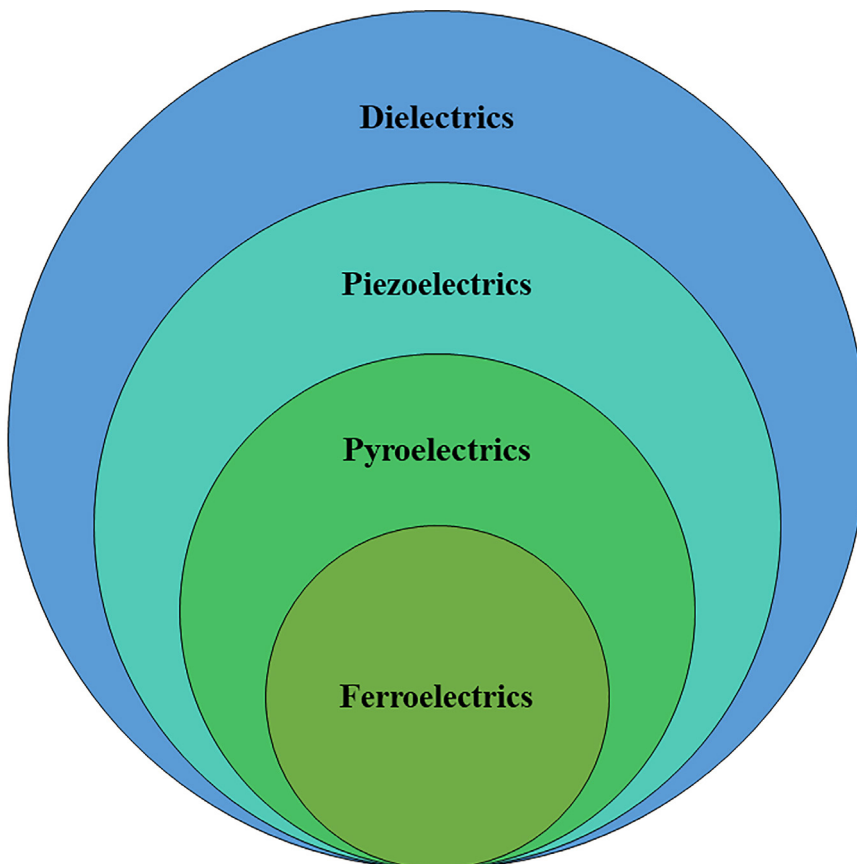

Figure 1   Different classes of dielectric materials.

A dielectric material is characterised by constituent atoms that can be ionised to a certain degree, either positively or negatively [12,13]. Piezoelectric materials are dielectric materials capable of generating negative and positive charges when an appropriate force is applied, conversely, exhibit a change in strain and stress when subjected to an external electrical field. Pyroelectric materials, on the other hand, are a category of piezoelectric materials that generate electrical charges in response to a change in temperature, in addition to external force. Ferroelectric materials encompass both pyroelectric and piezoelectric properties and show highly promising characteristics. Ferroelectric materials exhibit a spontaneous electrical polariaation that can be reversed by the application of an external electric field. In this section, the properties of dielectric, piezoelectric and ferroelectric materials are elaborated.

Dielectric materials are electrically insulating materials that possess electric dipoles, resulting in the separation of positive and negative charges at the molecular, atomic level. Within such materials, when an external electric filed is applied, cations and anions align themselves according to the direction of the electrical field, driven by electrostatic interactions. This phenomenon is referred to as electric polarisation of the dielectric materials, and it can be quantitatively expressed as the sum of the electric dipoles per unit volume (i.e. C/m^2). There are four main types of polarisation: electronic, ionic, orientational and interfacial. The type of polarisation exhibited by a material depends on the frequency of the alternating electrical field applied, as shown in Figure 2 [12].
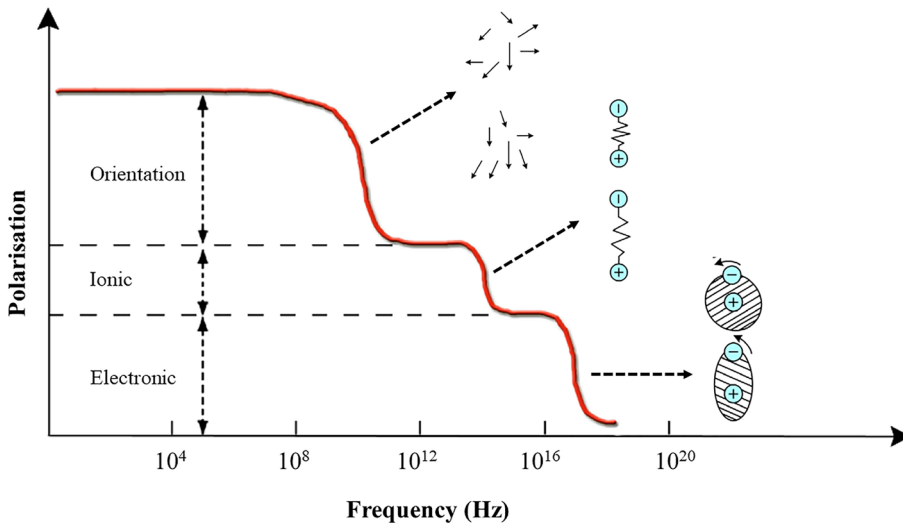

Figure 2   Polarisation types of a dielectric material under electrical field (adapted from [12]).

2

Electronic polarisation is present in all types of dielectric materials and arises from the displacement of negatively charges electron clouds relative to positively charged centres within an atom. Ionic polarisation is a characteristic of ionic material. When an electrical field is applied, cations and anions in the ionic material displace in opposite directions, forming a net dipole moment. Orientational polarisation is present only in substances having permanent dipole moments. The rotation of these permanent moments towards the direction of the electrical field contributes to the overall polarisation of the material. Interfacial polarisation, as the name suggests, occurs specifically at electrodes and grain boundaries. It is associated with charge accumulation and redistribution at these interfaces. Polar dielectric materials have a permanent electric dipole moment that aligns with the electrical field when externally applied. Non-polar dielectrics do not have a permanent dipole moment, but it can be induced in presence of an electrical field.

2.2.1   Piezoelectric materials: Mechanism

The term 'piezoelectricity' originates from the Greek term "piezein", meaning "to press". From this, piezoelectricity refers to the process of generating electrical charges by applying pressure to the materials. The piezoelectric effect can be defined as the electromechanical coupling between the mechanical and electrical states of the materials. A key requirement for piezoelectricity is the non-centrosymmetric structure of the materials, and thus no inversion centres.

A molecular model illustrating the piezoelectric mechanism is depicted in Figure 3 [14]. Before applying external force to the material, the centres of negative and positive charges coincide, resulting in no static surface charges within the material (see Figure 3a). When the material is deformed by an external force, the lattice structure also deforms, as shown in Figure 3b. In this configuration, positive and negative charges become separated, giving rise to an electric dipole. In an ideal situation, this occurs for all molecules in the material structure (Figure 3c), leading to electrical polarisation of the material. Materials with spontaneous polarisation like quartz, Rochelle salt, ZnO, conform to this molecular model depicted in Figure 3. Additionally, there exists another category of piezoelectric materials known as ferroelectric materials. These materials are characterised by spontaneous polarisation only below a certain temperature, called the Curie transition temperature. Hence, the spontaneous polarisation of ferroelectric materials can be oriented in a certain direction by applying a high electrical field during a process called 'poling,' which aligns the dipoles. Practically, molecules of ferroelectric materials, in certain conditions, already present dipoles, even in an unperturbed state,

as shown in Figure 3a. Examples of such ferroelectric materials are PZT, BT and PVDF. These materials possess the highest piezoelectric properties because piezoelectricity arises from the displacement of positive and negative charges and the change in dipole density. These aspects are further discussed in the next paragraph.
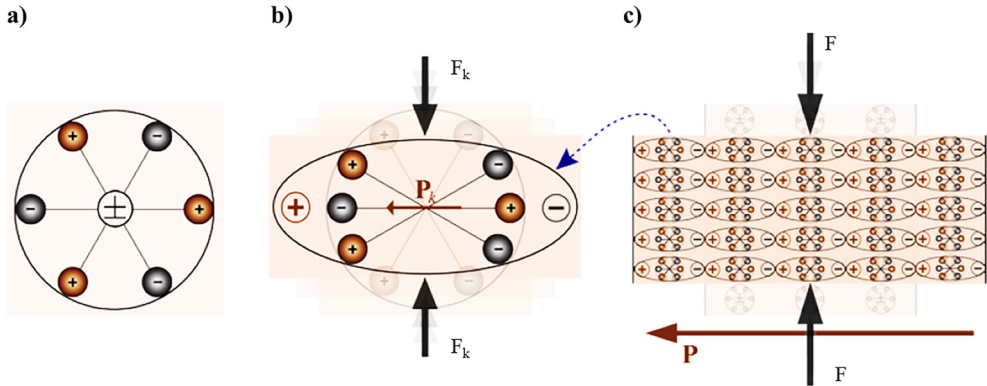
Figure 3 Molecular model of piezoelectric effect, showing the state (a) before and (b) after applying an external force and (c) the resulting polarizing effect on the surface of the piezoelectric material [14].

Piezoelectric effect is a reversible process, as mentioned earlier. Figure 4 shows the mechanism of both the direct and invert piezoelectric effects. The direct piezoelectric effect refers to the generation of electrical charges in the material under compressive and tensile stress as well as vibrations. Under deformation, the piezoelectric material becomes polarised. By applying electrodes to opposite surfaces of the piezoelectric material and connecting them through an external electrical circuit, the polarisation leads to the flow of charges. The inverse piezoelectric effect occurs when a voltage is applied across the surface of the material, resulting in mechanical deformation.

In this research project, the direct piezoelectric effect is considered due to the generation of electrical charges.
According to the linear theory of piezoelectricity, the mathematical formulation explaining the direct piezoelectric effect is as follows [15,16]:

$$D = d \cdot F + \varepsilon \cdot E \qquad (1)$$

where D is the dielectric displacement corresponding to the stored electric charge per unit area of the material, d is the piezoelectric strain coefficient, F is the force applied to the material, ε is the dielectric constant measured at a constant force, and E is the electrical field. The first term on the right-hand-side indicates that the density of generated charges in a piezoelectric material is proportional to the applied external

force when the external electrical field is zero ($E=0$). The second part of the equation accounts for the fact that the polarisation inside the piezoelectric material also creates an internal electrical field. This electrical field generates an electric displacement, resulting in surface charge density that depends on the dielectric constant of the material.
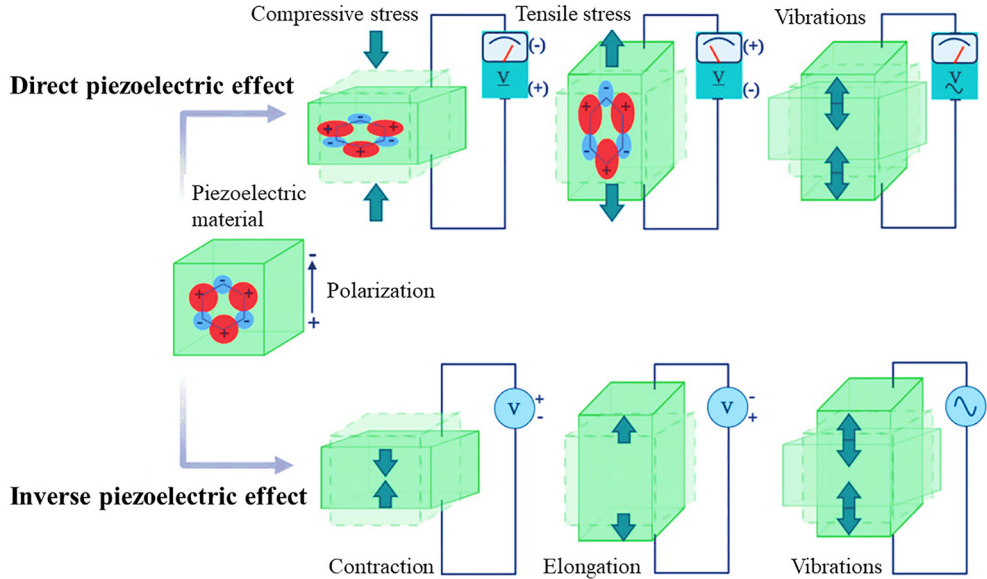
2

Figure 4   Mechanism of the direct and inverse piezoelectric effects [17].

According to the linear theory, the coupling between mechanical force, electrical field and displacement is identified using three orthogonal axes, X, Y and Z. Generally, these axes are depicted according to the labels shown in Figure 5, in which PVDF film is taken as an example. The Z axis, labelled as 3, represents the polarisation axis. While the X and Y axes are orthogonal, denoted as 1 and 2, respectively. The shear planes, labelled as 4, 5 and 6, are perpendicular to the directions 1, 2 and 3. Based on this, the equation (1) explaining the direct piezoelectric effect can be derived as:

$$D_i = d_{ij} \cdot F_j + \varepsilon_{ik} \cdot E_k \qquad (2)$$

where the indices i, j and k represent the three-dimensional axes.
d_{ij} is the piezoelectric strain coefficient of the piezoelectric material corresponding to the polarisation generated per unit of an external applied force in j direction. Thus, the first index i indicates the direction of the dielectric displacement, and the second

index j indicates the direction of the mechanical force. The unit of d_{ij} is Coulomb/Newton (i.e. C/N).

ε_{ik} is the dielectric constant in the direction of dielectric displacement i and in the direction of electrical field k. It signifies the dielectric displacement per unit of electrical field.
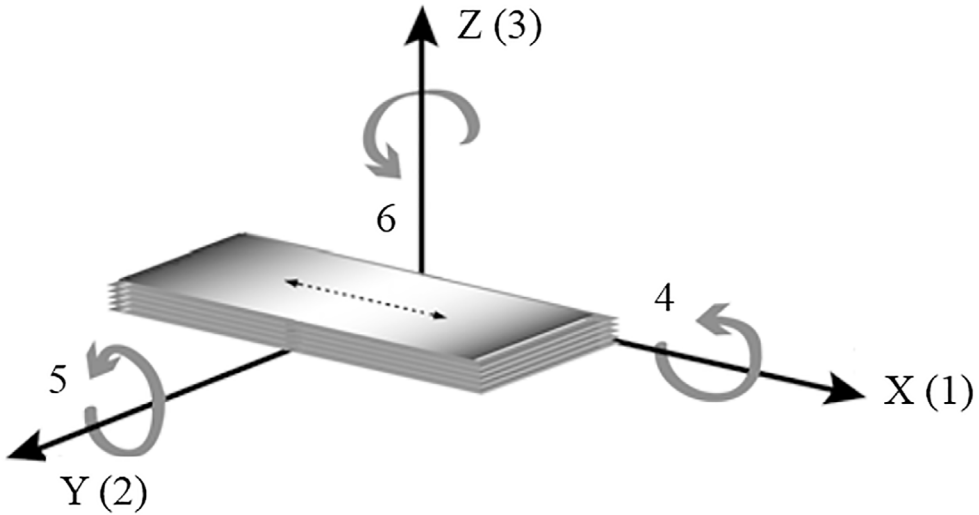

Figure 5   Tensor directions used for defining the constitutive equations from the linear theory of piezoelectricity [14].

2.2.2   Ferroelectric materials: Mechanism

Ferroelectric materials are a subclass of dielectric, piezoelectric materials [18-20]. The ferroelectric effect refers to the property of a material that exhibits spontaneous polarisation without the application of an electrical field. Permanent electric dipoles are responsible for this spontaneous polarisation in ferroelectric materials. Unlike in linear materials, the relationship between the applied electrical field and the resulting polarisation in ferroelectric materials is nonlinear and characterised by a hysteresis loop.

A bulk ferroelectric material contains microscopic regions, called domains, which can have randomly oriented electric dipoles, aligned in the same direction. In the absence of an external electrical field, when the domains are randomly oriented, the net polarisation is null. When an electrical field is applied, the domains are then aligned in the same direction, leading to the emergence of spontaneous polarisation in the material. The process of applying an external electrical field to align the domains of a ferroelectric material is called 'poling process'. Increasing the electrical

field further aligns more domains in the same direction. At a sufficiently high electrical field, almost all the domains are oriented in the same direction, resulting in the maximum polarisation. Increasing the poling temperature is also another factor enhancing the alignment of the domains. After cooling and removing the electrical field, the dipoles remain aligned. Various poling techniques, such as thermal, contact, corona, hysteresis, can be employed based on the specifications of the materials to achieve optimal alignment.

2
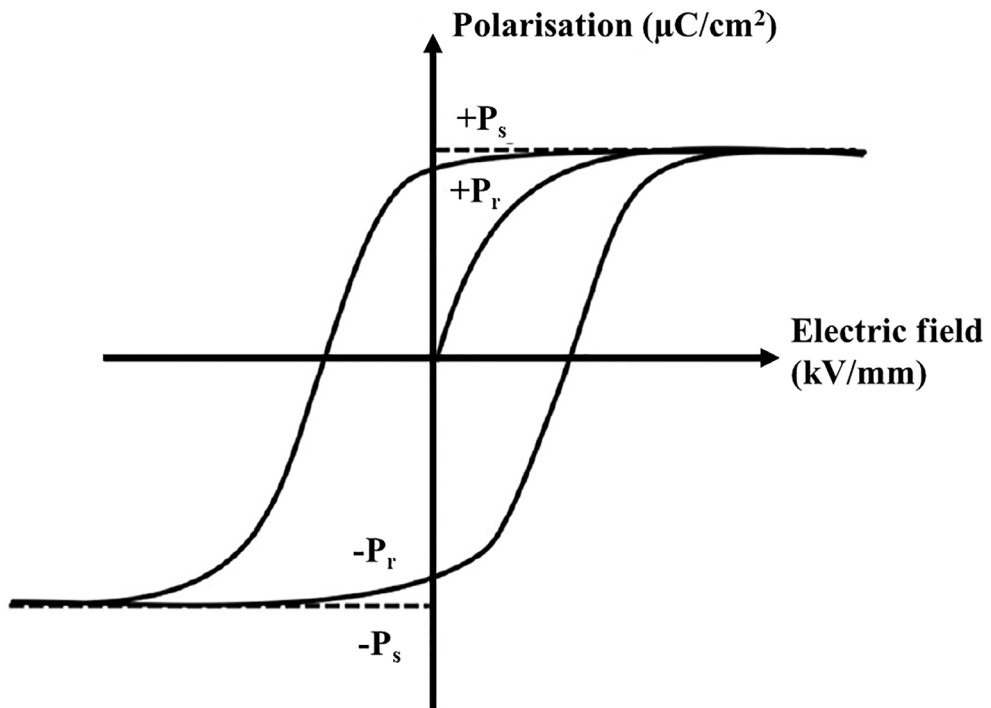
Figure 6   Ferroelectric hysteresis loop, depicting the polarisation as a function of the electrical field [23].

Typically, ferroelectric hysteresis loop measurements are carried out to measure the overall polarisation as a function of an externally applied electrical field [21-23]. The relationship between the electrical field and resulting polarisation displays hysteresis behaviour. The measurements start with a non-polarised sample. By applying an increasing electrical field, the domains in the ferroelectric material align, leading to an increase in polarisation until reaching the maximum value, called saturated polarisation P_s. At this state, the domains in the ferroelectric material are fully aligned, providing the highest degree of polarisation. The remnant polarisation P_r represents the polarisation of the ferroelectric material when the electrical field is

removed. This is slightly lower than P_s because some domains lose their ideal dipole orientation, when the electrical field is removed.

By applying a similar electrical field in the reverse direction, a reversal of the polarisation takes place, and the material becomes polarised in the opposite direction. The electrical field required to change the polarisation direction is known as the coercive field, which decreases with increasing temperature. For this reason, poling is usually performed at high temperatures.

2.3   Piezoelectric materials as energy harvesters

Piezoelectric materials have found applications in various fields due to their electromechanical coupling properties. One such application is in energy harvesting. Energy harvesters are devices designed to capture and utilise environmental energy, converting it, essentially but not exclusively, into electrical energy [24,25]. The working principle of piezoelectric energy harvesters is shown in Figure 7.
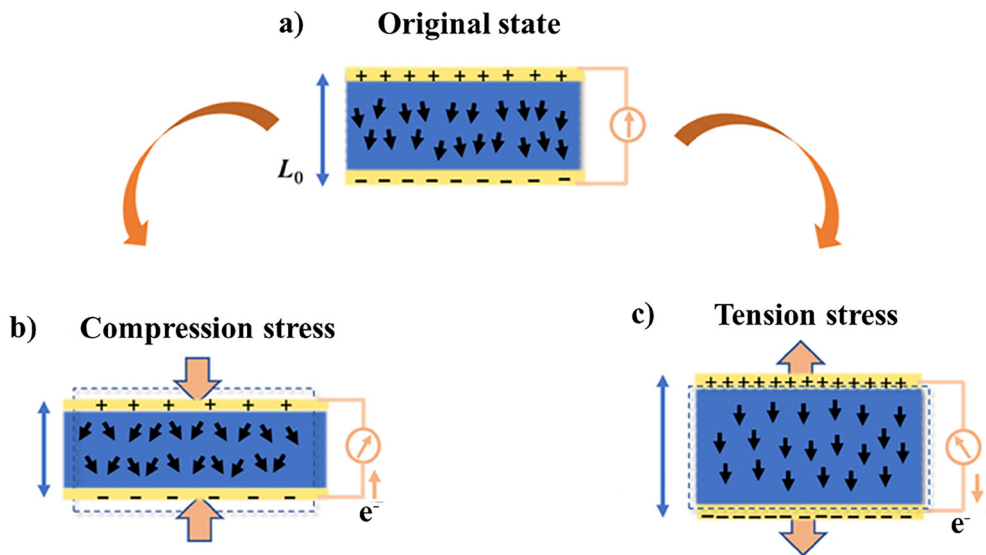
Figure 7   Working principle of piezoelectric energy harvesters (a) original state and under (b) compressive and (c) tensile stress [26].

By applying an external force to the material induces a polarisation in the poling direction and an accumulation of electrical charges on both surfaces of the piezoelectric material. Applying a compressive and tensile stress to the piezoelectric material, the polarisation decreases and increase, respectively. The connected electrodes on the surfaces of the piezoelectric materials generate a current flow.

When a stress σ is applied to the piezoelectric material, the generated charge across the electrode can be described according to the following equation [26]:

$$Q = d_{33} \cdot A \cdot \sigma \qquad (3)$$

where A is the contacting area of the piezoelectric material, d_{33} is the piezoelectric strain coefficient of the piezoelectric material corresponding to the polarisation generated in the direction *3* per unit of an external applied force in *3* direction. Considering a piezoelectric material with a thickness *h*, the capacitance of the capacitor that stores the electrical charges can be taken into account to calculate the output voltage from the material. As $C = A \cdot \varepsilon_{33}/h$, where ε_{33} is the dielectric constant in the direction of dielectric displacement *3* and in the direction of electrical field *3*, and $Q = C \cdot V$, the voltage can be expressed by Equation 4 [26]:

$$V = \frac{d_{33} \cdot \sigma \cdot h}{\varepsilon_{33}} \qquad (4)$$

The most significant advantage of the piezoelectric effect is the direct conversion of mechanical deformation into electrical charges, making it a valuable property for electrical devices and sensors. In the context of this study, the focus is on utilising piezoelectric materials in energy harvesters to power sensors, with a specific application in the automotive industry. In the following section, the principal mechanism of harvesting energy from rolling tyre conditions is discussed.

2.3.1 Piezoelectric energy harvesters for tyres

The transportation system in which vehicles can drive by themselves without human control is not far away from reality. This concept is called Autonomous Vehicles (AVs). It has a potential to improve the safety and efficiency of transportation by reducing traffic congestion, parking demands, insurance costs and accidents [27,28]. The level of autonomous driving can be distinguished by their level of autonomy, ranging from level 0, of which the driver is entirely responsible for driving, to level 5, of which all driving functions are performed by the vehicle itself. To achieve the highest level of autonomous driving, a variety of vehicle components need to be improved. To achieve full autonomous vehicles, the so-called intelligent tyres play an important role, since they serve as the sole contact between the vehicle and the road surface [29].

The intelligent tyres have an ability to report the information about road and tyre conditions to the driver, of which the information will be a real-time input for the vehicle's control system. By this function, the driving performance of the vehicle can subsequently be optimised. These tyres equipped with a sensor can provide

information related to tyre pressure, tyre-road interaction, tyre slippage, traction and maintenance requirements. The sensors are embedded in the tyres and need power to operate and collect the data, which is then transmitted to the central system of the vehicle.

One example of such a sensor is the Tyre Pressure Monitoring System (TPMS). Maintaining proper tyre pressure is a basic requirement for safe driving. Under-inflated tyres significantly contribute to accidents as they affect the braking and handling performance of the vehicle. Moreover, under-inflated tyres experience accelerated wear due to increased deflection of the tyres, leading to an unmaintainable shape. They become worn more rapidly in comparison to tyres under optimum inflation. On the other hand, over-inflated tyres result in an inappropriate traction due to reduced tyre footprints on the road surface. They become stiffer and more susceptible to damage from road defects. A TPMS indicates whether the running tyres are under- or over- inflated by monitoring the real-time pressure of tyres. The performance criteria of TPMS systems are mentioned in the regulations of the TREAD Act (USA) and EC 661/2009 (European Union): both organisations regulate that the use of a TPMS system is compulsory for all kinds of passenger cars manufactured from 2008 onwards [30,31].

Sensors like TPMS are commonly powered by batteries. However, the use of batteries results in several disadvantages, including limited battery lifetime leading to signal loss for the driver, negative environmental impact due to the presence of toxic chemicals, e.g. heavy metals, additional maintenance and costs associated with the replacement of empty batteries. Hence, in this context, piezoelectric energy harvesters reveal to be a fascinating and highly interesting alternative [32-34].

Rolling tyres undergo continuous cyclic motion while transporting a vehicle, supporting the compression loads of the vehicle plus driver and passenger(s), as shown in Figure 8. Thus, the tyres are continuously subjected to dynamic mechanical conditions that involve external forces, deformations, temperatures, as well as vibrations during rotation. When a tyre comes into contact with the road surface, the tyre partially flattens at the contact patch due to external loads and gravity. Therefore, by mounting energy harvesting materials on the inner liner in the tread region, where they are subjected to both compressive and tensile stresses, there is a potential to harvest electricity for powering a TPMS.

The tyre compounds are subjected to vibrations resulting from interaction with the road surface. The periodic bumps experienced by the car on the road lead to

variations in gravitational load during driving. Consequently, tyre vibrations can be periodic, resulting from tyre-road interaction. Likewise, the frequency of periodic vibrations is affected by the rotational speeds of the tyres, which depend on the radial and tangential accelerations of the car. The radial acceleration drops to zero in the contact patch and has a constant value in the rest of the tyre revolution, determined by the angular velocity of the wheel (ω) and a radius (r) of the tyre, $\omega^2 r$. The tangential acceleration depends on the deformation of the contact patch in the circumferential direction and only increases within the contact patch area. Both accelerations are highly dependent on driving speeds, road conditions and vehicle load.

2
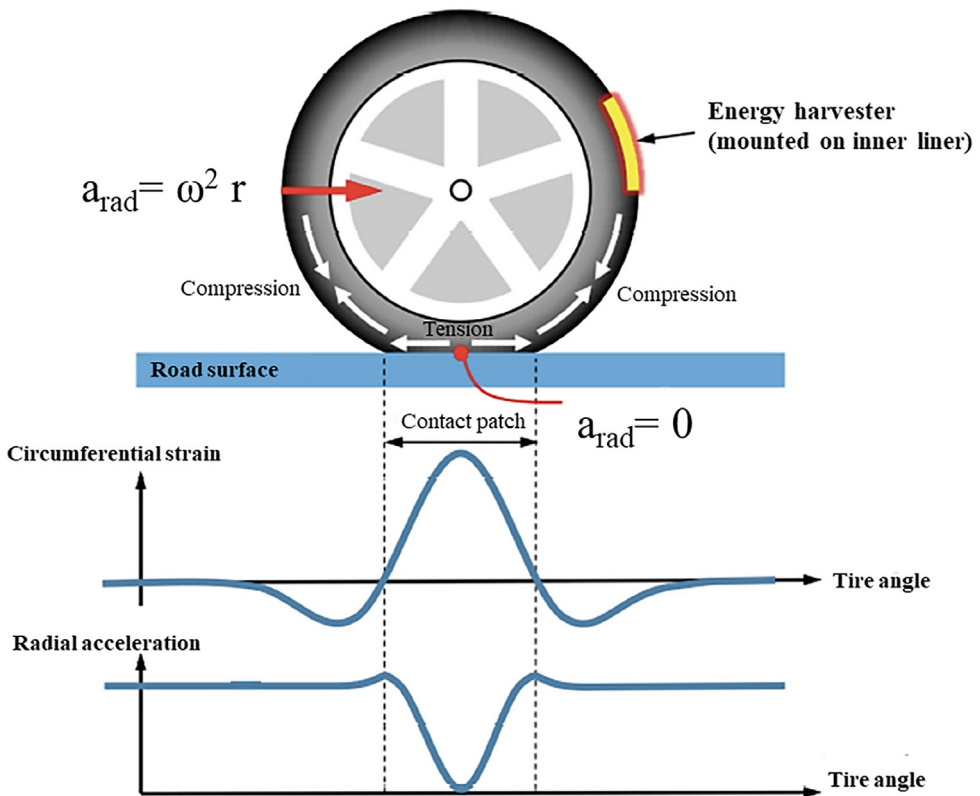
Figure 8   Dynamic mechanical conditions during tyre rolling on a road surface [34].

The vibrations in rolling tyres caused by tyre-road interactions are random and inconsistent during driving a vehicle, significantly influenced by different road conditions. The energy harvesters are therefore able to generate electricity across a wide range of frequencies due to the variations in the rolling tyres. For instance, when a car is travelling at 80 km/h, the revolution frequency is about 11 Hz (under

the assumption of a certain size of the passenger car tyre), which is considered as an average constant frequency for moving tyres at this speed. In addition, factors such as road surface roughness and fluctuations in the driving speed influence the dynamic conditions of the running tyres, further contributing to the vibrations inside the tyre. Therefore, an energy harvester must be sensitive to a wide range of frequencies, from 10 Hz up to values in the order of kHz.

Piezoelectric energy harvester can be assembled inside a tyre, on the inner liner, either on the treadwall and sidewall, as depicted in Figure 8. As being parts of a tyre, both components, piezoelectric material and electrode, need to have appropriate properties, including flexibility, durability and stability to tolerate the dynamic conditions experienced by rolling tyres, which involve variable loads, strains and temperature. Additionally, the compatibility and adhesion between the piezoelectric material and the electrodes must be sufficiently strong so that the energy harvester can withstand the harsh dynamic conditions of moving tyres. Besides flexibility, compatibility and stability, the piezoelectric material must generate sufficient electricity to power a tyre sensor (around 20-30 mJ/s), while the electrodes must be a conductive material, having an electrical conductivity above 10^{-3} S/cm [32-34].

As shown in Figure 7, the assembly of a piezoelectric energy harvester involves two main components:
1. The piezoelectric material for the electric charge generation;
2. The electrodes for inducing the flow of electric current.
In the following sections, the mechanisms of these two components are elaborated, and the state-of-the-art of their applications in tyres is reported.

2.4   Piezoelectric materials categories

Piezoelectric materials can be classified into three main categories: inorganic ceramics, polymers and composites.

2.4.1   Piezoelectric ceramic

Piezoelectric ceramics exist in the form of single crystals and polycrystalline ceramics. The main difference of single crystals and polycrystalline materials from amorphous materials is related to the length scale over which the atoms are arranged. Single crystals have a periodic atomic lattice structure throughout their entire volume, exhibiting long-range order. Polycrystalline ceramics consist of multiple grains, each characterised by a single crystal structure. Amorphous materials lack a periodic atomic arrangement and symmetry, making them unsuitable for piezoelectric applications. In other words, the pure random structure of amorphous

materials does not classify them as piezoelectric materials. The arrangements of atoms in single crystals, polycrystals and amorphous materials are shown in Figure 9.
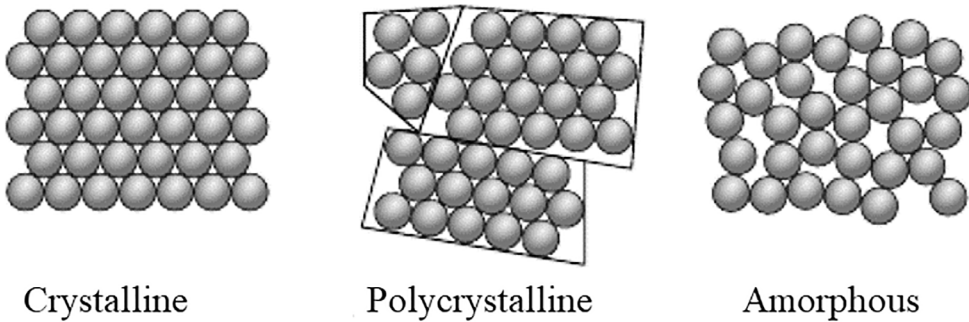
Crystalline   Polycrystalline   Amorphous

Figure 9   Arrangement of atoms in crystalline, polycrystalline and amorphous materials.

Crystalline structures exhibit a periodic arrangement of atoms in the unit cell and can be classified into 32 classes based on their symmetry properties of the unit cell. Among these classes, 20 are non-centrosymmetric and show piezoelectric properties. These piezoelectric crystal classes can be further grouped into seven crystal systems: triclinic, monoclinic, orthorhombic, tetragonal, rhombohedral, hexagonal, and cubic, as shown in Figure 10.

Piezoelectric single crystals can occur naturally, such as quartz, and synthetically produced, like lithium niobite and lithium tantalate. Quartz with the chemical formula SiO_2 is piezoelectric at room temperature in its trigonal crystal structure, known as α-quartz. At 573°C, a structural phase transition takes place, leading to the formation of the hexagonal structure, known as β-quartz. As a mineral, quartz is present in the Earth's composition up to about 12 wt%. Additionally, quartz can be prepared through the hydrothermal method, but its piezoelectric coefficient is very small, less than 3 pC/N [1]. This limitation makes it unsuitable for sensor applications. To overcome the small piezoelectric effect in natural crystals, synthetic single crystals with increased piezoelectric properties have been developed. One well-known synthetic single crystal is lithium niobate, which can achieve a piezoelectric coefficient d_{33} up to 5-6 pC/N and d_{15} up to 70 pC/N. The Curie temperature of 1140°C makes it an interesting material for high-temperature applications. Nevertheless, single crystal materials are not as widely developed as polycrystals due to their low piezoelectric coefficients. The complex manufacturing process and the low piezoelectric coefficient make them unsuitable for sensor applications [11].
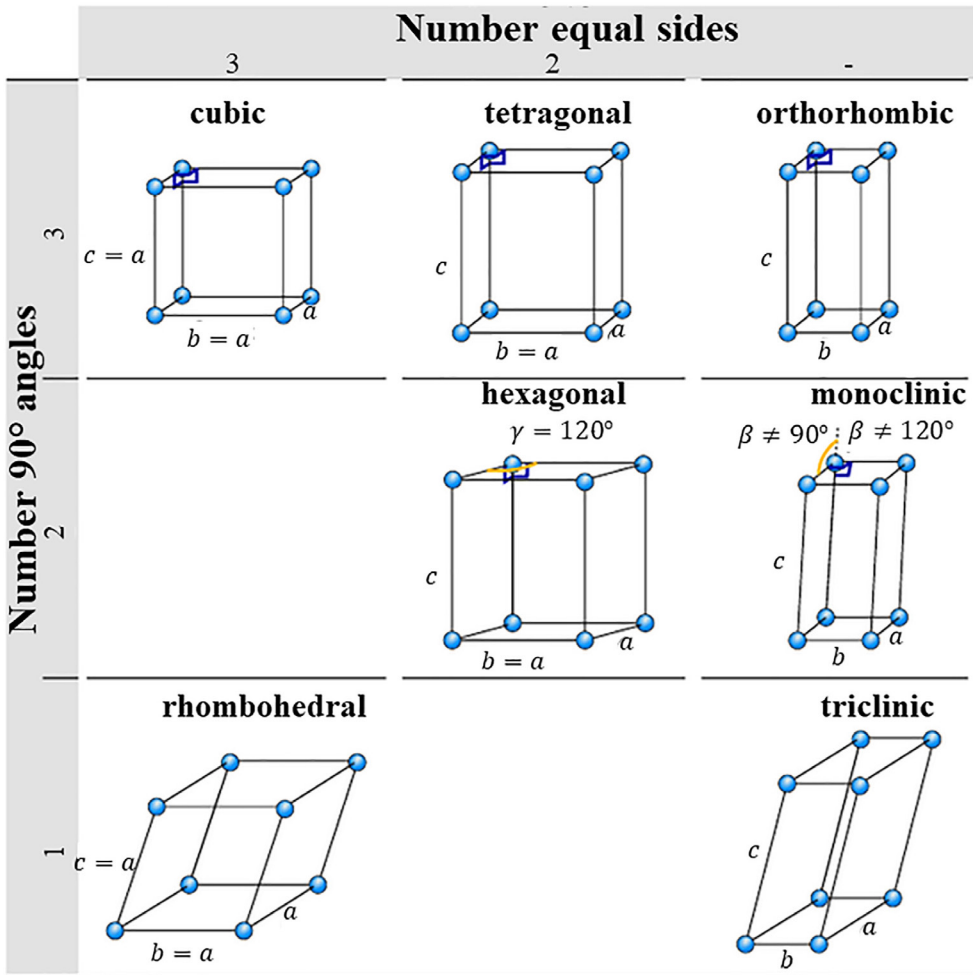
Figure 10 Seven types of crystal structures [35].

Polycrystalline ceramics are the most commonly used piezoelectric ceramics due to their outstanding piezoelectric coefficients as well as cost-effective manufacturing process. Barium Titanate (BT) and Lead Zirconate Titanate (PZT) were the first piezoelectric polycrystalline materials to be discovered. The manufacturing process of polycrystals involves five main phases [11]: (1) mixing of the raw ingredients, (2) calcination, (3) forming, (4) sintering and (5) poling process. Initially, powders of the raw materials, for example lead, zirconium and titanium oxide, are mixed in the desired proportions. Afterwards, a chemical reaction of these raw materials takes place during the calcination step, where the mixture is heated to a temperature between 700-900°C. From this step, it results in a polycrystalline substance, which is then ground and shaped into the desired geometry. If a bulk film of this material

is required, the polycrystals are compressed at high temperature. The sintered material is then cut and polished. The final step is the poling process. The material is then sputtered with a metal electrode and polarised by applying a high electrical field. It is possible to manufacture piezoelectric ceramics in different shapes, like disks, rings, plates, bars, cylinders.

Polycrystalline ceramics have a molecular structure with the formula ABO_3 and a perovskite structure, as shown in Figure 11. A^{2+} and B^{4+} are cations of different sizes and O^{2-} is the anion that bonds to both cations. A^{2+} is the larger cation located in the corners of the unit cell, and B^{4+} is the smaller cation situated in the centre of the unit cell, depending on its type [20,36]. The oxygen anions O^{2-} are positioned at the centre of the faces. In the perovskite structure, the cation A is coordinated with 12 oxygen ions, and the cation B is coordinated with 6 oxygen ions, forming an octahedra. The edge of the unit cell is normally a few angstroms (Å) in length (i.e. 1 Å = 0.1 nm).
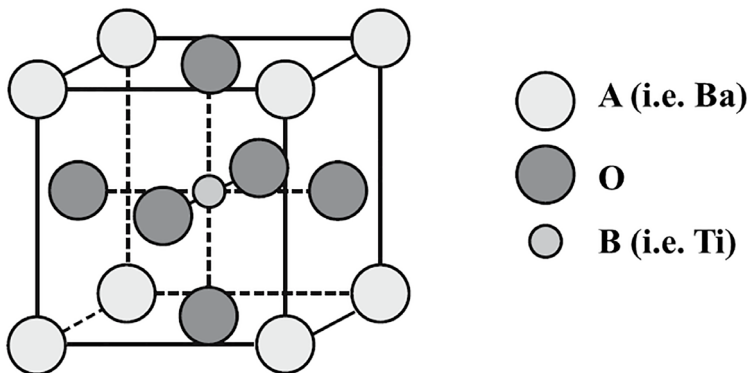
Figure 11   Perovskite structure ABO_3, for example $BaTiO_3$.

The unit cell of polycrystals undergoes a phase transition and deformation of the crystals, resulting in an increase in polarisation. The lattice shown in Figure 11 represents a cubic cell, where the B ion is located at the centre of the oxygen octahedron. $BaTiO_3$ has this structure only above 120°C. Below this temperature, $BaTiO_3$ undergoes a structural phase transition: the central titanium Ti^{4+} ion and the surrounding oxygen O^{2-} and barium Ba^{2+} ions move away from the centre of the unit cell along the c-direction. This transition is evident in Figure 12, showing the phase transition of the ferroelectric $BaTiO_3$ as a function of temperature. The unit cell of $BaTiO_3$ is tetragonal in the range of temperatures between 0 and 120°C. In this phase, the centres of positive and negative ions do not coincide, leading to the creation of a spontaneous polarisation. The temperature at which a transition occurs from a non-centrosymmetric to a centrosymmetric structure, i.e. 120°C for $BaTiO_3$, is called the

Curie temperature. This temperature is of high importance for ferroelectric materials, because it defines their range of applications. Below 0°C, two additional phase transitions occur: firstly, an orthorhombic transition, and at -80°C, a rhombohedral transition. These two structures are non-centrosymmetric, meaning that the central ion (Ti^{4+}) is displaced from the centre and a dipole moment is created. Thus, they exhibit ferroelectric properties.
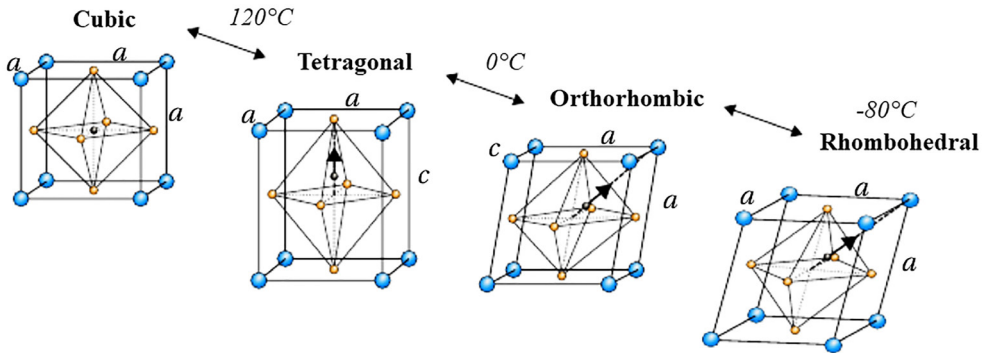

Figure 12   Phase transitions of $BaTiO_3$ as a function of temperature [37].

Beside the Curie temperature, another important aspect of polycrystalline materials is the Morphotropic Phase Boundary (MPB) [38]. Polycrystalline materials are produced from the metal oxide of the respective metal included in the perovskite structure. Changing the proportion of these metal oxides results in different structures of the polycrystal. The MBP is defined as the interface between two phases of the crystalline material. To better understand this, the phase diagram of a perovskite material is represented in Figure 13. The phase diagram shows the phase of a polycrystalline material as a function of temperature and the proportion of the metal oxides. Figure 13 shows the phase diagram of PZT with the chemical formula $Pb(Ti_xZr_{1-x})O_3$. The x-axis represents the molar amount of $PbTiO_3$, where the value x=0 corresponds to 0 mol% of $PbTiO_3$ and 100 mol% $PbZrO_3$, while x=100 corresponds to 100 mol% of $PbTiO_3$ and 0 mol% $PbZrO_3$. The Curie temperature of PZT varies with the composition of $PbTiO_3$ and $PbZrO_3$. Pure $PbZrO_3$ has a Curie temperature of around 234°C, converting from orthorhombic to cubic phase. Pure $PbTiO_3$ has a Curie temperature of 480°C, transitioning from tetragonal to cubic phase. Thus, PZT has a Curie temperature between 234°C and 480°C, depending on its composition, and loses its piezoelectric properties above this range. Below this temperature, three phases exist: orthorhombic, rhombohedral and tetragonal. All three phases are piezoelectric. The phase boundary between rhombohedral and tetragonal phases is MBP, as PZT contains approximately equal contents of

rhombohedral and tetragonal unit cells. The MBP composition results in $Pb(Ti_{0.48}Zr_{0.52})O_3$, and in this composition, PZT exhibits outstanding piezoelectric performance. A further advantage is that, for PZT, the MBP occurs at a relatively low temperature range. This makes PZT one of the most commonly used piezoelectric ceramics.

2
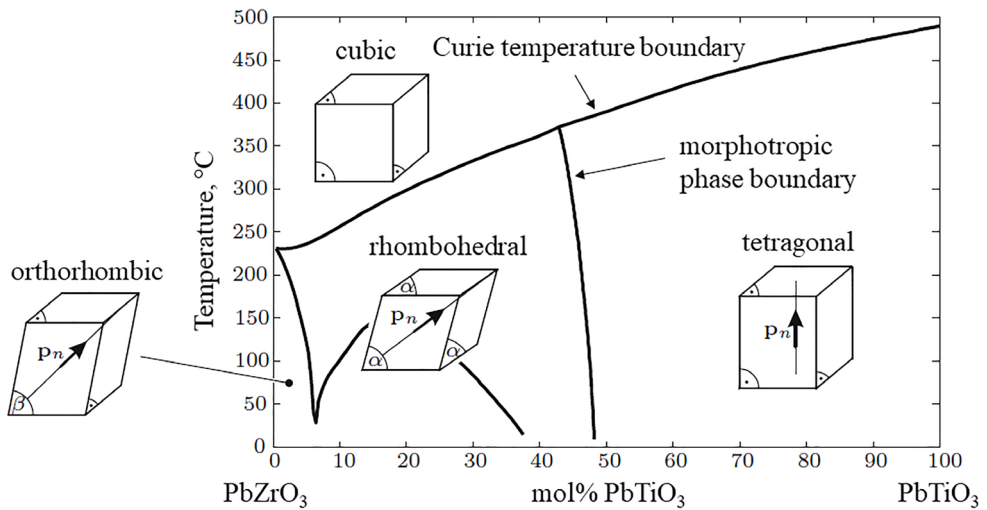
Figure 13   Phase diagram of PZT.

2.4.1.1   Lead-free polycrystalline materials

Lead-based composites are widely used in electronic devices due to their good piezoelectric properties. However, due to government regulations and classifications of lead as a hazardous substance, there is an increased interest in lead-free piezoelectric materials. In Europe, the directive on Restriction of Hazardous Substances (RoHS, 2002/95/EC) restricts hazardous substances used in electronics, including lead. The most important lead-free piezoelectric materials are based on bismuth sodium titanate $Bi_xNa_xTiO_3$ (BNT), bismuth potassium titanate $Bi_xK_xTiO_3$ (BKT) and sodium potassium niobate $K_{1-x}Na_xNbO_3$ (KNN).

Bismuth-based piezoelectric materials are characterised by Ti^{4+} as the central ion and Ba^{3+} as the ion in the corners of the perovskite structure. BNT is rhombohedral and BKT is tetragonal. However, the piezoelectric coefficients of BNT and BKT are still much lower than those of PZT. Therefore, researchers have been investigating methods to improve those properties [39]. KNN, with the formula $K_{1-x}Na_xNbO_3$, is based on $KNbO_3$ and $NaNbO_3$, both of which are orthorhombic at room temperature. The phase diagram of KNN is very complex, with several thermally induced phase

transitions and MBPs [40,41]. This complexity arises from the fact that pure $KNbO_3$ exhibits only three phase transitions, while in $NaNbO_3$ has seven phase transitions. The most investigated MB

PT is $K_{0.5}Na_{0.5}NbO_3$, that is also orthorhombic at room temperature. At 200°C, KNN undergoes a phase transition from orthorhombic to tetragonal, resulting in a slight decrease in spontaneous polarisation. At 400°C, KNN undergoes to a further phase transition, from tetragonal to cubic. Thus, the Curie temperature of KNN is 400°C. The high operational temperature as well as the high piezoelectric coefficients makes this lead-free piezoelectric ceramic, KNN, a plausible alternative for PZT.

2.4.2   Piezoelectric polymers

Although piezoelectric ceramics have high piezoelectric coefficients and thus perform well in sensor applications, they still have limiting aspects, particularly for tyre applications, such as brittleness (generally at less than 2% deformation). Piezoelectric polymers show better mechanical flexibility compared to ceramics. Although, they generally have lower piezoelectric coefficients, these materials can deform with larger strains and demonstrate better durability under dynamic applications. There are different subcategories within the group of piezoelectric polymers. Those are classified based on the origin of their piezoelectric mechanisms, including bulk polymers and polymeric composites [42,43].

Bulk polymers exhibit piezoelectric effects based on their molecular structure. The presence of molecular dipoles that can be oriented through the poling process is the main criteria for these polymers to exhibit piezoelectricity. There are two types of bulk polymers: amorphous and semi-crystalline. As above-mentioned, piezoelectricity and ferroelectricity are significantly affected by the crystallinity of the materials. Thus, also for polymers, the crystallinity plays a major role in piezoelectric effect. However, piezoelectricity in amorphous polymers has also been proven by a few researchers, as demonstrated in the case of polyimide, PolyVinyl Chloride (PVC). In these polymers, the orientation of the molecular dipoles contributes to the piezoelectric effect. During the poling process, the molecular dipoles are aligned, and the piezoelectric coefficient can be improved by 4-5 times. However, the literature of piezoelectric properties of amorphous polymers is limited due to their poor performance. PVC, for example, exhibits weak piezoelectric activity [10,44,45] due to its carbon-chloride dipole creating a dipole moment and resulting in a low level of piezoelectricity. The piezoelectric coefficient d_{31} of PVC ranges from 1.5 to 5 pC/N. PolyAcriloNitrile (PAN) has a large dipole moment in

the nitrile groups. The piezoelectric coefficient d_{31} of PAN ranges from 1 to 2 pC/N [46,47].

Semi-crystalline polymers are a more extensively investigated category compared to amorphous polymers due to their high piezoelectric performance. Their operational principle is similar to that of piezoelectric ceramics. The most known semi-crystalline polymer is PolyVinyliDene diFluoride (PVDF) [48]. It is the polymerised monomer of fluoroethylene and consists of the repeating unit CH_2-CF_2. PVDF exists in several phases: α-, β-, γ-PVDF, as shown in Figure 14, differing in the molecular chain orientation. PVDF has a net dipole moment due the presence of highly electronegative fluorine (F) and electropositive hydrogen (H). The dipoles can be oriented through the C-C single bonds, enabling the polarisation of the polymer itself. α-PVDF has Trans-Gauche-Trans-Gauche (TGTG) conformation and shows no piezoelectric effect due to the mutual compensation of the dipole moments. On the other hand, β-PVDF has a Trans-Trans-Trans-Trans (TTTT) conformation and exhibits piezoelectricity due to the alignment of H and F in two opposite parts of the C-C chains, resulting in a net dipole moment.
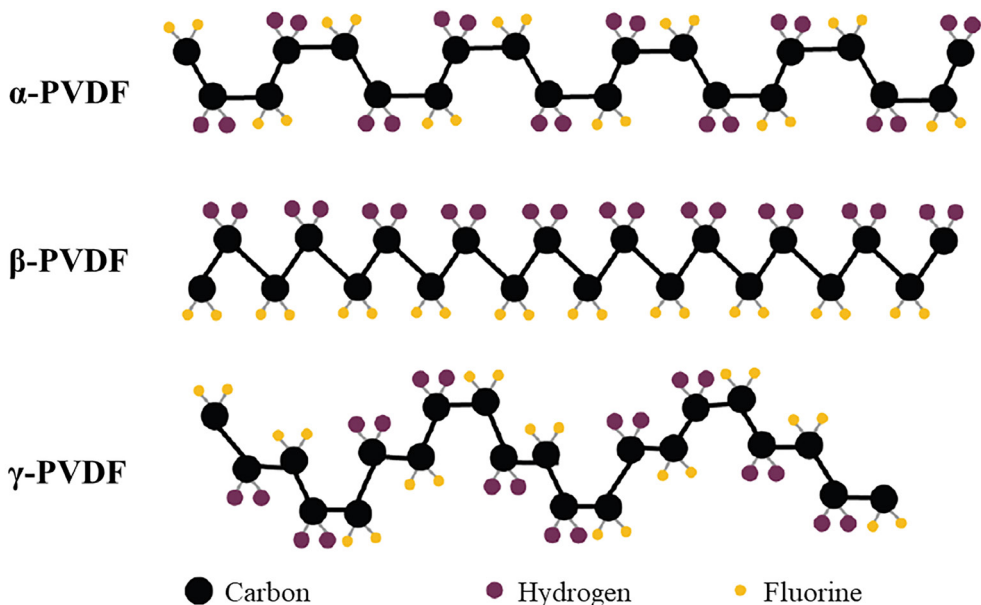

Figure 14   Chain conformation of three phases of PVDF [48].

The β-PVDF can be obtained through different methods: mechanical stretching, annealing and electric poling processes. PVDF is indeed piezoelectric and ferroelectric, as the spontaneous polarisation, i.e. the β phase, can be induced through

the poling process. The melting point of PVDF is 180°C and the glass transition temperature is -35°C. The Curie temperature is around 100°C, thus the application temperature is between room temperature and 90°C.

The piezoelectric coefficient d_{33} ranges from -24 to -34 pC/N, and d_{31} from 8 to 22 pC/N. Note that the negative sign indicates that deformation and electrical displacement have opposite directions. When the material undergoes compression (i.e. negative strain), PVDF generates electrical charges along the poling direction. Although the high entity of the dipole moment formed by H and F atoms, the piezoelectric coefficients of PVDF are still lower than of ceramics due to the crystalline state of the polymer. The polymer contains a relatively high amount of amorphous phase, up to 50%, lowering the piezoelectric properties. To increase the crystallinity and the piezoelectric properties, PVDF is commonly used in copolymers together with TriFluoroEthylene (TrFE), known as P(VDF-co-TrFE), characterised by 90% of crystallinity.

Several studies have been carried out by applying piezoelectric ceramics and polymers in tyres for powering sensors [34,49,50]. Piezoelectric ceramic disks with metal electrodes were mounted in tyres [51-53]. In all cases, the ceramics were able to generate the electrical power over a wide range of tyre running speeds, 30-180 km/h, but they did not fulfil the reliability and cost requirements. In 2012, Makki and Pop-Iliev [54-56] compared a piezoelectric ceramic PZT with a polymer PVDF, by applying both materials onto the inner liner of a tyre. The PZT disk with a thickness of 0.23 mm produced a higher electrical power output, i.e. 4.5 mW, compared to a PVDF film with a thickness of 0.11 mm and a lateral dimension of 40 x 40 mm, which gave only 0.85 mW. Nevertheless, the authors concluded that the higher flexibility of PVDF is advantageous over piezoelectric ceramics, which are limited in terms of rigidity and interfacial adhesion. The flexibility of PVDF leads to a longer lifetime and good performance under dynamic applications.

2.4.3   Piezoelectric composites

To summarize the previous paragraphs, bulk piezoelectric ceramics have undoubtedly high piezoelectric performance but are too brittle to be integrated into flexible electronics. Bulk piezoelectric polymers like PVDF have higher flexibility but lower piezoelectric properties. Their main drawback is the low operational temperature range, i.e. below 100°C. Composites that include piezoelectric ceramic particles in a polymeric matrix offer the advantage to tailoring both the mechanical and electrical properties [57-59].

2

The preparation of ceramic-polymer composites involves melt mixing the polymers with ceramic particles. If a ferroelectric ceramic is used as a filler, a poling process needs to be carried out after the mixing and the vulcanisation of the composite. The polymer type, the ceramic particle dispersion influence enormously the poling process, in addition to electrical field and the temperature.

The connectivity between the piezoelectric ceramic particles plays a crucial role in the physical and electrical properties of the composites. Newnham defined ten different connectivity patterns of piezoelectric composites, as shown in Figure 15 [60]. Those patterns have the following notations: 0-0, 0-1, 0-2, 0-3, 1-1, 2-1, 2-2, 2-3, 1-3, and 3-3. In the notation, the first number represents the physical connection and contact points of the ceramic phase, while the second number represents the polymeric phase.
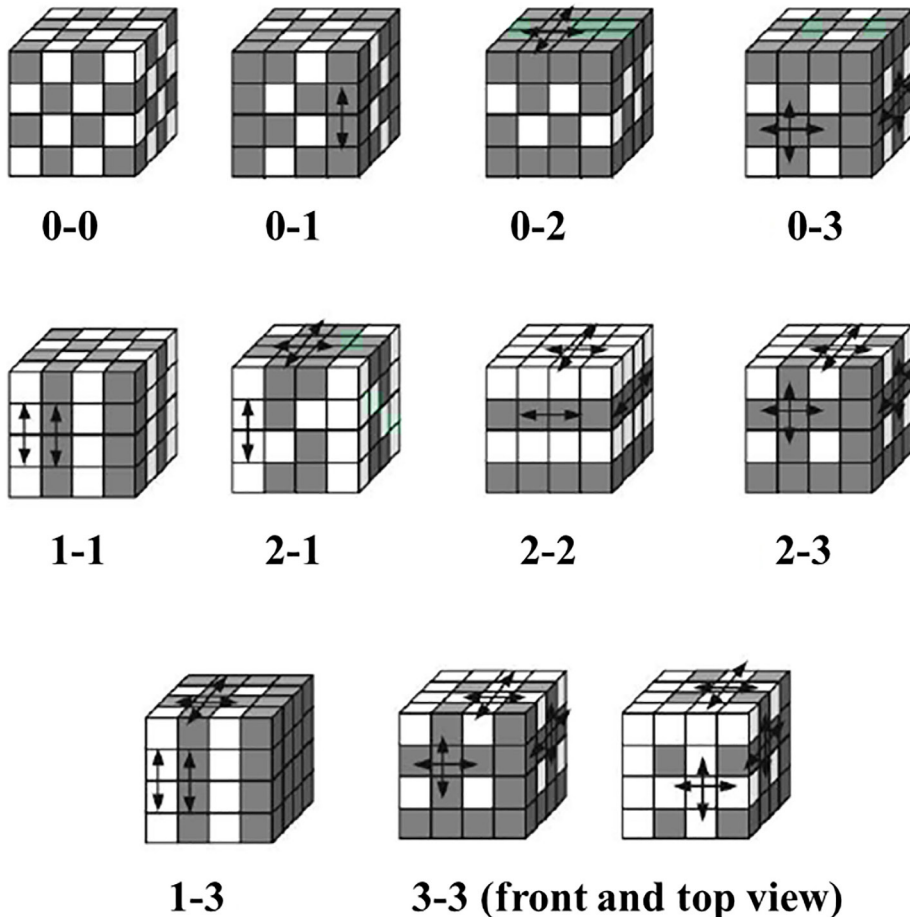
Figure 15 Connectivity patterns of piezoelectric composites [60].

In 0-0 composites, neither the ceramic nor polymeric phase is self-connected, while in 3-3 composites, both phases are self-connected in all three dimensions. The most common pattern is the 0-3 composites, consisting of the random dispersion of piezoelectric ceramic in the polymeric materials. This composite has an easy manufacturing process. However, achieving good connectivity in the ceramic phase requires a volume fraction above the percolation threshold. This compromises the mechanical flexibility of the composite. Composites with 1-3 connectivity have recently been investigated for their promising advantage of obtaining good piezoelectric coefficients at low volume fractions. This type of composite includes ceramic rods, fibres aligned along the poling direction. Several methodologies are used to prepare 1-3 composites, like injection moulding, co-extrusion, dielectrophoresis. The selection of proper piezoelectric ceramics and polymeric matrices is essential for tailoring the properties of piezoelectric composites. Several studies have reported the use of different types of ceramics in polymeric matrices like polyurethane [61,62] epoxy [21,62,63], polyimide [64], etc. In these works, the piezoelectric coefficients of the composites reached the values of 25-30 pC/N. Besides the properties of the ceramics, the matrix properties, including viscosity, microstructures, as well as compatibility with the filler, are crucial. The polymeric matrix plays a vital role in the piezoelectric efficiency of the composites. Stuber et al. [62,65] studied different types of ferroelectric ceramics: $BaTiO_3$ (BT), $K_{0.5}Na_{0.5}Li_{0.03}NbO_3$ (KNLN) and $PbZrTiO_3$ (PZT) in polymers such as polyurethane, epoxy resin and PolyDiMethylSiloxane (PDMS). The main conclusion from this work was that the conductivity of the matrix affects the poling process. After only 10 min of poling, the composites were fully polarised and reached a high value of the piezoelectric coefficient. Studies on modelling the behaviour of composites at varying volume fractions of ceramic confirmed that the dielectric constant of the matrix also plays an important role [66,67].

Tyres are made by elastomeric materials. Up to now, a piezoelectric composite based on a synthetic and natural rubber has not been optimally developed. Only a few investigations have been carried out on natural and synthetic elastomers [68,69]. In these studies, elastomers have not been able to reach piezoelectric coefficients higher than 1 pC/N.

Thus, piezoelectric composites are interesting material as they can be compatible with tyre compounds and have no limitations in terms of operational temperature. However, it remains challenging to prepare a piezoelectric compound that combines both compatibility with tyre compounds (i.e. elastomeric-based) and a high piezoelectric coefficient.

2.5 Conductive polymeric materials

From the literature described in the previous paragraph, piezoelectric energy harvesters typically included a metal electrode. This electrode has a high electrical conductivity, contributing to the optimal performance of the harvester by facilitating the transfer of electrical current from the piezoelectric material surface to the capacitor. However, the use of metal electrode is not appropriate for tyre applications due to its rigidity and incompatibility with tyre compounds. One of the most attractive alternatives to a metal electrode is the use of electrically conductive elastomers, which possess an elastic nature and compatibility with tyre compounds.

Elastomers consist of polymeric chains of carbon atoms covalently bonded to hydrogen and other chemical groups like methyl groups. As a result of these covalent bonds, the electrons are not delocalised along the polymeric chain, making elastomers insulating materials. The electrical conductivity of the elastomers increases when they are filled with fillers with high intrinsic electrical conductivity, like carbon black. Figure 16 illustrates the range of electrical conductivity for insulators, semi-conductors and conductors. Insulating elastomers typically exhibit electrical conductivity in the range of 10^{-18}-10^{-7} S/cm. Commonly, elastomers like Natural Rubber NR, Butadiene Rubbers BR have an electrical conductivity in the range of 10^{-15}-10^{-14} S/cm. Carbon blacks have a high intrinsic electrical conductivity, ranging from 10^{-2}-10^{1} S/cm. The incorporation of carbon black into rubbers increases their electrical conductivity, reaching the semiconductor range with conductivity values in the range of 10^{-7}-10^{1} S/cm.
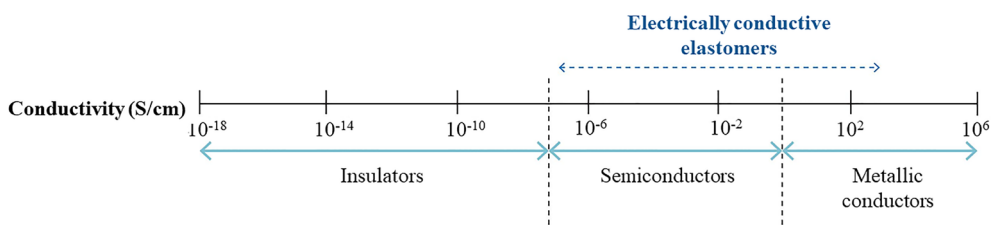
Figure 16   Conductivity range of elastomers, elastomeric composites and metals [70].

2.5.1 Carbon black as core for conductive polymers

Carbon black is produced through the thermal decomposition of hydrocarbons from various sources and is available in various grades with different particle sizes, specific surface areas, structures. Carbon black contains almost 95% of pure carbon with small amounts of hydrogen, oxygen and nitrogen. Structural properties of carbon black are shown in Figure 17.
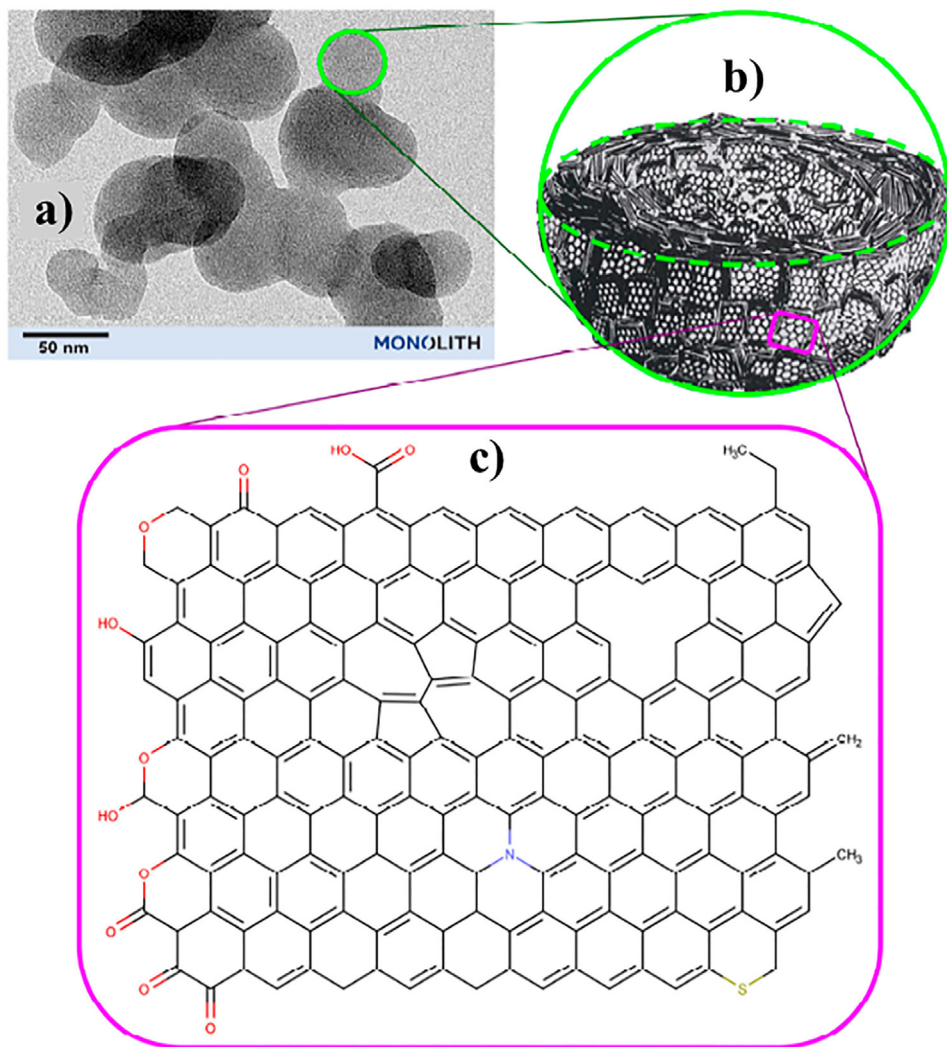
Figure 17 (a) Microscope image of carbon black particles; (b) schematic view of primary particle composition and (c) different chemical groups on a graphene layer [77].

The carbon structure of a carbon black particle consists of concentrically aligned vortex layers of graphite domains, as shown in Figure 17b [71]. Within each layer, the carbon atoms are aligned and at the edges of the graphite layers, carbon atoms are mostly bonded with hydrogen atoms. Sulphur and nitrogen atoms are also present, as originated from the precursor oil used as a feedstock, while oxygen is chemisorbed when heated carbon is exposed to air [72,73]. Several oxygen-based

functional groups have been detected and their presence has a profound effect on carbon black surface properties. Carbon blacks can have either acidic groups as carboxyl, anhydride, lactone, and phenol and basic character, as pyrone, carbonyl, ether and quinone, depending on the amount and type of the surface functional groups [72-74]. The surface chemistry of carbon black influences the curing process of the elastomeric composite. Acidic groups absorb the crosslinking agents, delaying the onset of curing process. Based on this property, carbon blacks are designated with the code "S" (slow curing) when with acidic nature and with the code "N" (normal curing) when with basic nature. Currently, the conventional carbon blacks used are those designated with the N-code [75].

Carbon black morphology, including specific surface area, structure and porosity, depends on its manufacturing process. This filler is produced by the partial combustion of oil and natural gases. Nowadays, the carbon blacks for rubber industry are primarily produced using the furnace process [74,76]. In the first stage of the process, hydrocarbon fuels such as natural gas in gaseous state are heated up to temperatures ranging between 1650-1900°C to initiate an exothermic combustion reaction. In the second stage of the process, an oil feedstock is added into the reactor for the formation of carbon black at elevated temperatures and pressures.

The initial exothermic reaction is important for the subsequent endothermic cracking reaction consisting of the breakdown of carbon-hydrogen bonds in the oil feedstock and the formation of carbon black particles. After losing hydrogen, these fragments precipitate from the gas phase and act as nuclei for further precipitation until all oil feedstock is consumed. The endothermic cracking reaction proceeds concurrently with exothermic reaction until the quenching water is added to the reactor. The different stages involved in carbon black formation include the atomization of feedstock, the formation of primary particles, and the subsequent development of particle aggregates. The specific surface area of carbon black depends on the reaction temperature. When more fuel is added, higher is the temperature and higher is the specific surface area. This is because the formation rate of nuclei increases at higher temperatures. The faster the formation rate of nuclei, the earlier the cessation of particle growth, thereby limiting their particle size [76,78]. Thus, highly reinforcing carbon blacks are produced at higher temperature and shorter residence time.

Carbon blacks are categorised based on their specific surface areas and structures. The specific surface area of the carbon blacks is determined by the primary particle size that determines the available contact area for interaction with other carbon black particles and the elastomeric matrix. This parameter is commonly determined using

2

standard methods that involve the adsorption of gas on the carbon black surface. Nitrogen surface area (Brunauer-Emmett-Teller BET method, ASTM D6556-21) is used to measure the total surface area of carbon blacks, while Iodine Adsorption Number (IAN, ASTM D1510-21) is utilised to measure the external surface area of carbon black, including porosity, due to the small size of the iodine molecule. The structure of the carbon black is measured using the Oil Adsorption Number OAN (ASTM D1765-21) which characterises the void volume of carbon black aggregates,agglomerates. Figure 18 clearly shows the effect of specific surface area and structure of carbon black on its dispersion in elastomeric composites. A higher specific surface area implies small particle size and in turn a higher number of particles at a given loading. The structure defines the aspect ratio of the aggregates. A higher structure of carbon black implies more branched aggregates.
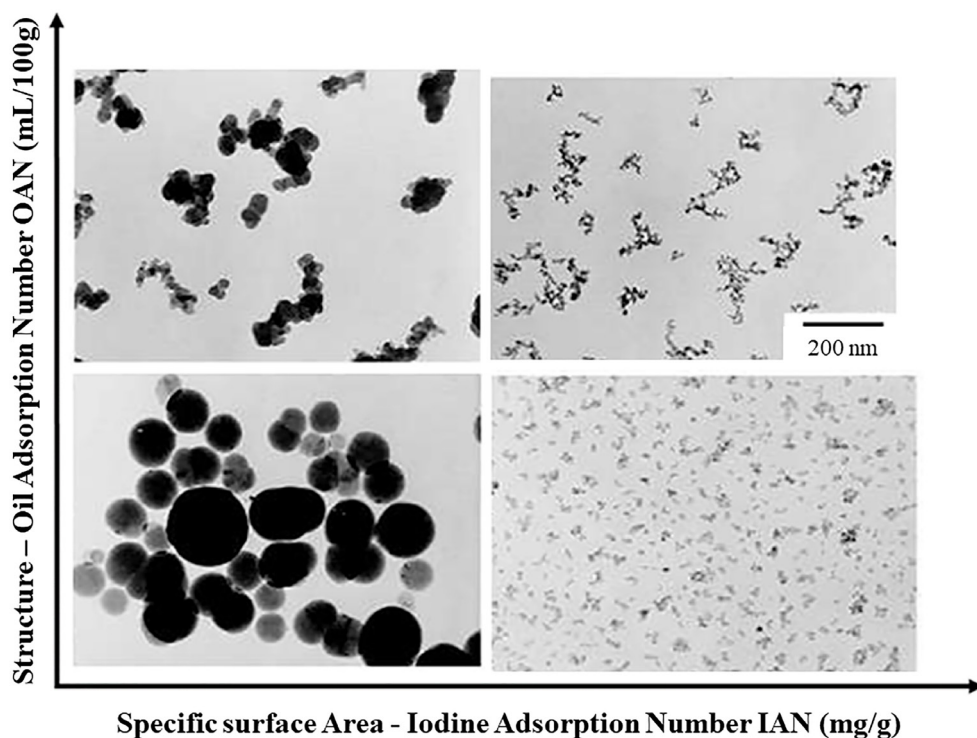
Figure 18   Relationship between specific surface area and structure of carbon blacks [76].

There are two categories of carbon blacks: conventional and conductive. The conventional carbon black classification was introduced with ASTM D1765. Carbon blacks of this category have a nomenclature consisting of a letter, i.e. N and S for normal and slow curing, followed by three digits. The first digit ranging from 1 to 9 indicates the specific surface area, with lower numbers corresponding to higher

specific surface areas. The following two digits are randomly assigned. For example, carbon blacks in the 100-series black have the largest specific surface area of around 130-145 m^2/g and exhibit the most reinforcing properties. In addition to conventional carbon blacks, there are special grades, known as conductive carbon blacks. These blacks are manufactured to have a specific surface area higher than 150 m^2/g and an OAN structure higher than 100 mL/100g. They were specifically designed to achieve high ultimate conductivity at lower loading levels. They are characterised by a unique structure consisting of spherical primary carbon particles with an average diameter of 10-30 nm. The specific surface area of conductive carbon black grades is relatively large, ca. 200 m^2/g for super-conductive carbon black grades, 800 m^2/g for extra-conductive carbon blacks, and 1400 m^2/g for ultra-conductive carbon blacks. For conductive carbon blacks, the presence of pores and porosity in the primary particles contributes to the specific surface area [79]. In Figure 19, TEM and SEM images of an ultra-conductive black are reported, clearly demonstrating the significant presence of pores within the primary particles. Since the mid-1970s, conductive carbon blacks like Ketjenblack EC300J (Akzo Nobel) and Printex XE-2 (Orion Engineered Carbons) have been produced as by-products from the gasification process used in the production of synthesis gas through the incomplete combustion of hydrocarbons. In this process, preheated oil feedstock reacts with air and vapor at relatively high temperatures to form synthesis gas (H_2/CO) and a carbon black by-product that is separated through filters. Since then, new conductive carbon black grades have been manufactured using specifically designed processes.
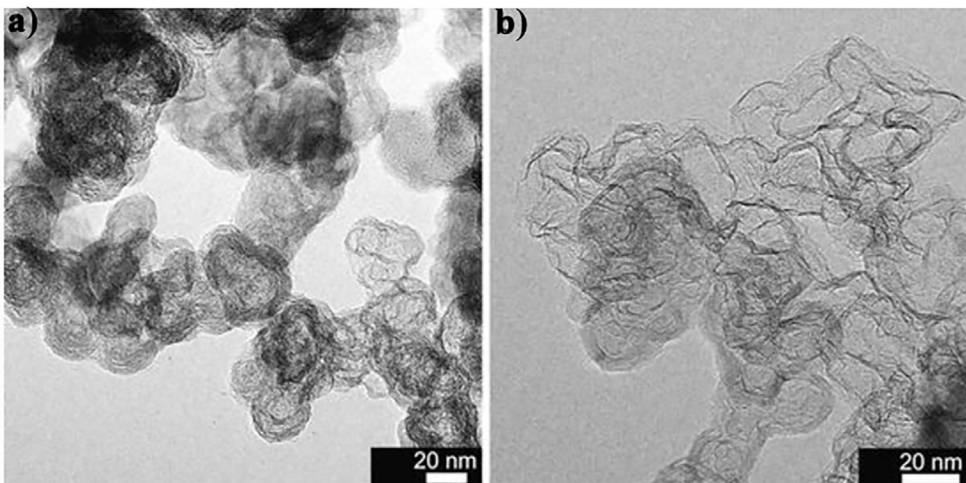
Figure 19   (a) TEM and (b) SEM images of ultra-conductive carbon blacks [79].

2.5.2   Electrically conductive elastomers

The electrical conductivity of elastomeric composites varies with increasing carbon black amount as shown in the percolation plot in Figure 20. The electrical conductivity of these elastomeric composites depends on the volume fraction of carbon black, and three distinct zones can be observed. At a low volume fraction of carbon black, the electrical conductivity of the composites is solely influenced by the intrinsic electrical properties of the rubber. In this range, the composite exhibits insulative behaviour. With increasing the volume fraction of carbon black, the filler particles start to form a continuous path, allowing charge carriers to travel across this network. The percolation zone marks the transition of elastomeric composites from insulative to conductive materials. The amount of carbon black to achieve this transition is known as the percolation threshold. By further increasing the amount of carbon black in the elastomeric composites, more conductive pathways are formed, and the electrical conductivity of the composites is increased. This continues until a constant value of electrical conductivity is reached in the conductive zone.

Figure 20   Percolation plot demonstrating the electrical conductivity of carbon black-polymer composites.

The conduction mechanism in elastomeric composites relies on electron tunnelling and electron hopping mechanisms. Above the percolation threshold, the gap size between primary aggregates of carbon black becomes so small that charge carriers

can tunnel through, determining the conductivity of the elastomeric composites. According to Kluppel [80], the electrical conductivity σ follows the power law equation:

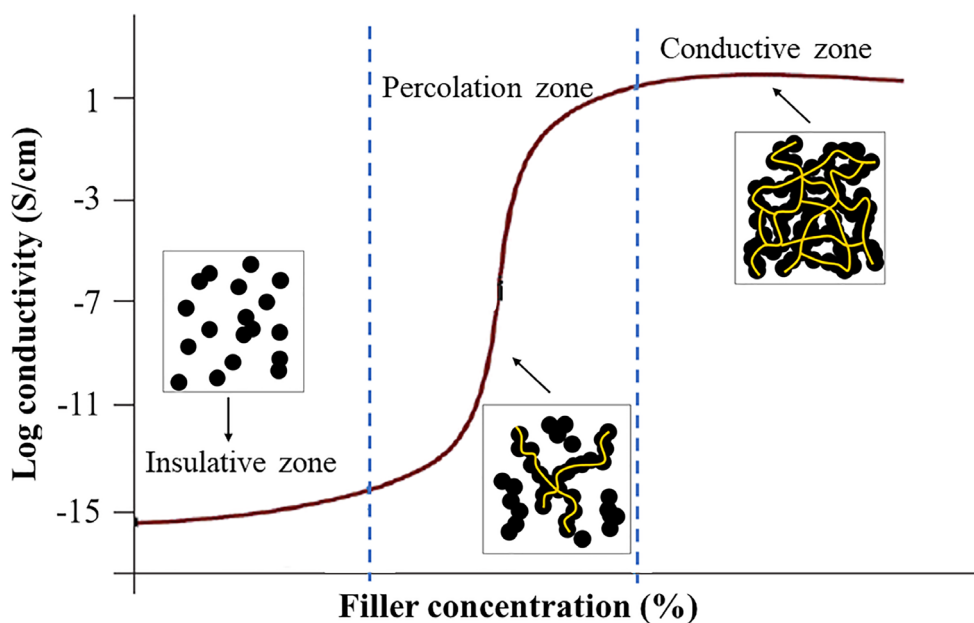$$\sigma = \sigma_0 \left(\frac{\Phi-\Phi_c}{1-\Phi_c}\right)^{\mu} \text{ for } \Phi > \Phi_c \tag{5}$$

where σ_0 is the limiting conductivity when $\Phi=1$, Φ_c is the percolation threshold, and μ is the percolation exponent, which has a value of 2 for all 3D lattice fillers. In general, the exponent μ depends on the carbon black grade and increases with particle size and specific surface area.

Three parameters describe the percolation plot: the percolation threshold, the slope of the percolation region and the ultimate electrical conductivity in the conductive zone. These three parameters are affected by the type and amount of carbon black used, as well as the polymer type and properties. The selection of the carbon black type and the amount depends on the application, its requirements and the desired electrical conductivity.

2.6 Concluding remarks

Piezoelectricity is a fascinating phenomenon giving the potential to enable autonomous operations of tyre sensors. Piezoelectric energy harvesters consist of two key components: a piezoelectric material and an electrode. Despite extensive research in this field, a piezoelectric device suitable for mounting in tyres to power sensors has not been established yet. Piezoelectric materials can be either ceramic and polymeric. Piezoelectric ceramics are characterised by high piezoelectric coefficients, thanks to their crystalline structure. However, their high brittleness and stiffness make them inadequate for applying in tyre compounds and rolling tyre conditions. Among piezoelectric polymers, bulk polymers like PVDF and piezoelectric elastomeric composites are particularly intriguing for tyre applications. In addition to the piezoelectric material, a piezoelectric energy harvester requires an electrode. Metallic electrodes have been predominantly used for this purpose. An alternative approach involves the use of electrically conductive elastomers. Electrical properties of elastomers, when incorporated with an amount of carbon black above the percolation threshold, can increase by several orders of magnitude. Depending on the type and amount of carbon black, as well as the rubber type, elastomeric composites can also reach an electro-conductive level falling in the semi-conductor range. This concept, combined with polymeric piezoelectric materials, forms the foundation of the present research.

Chapter 2

2.7   References

[1]   K. Uchino, The development of piezoelectric materials and the new perspective, Adv. Piezoelectric Mater. Sci. Technol. (2010) 1–85. https://doi.org/10.1533/9781845699758.1.

[2]   D. Damjanovic, Piezoelectricity, Encycl. Condens. Matter Phys. (2005) 300–309. https://doi.org/10.1016/B0-12-369401-9/00433-2.

[3]   C. Jacques, P. Curie, Development, via compression, of electric polarization in hemihedral crystals with inclined faces, Bull. La Soc. Minerol. Fr. 3 (1880) 90–93.

[4]   C. Jacques, P. Curie, Contractions and expansions produced by voltages in hemihedral crystals with inclined faces, Comptes Rendus Phys. 93 (1881) 1137–1140.

[5]   G. Lippman, rincipal of the conservation of electricity, Ann. Chemie Phys. 24 (1881) 145.

[6]   K. Uchino, Glory of piezoelectric perovskites, Sci. Technol. Adv. Mater. 16 (2015) 46001. https://doi.org/10.1088/1468-6996/16/4/046001.

[7]   H. Li, X. Bai, Y. Ling, al -, M. uk, M. El Moutamid, M.S. Tiscareno -, B. Eugene Wainer, High Titania Dielectrics, Trans. Electrochem. Soc. 89 (1946) 331. https://doi.org/10.1149/1.3071718.

[8]   B. Jaffe, Piezoelectric transducers using lead titanate and lead zirconate, 708 (1954) 244.

[9]   H. Kawai, The Piezoelectricity of Poly (vinylidene Fluoride), Jpn. J. Appl. Phys. 8 (1969) 975. https://doi.org/10.1143/JJAP.8.975.

[10]   H. Kawai, The Piezoelectricity of Poly (vinylidene Fluoride) Related content Piezoelectricity of Poly (vinylidene Fluoride) under high pressure, Japan. J. Appl. Phys. 8 (1969) 975–976. https://doi.org/10.1143/jjap.8.975.

[11]   Z.G. Ye, Handbook of Advanced Dielectric, Piezoelectric and Ferroelectric Materials: Synthesis, Properties and Applications, Handb. Adv. Dielectr. Piezoelectric Ferroelectr. Mater. Synth. Prop. Appl. (2008) 1–1060. https://doi.org/10.1533/9781845694005.

[12]   K.C. Kao, Dielectric Phenomena in Solids., (2004) 601.

[13]   I. Popov, S. Cheng, A.P. Sokolov, Broadband Dielectric Spectroscopy and Its Application in Polymeric Materials, Macromol. Eng. (2022) 1–39. https://doi.org/10.1002/9783527815562.MME0059.

[14]   R.S. Dahiya, M. Valle, Robotic tactile sensing: Technologies and system, Robot. Tactile Sens. Technol. Syst. 9789400705791 (2014) 1–245. https://doi.org/10.1007/978-94-007-0579-1/COVER.

[15]   A. American, N. Standard, IEEE Standard on Piezoelectricity: An American National Standard, ANSI/IEEE Std 176-1987. (1988) 8–10.

[16]   J. Yvonnet, Piezoelectricity, Solid Mech. Its Appl. 258 (2019) 91–102. https://doi.org/10.1007/978-3-030-18383-7_5.

[17]   A. Carter, K. Popowski, K. Cheng, A. Greenbaum, F.S. Ligler, A. Moatti, Enhancement of Bone Regeneration Through the Converse Piezoelectric Effect, A Novel Approach for Applying Mechanical Stimulation, Bioelectricity. 3 (2021) 255–271. https://doi.org/10.1089/BIOE.2021.0019.

[18]   S.B. Lang, H.L.W. Chan, Frontiers of ferroelectricity: A special issue of the journal of materials science, Front. Ferroelectr. A Spec. Issue J. Mater. Sci. (2007) 1–288. https://doi.org/10.1007/978-0-387-38039-1/COVER.

[19]   A.J. Bell, Factors influencing the piezoelectric behaviour of PZT and other morphotropic phase boundary ferroelectrics, Front. Ferroelectr. A Spec. Issue J. Mater. Sci. (2007) 13–25. https://doi.org/10.1007/978-0-387-38039-1_2.

[20]   A.A. Bokov, Z.G. Ye, Recent progress in relaxor ferroelectrics with perovskite structure, Front. Ferroelectr. A Spec. Issue J. Mater. Sci. (2007) 31–52. https://doi.org/10.1007/978-0-387-38039-1_4.

[21]   D.B. Deutz, N.T. Mascarenhas, J.B.J. Schelen, D.M. de Leeuw, S. van der Zwaag, P. Groen, Flexible Piezoelectric Touch Sensor by Alignment of Lead-Free Alkaline Niobate Microcubes in PDMS, Adv. Funct. Mater. 27 (2017) 1. https://doi.org/10.1002/adfm.201700728.

[22]   V.L. Stuber, D.B. Deutz, J. Bennett, D. Cannel, D.M. de Leeuw, S. van der Zwaag, P. Groen, Flexible Lead-Free Piezoelectric Composite Materials for Energy Harvesting Applications, Energy Technol. 7 (2019) 177–185. https://doi.org/10.1002/ENTE.201800419.

[23]   A. Batra, Power Harvesting via Smart Materials Power Harvesting via Smart Materials Book Description Book Details, (2017).

[24]   H. Elahi, K. Munir, M. Eugeni, S. Atek, P. Gaudenzi, Energy harvesting towards self-powered iot devices, Energies. 13 (2020) 5528. https://doi.org/10.3390/EN13215528.

[25]   H. Kim, Y. Tadesse, S. Priya, Piezoelectric energy harvesting, in: Energy Harvest. Technol., Springer US, New York, USA, 2009: pp. 3–39. https://doi.org/10.1007/978-0-387-76464-1_1.

[26]   F. Lv, Z. Hong, Z. Ahmad, H. Li, Y. Wu, Y. Huang, Design of Flexible Piezoelectric Nanocomposite for Energy Harvesters: A Review, Energy Mater. Adv. 4 (2023) 0043. https://doi.org/10.34133/ENERGYMATADV.0043.

[27]   T. Sharma, A. Chehri, P. Fortier, Communication Trends, Research Challenges in Autonomous Driving and Different Paradigms of Object Detection, Smart Innov. Syst. Technol. 359 (2023) 57–66. https://doi.org/10.1007/978-981-99-3424-9_6/COVER.

[28]   Y. Zhang, A. Carballo, H. Yang, K. Takeda, Perception and sensing for autonomous vehicles under adverse weather conditions: A survey, ISPRS J. Photogramm. Remote Sens. 196 (2023) 146–177. https://doi.org/10.1016/J.ISPRSJPRS.2022.12.021.

2

[29]   O.J. Jousimaa, Y. Xiong, A.J. Niskanen, A.J. Tuononen, Energy harvesting system for intelligent tyre sensors, in: IEEE Intell. Veh. Symp. Proc., IEEE, Gothenburg, Sweden, 2016: pp. 578–583. https://doi.org/10.1109/IVS.2016.7535445.

[30]   R. Matsuzaki, A. Todoroki, Wireless monitoring of automobile tires for intelligent tires, Sensors. 8 (2008) 8123–8138. https://doi.org/10.3390/s8128123.

[31]   A.E. Kubba, K. Jiang, A comprehensive study on technologies of tyre monitoring systems and possible energy solutions, Sensors. 14 (2014) 10306–10345. https://doi.org/10.3390/s140610306.

[32]   M. Germer, U. Marschner, A. Richter, Energy Harvesting for Tire Pressure Monitoring Systems from a Mechanical Energy Point of View, IEEE Internet Things J. 9 (2022) 7700-7714. https://doi.org/10.1109/JIOT.2022.3152547.

[33]   A. Toghi Eshghi, S. Lee, H. Lee, Y.-C. Kim, Parameter study and optimization for piezoelectric energy harvester for TPMS considering speed variation, Smart Mater. Nondestruct. Eval. Energy Syst. 9806 (2016) 1–19. https://doi.org/10.1117/12.2219567.

[34]   C.R. Bowen, M.H. Arafa, Energy harvesting technologies for tire pressure monitoring systems, Adv. Energy Mater. 5 (2015) 1–17. https://doi.org/10.1002/aenm.201401787.

[35]   H. Jan, P. Groen, An introduction to piezoelectric materials and components, 2012.

[36]   G. Helke, K. Lubitz, Piezoelectric PZT Ceramics, Springer Ser. Mater. Sci. 114 (2008) 89–130. https://doi.org/10.1007/978-3-540-68683-5_4/COVER.

[37]   H. Khanbareh, V.Y. Topolov, C.R. Bowen, Piezo-particulate composites: Manufacturing, properties, applications, Springer Series in Materials Science 283 (2019) 1-146. https://doi.org/10.1007/978-3-030-19204-4

[38]   E.D. Politova, E.A. Fortalnova, M.G. Safronenko, G.M. Kaleva, N. V Golubko, A. V Mosunov, S.Y. Stefanovich, N.U. Venskovskii, Phase formation, structure and dielectric properties of lead-free ceramics on the base of (Na0.5Bi0.5)TiO3, Ferroelectrics. 515 (2017) 59–67. https://doi.org/10.1080/00150193.2017.1360109.

[39]   M. Shen, Y. Qin, Y. Zhang, M.A. Marwat, C. Zhang, W. Wang, M. Li, H. Zhang, G. Zhang, S. Jiang, Enhanced pyroelectric properties of lead-free BNT-BA-KNN ceramics for thermal energy harvesting, J. Am. Ceram. Soc. 102 (2019) 3990–3999. https://doi.org/10.1111/JACE.16250.

[40]   J.F. Li, K. Wang, F.Y. Zhu, L.Q. Cheng, F.Z. Yao, (K, Na) NbO3-based lead-free piezoceramics: Fundamental aspects, processing technologies, and remaining challenges, J. Am. Ceram. Soc. 96 (2013) 3677–3696. https://doi.org/10.1111/JACE.12715.

[41]   S.O. Leontsev, R.E. Eitel, Progress in engineering high strain lead-free piezoelectric ceramics, Sci. Technol. Adv. Mater. 11 (2010) 13. https://doi.org/10.1088/1468-6996/11/4/044302.

[42]   S. Bauer, F. Bauer, Piezoelectric polymers and their applications, in: Springer Ser. Mater. Sci., Springer Verlag, 2008: pp. 157–177. https://doi.org/10.1007/978-3-540-68683-5_6.

[43]   K.K. Sappati, S. Bhadra, Piezoelectric polymer and paper substrates: A review, Sensors (Switzerland). 18 (2018). https://doi.org/10.3390/S18113605.

[44]   V. Bharti, R. Nath, Quantitative analysis of piezoelectricity in simultaneously stretched and corona poled polyvinyl chloride films, J. Appl. Phys. 82 (1997) 3488–3492. https://doi.org/10.1063/1.365666.

[45]   J.S. Harrison, Z. Ounaies, Piezoelectric Polymers, Encycl. Polym. Sci. Technol. (2003). https://doi.org/10.1002/0471440264.PST427.

[46]   H. Ueda, S.H. Carr, Piezoelectricity in Polyacrylonitrile, Polym. J. 1984 169. 16 (1984) 661–667. https://doi.org/10.1295/polymj.16.661.

[47]   R.J. Comstock, S.I. Stupp, S.H. Carr, Thermally stimulated discharge currents from polyacrylonitrile, J. Macromol. Sci. Part B Phys. 13 (1977) 101–115. https://doi.org/10.1080/00222347708208756.

[48]   M.M. Alam, X. Crispin, The past, present, and future of piezoelectric fluoropolymers: Towards efficient and robust wearable nanogenerators, Nano Res. Energy. 2 (2023). https://doi.org/10.26599/NRE.2023.9120076.

[49]   Z. Yang, S. Zhou, J. Zu, D. Inman, High-performance piezoelectric energy harvesters and their applications, Joule. 2 (2018) 642–697. https://doi.org/10.1016/j.joule.2018.03.011.

[50]   C.R. Bowen, H.A. Kim, P.M. Weaver, S. Dunn, Piezoelectric and ferroelectric materials and structures for energy harvesting applications, Energy Environ. Sci. 7 (2014) 25–44. https://doi.org/10.1039/C3EE42454E.

[51]   M. Keck, A new approach of a piezoelectric vibration-based power generator to supply next generation tire sensor systems, in: Proc. IEEE Sensors, IEEE, Atlanta, USA, 2007: pp. 1299–1302. https://doi.org/10.1109/ICSENS.2007.4388648.

[52]   Q. Zheng, H. Tu, A. Agee, Y. Xu, Vibration energy harvesting device based on asymmetric air-spaced cantilevers for tire pressure monitoring system, in: Proc. Power MEMS, PowerMEMS, Washington, USA, 2009: pp. 403–406.

[53]   R. Elfrink, S. Matova, C. De Nooijer, M. Jambunathan, M. Goedbloed, J. Van De Molengraft, V. Pop, R.J.M. Vullers, M. Renaud, R. Van Schaijk, Shock induced energy harvesting with a MEMS harvester for automotive applications, in: Tech. Dig. - Int. Electron Devices Meet. IEDM, IEEE, Washington, USA, 2011: pp. 677–680. https://doi.org/10.1109/IEDM.2011.6131639.

[54]   N. Makki, R.P.-I.-& S. in A. in Canada, U. 2011, Piezoelectric power generation in automotive tires, 2011.

2

[55]   N. Makki, R. Pop-Iliev, Piezoelectric power generation in automotive tires, in: Proc. Smart Mater. Struct. Aerospace/NDT, Aerospace/NDT, Montreal, Canada, 2011.

[56]   N. Makki, R. Pop-Iliev, Pneumatic tire-based piezoelectric power generation, Act. Passiv. Smart Struct. Integr. Syst. 2011. 7977 (2011) 1–10. https://doi.org/10.1117/12.880636.

[57]   G. Sa-Gong, A. Safari, S.J. Jang, R.E. Newnham, Poling flexible piezoelectric composites, Ferroelectr. Lett. Sect. 5 (1986) 131–142. https://doi.org/10.1080/07315178608202472.

[58]   K. Maity, D. Mandal, Piezoelectric polymers and composites for multifunctional materials, Adv. Light. Multifunct. Mater. 9 (2021) 239–282. https://doi.org/10.1016/B978-0-12-818501-8.00001-9.

[59]   J.F. Tressler, L. Qin, K. Uchino, 7.21 Piezoelectric Composite Sensors, Compr. Compos. Mater. II. (2018) 408–419. https://doi.org/10.1016/B978-0-12-803581-8.03937-0.

[60]   R.E. Newnham, D.P. Skinner, L.E. Cross, Connectivity and piezoelectric-pyroelectric composites, Mater. Res. Bull. 13 (1978) 525–536. https://doi.org/10.1016/0025-5408(78)90161-7.

[61]   R. Mitkus, L. Piechowiak, M. Sinapius, Characterization of UV Light Curable Piezoelectric 0-0-3 Composites Filled with Lead-Free Ceramics and Conductive Nanoparticles, J. Compos. Sci. 7 (2023) 89. https://doi.org/10.3390/JCS7020089/S1.

[62]   V.L. Stuber, T.R. Mahon, S. Van Der Zwaag, P. Groen, The effect of the intrinsic electrical matrix conductivity on the piezoelectric charge constant of piezoelectric composites, Mater. Res. Express. 7 (2019) 1591. https://doi.org/10.1088/2053-1591/AB5BB3.

[63]   H. Khanbareh, S. Van Der Zwaag, W.A. Groen, Effect of dielectrophoretic structuring on piezoelectric and pyroelectric properties of lead titanate-epoxy composites, Smart Mater. Struct. 23 (2014) 105030. https://doi.org/10.1088/0964-1726/23/10/105030.

[64]   D.Y. Hyeon, G.J. Lee, S.H. Lee, J.J. Park, S. Kim, M.K. Lee, K. Il Park, High-temperature workable flexible piezoelectric energy harvester comprising thermally stable (K,Na)NbO3-based ceramic and polyimide composites, Compos. Part B Eng. 234 (2022) 109671. https://doi.org/10.1016/J.COMPOSITESB.2022.109671.

[65]   V.L. Stuber, T.R. Mahon, S. Van Der Zwaag, P. Groen, The effect of the intrinsic electrical matrix conductivity on the piezoelectric charge constant of piezoelectric composites, Mater. Res. Express. 7 (2019) 15703. https://doi.org/10.1088/2053-1591/AB5BB3.

[66]   J.E.Q. Quinsaat, T. de Wild, F.A. Nüesch, D. Damjanovic, R. Krämer, G. Schürch, D. Häfliger, F. Clemens, T. Sebastian, M. Dascalu, D.M. Opris, Stretchable

piezoelectric elastic composites for sensors and energy generators, Compos. Part B Eng. 198 (2020) 108211. https://doi.org/10.1016/J.COMPOSITESB.2020.108211.

[67] I. Babu, G. de With, Enhanced electromechanical properties of piezoelectric thin flexible films, Compos. Sci. Technol. 104 (2014) 74–80. https://doi.org/10.1016/J.COMPSCITECH.2014.08.022.

[68] M. Promsawat, K.U. Boonsri, S. Samadoloh, N. Promsawat, E. Kalkornsurapranee, Effects of Poling on Electrical Properties of Flexible Piezoelectric Composites with Natural Rubber Matrix, IOP Conf. Ser. Mater. Sci. Eng. 553 (2019) 012008. https://doi.org/10.1088/1757-899X/553/1/012008.

[69] S. Samadoloh, N. Promsawat, E. Kalkornsurapranee, S. Pojprapai, M. Promsawat, Fabrication and characterization of flexible piezoelectric composites with natural rubber matrix, Integrated Ferroelectrics, 195 (2019) 30-38. https://doi.org/10.1080/10584587.2019.1570041.

[70] B. Alemour, O. Badran, M.R. Hassan, A review of using conductive composite materials in solving lightening strike and ice accumulation problems in aviation, J. Aerosp. Technol. Manag. 11 (2019) 1022. https://doi.org/10.5028/JATM.V11.1022.

[71] R.D. Heidenreich, W.M. Hess, L.L. Ban, IUCr, A test object and criteria for high resolution electron microscopy, Urn:Issn:0021-8898. 1 (1968) 1–19. https://doi.org/10.1107/S0021889868004930.

[72] H.P. Boehm, Surface oxides on carbon and their analysis: a critical assessment, Carbon N. Y. 40 (2002) 145–149. https://doi.org/10.1016/S0008-6223(01)00165-8.

[73] H.P. Boehm, Some aspects of the surface chemistry of carbon blacks and other carbons, Carbon N. Y. 32 (1994) 759–769. https://doi.org/10.1016/0008-6223(94)90031-0.

[74] J.B. Donnet, R.C. Bansal, M.J. Wang, Carbon Black: Science and Technology, Second Edition, Routledge, Boca Raton, USA, 2018. https://doi.org/10.1201/9781315138763.

[75] J.W.M. Noordermeer, W.K. Dierkes, Carbon Black Reinforced Elastomers, Encycl. Polym. Nanomater. 2 (2015) 287–299. https://doi.org/10.1007/978-3-642-29648-2_287.

[76] M.E. Spahr, R. Rothon, Carbon Black as a Polymer Filler, in: Polym. Polym. Compos. A Ref. Ser., Springer, Berlin-Heidelberg, Germany, 2016: pp. 1–31. https://doi.org/10.1007/978-3-642-37179-0_36-2.

[77] C.G. Robertson, N.J. Hardman, Nature of Carbon Black Reinforcement of Rubber: Perspective on the Original Polymer Nanocomposite, Polym. 2021, 13 (2021) 538. https://doi.org/10.3390/POLYM13040538.

[78] B. Rodgers, Rubber compounding : chemistry and applications, CRC Press, 2015.

2

[79]   M.E. Spahr, R. Gilardi, D. Bonacchi, Carbon Black for Electrically Conductive Polymer Applications, (2017) 375–400. https://doi.org/10.1007/978-3-319-28117-9_32.

[80]   M. Klüppel, The Role of Disorder in Filler Reinforcement of Elastomers on Various Length Scales, Adv. Polym. Sci. 164 (2003) 1–86. https://doi.org/10.1007/B11054.

2

Chapter 3

Dynamic measurement setups for validating piezoelectric energy harvesters in driving conditions

3

Sustainable power supply to flexible electronics is currently of high interest due to the transition to autonomous and self-driving vehicles. Piezoelectric Energy Harvesters (PEH) can be used as sustainable energy sources by harvesting electrical power through the material deformation occurring in a tyre. In this work, an analytical setup was developed to experimentally validate the energy harvesters for their use in tyres. It was designed to measure the harvested electrical energy under simulated driving conditions. The setup includes a Dynamic Mechanical Analysis (DMA) as foundation to simulate the vibrations and dynamic responses occurring in a rolling tyre. The dynamic properties and the output voltage from the harvesters were monitored under these sinusoidal conditions. For this, a PEH for tyre applications was prepared in a sandwich configuration. It consists of a piezoelectric material, i.e. PolyVinyliDene diFluoride (PVDF) film, inserted in between two layers of electrodes, i.e. elastomers filled with conductive carbon black fillers. The electrical conductivity of elastomeric composites was measured under dynamic conditions varying dynamic strain, frequencies, and temperatures. Dynamic strain and temperature resulted to be the most significant factors influencing the electrical conductivity of elastomers. Output power from the piezoelectric energy harvester was also measured at varied frequencies and temperatures. Both properties increase considerably the piezoelectric power. This development gives a promising method for analysing the electro-mechanical properties of conductive and piezoelectric materials and optimising their performance according to simulated tyre-rolling conditions.

Chapter 3

3.1. Introduction

Nowadays, an increasing number of sensors are being integrated into a vehicle to ensure safe driving, consistent operations, and efficient tyre performance [1-4]. The new generation of tyres, namely 'smart tyres', combines an advanced monitoring system to observe real-time tyre performances, e.g. tread wear, temperature and heat build-up and pressure of the running tyres. Attempts to further improve the performance of tyre sensors have continuously been made. One of the potential attractive features is the integration of a piezoelectric energy harvester in tyres. This has currently been researched due to its key advantage of providing a battery-less system to sensors for autonomous operations [5,6].

Piezoelectric Energy Harvester (PEH) is one of the promising technologies that can potentially replace a battery as power source for sensors in tyres. Piezoelectricity is a principle in which the mechanical energy introduced to a dielectric material under dynamic deformations (i.e. shear, tension, compression) is converted into electrical energy [7]. During the running of a vehicle, tyres are continuously subjected to dynamic mechanical conditions that involve external forces, deformations, as well as varied vibrations and excitations during their rotation at various temperatures. When a tyre is in contact with the road surface, the tyre partially flattens at the contact patch, due to external loads and gravity. The contact patch deforms in tension and compression. In addition, the vibrations in running tyres occur due to the interactions between the tyres and the road surface. Therefore, mounting a PEH in a tyre has a potential to produce electrical energy [2,8].

A PEH consists of two components: a piezoelectric material which generates electricity under mechanical stress and applied electrodes on both sides of the piezoelectric material to induce the flow of the electric charges and store them in a capacitor. To be embedded in a tyre, both components of the PEH need to have appropriate design and properties i.e. elasticity, durability and stability. They need to withstand the dynamic service conditions of the rolling tyres, which involve variable parameters, i.e. loads, strains and temperatures. Therefore, it is essential to evaluate and validate the conductive and piezoelectric properties of newly developed materials under simulated tyre-rolling conditions.

A variety of piezoelectric energy harvesters have been investigated for use as supply power to tyre sensors by using various approaches like mathematical models, numerical simulations and experiments in laboratory conditions as well as in actual tyres [1,4,6,9-19]. The piezoelectric efficacy is mainly affected by the following

parameters: temperature, car speeds, on-road noise excitations/vibrations and vehicle loads/deformations [9,10,16,17]. Various theoretical models reported in literature introduced useful tools to predict the electrical output from PEHs based on the kinematics of a car tyre. The strain variation associated with the cyclic deformation of a tyre is substantial. The tread and sidewall of a tyre deform to a larger extent at the contact patch area compared to other positions. It was proven that the piezoelectric energy harvesters generate the highest amount of electrical power in the middle of the contact patch area [3,20]. It is based on the fact that the contact patch area experiences compressive strain in the radial direction on each side and an additional tensile strain within the area in the circumferential direction, i.e. 0.1-2%. Tyre sidewall and wheel rim were not considered as optimal locations in a tyre due to an undesired high deformation of the sidewall, a more difficult installation process and low durability [4,13,20]. The sidewall experiences compressive strain in the radial direction, with a deformation that can be as high as 10-50 mm. The feasibility of using a piezoelectric energy harvester in a tyre can be assessed by experiments under laboratory conditions and by embedding it into an actual tyre [11,12]. The output power from a piezoceramic-based PEH was analysed on a lab-scale under sinusoidal vibrations and shock-induced excitations, which confirmed the major influence of these two factors on the electricity harvester performance. Van den Ende et al. [15] were able to measure the output power from a piezoelectric harvester using a tensile test machine coupled with an oscilloscope and then directly attaching it to a real tyre. Nevertheless, the authors measured a substantial change in output power when varying tensile and compression strain, as well as temperature. Some researchers investigated further piezoelectric material category (ceramics and polymers) and other factors influencing PEHs performance, e.g. optimal location in the tyre (wheel rim and inner liner) and road roughness conditions, by embedding the PEHs in actual tyres [6,8,13,14,18,19-21].

It was confirmed in literature that the piezoelectric energy harvester is suitable for replacing the batteries in tyre sensors. Relevant aforementioned investigations were conducted in actual tyres. However, some crucial factors influencing the performance of PEH components, e.g. temperature, vibrations/excitations, vehicle load, and tyre deformation, remain unclear. Therefore, in the present work a tool that exploits the piezoelectric and conductive properties of flexible harvesters under dynamic mechanical conditions of tyres was successfully developed. This setup allows to study the feasibility of a PEH for powering tyre sensors by exploring the effects of solely compression deformation, excitations/vibrations and temperature. A Dynamic Mechanic Analysis (DMA) is the fundamental instrument employed for

3

this setup as it is well-recognised as an extremely sensitive and efficient dynamic analyser for polymers and so a most appropriate technique for simulating tyre-rolling conditions. The DMA is capable of analysing the behavior of polymers under various conditions, e.g. static and dynamic strains and stresses, frequencies, and temperatures. Hence, the DMA can give relevant information on viscoelastic properties of the composites used to manufacture a tyre as well as the input data to model and predict the quality of the final tyres like rolling resistance, heat build-up, and ice and wet grip. By selecting the proper values of variable parameters like strain, frequency and temperature, DMA can assess the degree of tread deformation under a given load, which is crucial for simulating rolling tyre conditions. Therefore, the use of DMA represents a good analytical method to gain a deeper insight into the electro-dynamics of rubbers.

In the present work, analytical setups based on a combination of DMA and electrical circuits were developed to measure the conductive and piezoelectric properties of polymeric materials as a function of frequency and temperature. Conductive elastomers and flexible piezoelectric polymers were prepared and used for evaluating the setups.

3.2.   Experimental

3.2.1.   Materials

Piezoelectric polymer PolyVinyliDene diFluoride (PVDF) was supplied by PolyK Technologies LLC (Philipsburg, USA) in a form of a 100 μm thick film. The electrical and chemical properties of this polymer film are given in Table 1. PVDF surface was cleaned with chloroform (99.5%, Sigma-Aldrich, St. Louis, MO) and treated with 3-thiocyanatopropyltriethoxy silane (Si-264, Evonik Industries AG, Essen, Germany) were used. This silane has a sulphur content of 12.5 wt%, an average molecular weight of 263 g/mol and a density of 1 g/cm^3.

Further investigations were carried out with conductive elastomeric composites containing Natural Rubber (NR TSR20, Wurfbain Nordmann B.V., Zaandam, Netherlands), and Conductive Carbon Black CCB filler (Vulcan XC72, Cabot Corporation GmbH, Baden, Germany) with a specific surface area (BET method, ASTM D-6556) of 232 m^2/g and a structure (OAN method, ASTM D-2414) of 174 mL/100g.

Other compounding ingredients were of technical quality:

- Treated Distillate Aromatic Extracts (TDAE) oil (Vivatec 500, Hansen & Rosenthal KG, Hamburg, Germany);
- N-(1,3-dimethylbutyl)-N'-phenyl-p-phenylenediamine (6PPD), (Vulkanox 4020/LG, Lanxess Deutschland GmbH, Cologne, Germany);
- 2,2,4-TriMethyl-Quinoline (TMQ), (Vulkanox HS/LG, Lanxess Deutschland GmbH, Cologne, Germany);
- Stearic acid, (Edenor ST1 GS, Emery Oleochemicals GmbH, Düsseldorf, Germany);
- Zinc Oxide (ZnO), (Merck & Co, Darmstadt, Germany);
- Rhombic Sulphur (α-sulphur, Eastman Chemical Corporation, Langenfeld, Germany);
- N-Tert-Butyl-Benzothiazole Sulfenamide (TBBS), (Rhenogran TBBS-80, Lanxess Deutschland GmbH, Cologne, Germany).

Table 2 shows the compositions of these composites.

Table 1 Properties of the PVDF film with 100 μm thickness.

Properties*	Value
Charge coefficient, d_{31}	30 pC/N
Charge coefficient, d_{33}	-30 pC/N
Glass transition temperature	-34°C
Melting temperature	170-175°C
Curie temperature	100°C
Tensile strength	400-600 MPa
Young's modulus	2300 MPa
Elongation at break	20-30%

*Technical data derived from PolyK Technologies LLC, USA.

Table 2 Compositions of conductive elastomeric composites.

Conductive elastomeric composites	
Ingredients	**Amount (phr)**
Natural Rubber NR TSR20	100
Carbon Black CCB	Variable
Processing oil TDAE	Half of CCB amount
Antidegradants (6PPD, TMQ)	5.5
Activators (Stearic acid, ZnO)	6.5
Curatives (α-sulphur, TBBS)	3.2

3.2.2.   Sample preparations

3.2.2.1. Conductive elastomeric composites

All conductive elastomeric composites were prepared using a two-steps procedure in an internal mixer (Brabender Plastograph EC plus, Brabender GmbH & Co KG, Germany), at 80°C as starting temperature and 75% as fill factor. The rotor speed and mixing time were selected at 100 rpm and 10 min, respectively, based on the results of a preliminary study. NR was initially masticated for 1 min. Then, carbon black and oil were added in two portions, each one mixed for half of the pre-set filler mixing time. For the remaining 2 min, the rest of the ingredients (e.g. 6PPD, TMQ, ZnO and stearic acid) were added and mixed. The composites were then discharged and sheeted out on a two-roll mill for 2 min at 2 mm nip width (Polymix 80 T, Schwabenthan-Maschinen GmbH & Co. KG, Berlin, Germany) and kept overnight before sulphur and TBBS were added to the composite on the above mentioned two-roll mill at 50°C for 5 min. The vulcanisation characteristics of the composites were analysed using a Rubber Process Analyser (RPA 2000, Alpha Technologies, Ohio, USA). Each measurement was done for 20 min at 160°C at a frequency of 1.667 Hz and an oscillating shear angle of 0.5°. Conductive elastomeric composites were vulcanised in a cylindrical shape at t_{c95} values at 160°C in a Wickert press WLP 1600 at 100 bar (Wickert Maschinenbau GmbH, Landau, Germany) by using 4 mm thick steel sheets with cavities of 10 mm as diameter.

3.2.2.2. Piezoelectric energy harvester

Piezoelectric energy harvesters were prepared by adhering a surface modified PVDF film (Table 1) with the conductive elastomeric composites (Table 2). A surface modification of the piezoelectric PVDF film was carried out to improve the interfacial adhesion between the PVDF film and the conductive elastomeric composites. First, the PVDF film was treated with oxygen plasma using a plasma reactor Plasma-Prep II (SPI Supplies, West Chester, Pennsylvania, USA) consisting of a plasma vacuum chamber, in which the PVDF film was placed. A mechanical vacuum pump (Oerlikon, Lafert S.p.A., Piave, Italy) reduced the pressure inside the chamber to around 100-200 mTorr. After reaching this pressure, the chamber was refilled with oxygen gas. A Radio Frequency (RF) power at 13.56 MHz was applied to the chamber to excite and charge the oxygen molecules by turning them into oxygen radicals. The film was treated with this oxygen plasma for 15 min at room temperature. After this, the PVDF film surface is expected to be randomly covered with hydroxyl and carbonyl groups which are highly reactive towards silanes. The silanisation of the oxygen-treated PVDF film was carried out using the silane

coupling agent 3-thiocyanatopropyltriethoxysilane. For this, the PVDF film, directly after the plasma treatment, was placed in a desiccator under vacuum at room temperature with 3 ml of 3-thiocyanatopropyltriethoxysilane silane in a small Petri dish for 24 h. The film was fixed with a holder to fully expose both sides of the film to the silane vapor. More details of this methodology are reported in [21-23] and in the Chapter 4.

After the silane treatment, the PVDF films were assembled in between two layers of conductive elastomeric composites. Novel molds were designed for the vulcanisation of piezoelectric harvester in a cylindrical shape by using Solidworks software; the components are shown in Figure 1a. The molds were made of structural steel and they included a bottom plate in which 2 mm-thick steel sheets were placed. Each sheet has cylindrical cavities with 10 mm diameter in which unvulcanised rubber was placed. An upper plate is then needed to exert pressure on the composites and vulcanise it. In between the two sheets, a 0.1 mm PVDF film was inserted in order to obtain the configuration as shown in Figure 1b. Piezoelectric energy harvesters in sandwich design were vulcanised using compression molding in a press at 160°C to their t_{c95} in cylindrical shapes with a diameter of 10 mm.
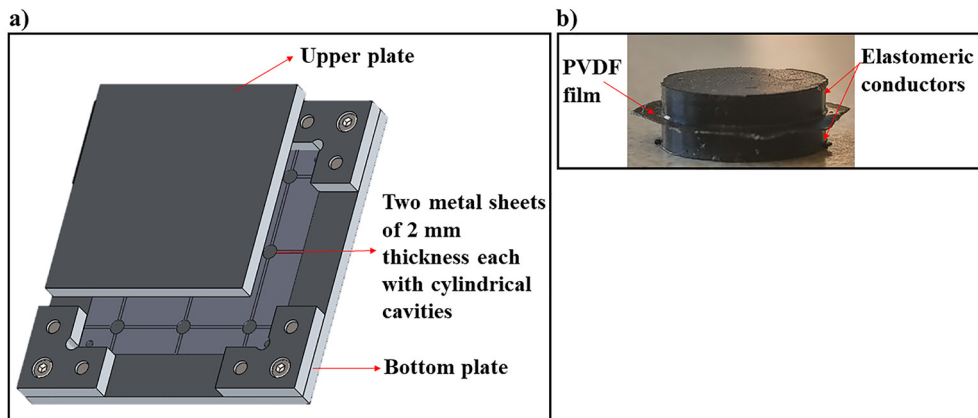
Figure 1   (a) Three-dimensional drawing of the rubber mold designed via Solidworks software for the preparation of PEHs and (b) example of a PEH with a diameter of 10 mm and a thickness of 4.1 mm.

3.2.3.   Setups for electro-dynamic characterisations

The conductivity and piezoelectricity of the investigated materials were characterised using in-house developed setups. They consisted of a Dynamic Mechanical Analyser (DMA) to simulate the dynamic mechanical conditions of running tyres. The DMA used in this work was the DMA Gabo Eplexor 9 (Netzsch

Gabo Instruments GmbH, Ahlden, Germany). DMA is used to determine the viscoelastic properties of elastomeric samples under static and dynamic excitation. Static and dynamic loads, frequency and temperature can be varied. When a sinusoidal deformation is applied, the elastomeric sample response is time-delayed due to the viscoelastic properties. For elastic materials, the modulus of elasticity is the complex modulus E*, defined as a combination of the storage modulus E' (elastic part) and the loss modulus E'' (viscous part). The ratio of loss modulus and storage modulus is called tan δ.
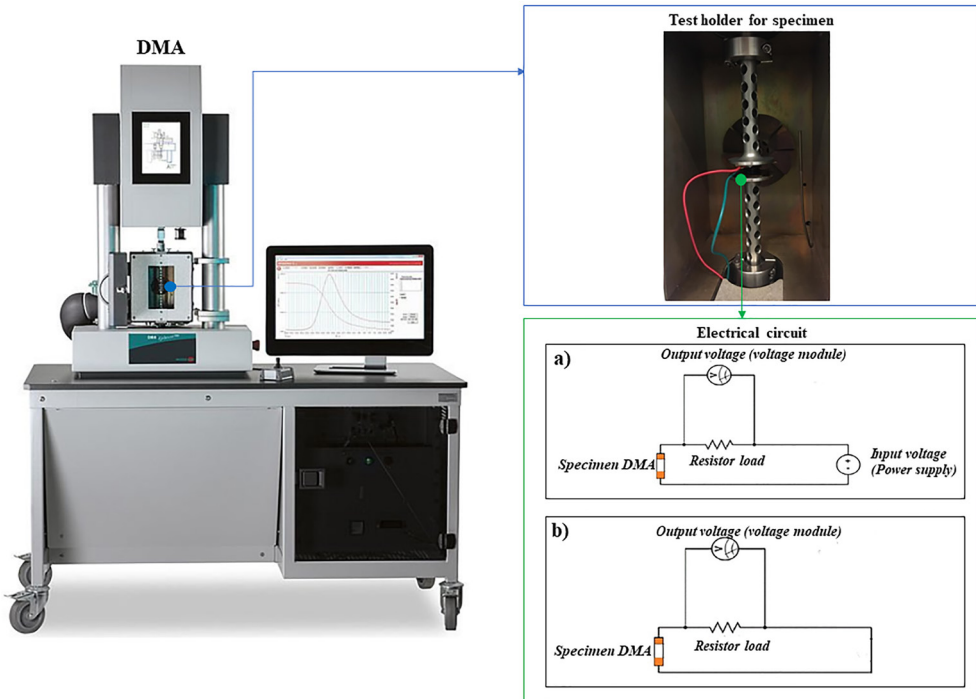
Figure 2   Schematic view of the setups: DMA with the specimen compression-mode holder coupled to the electrical circuits for (a) conductive and (b) piezoelectric measurements.

The measurements were performed in compression mode with a pre-conditioning of 3.5 N as load, following two methodologies: (1) a temperature sweep from -120 to 120°C at frequencies of 10 and 100 Hz; (2) a frequency sweep from 0.1 to 100 Hz at 25°C. The dynamic analyses were developed based on the assumption for a certain passenger car tyre. The applied load on each tyre was estimated for such a car and the analysis conditions were simulated by DMA, i.e. 10% as static strain and 2% as dynamic strain [24]. It is worth remarking that the static and dynamic strains of compression were 0.5% at a temperature lower than -35°C which is the glassy region of the selected rubber. To determine the repeatability of these dynamic analyses,

three individually prepared conductive and PEH samples at the center point were measured.

3.2.3.1. Electrical conductivity measurements

Concerning the electrical properties, the voltage was measured during the temperature and frequency sweeps of DMA. To measure the electrical conductivity of the materials, copper plates with electrical wires were attached to the upper and lower parts of the specimen (i.e. cylindrical sample containing conductive elastomeric composites) to create a connection with the electrical measuring devices. The attachment of the copper plates to the compression clamp of the DMA is shown in Figure 2. To avoid an electrical short circuit, the specimen needs to be isolated from the metal clamps. Therefore, the clamps were covered with Kapton tape, i.e. polyimide (PrintTec, Geldermalsen, the Netherlands).

The electrical conductivity of the elastomeric composites was determined by transmitting a specific current, where the voltage between two copper plates attached to both ends of the conductive elastomeric composites was measured. The measurement setup included a Direct Current (DC) power supply (0-30 V, 3 A, TENMA, Farnell House, Leeds, UK) to transmit an electrical current to the specimen and a voltage module (Model NI-9215, National Instruments, Austin, TX, USA) to monitor the corresponding voltage drop over a shunt resistor placed in series with the specimen. A circuit with a shunt resistor was used to divert a small part of the current flow and to detect the current across the circuit. Thereby, the conductivity of the specimen was calculated. A compact-DAQ chassis (Model cDAQ-9171, National Instruments, Austin, TX, USA) connected the voltage module (Model NI-9215, National Instruments, Austin, TX, USA) to a USB port and recorded the changes in voltage using computing software. In Figure 2a the electrical circuit for the conductive measurements is shown.

The measured voltage was used to calculate the electrical conductivity, as expressed by the following equation [25]:

$$\sigma = \frac{(V_{PS} - V_s)}{I_s} \frac{l}{A_i} = \frac{R(V_{PS} - V_{out})}{V_{out}} \frac{l}{A_i} \ (S \cdot cm^{-1}) \tag{1}$$

The voltage drop over the sample is the difference between the voltage from the power supply (V_{PS}, i.e. 4 V for the tests) and the voltage measured by the module (V_S). The current I_s was calculated using Ohm's law by inserting the output voltage from the specimen (V_{out}) and the value of the resistance (R) of the resistor load. The

DMA registered the distance l between the copper plates, i.e. the thickness of the sample during the measurement, while the cross-sectional area A_i is calculated considering the cylindrical shape of the specimen, i.e. 10 mm diameter.

3.2.3.2. Piezoelectric measurements

With the same concept as the conductivity measurement setup, the output voltage generated by the piezoelectric patch was monitored. To measure the output voltage of the materials, copper plates with electrical wires were attached to the upper and lower parts of the specimen (i.e. cylindrical sample containing sandwich design) to create a connection with the electrical measuring devices and the clamps were covered with Kapton tape for the electrical insulation of the specimen. For this piezoelectric measurement, the electrical circuit was simplified: Figure 2b. It included a shunt resistor placed in series with the specimen to divert the current flow generated by the specimen across the voltage module. The PVDF film in a piezoelectric patch produces electrical charges that move to the patch surface. Then, the conductive elastomer layers enable the transport of the generated electrical current to a voltage module, used to monitor the output voltage. The application of sinusoidal stresses to the piezoelectric patch leads to sinusoidal voltages due to the generation of Alternating Current (AC). The output power (P, μW/cm^2) of the piezoelectric patch is calculated using Equation 2 [26]:

$$P = \frac{<V^2>}{R} \frac{1}{Instantaneous\ cross-sectional\ area} \ (\text{μW/cm}^2) \qquad (2)$$

Where $<V^2>$ is the average of the squared generated voltage in the dynamic phase while the calculation of the cross-sectional area includes the exact dimensions of cylindrical shape of the specimen. The maximum amount of power is reached when the resistor value (R) is equal to the internal resistance of the piezoelectric patch. Therefore, the effect of the resistor value on the output power was investigated.

3.3.   Results and discussion

3.3.1.   Assessment of the electro-dynamic setups

First of all, the impact of the required electrical connections at the DMA to measure the electricity was evaluated. Therefore, the influence of the clamps with and without Kapton tape and copper plates on the electrical properties of the samples analysed in compression mode was investigated. This was done by using a conductive elastomer composite (Table 2) and the setup and specimen for conductive measurement. Figure

3 shows the complex modulus E* and the tan δ of NR filled with 15 vol% of CCB in a temperature range of -120 to 120°C at a frequency of 10 Hz.

The results show that the presence of Kapton tape and copper plates does not considerably affect the measurements of the complex modulus and tan δ. In this range of temperatures, the differences in the output values are negligibly small, ascertaining that this setup can be utilised for determining the conductivity and piezoelectricity of the materials.

3
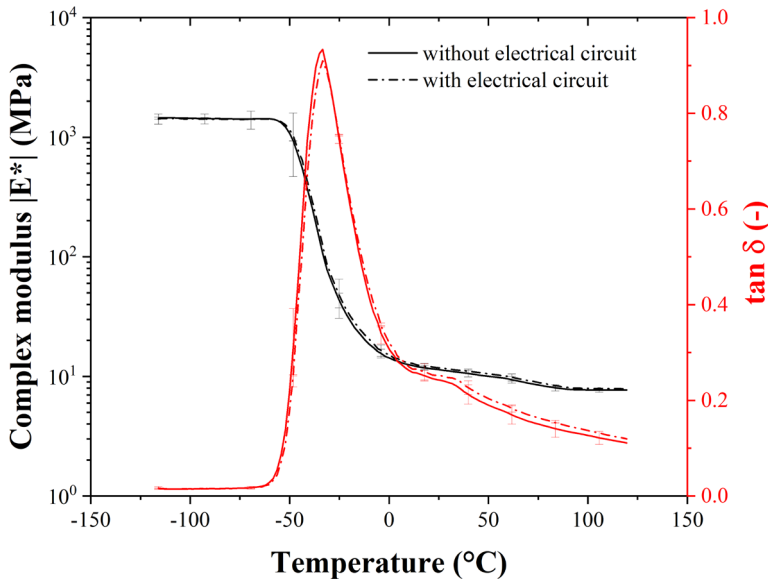
Figure 3 Comparison of E* (in black) and tan δ (in red) measured in compression mode by using the clamps with and without the set of a voltage module plus Kapton tape and copper plates.

3.3.2.   Electrical conductivity of elastomeric composites

3.3.2.1. Progress of conductivity in dynamic conditions

Firstly, the conductive elastomeric composites of the PEH sandwich design were investigated. Conductive elastomeric composites operate in various conditions, such as diversified mechanical loads, temperatures and frequencies during their service life in rolling tyres. Figure 4 shows a typical example of a simultaneous record of the applied dynamic force and the resulting voltage at set parameters. Before starting the measurement, all conductive elastomeric composites were conditioned with a pre-load of 3.5 N in order to overcome the impact of deformation history on the measurements, i.e. Mullins effect [27]. After having applied this pre-load (Figure 4a), the measurement starts by applying static and dynamic strains, of 10% and 2% respectively, as shown in Figure 4b. When the specimen is a conductive elastomeric

composite, filled at least with a critical amount of conductive carbon black (i.e. at 50% percolation threshold), the sinusoidal dynamic load causes a periodic disruption of filler network due to the oscillating deformation, resulting in an alternating connection and disconnection of the filler particles. It results in a sinusoidal voltage as well.
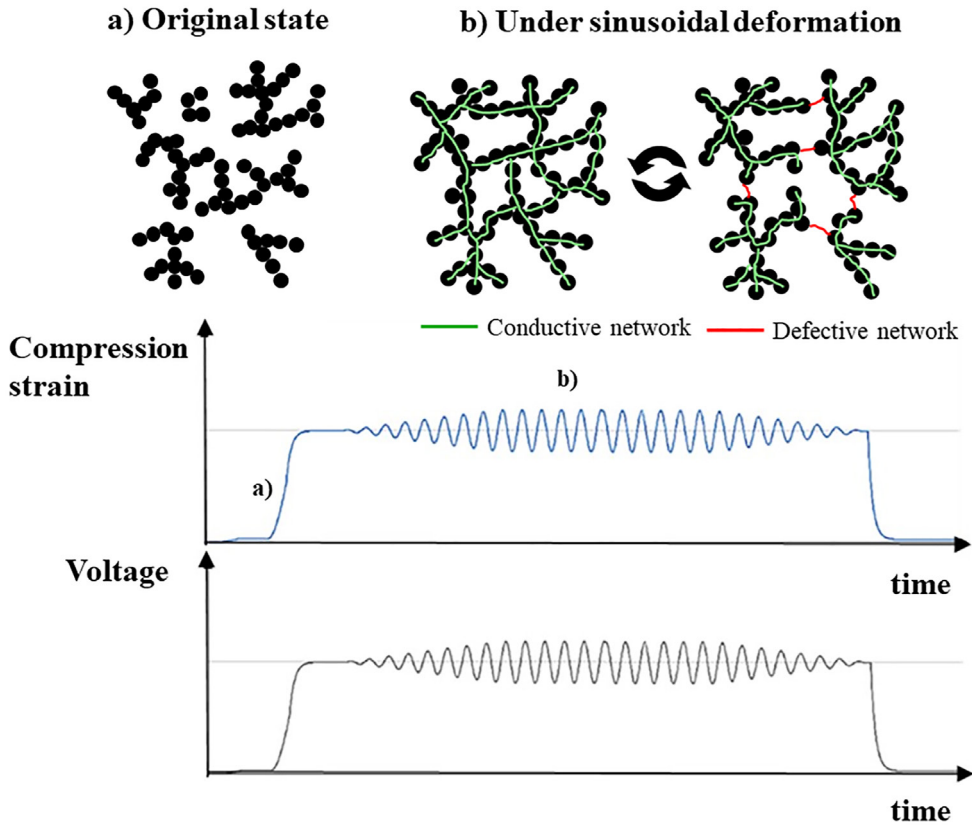
Figure 4 Force and voltage changes with the schematic structures of carbon black networks at different states of the conductive measurements in DMA: (a) under pre-load and (b) sinusoidal deformation.

This concept was recently studied in detail by Bhagavatheswaran et al. [28]. They studied the piezoresistive properties of elastomeric composites. In carbon black and carbon nanotubes filled elastomers under dynamic strain, the filler network disrupted and recovered harmoniously, increasing and decreasing the interparticle distances and causing the sinusoidal changes in electrical conductivity over time.

Applying a static and dynamic strain on a conductive elastomeric composite causes the rearrangement of filler network due to an increased internal friction in the

material [29]. Measurements of electrical conductivity of conductive elastomers as a function of volume fraction of CCB, called percolation plot, for two values of dynamic strains, 1 and 2%, are shown in Figure 5.

3
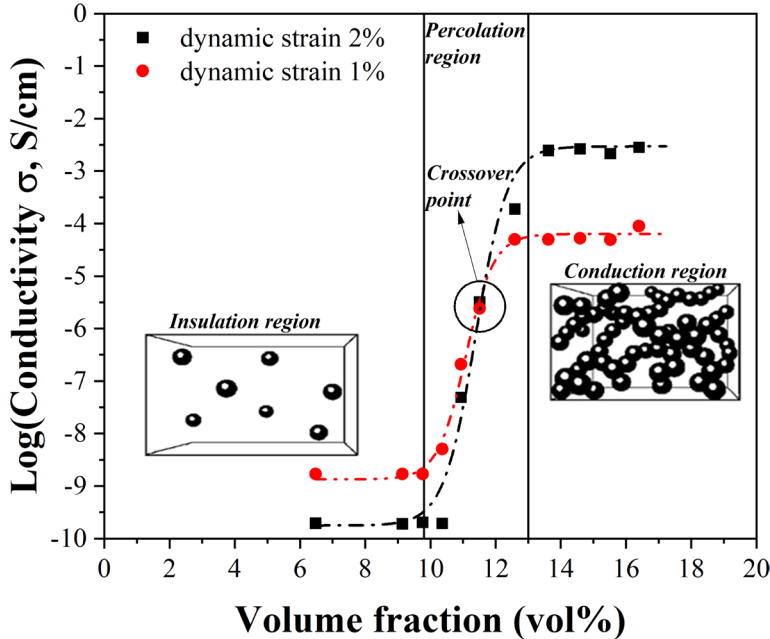
Figure 5   Conductivity as a function of volume fraction of CCB for dynamic strains of 1% and 2% at 100°C and 100 Hz.

The electrical conductivity was calculated from the voltage measured over time at 100°C and 100 Hz. In this way, the deformation history was neglected and the conductivity was calculated after ca. 60 min, when the voltage reached a plateau. In this plot, it is possible to distinguish three zones: (1) the insulation region, at a low filler amount; (2) the percolation region with a sharp increase in conductivity and a transition of the material from insulator to conductor; (3) and the conductive region at a high filler amount. Based on these trends, a crossover point in the percolation region can be identified. In the conducting zone, the conductivity increases by ca. 2 orders of magnitude at the higher dynamic strain. This is due to the fact that dynamic deformation affects the physical contact between the particles, implying a decreasing tunneling gap between carbon black particles and increased charge carriers transfer across this conductive path. In the insulating region, the conductivity decreases ca. 1 order of magnitude at higher dynamic strain. This might be because a continuous filler network is not formed at this stage and a higher dynamic strain increases the tunneling distance across the conductive path.

Chapter 3

3.3.2.2. Effects of temperature and frequency

To study the effects of temperature and frequency on electrical conductivity measured in dynamic conditions, five different amounts of the CCB were selected: unfilled composite and 9 vol% of CCB (insulating region), 11 vol% of CCB (percolation region), 15 and 17 vol% of CCB (conducting region).

To determine the repeatability, three individually prepared conductive elastomeric composites filled with 15 vol% of CCB were measured and the standard deviation of electrical conductivity was 5%. Figures 6a and 6b show tan δ and electrical conductivity as a function of temperature from -120 to 120°C. Based on the tan δ curve, it is possible to distinguish the glassy region (below -62.5°C), glass transition region (from -62.5 to 12.5°C) and rubbery region (from 12.5 to 120°C). The temperature has a strong impact on the electrical conductivity of the conductive elastomeric composites. Elevated temperatures accelerate the transfer of charge carriers across the conductive path. This concept is mainly valid in the rubbery region due to the higher flexibility of the material in this state. Noteworthy, there are different trends of the electrical conductivity in the glass transition region of the composites.

Composite in the percolation zone (i.e. 11 vol% of CCB) shows a sharp decrease in the electrical conductivity in the glass transition region. Due to the limitation of the setup, it is not possible to measure a value of conductivity lower than 10^{-10} S/cm. Thus, it was not possible to investigate in this study the sharp decreases of electrical conductivity in the glass transition region for composites in the insulation zone (i.e. 9 vol%). As shown in Figure 6c, the glass transition phenomenon results in the coexistence of rubbery and glassy polymeric chains and morphological change of filler network.

In the range of temperature from -62.5 to -37.5°C, the electrical conductivity decreases as rubbery polymeric chains are present next to the glassy chains, affecting the mobility of charge carriers across the carbon black particles and the tunneling effect. From ca. -37.5°C, the electrical conductivity increases as in this region the composite is characterised by solely rubbery polymeric chains and an increased free volume [30,31]. This implies higher mobility of charge carriers inside the composites leading to a filler network orientation with a lower tunneling gap across the conductive path and thus an increased electrical conductivity.

70

a)

b)

c)
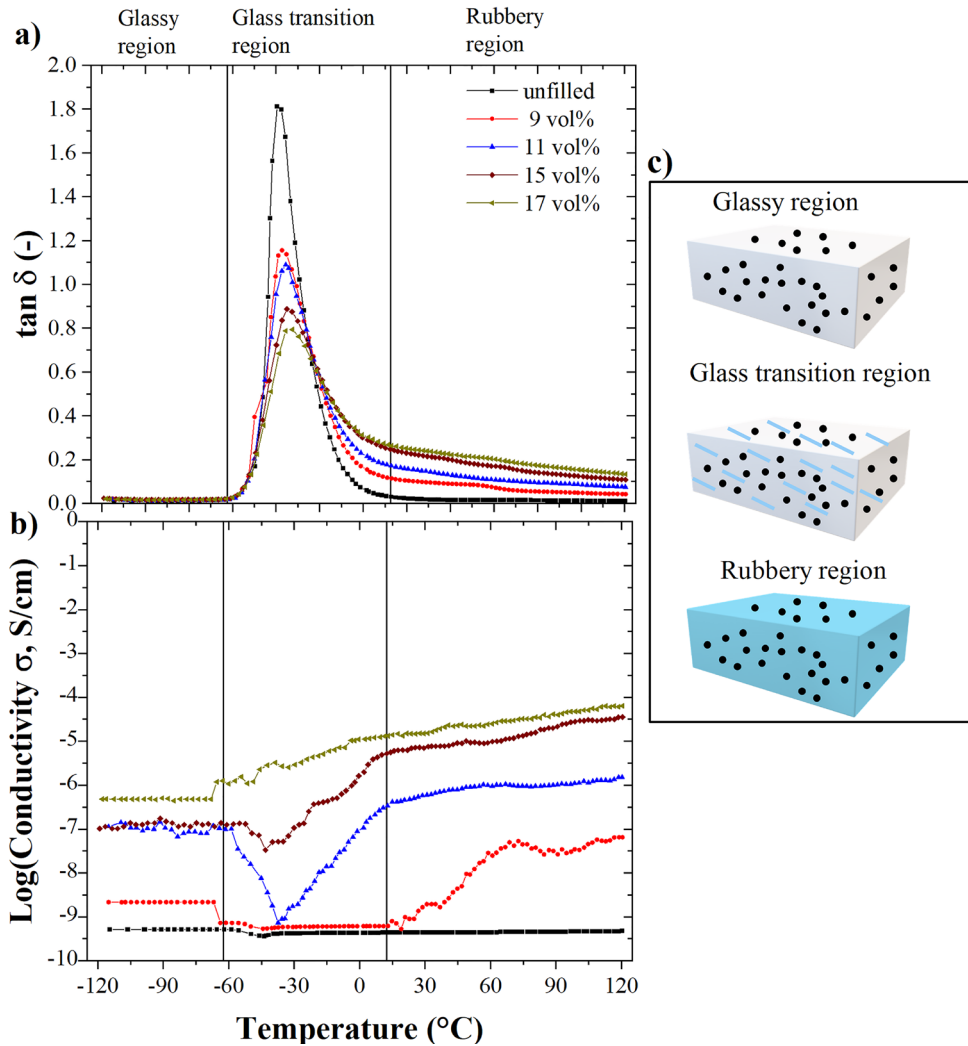
Figure 6   (a) tan δ and (b) electrical conductivity of conductive elastomeric compound as a function
of temperature at 10 Hz. Note that the static and dynamic strains of compression were 0.5%
at a temperature lower than -35°C, and 10 and 2% above -35°C. (c) Schematic transition
from glassy to rubbery region of elastomeric composites.

This phenomenon has a much lower impact in the case of composites in the
conducting zone; the conductive elastomeric composite filled with 17 vol% of CCB
shows a continuously increasing trend with rising temperature. This is probably due
to the fact that the amount of conductive filler is much larger, and the higher free
volume for the glassy-to-rubbery transition has a negligible effect on the
conductivity. This concept agrees with the results reported in literature [28,32].
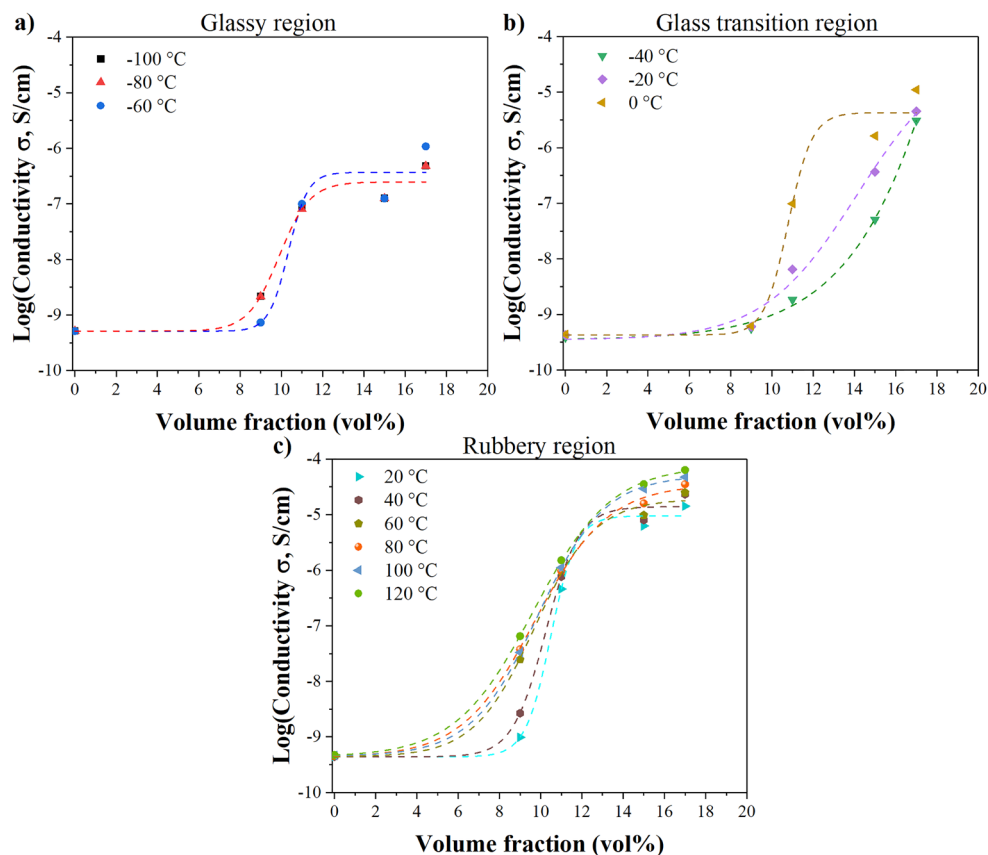
Figure 7   Electrical conductivity of conductive elastomeric composites as a function of volume fraction of carbon black CCB at different temperatures in (a) glassy, (b) glass transition and (c) rubbery regions.

In the whole temperature range, the electrical conductivity of the composites increases with increasing CCB amount, due to a more extensive filler network. To provide a deeper insight into how the filler network affects this phenomenon, Figure 7 shows the electrical conductivity as a function of volume fraction of carbon black at different temperatures in the three different regions. In the rubbery region, higher temperature causes a decrease in percolation threshold and an increase of conductivity in the conductive region. This confirms the acceleration of the charge carrier across the conductive path and a decreased percolation threshold. In the glass transition region, the fitting does not reach a plateau, as in the other regions. As above-mentioned, the glass transition affects the mobility of charge carriers and the percolation threshold. Thus, a higher amount of carbon black is needed in the material to be conductive in this region. Figure 8 shows the electrical conductivity as a function of frequency from 0.1 to 100 Hz at room temperature.
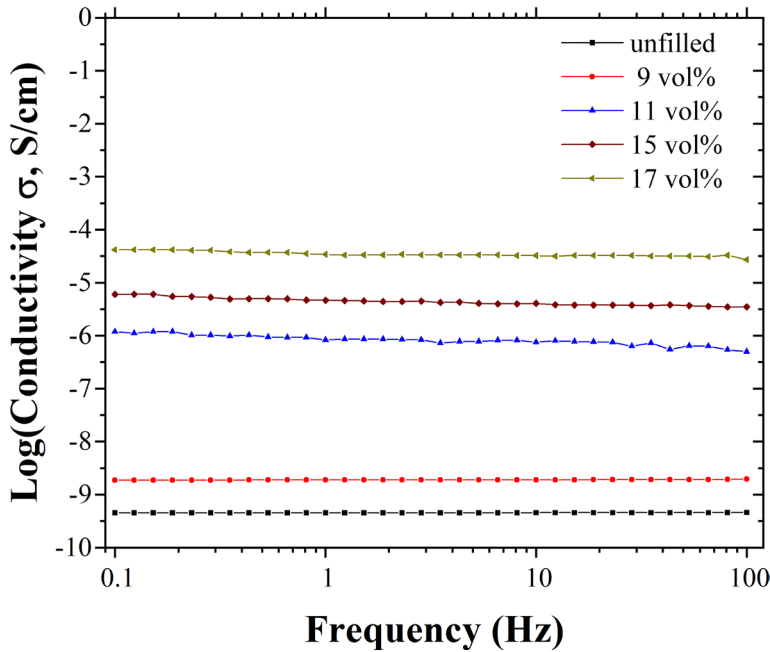
Figure 8   Electrical conductivity of conductive elastomeric composites filled with various amounts of CCB as a function of frequency at room temperature.

In the entire investigated range of frequencies, the electrical conductivity increases with the carbon black amount, as in the results of the temperature sweep analysis (Figure 6, rubbery region). Additionally, the conductivity of all composites seems to be not affected by the frequency. This is commonly called Direct Current (DC) conductivity and it is associated with the diffusion process of charge carriers across the conductive path [29,33].

3.3.3.   Piezoelectric properties of PEH

3.3.3.1. Progress of piezoelectricity in dynamic conditions

After the confirmation of the negligible influence of the electrical circuit presence and after the optimisation of the conductive elastomeric composite, the measurement device is now settled, ready to be used for the characterisation of the PEH. The applied static and dynamic loads cause a deformation of the repeating units (CH_2-CF_2) in piezoelectric polymer PVDF, forming dipole moments inside the material and consequently charges generation. The conductive elastomeric composites are present on each side of the PVDF film to induce the flow of the electrical charges. The structure of the piezoelectric energy harvester at its original state is shown in Figure 9a.
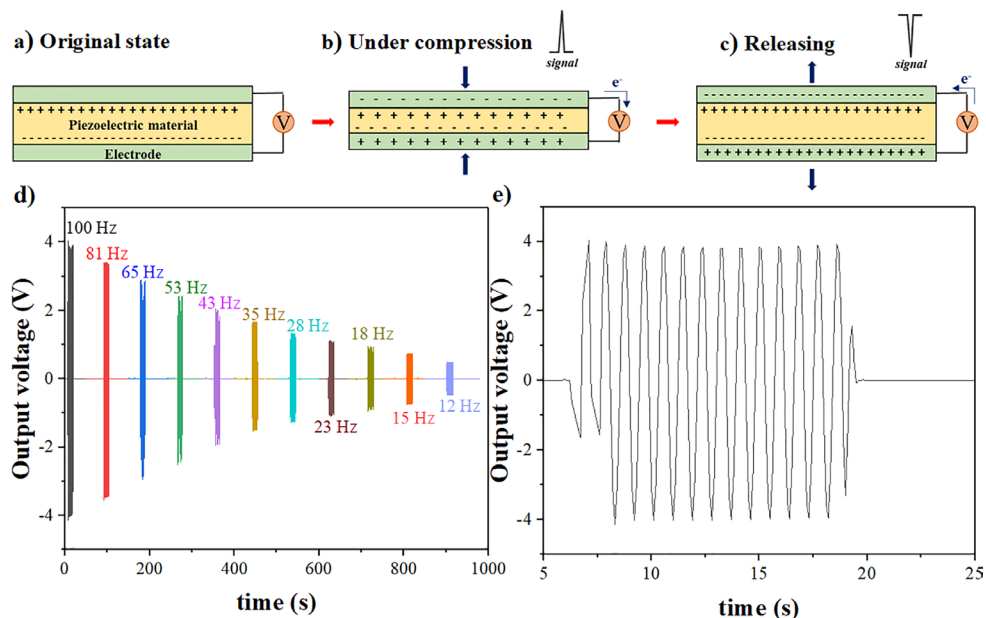
Figure 9 Working principle of PEH in dynamic conditions: (a) original state, (b) when compressed and (c) released. Output voltage of PVDF sandwiched by NR filled with 15 vol% of CCB (d) in the frequency range from 100 to 12 Hz and (e) at 100 Hz.

Both surfaces of the piezoelectric material are characterised by opposite charges. When a compressive strain is applied (in Figure 9b), the dipoles deflect, leading to a weakening of the internal dipole moments and their polarity. Consequently, the positive-charged surface attracts the electrons via the electrical circuit connected to both electrodes. When the strain is removed, the charges flow in the opposite direction. During the DMA measurements, when a sinusoidal dynamic load is applied to the material, the resulting voltage follows a sinusoidal trend as well. The positive and negative peaks of the voltage are caused by the flow of the charges between the upper and lower conductive layers of the PEH. Figure 9d shows the progress of the piezoelectric measurement of a harvester, i.e. PVDF sandwiched by NR filled with 15 vol% of CCB, during a frequency sweep in the range of 0.1 to 100 Hz. With decreasing frequency, a lower voltage is generated when the dynamic load is applied and, in turn, a lower power, which can be calculated using Equation (2). This is due to the vibrational displacements of dipoles of the piezoelectric material. To harvest power from piezoelectric harvesters, the device needs to be connected to a resistor load. The output power from the piezoelectric harvester is maximised when the resistor load matches the internal resistance of the piezoelectric material. Thus, the effect of the resistor load on a PVDF-based harvester was first investigated. Five

different resistor loads (see Figure 2b) were tested for the piezoelectric measurements, i.e. 1.5, 2.2, 3.9, 4.7 and 10 MΩ. Figure 10 shows the output power at 25°C and 100 Hz from the piezoelectric harvester patch having PVDF and the conductive elastomeric composite NR filled with 15 vol% of CCB. This conductive elastomeric composite was selected as it corresponds to the minimum amount of carbon black above which there is not any meaningful change of electrical conductivity (see Figures 6 and 7).

3
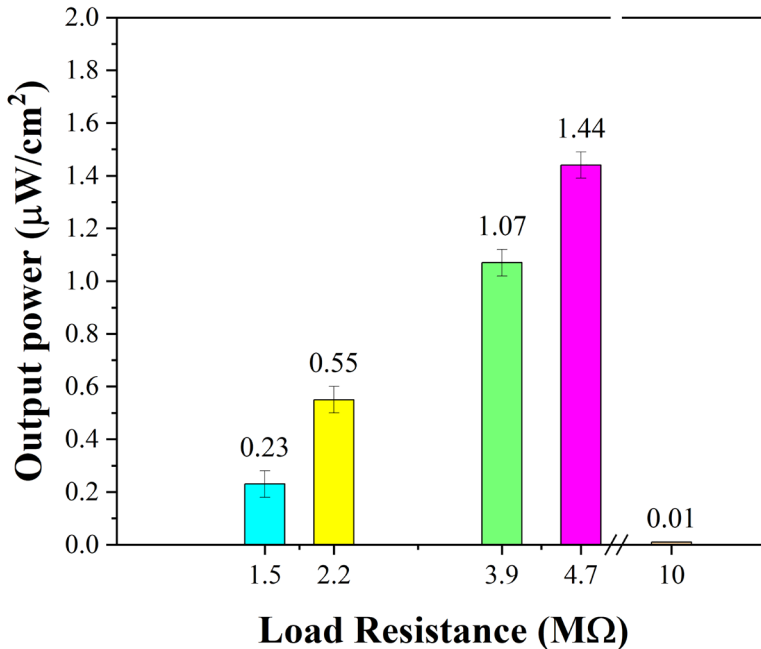
Figure 10   Output power generated at 100 Hz and 25°C across various resistor loads by the harvester consisting of PVDF and conductive elastomeric compound with NR filled with 15 vol% of CCB.

To determine the repeatability, three individually prepared piezoelectric harvester patches were measured at 4.7 MΩ and the standard deviation of electrical conductivity was 5%. The output power across a resistor load gradually increases to reach a maximum and then decreases with further increasing resistance. In the experiments performed with the resistors listed above, the maximum electrical power of 1.44 $\mu W/cm^2$ was obtained with a resistor of 4.7 MΩ. In the electrical circuit for piezoelectric measurements (Figure 2b), the resistor load is in series with the piezoelectric harvester. Thus, the electrical current generated by the piezoelectric patch goes through the resistor load. The output is then maximised only when the resistor load is close to the internal resistance of the piezoelectric harvester. The

resistor with a load value of 4.7 MΩ was selected for further analyses of the piezoelectric patches prepared with different conductive elastomeric composites.

3.3.3.2. Effects of temperature and frequency

The output power derived from the sandwich-designed harvester PVDF and the conductive elastomeric compounds filled with 11, 15 and 17 vol% was measured as a function of frequency and temperature with a resistance load of 4.7 MΩ. The results are shown in Figure 11.
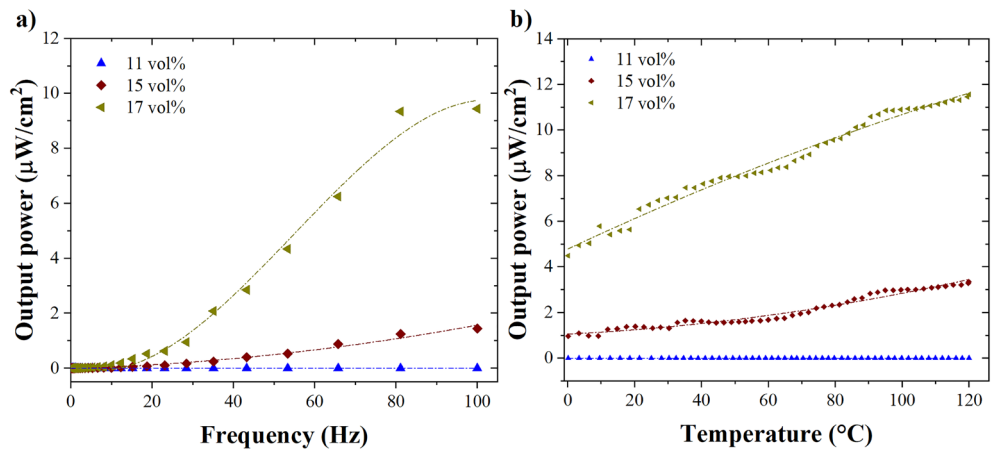
Figure 11   Output power generated by PVDF sandwiched with NR filled with 11, 15 and 17 vol% of CCB in (a) frequency sweep at 25°C and (b) temperature sweep at 100 Hz across a resistor load of 4.7 MΩ.

To determine the repeatability, three individually prepared piezoelectric harvester patches including PVDF and conductive elastomeric composite filled with 15 vol% of CCB were measured. The standard deviation of electrical conductivity was 5%. Figure 11a indicates that the output power increases at elevated frequencies, because there is a higher number of mechanical excitations to the material in a given timespan, activating the dipoles inside the PVDF film more frequently. It is reported that a value of frequency exists, called resonant frequency, in which the piezoelectric material has the highest efficiency [34]. This resonance frequency depends on the materials themselves and the mechanical load. The maximum power of the investigated piezoelectric harvester is found at 100 Hz, the highest frequency value of the DMA used in this study. By increasing the temperature (Figure 11b), the generated power rises considerably. This behavior confirms the already observed phenomena (Figure 6b) that the temperature increases considerably the electrical conductivity. Additionally, the piezoelectric effect increases with increasing temperature due to the higher mobility of dipoles in the PVDF film, resulting in

higher output power. The piezoelectric patch within the conductive elastomeric composite NR filled with 17 vol% of CCB provides the highest generated electricity due to the highest value of conductivity.

3.4. Conclusions

Novel setups to characterise the components of piezoelectric energy harvester (PEH) under simulated conditions of tyres were successfully developed. The setups include a DMA coupled with electrical circuits. These analyses lead to a better understanding of the main factors influencing the electrical conductivity of elastomers and the output voltage from piezoelectric materials. Moreover, by selecting the parameters in DMA for simulating the tyre-rolling conditions, piezoelectric energy harvester components were studied and optimised.

The electrical conductivity of elastomers is increased via the so-called mechanism tunneling effect, by the addition of carbon black. Increasing carbon black amounts and dynamic strain level results in the electrical conductivity increase due to a reduced tunneling distance. The electrical conductivity of elastomeric composites (used as electrodes of PEH) showed a strong temperature dependency. The compounds with an amount of carbon black below and at the percolation threshold lost their electrical properties in the glass transition region, but the conductivity increased again with increasing temperature. This phenomenon is attributed to the chain and segmental mobility and structural change of filler in this region. In the investigated range of frequencies from 0.1 to 100 Hz, the electrical conductivity shows a frequency-independent trend.

PVDF film with 0.1 mm thickness was sandwiched between two layers of elastomeric conductive composite to form a flexible piezoelectric energy harvester. With the developed setup it was possible to select a resistor load in order to maximise the output power and determine a temperature and frequency range in which the output power is the highest.

3

3.5. References

[1]   B. Wu, Y. Fang, L. Deng, Summary of energy collection application in vehicle tire pressure monitoring system, 4th International Conference on Automation, Control and Robotics Engineering, Association for Computing Machinery, Shenzhen 2019, pp. 1-6.

[2]   C.R. Bowen, M.H. Arafa, Energy harvesting technologies for tire pressure monitoring systems, Adv. Energy Mater., 5 (2015) 1401787.

[3]   A.E. Kubba, K. Jiang, A comprehensive study on technologies of tyre monitoring systems and possible energy solutions, Sensors, 14 (2014) 10306-10345.

[4]   Z. Yang, S. Zhou, J. Zu, D. Inman, High-performance piezoelectric energy harvesters and their applications, Joule, 2 (2018) 642-697.

[5]   O.J. Jousimaa, Y. Xiong, A.J. Niskanen, A.J. Tuononen, Energy harvesting system for intelligent tyre sensors, 2016 IEEE Intelligent Vehicles Symposium (IV), IEEE, Gothenburg, 2016, pp. 578-583.

[6]   D. Maurya, P. Kumar, S. Khaleghian, R. Sriramdas, M.G. Kang, R.A. Kishore, V. Kumar, H.-C. Song, J.-M. Park, S. Taheri, S. Priya, Energy harvesting and strain sensing in smart tire for next generation autonomous vehicles, Applied Energy, 232 (2018) 312-322.

[7]   H. Kim, Y. Tadesse, S. Priya, Piezoelectric energy harvesting, in: S. Priya, D.J. Inman (Eds.) Energy Harvesting Technologies, Springer US, Boston 2009, pp. 3-39.

[8]   J. Lee, S. Kim, J. Oh, B. Choi, A self-powering system based on tire deformation during driving, Int. J. Automot. Technol., 13 (2012) 963-969.

[9]   K.H. Mak, S. McWilliam, A.A. Popov, Piezoelectric energy harvesting for tyre pressure measurement applications, Proc. Inst. Mech. Eng. D, 227 (2013) 842-852.

[10]   X. Wu, M. Parmar, D.W. Lee, A seesaw-structured energy harvester with superwide bandwidth for TPMS application, IEEE/ASME Trans. Mechatron., 19 (2014) 1514-1522.

[11]   R. Elfrink, S. Matova, C.d. Nooijer, M. Jambunathan, M. Goedbloed, J.v.d. Molengraft, V. Pop, R.J.M. Vullers, M. Renaud, R.v. Schaijk, Shock induced energy harvesting with a MEMS harvester for automotive applications, 2011 International Electron Devices Meeting, International Electron Devices Meeting IEDM Technical Digest, Washington, 2011, pp. 677-680.

[12]   Q.C. Tang, X.X. Li, Non-contact frequency-up-conversion energy harvester for durable & broad-band automotive TPMS application, 2012 IEEE 25th International Conference on Micro Electro Mechanical Systems (MEMS), IEEE, Paris, 2012, pp. 1273-1276.

[13]   N. Makki, R. Pop-Iliev, Pneumatic tire-based piezoelectric power generation, SPIE Smart Structures and Materials + Nondestructive Evaluation and Health Monitoring, SPIE, San Diego, 2011, pp. 1-10.

[14]   N. Makki, R. Pop-Iliev, Piezoelectric power generation in automotive tires Smart Materials, Structure & NDT in aerospaceMontreal, 2011.

[15]   D.A. Van den Ende, H.J. van de Wiel, W.A. Groen, S. van der Zwaag, Direct strain energy harvesting in automobile tires using piezoelectric PZT–polymer composites, Smart Mater. Struct., 21 (2011) 015011.

[16]   S. Sadeqi, S. Arzanpour, K.H. Hajikolaei, Broadening the Frequency Bandwidth of a Tire-Embedded Piezoelectric-Based Energy Harvesting System Using Coupled Linear Resonating Structure, IEEE/ASME Trans. Mechatron., 20 (2015) 2085-2094.

[17]   Y. Zhang, R. Zheng, K. Shimono, T. Kaizuka, K. Nakano, Effectiveness Testing of a Piezoelectric Energy Harvester for an Automobile Wheel Using Stochastic Resonance, Sensors, 16 (2016) 1727.

[18]   R. van Schaijk, R. Elfrink, J. Oudenhoven, V. Pop, Z. Wang, M. Renaud, A MEMS vibration energy harvester for automotive applications, SPIE2013.

[19]   K.B. Singh, V. Bedekar, S. Taheri, S. Priya, Piezoelectric vibration energy harvesting system with an adaptive frequency tuning mechanism for intelligent tires, Mechatronics, 22 (2012) 970-988.

[20]   I.A.H. Al-Najati, K.W. Chan, S.Y. Pung, Tire strain piezoelectric energy harvesters: a systematic review, International Journal of Power Electronics and Drive Systems, 13 (2022) 444-459.

[21]   C. Mangone, W. Kaewsakul, M. Klein Gunnewiek, L.A.E.M. Reuvekamp, J.W.M. Noordermeer, A. Blume, Design and performance of flexible polymeric piezoelectric energy harvesters for battery-less tyre sensors, Smart Mater. Struct., (2022).

[22]   C. Mangone, M. Klein Gunnewiek, L. Reuvekamp, Tyre comprising a piezoelectric device, 2021.

[23]   C. Mangone, M.K. Gunnewiek, L. Reuvekamp, W. Kaewsakul, A. Blume, Method for chemically adhering a diene rubber to a piezoelectric polymer, 2021.

[24]   G. Wang, K. Yu, C. Liang, Y. Mei, Influence of Contact Area Deformation Distribution of Tire on Tire Noise, Rolling Resistance and Dry Grip Performance, Int. J. Automot. Technol., 22 (2021) 231-242.

[25]   K. Yamaguchi, J.J.C. Busfield, A.G. Thomas, Electrical and mechanical behavior of filled elastomers I. The effect of strain, J. Polym. Sci. B Polym. Phys., 41 (2003) 2079-2089.

[26]   F. Khameneifar, S. Arzanpour, M. Moallem, A piezoelectric energy harvester for rotary motion applications: design and experiments, IEEE/ASME Trans. Mechatron., 18 (2013) 1527-1534.

[27]   V. Annarasa, Modelling the mechanical response of elastomers: the roles of the network, the filler and the deformation history, University of Nottingham, 2021.

[28]   E.S. Bhagavatheswaran, Exploring the Piezoresistive Characteristics of Solution Styrene Butadiene Rubber composites under static and Dynamic Conditions - A

Novel Route to Visualize Filler Network Behavior in Rubbers, Technische Universität Dresden, 2019.

[29]   S. Aloui, A. Lang, H. Deckmann, M. Klüppel, U. Giese, Simultaneous characterization of dielectric and dynamic-mechanical properties of elastomeric materials under static and dynamic load, Polymer, 215 (2021) 123413.

[30]   A. Rathi, Investigating safe mineral-based and bio-based process oils for tire tread application, University of Twente, 2019, pp. 250 p.

[31]   D. Ponnamma, R. Ramachandran, S. Hussain, R. Rajaraman, G. Amarendra, K.T. Varughese, S. Thomas, Free-volume correlation with mechanical and dielectric properties of natural rubber/multi walled carbon nanotubes composites, Composites Part A: Applied Science and Manufacturing, 77 (2015) 164-171.

[32]   X. Xia, Z. Du, J. Zhang, J. Li, G.J. Weng, Modeling the impact of glass transition on the frequency-dependent complex conductivity of CNT-polymer nanocomposites, Mechanics of Materials, 165 (2022) 104195.

[33]   J.G. Meier, M. Klüppel, Carbon black networking in elastomers monitored by dynamic mechanical and dielectric spectroscopy, Macromol. Mater. Eng., 293 (2008) 12-38.

[34]   Y.-H. Huang, C.-Y. Yen, T.-R. Huang, Dynamic Non-Destructive Evaluation of Piezoelectric Materials to Verify on Accuracy of Transversely Isotropic Material Property Measured by Resonance Method, Applied Sciences, 10 (2020) 5072.

Dynamic measurement setups for validating piezoelectric energy harvesters in driving conditions

3

Chapter 4

Enabling interfacial adhesion between conductive rubber and piezoelectric polymer

4

A piezoelectric energy harvester for battery-less tyre sensors has been developed. It consists of two elements: 1) a piezoelectric material - PolyVinyliDene diFluoride (PVDF) film and 2) an electrode - a conductive elastomer filled with carbon black and Single-Wall Carbon NanoTubes (SWCNT). It was designed as a flexible patch in a sandwich-like configuration, which can be mounted onto the inner liner of a tyre. The patch was fabricated by inserting a PVDF film in between two conductive elastomer sheets. The development started with improving the conductivity of the elastomer by adding 6 wt% of SWCNT masterbatch. The adhesion between the interfaces was improved through surface modification of the PVDF film by introducing oxygen functional groups via a plasma treatment and further modification with a thiocyanate silane. The successful surface modification of the PVDF film was confirmed by x-ray photoelectron spectroscopy. T-peel and fatigue tests showed durable and stable adhesion between PVDF and conductive elastomer, confirming that the silane can effectively bridge the two components. A glueing method is proposed to adhere the patch to the tyre inner liner compound. The harvester is estimated to sufficiently power a reference tyre sensor, producing 28 μW/cm^2.

Chapter 4

4.1.   Introduction

Over the last decades, energy-harvesting systems have received growing attention for their unique potential in enabling battery-less sensors and self-powered operations [1,2]. Energy harvesters are capable of deriving energy from environmental sources, like heat, solar light, mechanical vibrations. The obtainable energies can be converted into a useable form as electrical power. These self-generating electricity systems can function as power sources for electronic devices, mitigating the disadvantages associated with the use of batteries, such as the limited lifetime of such a device due to emptied energy, environmental pollution, and undesired high maintenance costs.

The automotive industry is one of the most profitable stakeholders of this energy-harvesting technology [3,4]. The rapid development of autonomous and electric driving results in the use of multiple sensors installed in vehicles. A good example of such sensor systems is a Tyre Pressure Monitoring System (TPMS) mounted in car tyres. This device is growing in use to monitor the conditions of tyres while running. The online data derived from the TPMS can be used to evaluate the tyre performances, e.g. fuel consumption efficiency and safety aspects according to the regulations established in Europe, the US and Asia [5]. A TPMS system can indicate whether the running tyres are under- or over-inflated by monitoring the real-time pressure of the tyres. Attempts to further improve the TPMS features are continuously made [6,7]. Therefore, developing a self-powered TPMS is highly attractive for this advancement.

Various energy harvesters have evolved for powering autonomous TPMSs [8-11]. Among those, Piezoelectric Energy Harvesters (PEHs) are highlighted as the most suitable technique. This technology includes a piezoelectric material placed between two electrodes. Upon externally applied mechanical forces, electrical charges are accumulated on both sides of the piezoelectric material and therefore, the electrodes induce a flow of electrical current. This mechanism may be employed within the operating conditions of car tyres. When a tyre is in contact with the road surface, it is continuously subjected to dynamic mechanical excitations involving externally applied forces, deformations, temperatures, as well as varied vibrations during rotating. The repetitious deformations of the piezoelectric materials, when installed as a part of a tyre at an appropriate position, provide the potential to continually produce electricity that can then be stored in the capacitor of a TPMS [11].

A variety of PEHs has been proposed to be fabricated for powering such sensors in tyres; different categories of piezoelectric materials were previously investigated and reported in the literature [4,8,10,14]. Several studies proposed multiple designs of piezoelectric ceramic disks with a metal electrode mounted in tyres, which were able to generate the electrical power over a wide range of running speeds of a tyre, 30-180 km/h [15-17]. In all cases, the designs fulfilled the reliability and cost requirements. However, the use of a metal electrode was a major disadvantage, due to large acceleration shocks. Later, the use of bump stops was suggested as a solution to limit the vibration amplitude and to maintain the structural integrity of the harvesters [18]. The use of a bump stop decreased the maximum bending stress generated on the harvesters but tended to reduce the generated power. Other researchers investigated the use of an elastomeric material to attach the piezoelectric disk on a tyre wheel, and the configuration of a harvester was mounted perpendicular to the tyre tread inner-wall surface [19,20]. For the first case, the piezoelectric ceramic based on Lead Zirconium Titanate (with formula $PbZr_{0.58}Ti_{0.42}O_3$: PZT) survived for only 10 minutes when an endurance test was carried out at 60 km/h. In the second case, a cantilever PZT with dimensions of 70 x 7 x 0.32 mm produced 500 µW at 50 km/h, but it was reported to be difficult to install the PEH in a configuration perpendicular to the tyre tread area. In 2012, Makki and Pop-Iliev [21,22] made a comparison between a piezoelectric ceramic PZT and polymer – PolyVinyliDene diFluoride (PVDF) by applying both materials to the inner liner of a tyre. The PZT disk with a thickness of 0.23 mm produced a higher value of electrical power, i.e. 4.5 mW, compared to a PVDF film with a thickness of 0.11 mm and a lateral dimension of 40 x 40 mm that gave only 0.85 mW. Nevertheless, the authors concluded that the higher flexibility of PVDF is advantageous over piezoelectric ceramics, limited in terms of rigidity and interfacial adhesion. This flexibility leads to a longer lifetime and good performance under dynamic applications [23-25].

From the literature described above, the use of a metal electrode does not lead to the best performance of a piezoelectric energy harvester when applied to a rolling tyre. Extensive investigation has been conducted to find a replacement for a flexible electrode, such as graphene [26,27], metal nanowires [28,29], conductive ink [29,30]. Among these candidates for flexible electronics, electrically conductive elastomers are the most promising alternative due to their elastic nature and the ease of mounting into the tyre. Generally, elastomers are insulating materials because their molecules are hydrocarbons with single carbon-carbon bonds along their polymeric chains, which do not allow delocalisation of electrons between atoms and

the transfer of electrical current [31]. Introducing carbon black particulates in the elastomeric matrix can create a continuous particles network, through which electrons are transferred [31,32]. Hence, the formation of such carbon black particulates network can establish electrically conductive pathways within an elastomer matrix.

In the present study, a piezoelectric polymer and an electrically conductive elastomer were investigated as components of a flexible piezoelectric energy harvester able to withstand tyre rolling conditions. Among polymer materials, β-PVDF is the most investigated candidate for energy harvesting due to its high piezoelectric coefficient and stability. Elastomeric electrodes were then selected to ensure maintaining the structural integrity of the elastomer under tyre rolling conditions. Conductive particles, such as carbon black and Single-Wall Carbon Nanotubes (SWCNT), were incorporated into this elastomeric phase to increase its electrical properties. The PEH prototype in the current study was designed as a sandwich configuration, based on a PVDF film inserted in between two layers of an elastomeric conductive composite. To fabricate this PEH, there are crucial developing procedures involved, like enhancing the electrical conductivity of the elastomeric layers and energy generation of the piezoelectric polymer, achieving sufficient adhesion of both components as well as to the inner liner of a tyre. Additionally, measurements are conducted to validate the performance of a resulting prototype in tyre rolling conditions. The design concept and methodologies to optimise and validate the component materials and the final prototype are described in this manuscript. The resulting harvester patch is finally verified to substantiate if the output electrical power can sufficiently support a reference TPMS sensor.

4.2.   Conceptual design

The PEH in this study was developed through several steps. As it should be attached to the inner liner of tyres, it needs to tolerate the dynamic operational conditions of the rolling tyres, which involves variable parameters, i.e. loads, strains, and temperatures. Thus, the compatibility and the adhesion between these two components must be sufficient, so that the designed prototype can withstand these harsh dynamic conditions. For this design system, based on proprietary information the piezoelectric harvester needs to generate a sufficient amount of electricity of approximately 28 mW to power a TPMS sensor [4]. The conductive composite needs to have adequate conductivity of around 10^{-5}-10^{-2} S/cm, to ensure that the desired amount of generated electricity can be transported to the TPMS device [31]. In addition, safety, reliability and cost should also be taken into consideration.

Regarding the aforementioned requirements, the PEH was designed as a sandwich configuration consisting of two key elements, as shown in Figure 1: a piezoelectric polymer β-PVDF film constructed in between two layers of a conductive elastomeric composite. PVDF is a semi-crystalline polymer with repeating units (CH_2-CF_2). Among the four crystalline polymorphic phases, β-PVDF is piezoelectric due to the presence of a dipole moment induced by an all-trans planar conformation. When an external load is applied, dielectrics of the material are deformed and equal, opposite charges are generated on the film surface. The conductive composite applied on each side of the material induces the flow of the charge carriers. The conductive composite is an elastomer filled with conventional reinforcing carbon black and single-wall carbon nanotubes.

According to the design concept, the project is divided into four steps:
- Preliminary tests of separate components by measuring the electrical properties of the piezoelectric polymer PVDF film and the elastomeric conductive composites;
- Verifying and improving the conductive and piezoelectric properties of the selected materials under dynamic deformations simulating tyre rolling conditions;
- Evaluation of the PEH regarding the adhesion of the key system elements and output power under tyre rolling conditions;
- Investigation of the adhesion performance between the PEH and the inner liner of a tyre.

Validation of the design is the final development step that primarily confirms the feasibility of the application in a pragmatically operational situation.
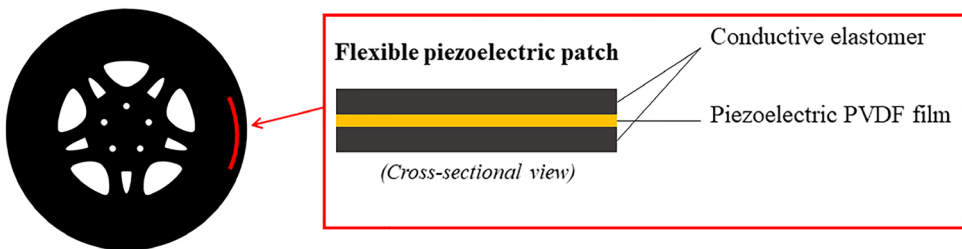
Figure 1   Conceptual design of piezoelectric energy harvester proposed in this study.

Chapter 4

4.3. Experimental

4.3.1. Materials

The piezoelectric polymer PVDF was supplied by PolyK Technologies LLC (Philipsburg, USA) in the form of a 100 μm thin film with A4 size. The chemical properties of this polymer film are given in Table 1. The PVDF surface was cleaned by chloroform (99.5%, Sigma-Aldrich, St. Louis, MO, USA), modified with 3-thiocyanatopropyltriethoxysilane (Si-264, Evonik Industries, Essen, Germany). The physical and chemical properties of this silame are reported in Table 2.

Table 1   Properties of the PVDF film with 100 μm thickness.

Properties *	Value
Charge coefficient, d_{31}	30 pC/N
Charge coefficient, d_{33}	-30 pC/N
Glass Transition Temperature	-34°C
Melting Temperature	170-175°C
Curie Temperature	100°C
Tensile strength	400-600 MPa
Young's Modulus	2300 MPa
Elongation at break	20-30%

*From PolyK Technologies LLC, USA.

Table 2   Physical and chemical properties of 3-thiocyanatopropyltriethoxysilane.

3-Thiocyanatopropyltriethoxysilane (Si-264)*	
Sulphur Content	12.5%
Average molecular weight	263 g/mol
Density	1.00 g/cm^3

*From Evonik Industries AG.

The reference composite C_{ref} includes the rubbers Natural Rubber (NR TSR20), high-cis branched Butadiene Rubber (BR 1280) and Styrene Butadiene Rubber (SBR 1502). The Carbon Black (CB) type with the relative values of BET specific surface area (ASTM D-6556) and OAN structure (ASTM D-2414) is N330, 78 m^2/g and 88 mL/100g). Rubbers, carbon black, processing oil, curing agents and antidegradants of C_{ref} were supplied by Apollo Tyres Global R&D. The conductivity of C_{ref} was further improved by adding highly conductive Single-Wall Carbon NanoTubes (SWCNT), 10 wt% dispersed in a low aromatic plasticiser, Treated Distillate Aromatic Extract TDAE oil, as masterbatch Matrix 603 (OCSiAl Europe, Luxemburg). Three composites were prepared with 2, 4 and 6 wt% of the SWCNT

Enabling interfacial adhesion between conductive rubber and piezoelectric polymer

masterbatch, coded C_1, C_2 and C_3, respectively. Table 3 shows the compositions of the C_{ref}, C_1, C_2 and C_3 composites.

Table 3   Compositions of conductive elastomeric composites.

Ingredients	Amount (phr)			
	C_{ref}	C_1	C_2	C_3
Natural Rubber NR TSR20	25	25	25	25
Styrene Butadiene Rubber SBR 1502	25	25	25	25
Butadiene Rubber Ni-BR	50	50	50	50
Carbon Black CB N 330	60	60	60	60
Processing oil	14	14	14	14
Curing agents	10	10	10	10
Antidegradation agents	7	7	7	7
SWCNT/TDAE	0	4	8	12

To investigate the possible application of the piezoelectric harvester in a tyre, the adhesion of the system towards an inner liner was investigated. The composite used for the inner liner was provided by Apollo Tyres Global R&D, coded C_{IL}. The piezoelectric system was glued to the vulcanised inner liner using an amine-silicone sealant: Teroson SI 33 from Henkel AG & C (Düsseldorf, Germany).

4.3.2.   Sample preparation

4.3.2.1. Preparation of conductive elastomeric composites

The composites C_1, C_2 and C_3 were prepared by adding 2, 4 and 6 wt% of the SWCNT/TDAE masterbatch to C_{ref} on a two-roll mill for 7 minutes and 2 mm nip width (Polymix 80 T, Schwabenthan-Maschinen GmbH & Co. KG, Berlin, Germany). To obtain a good dispersion level of the nanofillers, the composite C_{ref} mixed with the required amount of SWCNT/TDAE masterbatch was passed through the two-roll mill ten times. To vulcanise the conductive elastomeric composites, the vulcanisation characteristics of the composites were analysed using a Rubber Process Analyser (RPA 2000, Alpha Technologies, Ohio, USA). Each measurement was done for 40 minutes at 140°C at a frequency of 1.667 Hz and a strain amplitude of 0.5 degrees. The optimum vulcanisation time, i.e. the time when the cure torque reaches 90% of its maximum, known as t_{c90}, was taken as input for the vulcanisation. The composites were vulcanised at 100 bar in a Wickert press WLP 1600 (Wickert Maschinenbau GmbH, Landau, Germany) to their t_{c90} at 140°C. The samples obtained had a cylindrical shape with a diameter of 10 mm and a thickness of 4 mm.

Chapter 4

4.3.2.2. Preparation of piezoelectric harvesters

Surface modification of the piezoelectric PVDF film was carried out to improve the interfacial adhesion between the PVDF film and the elastomeric conductive composites. First, the PVDF film was treated with an oxygen plasma method using a Plasma-Prep II (SPI Supplies, West Chester, Pennsylvania, USA) consisting of a plasma vacuum chamber, in which the PVDF film was placed. A mechanical vacuum pump (Oerlikon, Lafert S.p.A., Piave, Italy) reduced the pressure inside the chamber to around 100-200 mTorr. After reaching this optimal pressure, oxygen gas was led into the chamber. A Radio-Frequency (RF) power at 13.56 MHz was applied to the chamber to excite and charge the oxygen molecules by turning them in oxygen radicals. The film was treated with this oxygen plasma for 15 minutes at room temperature. After this stage, the PVDF film surface had been randomly covered with hydroxyl and carbonyl groups which are highly reactive towards the subsequent treatment step known as 'silanisation'. The silanisation of the oxygen-treated PVDF film was carried out using the silane coupling agent 3-thiocyanatopropyltriethoxysilane. For this, the plasma-treated film was introduced into a desiccator under vacuum at room temperature for 1 and 24 hours. Inside the desiccator, the film was fixed with a holder to fully expose the surface of the film to the silane vapour. 3 ml of 3-thiocyanatopropyltriethoxysilane silane in a small Petri dish was placed close to the film.

The chemical structure of the modified PVDF film surface was characterised and confirmed for its modification efficacy using X-ray Photoelectron Spectroscopy XPS (PHI Quantera SXM, Chanhassen, Minnesota, USA). The PVDF films were irradiated using a monochromatic X-ray beam (Al Kα, 1486.6 eV) with a spot size of 100 μm. The XPS measurements were performed after each step of the surface treatment, i.e. after the oxygen plasma modification and after the silanisation at two different reaction times – 1 and 24 hours. The two reaction times were applied to verify which reaction time was adequate. Each spectrum was compared with the spectrum of a pure PVDF film cleaned before the analysis using chloroform. All samples were analysed at four different spots to confirm the evenness of the modification over the films.

After the silane treatment, the PVDF films were assembled with the conductive composites. This sandwich design was vulcanised into the desired cylindrical shape using compression moulding in the Wickert press WLP 1600 at 100 bar to their t_{c90}. The applied curing temperature of the piezoelectric sandwich is highly important. This is due to the fact that at around 100°C, named Curie temperature, a transition

from β-PVDF to δ-PVDF takes place. This reorientation of the β-dipoles affect the depolarisation of the polymer, implying a decreasing of piezoelectric performance [33]. Therefore, the effect of the curing temperature was investigated and PVDF film and conductive elastomer were vulcanised at three different temperatures, 120, 140 and 160°C.

The piezoelectric patch was fabricated into a sandwich configuration with a 0.1 mm thick PVDF film inserted in between the two sheets of a 2.0 mm thick conductive composite. Thus, a piezoelectric patch with about 4.1 mm thickness was achieved. In Figure 2a, the final piezoelectric patch is shown.

4.4. Sample characterisations

4.4.1. Adhesion between PVDF and conductive composite

The adhesive strength between the PVDF film and elastomeric conductive composite was investigated using a T-peel test. The measurement was performed in a tensile machine (Zwick Z1.0, Zwick/Roell, Venlo, the Netherlands) according to the ASTM D413 test standard. The specimen includes the PVDF film (with and without surface modification), a 2 mm thick reference composite C_{ref} and a 0.1 mm thick cotton fabric cloth (Twentse Damast Linnen en Katoenfabriek B.V., Losser, the Netherlands). The layers were vulcanised into the desired tensile sheet at 100 bar using compression moulding in the Wickert press WLP 1600 to their t_{c90} at 140°C. The dimensions of the obtained specimen were 20 mm in width and 120 mm in length. The cotton fabric cloth was inserted on the external side of the conductive composite so that the adhesion strength will not be influenced by this large deformation of the elastomer during the test. After having mounted the two components into the two 20 mm distant fixtures of the tensile machine, the two components were peeled apart at a constant rate of 20 mm/min. The adhesive strength needed to separate the virgin and surface modified PVDF from the reference conductive composite was measured. Five samples were tested and the data were averaged.

The adhesion bond stability between the two components – the PVDF film and the conductive elastomeric composites, was investigated using a Dynamic Mechanical Analysis DMA Eplexor 9 (Netzsch Gabo Instruments GmbH, Ahlden, Germany) with a time sweep measurement. Two piezoelectric sandwich patches were glued using a cyanoacrylate adhesive – Sicomet 7000 (Henkel AG & C, Düsseldorf, Germany), to three metal cylinders as double shear configuration (see Figure 2b). Then, they were clamped between the three metal cylindrical sample holders for the

double shear analysis (Figure 2c). The two side cylinders were fixed in the clamping assembly while the oscillating force acts on the middle cylinder. The time sweep test was performed at 10 Hz, room temperature, 2% of dynamic strain, for 20 hours. This measurement was also applied for validating the adhesion performance between the inner liner and the conductive composite. The conductive elastomeric composite and the inner liner were separately vulcanised into a thickness of 2 mm at 140 and 180°C, respectively. Afterwards, these two components were prepared into a small cylinder with a diameter of 10 mm and then glued together by the silicon adhesive – Teroson Si 33. Finally, the glued rubber parts were adhered to the metal cylinders for a double shear analysis using Sicomet 7000 cyanoacrylate adhesive. To quantify the repeatability, three samples were measured individually prepared by assembling conductive composites from the same masterbatch with PVDF films subjected to surface modification in one batch. The same for the adhesion of conductive composite and inner liner, three samples from the same masterbatch were vulcanised and measured.
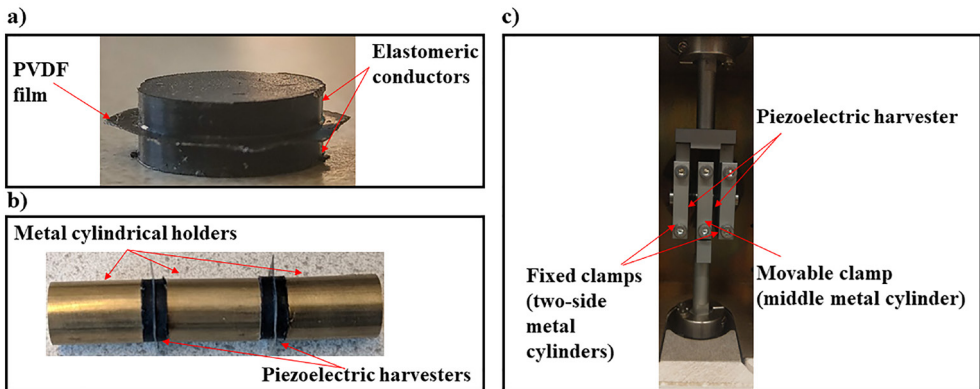
Figure 2   (a) Configurations of piezoelectric harvester; (b) piezoelectric harvesters with double shear sample holder; (c) DMA clamp for double shear analysis**.**

4.4.2. Setup for electro-dynamic measurements

The conductivity and piezoelectricity of the investigated materials were characterised using in-house developed setups, described in Chapter 3.

4.5.   Results and discussion

4.5.1.   Measuring parameters based on a reference car

The analysis of the material conductivity and piezoelectricity was performed according to the actual conditions of a rolling tyre. The DMA analysis was used to simulate these conditions, by selecting a proper value of temperature, frequency and

deformation. During car driving, the temperature inside a tyre can increase up to around 100°C [38]. On the other side, conductive elastomers lose their conductivity in the region of the glass transition, as reported in Chapter 3 [35]. The composites analysed in this study have a glass transition temperature at around -40°C and the transition region ends at appr. 0°C. Therefore, a temperature sweep analysis was performed in the range between 0 and 100°C at 10 Hz, which is a rotational frequency of a car driving at a speed of 80 km/h.

Tyre-road interactions also contribute to vibrations in the tyre. The operating frequency varies in the range between 1 and 100 Hz. Assuming as a reference a passenger tyre of the size 205/55R16 94R in Volkswagen Golf running at a speed of 80 km/h, the frequency due to tyre-road interactions is calculated via the following equation:

$$f = n \cdot \left[\frac{v\ (km/h)}{C\ (m) \cdot 3.6} \right] \tag{1}$$

Where n is the number of excitations per revolution and the term in the bracket is the rotations per second, v is the speed of the vehicle and C is the tyre circumference. Based on proprietary information, the order n was measured at 80 km/h, an average value of 10th order was selected. The circumference C of the selected tyre is 1.98 m. From these, the conductivity and piezoelectricity were measured in the frequency sweep from 1 to 100 Hz at room temperature.

The static and dynamic stresses applied for the measurements were based on the compression pressure under which the tyres are subjected during driving. Based on the assumed tyre size 205/55R16 94R with a total surface area A_{tyre} and the Volkswagen Golf with a total weight ($W_{vehicle}$) of 2100 kgf, the surface area of the tyre in contact with the road, the contact patch area ($A_{contact\ patch}$) is as follows:

$$A_{contact\ patch} = 7\%\ A_{tyre} = 0.029\ m^2 \tag{2}$$

The force F_{tyre} exerted on each tyre is calculated from the vehicle weight $W_{vehicle}$, the gravity constant g (9.81 m/s^2) and the number of tyres in a vehicle (i.e. 4 wheels), as follows:

$$F_{tyre} = \frac{W_{vehicle} \cdot g}{4} = 5150.25\ N \tag{3}$$

The average pressure exerted on a tyre (P_{tyre}) by a car-load was calculated with the ratio between the forces exerted on the tyre and the surface area of the contact patch:

$$P_{tyre} = \frac{F_{tyre}}{A_{contact\ patch}} \approx 0.18\ MPa \qquad (4)$$

However, the tread pattern of the tyre includes 30% of voids, i.e. grooves; this means that only 70% of the tyre tread is in contact with the road surface. Thus, the average pressure exerted on the contact patch area ($P_{contact\ patch}$):

$$P_{contact\ patch} = \frac{P_{tyre}}{70\%} \approx 0.26\ MPa \qquad (5)$$

A static stress of 0.35 MPa was then selected for the electro-mechanical measurements taking into account any possible extra loads from a driver, passenger(s) and carried luggage. The dynamic stress peak-to-peak was set at 0.25 MPa.

4.5.2.   Conductive properties of elastomer composites

The dynamic mechanical condition causes a periodic disruption of the filler network in the elastomeric sample due to the oscillating deformation, resulting in an alternating connection and disconnection of the filler particles. This concept was recently studied in detail by Bhagavatheswaran in his work in which the piezoresistive properties of elastomeric composites under dynamic conditions and the relationship between dynamic mechanic analysis and electrical resistivity were studied [39]. In carbon black and carbon-nanotubes filled elastomers under dynamic strain, the filler network disrupts and recover harmoniously, increasing and decreasing the interparticle distance and causing the change in electrical conductivity over time. When applying subsequent cycles, the rearrangement of the filler network happens already in the first cycle, after which a stable response is observed. Therefore, the effect of consecutive cycles of a temperature sweep was investigated.

The electrical conductivity of the elastomeric composites as a function of frequency is shown in Figure 3a. The use of carbon nanotubes improves the conductivity of the reference composite C_{ref}, in particular the composite C_3 with the 6 wt% of SWCNT masterbatch. Increasing the nanofiller concentration results in a denser filler network above the percolation threshold and closer distances between the filler particles, promoting denser conductive pathways in the material. The conductivity shows no frequency-dependent trend in case of C_{ref}, commonly called "DC conductivity". In contrast, it tends to increase with frequency for the composites C_1-C_3, called "AC conductivity". In C_{ref}, filled with 60 phr of CB N330, a conductive path of carbon black particles is present and the conduction mechanism is due to an electrical tunnelling effect between close aggregates of the filler. The composites C_1-C_3

contain joint conductive networks of carbon black and SWCNT. Therefore, the frequency-dependent conductivity of these composites depends on the fact that the amount of SWCNT added is not high enough to form another conductive percolation network next to the one already existing based on the regular carbon black. This implies the existence of a regime in which the AC conductivity varies based on the diffusion of charge carriers in the fractal aggregates and obeys a power-law relationship. These results are in agreement with the results reported in literature [40,41].
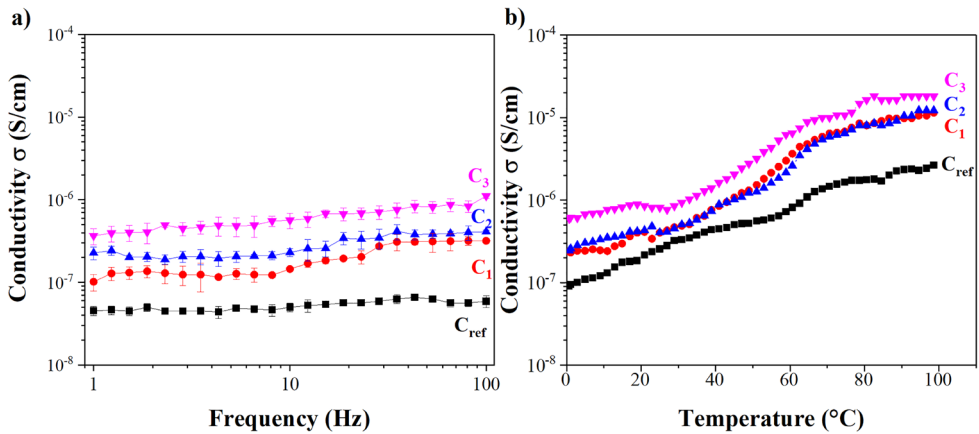
Figure 3 Electrical conductivity σ of the composites C_{ref}, C_1, C_2 and C_3, analysed with static and dynamic stresses of 0.35 and 0.25 MPa (a) at varying frequencies of at 20°C and (b) varying temperatures at 100 Hz.

The electrical conductivity of all composites as a function of temperature is depicted in Figure 3b. The composites exhibit an increased conductivity by increasing the temperature from 0 to 100°C. Elevated temperatures accelerate the charge carriers. This result is in good agreement with the observation from the frequency sweep analysis. It can be interpreted following the same concept of the higher extent of filler networks of conductive paths in the materials when a higher concentration of carbon nanotubes is applied. The increase in the conductivity with higher temperature seems to level off at a certain temperature as a result of lower volume density.

The results from the dynamic analysis using three consecutive temperature sweeps of the conductive composites are shown in Figure 4. The electrical conductivity of all vulcanisates increases with increasing measurement cycles due to orientation effect of the filler networks. The filler particles tend to align in longitudinal direction of the deformation, which is induced by the applied static and dynamic forces. The conductivity from the second and third measurement cycles is mostly independent

of temperature, implying that the materials have their optimum conductivity after the first cycle. This suggests that the filler particles are aligned coherently along the longitudinal direction during the first measurement cycle and the acceleration of the charges mobility has a negligible effect on electrical conductivity in the following cycles. According to the percolation theory, elastomers are conductive if filled with an amount of conductive fillers which exceeds a critical value, called percolation threshold. Higher surface area and aspect ratio of conductive particles implies a lower percolation threshold. Therefore, it is possible to conclude that the composite C_3 has the highest electrical conductivity compared to the other composites as it contains the largest amount of nanofillers.
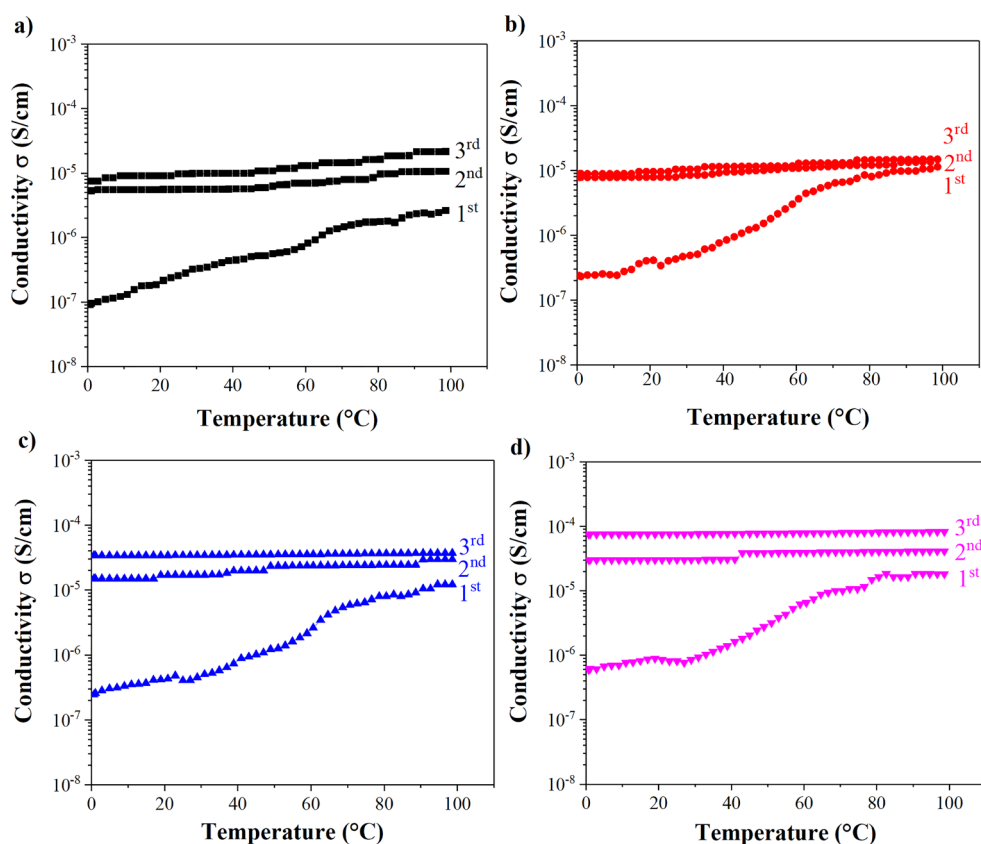

Figure 4   Electrical conductivity σ from a cyclic temperature sweep of the conductive composites at 10 Hz and 0.35 and 0.25 MPa of static and dynamic stresses: (a) C_{ref}, (b) C_1, (c) C_2 and (d) C_3.

4.5.3. Adhesion between PVDF and conductive composites

PVDF is a fluoropolymer possessing low surface energy and is therefore very inert to chemical reactions. To prepare the piezoelectric patch with a sandwich-like configuration, the PVDF film and the conductive elastomer composite need to have good interfacial adhesion. Proper surface treatment of the PVDF film seems to be a good solution. An oxygen plasma treatment was used to generate the hydroxyl and carbonyl groups at the surface of the PVDF film [42], see Figure 5a. These functionalities are reactive towards further chemical species.

The modified PVDF film was silanised with 3-thiocyanatopropyltriethoxysilane, as shown in Figure 5. The ethoxy groups of the silane can react with the active functionalities on the PVDF surface, by releasing ethanol as by-product. The other end group is a thiocyanate moiety, which introduces sulphur to the surface of the film, and participates in the vulcanisation reaction. This is expected to result in a strong adhesion between the interfaces [43].

To confirm the chemical modification of the PVDF surface, XPS spectroscopy was used to analyse the surface chemistry. Figure 5a shows the spectra of unmodified pure PVDF, plasma-treated PVDF and silanised PVDF using two different silanisation times: 1 and 24 hours. Table 4 summarises the atomic percentages of specific elements. The unmodified PVDF film cleaned with chloroform shows a clear fluorine (F) peak at 688 eV and two peaks of carbon (C) at 286 to 290 eV. The spectrum of unmodified PVDF shows a small peak of oxygen (O) at 533 eV, but the spectrum of the plasma-treated PVDF shows an increased concentration of oxygen at the surface, the amount is increased from 8.7 to 11.3 atomic percent. The silanisation reaction was proven by the decrease in fluorine and the increase in sulphur at the surface. As the silane is introduced to the surface, the amount of visible fluorine decreases, while the amount of sulphur increases. Increasing the silanisation time from 1 to 24 hours, the fluorine amount significantly decreases from 29.1 to 1.1 atomic percent. This confirms that the fluorine atoms are covered by the silane coupling agent. Additionally, the amount of sulphur increases from 0.9 to 2.9 atomic percent, which also confirms the higher concentration of the modifying silane. This is expected to promote the chemical coupling to the conductive composites. All the spectra of the different PVDF films contain a certain amount of silicon at the surface. This is probably due to contaminants that remained on the surface after the polymerisation and poling process of the PVDF film.
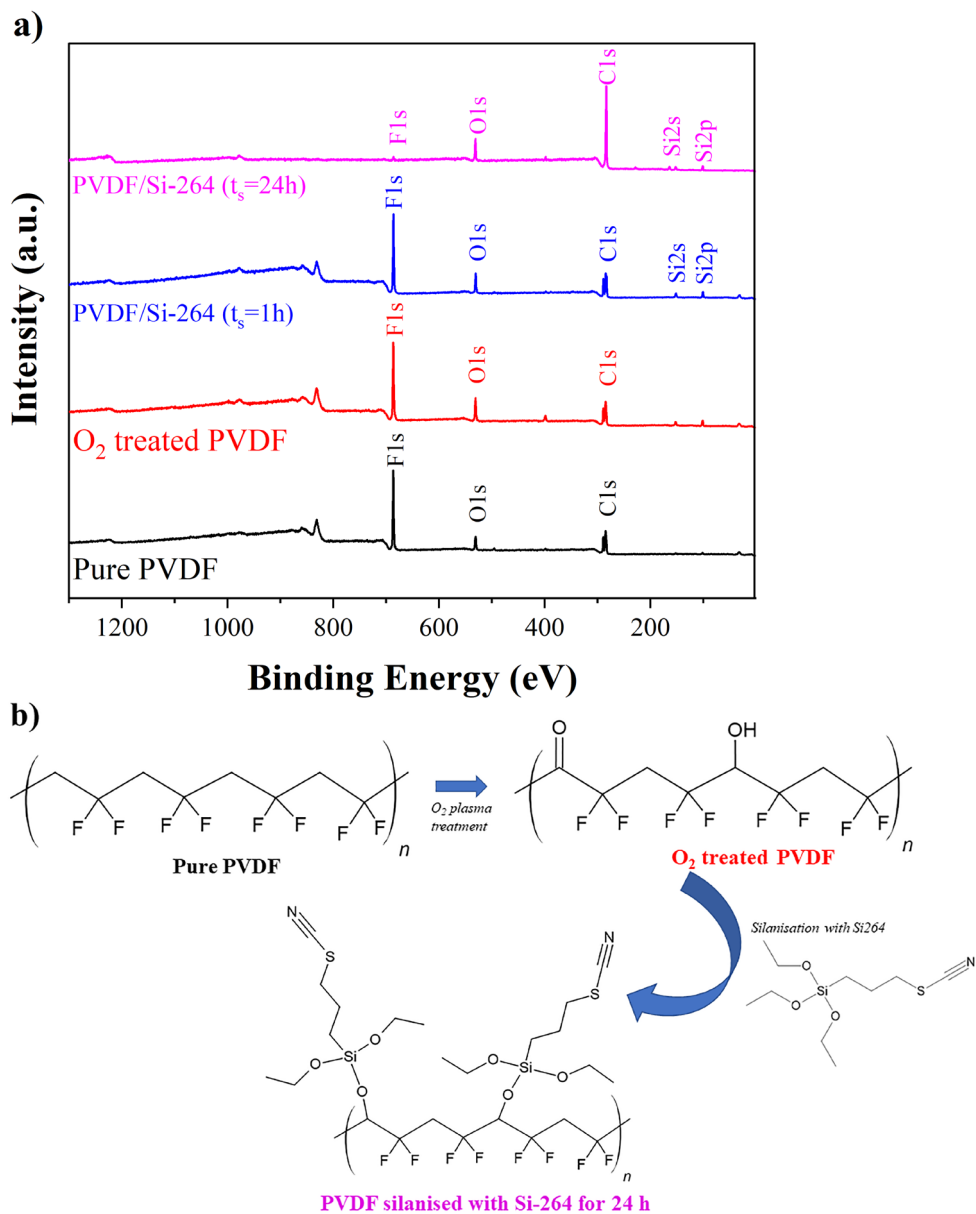
4

a)

b)

Figure 5 (a) XPS spectra of PVDF film and untreated and treated with oxygen plasma and silanisation with Si-264 for 1 and 24 hours and (b) the proposed coupling mechanisms.

Table 4 Atomic percentages of elements on the surface of PVDF films derived from XPS.

Sample	Atomic percentage					
	Carbon	Nitrogen	Oxygen	Fluorine	Silicon	Sulphur
Pure PVDF	54.2	1.4	8.7	33.2	2.1	/
Plasma treated	48.5	5.0	11.3	30.4	4.4	0.1*
Si-264 (1 h)	49.7	2.0	13.2	29.1	4.6	0.9
Si-264 (24 h)	77.8	2.9	11.0	1.1	4.3	2.9

*This data is doubtful and close to the detection limit of the machine.

The surface-treated PVDF films were then assembled with the electrically conductive composite at 140°C. During curing, the thiocyanate group is expected to react with rubber molecules, promoting the interfacial interaction between the two components. A T-peel test was carried out to measure the adhesive strength between the PVDF film and the reference composite C_{ref}. Figure 6a shows the forces used to peel the two components apart. A comparison between unmodified and 24 hours silanised PVDF/C_{ref} was made. It is shown that a surface modification of the PVDF film by 3-thiocyanatopropyltriethoxysilane improves the adhesion between PVDF and the rubber. There is some standard deviation of the forces, either due to the peel test itself and not a fully homogeneous silanisation on the PVDF surface.
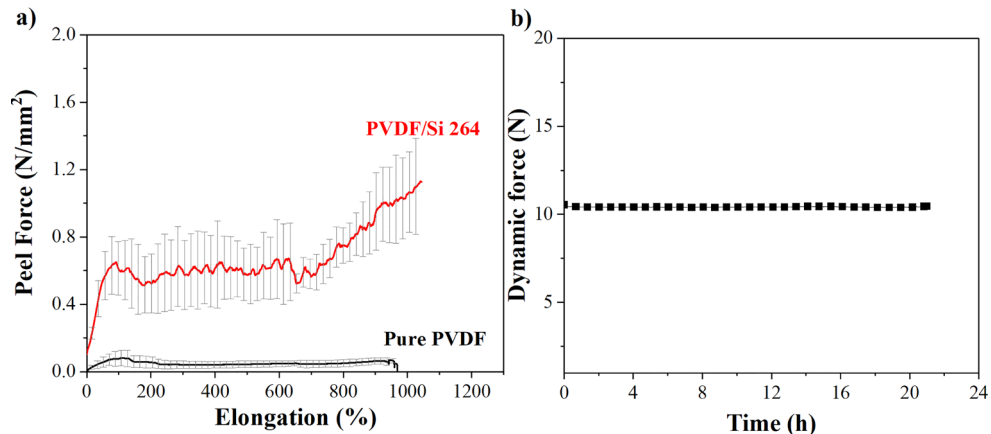
Figure 6 (a) T-peel test in tensile machine, (b) fatigue test in double shear mode in DMA at dynamic force F_{dyn} 10.5 N of the piezoelectric harvester 24 h silanised PVDF/C_{ref}.

Since the PVDF/C_{ref} piezoelectric patch has to withstand the rolling conditions of tyres, a time sweep analysis using a DMA was carried out. Figure 6b shows the results from the durability test of the piezoelectric sample under dynamic mechanical conditions with a double shear mode. Applying a constant dynamic strain during the measurements, a constant value of the dynamic force is observed over the testing time, meaning that the adhesion between the PVDF film and the conductive

composite C_{ref} is stable. This gives a good validation that the adhesion between the components of the piezoelectric patch is durable.

4.5.4. Piezoelectric property of PVDF-based harvester

After optimisation of the electrically conductive composites, the piezoelectric properties of the designed PEH were then studied. Figure 7 shows the output power derived from the harvesters as a function of frequency and temperature. It indicates that the output power increases at elevated frequencies, because there is a higher number of mechanical excitations to the material in a given time-span, activating the dipoles inside the PVDF film more frequently. The chemical adhesion between the piezoelectric film and the electrodes plays also an essential role on this. This adhesion creates many activation sites on PVDF surface. In this way, the current generated by the piezoelectric PVDF can flow in a more efficient way and the electrical conductivity of the electrodes is then crucial for the transferred current [44,47]. By increasing the temperature, Figure 7b, the generated power rises significantly because elevated temperatures increase the electrical conductivity as already shown in Figure 3. Additionally, the piezoelectric effect increases with increasing temperature due to the higher mobility of dipoles in the PVDF film, resulting in higher output power. The piezoelectric patch within the conductive composite C_3 with 6 wt% of carbon nanotubes masterbatch provides most generated electricity due to the highest value of conductivity of C_3. The generated electrical power of the piezoelectric patch PVDF/C_3 varies between 10 and 14 $\mu W/cm^2$ at 80 – 100°C, which is the operating temperature of rolling tyres.

For PVDF films, the maximum operating temperature at which the films can still generate electricity is usually 100°C depending on how the films are processed [48]. According to the information from the supplier, the PVDF film investigated in this study has still more than 50% piezoelectric performance at 120°C. In Figures 8a and b, the piezoelectric samples were vulcanised at 140°C. To study more in-depth the effect of vulcanisation temperature, the PVDF film was assembled into the piezoelectric patch with the conductive composite C_1 and vulcanised at 120 and 160°C. Figures 8c and d show the output power from the piezoelectric samples based on PVDF/C_1 vulcanised at 120, 140 and 160°C. The curing temperature has a strong influence on the output power generated by the piezoelectric samples. From the frequency dependence test, Figure 7c, the sample vulcanised at 120°C exhibits the highest power at 100 Hz, which is around 65% higher than for the sample vulcanised at 140°C and around 75% higher than for the sample vulcanised at 160°C. Similarly, in Figure 7d, the sample vulcanised at 120°C produced a higher power of around

68% compared to the sample vulcanised at 140°C and around 82% higher than the sample vulcanised at 160°C.
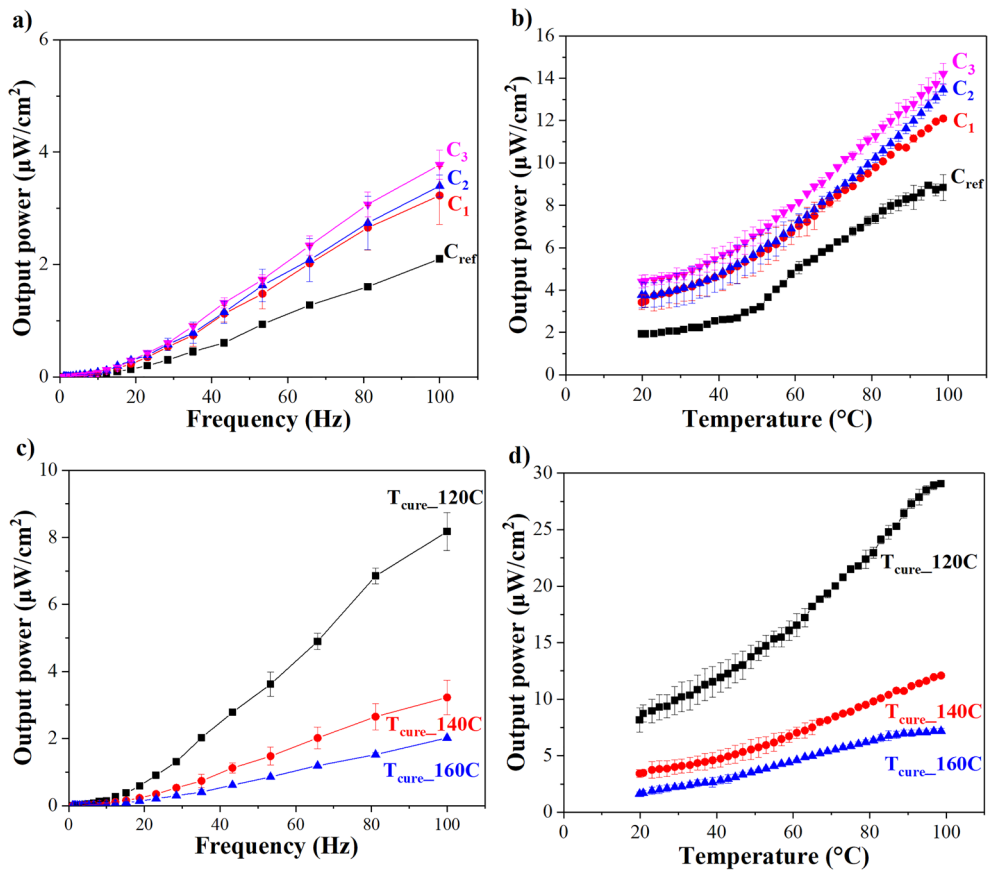
Figure 7   (a and b) Output power from frequency sweep at 20°C and temperature sweep at 100 Hz of piezoelectric patches with PVDF and conductive composites C_{ref}, C_1, C_2 and C_3 and (c and d) PVDF/C_1 vulcanised at 120, 140 and 160°C.

4.5.5.   Adhesion of conductive and inner liner composites

To investigate the adhesion performance of the piezoelectric patch to the inner liner of a tyre, two approaches can be considered, to co-vulcanise the two components and to use a suitable glue. The first option introduces some problems with the curing temperature of a tyre, which is in the range of 160 to 180°C. These temperatures will lead to a significantly reduced output power of the patch, as shown in Figure 7. Therefore, the second option was taken for the trial. The durability of the sample prepared by combining layers of conductive and inner liner composites was investigated using a DMA. The patch of the conductive composite added with 6 wt%

of carbon nanotube masterbatch (C_3), with a width of 10 mm and a thickness of 2 mm, was glued to the inner liner masterbatch (C_{IL}) with the same dimensions. Subsequently, the sample was analysed for its durability with a double shear fatigue test at 2% dynamic strain, and the obtained results are shown in Figure 8. The result shows a good stability of the sample over a measurement time of 20 hours. Therefore, the glue used between these two components is potentially effective for this system.
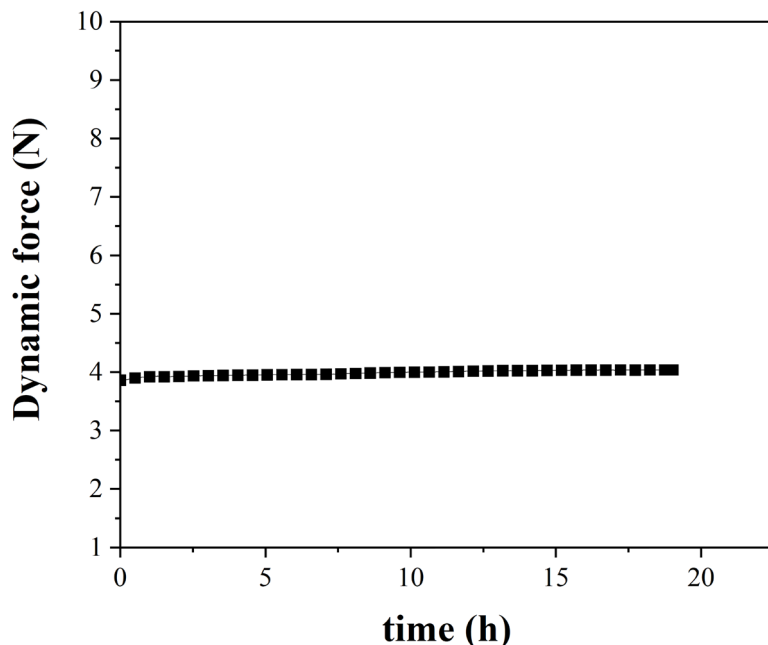
Figure 8 Fatigue test of conductive and inner liner composites using a time sweep analysis with a double shear mode at 2% dynamic strain.

4.5.6. Validation and evaluation of the prototyped PEH patch

To validate the processability of the designed system, all experimental results were considered in relation to the actual application of the prototype in a tyre. In Figure 9, the output power generated by the harvester, composed of PVDF film and the elastomeric conductive composites with 6 wt% of carbon nanotubes masterbatch and vulcanised at 120°C, is reported. Based on these results, it is clear that this piezoelectric patch generates more electricity with increasing frequency and temperature again. These values were taken for a calculation linking the lab conditions to the actual rolling conditions of the reference tyre. At 100 Hz and 90°C in a DMA, the output power from the piezoelectric patch developed in this work produced 28 μW/cm². To ensure that a sufficient amount of energy is supplied to the

reference TPMS sensor, which needs 28 mW, the piezoelectric patch should have surface area of 1000 cm^2. Therefore, the patch can be installed inside a tyre as a continuous layer along the circumference, ca. 200 cm.

The piezoelectric patch can also have a smaller area, taking into account that TPMS measures the pressure every 10 and 100 s. This allows the possibility to have a TPMS with lower power consumption, as well as safe driving. For collecting the measurement points every 10 and 100 s, the TPMS requires a power of 2.8 mW and 0.28 mW, respectively. As a result, the area of the piezoelectric patch to power the TPMS can be decreased resulting respectively in 100 and 10 cm^2. Consequently, the patch must be a square strip attached to the inner liner with dimensions of 10 x 10 cm^2 for a sampling rate of 0.1 measurement points/s and of 3.2 x 3.2 cm^2 for a sampling rate of 0.01 points/s.

Another important point to mention concerns the adhesion of the PEH to the inner liner of a tyre. In the present work, it was considered to prepare the PEH first and then adhere it to the inner liner. This two-steps fabrication of PEH implies a small-sized harvester due to higher output power, but a slightly more complex manufacturing process. The other approach is to vulcanise the PEH components directly onto the inner liner of the tyre at 160°C. This would imply an easier manufacturing process but 4-times lower output power and in turn a 4-times larger patch (as shown in Figure 7d). This aspect of the current design depends on factors like customer demands and the specific TPMS device.

Confirmation of the efficiency of the designed prototype to generate electricity is the evidence that this piezoelectric patch is capable of powering a light-emitting diode (LED) bulb. This experiment was set by connecting the LED to the piezoelectric system, using the same measurement setup as discussed in Section 4.3. The piezoelectric patch was installed in a DMA and coupled to a bridge rectifier which converts the AC output into DC input for the LED. A blue LED (TessaTronic, Hengelo, the Netherlands) was able to be powered by a voltage of around 2.0 V. Figure 9 shows the images of the LED powered with different frequencies: 10 and 100 Hz; and temperatures: room temperature and 80°C. The LED light becomes more intence with increasing temperature and frequency. At 10 Hz and room temperature, the LED could not be powered, but at 100 Hz and 80°C it gave the brightest light. Therefore, this result provides a clear validation of the performance of the piezoelectric patch designed in the present work.

4

4.6.　　Conclusions

A flexible piezoelectric energy harvester was developed. The designed piezoelectric patch includes two components configured in a sandwich structure: a piezoelectric polymer film inserted in between two layers of conductive elastomeric composite. The selected piezoelectric polymer was a PVDF film with a thickness of 0.1 mm with high piezoelectric coefficient and acceptable flexibility. A conductive elastomeric composite filled with carbon black was employed because of its high elasticity and good adherence to tyre compounds, in particular to the inner liner. The electrical conductivity of the composite can significantly be increased using a SWCNT masterbatch with TDAE oil as base. 6 wt% of the masterbatch is the minimum amount of nanofillers which is required to have an elastomeric composite with a conductivity of 10^{-4} S/cm. The conductivity of the composites tends to be constant after the first temperature sweep analysis, since the particles of carbon black and carbon nanotubes are well aligned, forming a conductive networking path throughout the matrix.
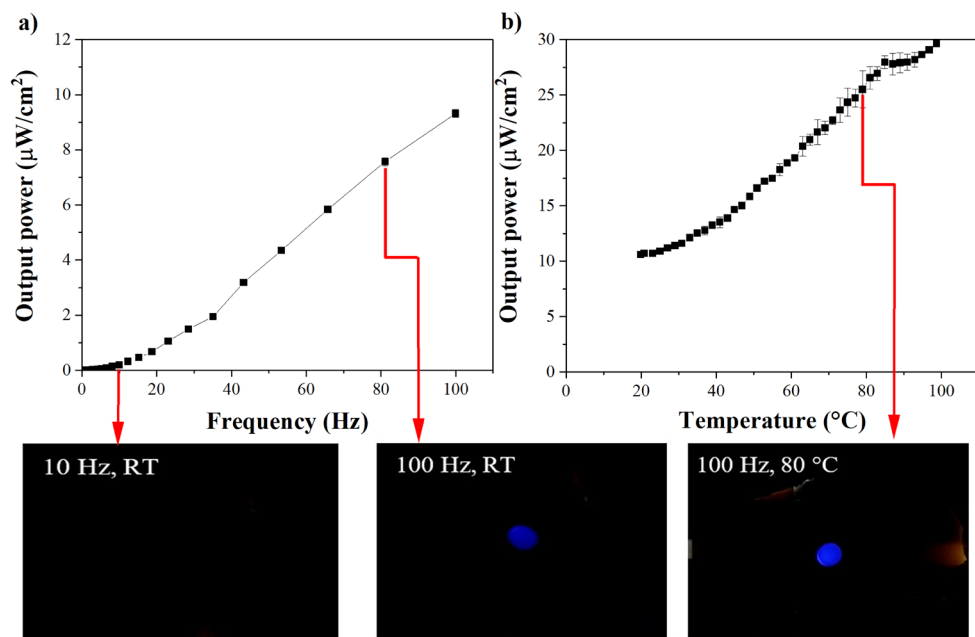
Figure 9　(a) Output power generated by the prototyped PEH analysed under frequency sweep at 20°C and (b) temperature sweep at 100 Hz with images of LED light at 10 and 100 Hz and room temperature (RT) and 80°C.

To fabricate all into a flexible energy harvester patch, a surface treatment of the PVDF film using a silane coupling agent was required to enable the adhesion

between the film and the conductive elastomer. XPS analyses confirm that the surface modifications of the PVDF film by an oxygen-plasma treatment followed by a silanisation reaction via a thiocyanate silane were successful. The adhesion strength between the PVDF film and the conductive composite was increased during T-peel test and it was durable during a time-sweep dynamic mechanical analysis simulating the actual conditions of a rolling tyre. Finally, the surface-treated PVDF was vulcanised in between two layers of the elastomeric conductive composite at 120°C. Under the assumption of a reference passenger car, the piezoelectric patch with dimensions of 10 x 10 cm^2 can power a TPMS device that requires 28 mW of electricity. Assembly of this harvester to the inner liner of a tyre can be done by glueing it with a silicone adhesive.

4

4.7.   References

[1]   F.K. Shaikh, S. Zeadally, Energy harvesting in wireless sensor networks: A comprehensive review, Renew. Sustain. Energ. Rev. 55 (2016) 1041-1054.

[2]   H. Kim, Y. Tadesse, S. Priya, Piezoelectric energy harvesting, in: S. Priya, D.J. Inman (Eds.), Energy Harvesting Technologies, Springer US, Boston 2009, pp. 3-39.

[3]   M. Löhndorf, T. Lange, MEMS for automotive tire pressure monitoring systems, in: M. Kraft, N.M. White (Eds.), MEMS for Automotive and Aerospace Applications, Woodhead Publishing, Philadelphia, 2013, pp. 54-77.

[4]   C.R. Bowen, M.H. Arafa, Energy harvestingtechnologies for tire pressure monitoring systems, Adv. Energy Mater. 5(7) (2015) 1401787.

[5]   R. Matsuzaki, A. Todoroki, Wireless monitoring of automobile tires for intelligent tires, Sensors 8(12) (2008) 8123-8138.

[6]   B. Wu, Y. Fang, L. Deng, Summary of energy collection application in vehicle tire pressure monitoring system, 4th International Conference on Automation, Control and Robotics Engineering, Association for Computing Machinery, Shenzhen 2019, pp. 1-6.

[7]   A.E. Kubba, K. Jiang, A comprehensive study on technologies of tyre monitoring systems and possible energy solutions, Sensors 14(6) (2014) 10306-10345.

[8]   Z. Yang, S. Zhou, J. Zu, D. Inman, High-performance piezoelectric energy harvesters and their applications, Joule 2(4) (2018) 642-697.

[9]   S.R. Anton, H.A. Sodano, A review of power harvesting using piezoelectric materials (2003–2006), Smart Mater. Struct. 16(3) (2007) R1-R21.

[10]   A. Toghi Eshghi, S. Lee, H. Lee, Y.-C. Kim, Parameter study and optimization for piezoelectric energy harvester for TPMS considering speed variation, SPIE Smart Structures and Materials + Nondestructive Evaluation and Health Monitoring, SPIE, Las Vegas, 2016, pp. 1-19.

[11]   J. Lee, S. Kim, J. Oh, B. Choi, A self-powering system based on tire deformation during driving, Int. J. Automot. Technol. 13(6) (2012) 963-969.

[12]   I.A.H. Al-Najati, K.W. Chan, S.Y. Pung, Tire strain piezoelectric energy harvesters: a systematic review, International Journal of Power Electronics and Drive Systems 13(1) (2022) 444-459.

[13]   H.J. Chilabi, H. Salleh, W. Al-Ashtari, E.E. Supeni, L.C. Abdullah, A.B. As'arry, K.A.M. Rezali, M.K. Azwan, Rotational piezoelectric energy harvesting: A comprehensive review on excitation elements, designs, and performances, Energies 14(11) (2021).

[14]   D. Al-Yafeai, T. Darabseh, A.H.I. Mourad, A state-of-the-art review of car suspension-based piezoelectric energy harvesting systems, Energies 13(9) (2020).

[15]   M. Keck, A new approach of a piezoelectric vibration-based power generator to supply next generation tire sensor systems, Proceedings IEEE Sensors, IEEE, Atlanta, 2007, pp. 1299-1302.

[16]   Q. Zheng, H. Tu, A. Agee, Y. Xu, Vibration energy harvesting device based on asymmetric air-spaced cantilevers for tire pressure monitoring system, Proceedings Power MEMS, Power MEMS, Washington, 2009, pp. 403-406.

[17]   R. Elfrink, S. Matova, C.d. Nooijer, M. Jambunathan, M. Goedbloed, J.v.d. Molengraft, V. Pop, R.J.M. Vullers, M. Renaud, R.v. Schaijk, Shock induced energy harvesting with a MEMS harvester for automotive applications, 2011 International Electron Devices Meeting, International Electron Devices Meeting IEDM Technical Digest, Washington, 2011, pp. 677-680.

[18]   K.H. Mak, S. McWilliam, A.A. Popov, Piezoelectric energy harvesting for tyre pressure measurement applications, Proc. Inst. Mech. Eng. D 227(6) (2013) 842-852.

[19]   O.J. Jousimaa, Y. Xiong, A.J. Niskanen, A.J. Tuononen, Energy harvesting system for intelligent tyre sensors, 2016 IEEE Intelligent Vehicles Symposium (IV), IEEE, Gothenburg, 2016, pp. 578-583.

[20]   B. Zhu, J. Han, J. Zhao, W. Deng, Practical design of an energy harvester considering wheel rotation for powering intelligent tire systems, J. Electron. Mater. 46(4) (2017) 2483-2493.

[21]   N. Makki, R. Pop-Iliev, Piezoelectric power generation in automotive tires Smart Materials, Structure & NDT in aerospace, Montreal, 2011.

[22]   N. Makki, R. Pop-Iliev, Pneumatic tire-based piezoelectric power generation, SPIE Smart Structures and Materials + Nondestructive Evaluation and Health Monitoring, SPIE, San Diego, 2011, pp. 1-10.

[23]   D.A. Van den Ende, H.J. van de Wiel, W.A. Groen, S. van der Zwaag, Direct strain energy harvesting in automobile tires using piezoelectric PZT–polymer composites, Smart Mater. Struct. 21(1) (2011) 015011.

[24]   Q.C. Tang, X.X. Li, Non-contact frequency-up-conversion energy harvester for durable & broad-band automotive TPMS application, 2012 IEEE 25th International Conference on Micro Electro Mechanical Systems (MEMS), IEEE, Paris, 2012, pp. 1273-1276.

[25]   X. Wu, M. Parmar, D.W. Lee, A seesaw-structured energy harvester with superwide bandwidth for TPMS application, IEEE/ASME Trans. Mechatron. 19(5) (2014) 1514-1522.

[26]   H. Fan, Z. Tan, H. Liu, L. Zhang, F. Zhang, W. Du, Z. Fan, X. Gao, F. Pan, D. Yu, Y. Zhao, Enhanced Ferroelectric and Piezoelectric Properties in Graphene-Electroded Pb(Zr,Ti)O3 Thin Films, ACS Applied Materials and Interfaces 14(15) (2022) 17987-17994.

[27]   H. Zheng, H. Zhang, P. Wen, D. He, Flexible piezoelectric energy harvester based on graphene macro-film electrode enabled by exploiting auxetic mechanical property, Materials Letters 318 (2022).

4

[28]   H.-G. Cheong, J.-H. Kim, J.-H. Song, U. Jeong, J.-W. Park, Highly flexible transparent thin film heaters based on silver nanowires and aluminum zinc oxides, Thin Solid Films 589 (2015) 633-641.

[29]   T. Kim, Z. Cui, W.Y. Chang, H. Kim, Y. Zhu, X. Jiang, Flexible 1-3 Composite Ultrasound Transducers with Silver-Nanowire-Based Stretchable Electrodes, IEEE Transactions on Industrial Electronics 67(8) (2020) 6955-6962.

[30]   A. Renteria, V.H. Balcorta, C. Marquez, A.A. Rodriguez, I. Renteria-Marquez, J. Regis, B. Wilburn, S. Patterson, D. Espalin, T.L. Tseng, Y. Lin, Direct ink write multi-material printing of PDMS-BTO composites with MWCNT electrodes for flexible force sensors, Flexible and Printed Electronics 7(1) (2022).

[31]   J.B. Donnet, R.C. Bansal, M.J. Wang, Carbon black: science and technology (2nd ed.), CRC Press Taylor & Francis, Boca Raton, 1993.

[32]   M.E. Spahr, R. Rothon, Carbon black as a polymer filler, in: S. Palsule (Ed.), Polymers and Polymeric Composites: A Reference Series, Springer Berlin-Heidelberg, 2016, pp. 1-31.

[33]   V.V. Kochervinskii, Ferroelectricity of polymers based on vinylidene fluoride, Russ. Chem. Rev. 68 (1999) 821-857.

[34]   C. Mangone, M. Klein Gunnewiek, L. Reuvekamp, Tyre comprising a piezoelectric device, 2021.

[35]   E.S. Bhagavatheswaran, K.W. Stöckelhuber, S.R. Vaikuntam, S. Wießner, P. Pötschke, G. Heinrich, A. Das, Time and temperature dependent piezoresistive behavior of conductive elastomeric composites, Rubber Chem. Technol. 91(4) (2018) 651-667.

[36]   K. Yamaguchi, J.J.C. Busfield, A.G. Thomas, Electrical and mechanical behavior of filled elastomers I. The effect of strain, J. Polym. Sci. B Polym. Phys. 41(17) (2003) 2079-2089.

[37]   F. Khameneifar, S. Arzanpour, M. Moallem, A piezoelectric energy harvester for rotary motion applications: design and experiments, IEEE/ASME Trans. Mechatron. 18(5) (2013) 1527-1534.

[38]   B. Rodgers, W. Waddell, 14 - Tire engineering, in: J.E. Mark, B. Erman, F.R. Eirich (Eds.), Science and Technology of Rubber (Third Edition), Academic Press, Burlington, 2005, pp. 619-II.

[39]   E.S. Bhagavatheswaran, Exploring the Piezoresistive Characteristics of Solution Styrene Butadiene Rubber composites under static and Dynamic Conditions - A Novel Route to Visualize Filler Network Behavior in Rubbers, Technische Universität Dresden, 2019.

[40]   J.G. Meier, M. Klüppel, Carbon black networking in elastomers monitored by dynamic mechanical and dielectric spectroscopy, Macromol. Mater. Eng. 293(1) (2008) 12-38.

[41]   Y. Nakaramontri, S. Pichaiyut, S. Wisunthorn, C. Nakason, Hybrid carbon nanotubes and conductive carbon black in natural rubber composites to enhance

electrical conductivity by reducing gaps separating carbon nanotube encapsulates, Eur. Polym. J. 90 (2017) 467-484.

[42]   D.M. Correia, C. Ribeiro, V. Sencadas, G. Botelho, S.A.C. Carabineiro, J.L.G. Ribelles, S. Lanceros-Méndez, Influence of oxygen plasma treatment parameters on poly(vinylidene fluoride) electrospun fiber mats wettability, Prog. Org. Coat. 85 (2015) 151-158.

[43]   C. Mangone, M. Klein Gunnewiek, L. Reuvekamp, W. Kaewsakul, A. Blume, Method for chemically adhering a diene rubber to a piezoelectric polymer, 2021.

[44]   N.N. Wathore, B. Rawal, P. Dixit, S. Mandave, B. Praveenkumar, K.M. Rajan, Effect of Silver Electrode Annealing Temperature on Electrical Properties of Sodium Potassium Niobate Based Ceramics, J. Electron. Mater. 48(2) (2019) 845-852.

[45]   K. Baik, S. Park, C. Yun, C.H. Park, Integration of polypyrrole electrode into piezoelectric PVDF energy harvester with improved adhesion and over-oxidation resistance, Polymers 11(6) (2019).

[46]   T.C. Ahn, H.S. Hong, S.S. Kim, H.Y. Hwang, Improvement of adhesion characteristics of copper electrodes on polyvinylidene fluoride films using bovine serum albumin, International Journal of Adhesion and Adhesives 112 (2022).

[47]   G.K. Elyashevich, I.Y. Dmitriev, E.Y. Rozova, Electroconducting Polypyrrole Coatings as an Electrode Contact Material on Porous Poly(vinylidene fluoride) Piezofilm, Polymer Science - Series A 63(1) (2021) 45-53.

[48]   S. Bauer, F. Bauer, Piezoelectric polymers and their applications, in: W. Heywang, K. Lubitz, W. Wersing (Eds.), Piezoelectricity: evolution and future of a technology, Springer Berlin-Heidelberg, 2008, pp. 157-177.

4

Chapter 5

Key factors affecting dynamic electrical conductivity of carbon black-based elastomeric composites

5

Flexible active materials for powering tyre sensors become increasingly relevant, leading to a growing interest in the development of conductive elastomers. The present work aims to identify the most influential factors on dynamic electrical conductivity of carbon black-based elastomeric composites. The conductivity was measured using an in-house developed measurement setup based on a dynamic mechanical analyser. Conductive carbon blacks with specific surface areas in the range of 200 and 1400 m^2/g were used. In accordance with the results from a full factorial Design of Experiment (DoE) screening and optimisation studies, the rubber types with different polarities, i.e. Natural Rubber (NR), Butadiene Rubber (BR), Epoxidised Natural Rubber (ENR), functionalised BR and acryloNitrile Butadiene Rubber (NBR), as well as rubber blend ratios and carbon black types appeared to be statistically insignificant. The carbon black amount expressed in terms of total surface area was the only significant factor. Sigmoidal-Boltzmann model was applied to predict the percolation threshold of NR/BR composites. This model proved a novel predicting approach based on the correlation between the dynamic electrical conductivity of NR/BR composites and the measured Payne effect data as an indicator of filler network of carbon black particles dispersed in the composites.

Chapter 5

5.1.   Introduction

Electrically conductive elastomers are widespread and being applied for eco- and human-friendly electronics, such as wearable implantable devices and flexible electronic components like sensors, actuators and energy harvesters [1-5]. One of the potential attractive applications of those conductive elastomers is their integration in piezoelectric energy harvesters, capable of providing a battery-less system for autonomous operations and sensors [4-6]. These harvesters include a piezoelectric material which generates electricity under mechanical stress and an electrode applied on both sides of the piezoelectric material to induce the flow and the storage of the generated electrical charges. For tyre application, these components need to withstand the dynamic service conditions of the rolling tyres, and are hence characterised with appropriate properties, such as elasticity and stability. Therefore, acquiring an appropriate electrode for dynamic applications is of a challenge.

Incorporating conductive carbon blacks in an insulating polymeric matrix increases the electrical properties of such composites [7-9]. This behaviour relies on a hopping and tunnelling phenomena of charge carriers across the conductive path of carbon black particles dispersed in a polymeric matrix. The gap distance between the black aggregates plays a crucial role in the electrical conduction mechanism. The filler amount at which a conductive path is established is called percolation threshold. From this state, the gap distance between the aggregates is small enough for the electrons to jump between the aggregates, forming electron tunnelling bands. The conductivity level of such composites varies from insulation 10^{-14} S/cm to conduction 1 S/cm, depending on filler type and amount, filler dispersibility and polymeric matrix. Moreover, the dynamic mechanical deformation, occurring during tyre-rolling conditions, affects the physical contact and the tunnelling gap between carbon black particles. Although the phenomena of forming a conductive pathway in elastomers have been investigated intensively in static conditions [9,10], the characterisation of those materials under dynamic conditions was not fully comprehended.

Busfield et al. and Yamaguchi et al. investigated the electrical resistivity of elastomeric composites under tensile, compression and double-shear loads [11-13]. In the first work, they studied the change of electrical resistance with increasing strain of Natural Rubber (NR) and Styrene Butadiene Rubber (SBR) filled with 70 phr of carbon black N330 [11]. It was performed using a tensile machine in tension and compression modes. Stretching the sample in a tension mode at small

deformations (tensile extension ratio lower than 1.5), the conductivity decreased due to the breakdown of the carbon black network. At large deformations, the conductive particles tended to align along the direction of the strains, contributing to an increased electrical conductivity of one order of magnitude. During the compression test, a greater extent of carbon black network alignment than that from the tensile mode occurred. This explains the observation that after unloading, the electrical conductivity decreased at a much higher extend in the compression test compared to the values measured in tension mode. In a second work, the same authors studied the changes of electrical conductivity as a result of static and dynamic deformations in a double-shear mode by using the same samples [13]. Particularly, the changes of electrical conductivity with increasing dynamic shear strain was studied. The change of electrical conductivity of elastomeric composite under dynamic shear strain was ascribed to the breakdown of the carbon black network under strain. It was noted that during the loading of elastomeric composite under shear strain, a carbon black network breakdown occurred, resulting in a high intensity peak of electrical resistivity. However, increasing the strain resulted in a carbon black network with a different recovery mechanism. At small strain (i.e. lower than 4.5%), the carbon black network breakdown can still be recovered during the unloading. Increasing the strain from 4.5% to 16.6% and 61%, the breakdown of carbon black network becomes more pronounced and not-recoverable.

5

Bhagavatheswaren et al. analysed in detail the piezoresistive properties of elastomeric composites in dynamic conditions regarding the changes of electrical conductivity with varied strains. They correlated the mechanical and electrical performances of the investigated elastomers [14-16]. A setup offering a possibility to monitor the electrical resistance under dynamic deformations of elastomers was developed. A phase shift value between the sinusoidal trends of electrical resistance and stress values were considered as main parameters, giving the information on the time required by the filler to respond to the applied deformation. Most of the findings in literature were based on the analyses of electrical conductivity under static conditions rather than under dynamic conditions. Thus, it is essential to pay more attention to the influential factors for increasing electrical conductivity measured under dynamic conditions.

In a previous research included in Chapter 3, the setups capable of measuring electrical conductivity and piezoelectric properties of polymeric materials under tyre-rolling conditions were successfully designed [5]. Additionally, a piezoelectric energy harvester including a piezoelectric polymer polyvinylidene difluoride and an

elastomeric electrode in a sandwich-like structure was developed [4]. This study included in Chapter 4 highlighted the efficiency of an elastomer-based piezoelectric harvester, the importance of a flexible electrode and of the chemical bond between electrode and piezoelectric material.

Therefore, the present work aims to study the effects of elastomer types, blends, as well as type and total surface area of carbon blacks on dynamic electrical conductivity of elastomers. To identify which factor(s) show(s) the major effect, a Design of Experiments (DoE) approach was applied to screen the possible crucial factors by taking into account the key determinant response(s) of the system. DoE is a highly effective technique used to reduce systematic errors and number of tests [17-19]. In a preliminary section, the formulations of the elastomeric composites were optimised. Blends of NR, BR and functionalised counterparts were taken into consideration as elastomers. Aiming to identify the most significant factors on dynamic electrical conductivity of elastomeric composites, a DoE methodology comprising of two levels full factorial design was carried out for screening. The investigated four factors include rubber polarity, rubber blends, carbon black types and amounts. The electrical conductivity measured under dynamic conditions was the key response. After the screening process, the most significant factor was further studied by using a sigmoidal-Boltzmann model. This model was employed to further analyse the electrical conductivity and find the correlations with carbon black properties for a possible prediction.

5.2.   Experimental

5.2.1.   Materials

For the preliminary experiments, the rubbers used were Natural Rubber (NR, Technical Specified Rubber graded 20 TSR20, Wurfbain Nordmann B.V., Zaandam, the Netherlands) and high-cis branched Butadiene Rubber (BR, 1280 grade, LG Chem Europe GmbH, Eschborn, Germany). Fillers employed in this step included:

- Conventional Carbon Black (CB), grade N330 (Cabot Corporation GmbH, Baden, Germany), with a specific surface area Braunauer-Emmet-Teller BET (ASTM D-6556) of 78 m^2/g and an Oil Adsorption Number OAN indicating the filler structure (ASTM D-2414) of 88 mL/100g;
- Conductive Carbon Black (CCB), tradename Vulcan XC72 with a BET of 200 m^2/g and an OAN of 174 mL/100g (Cabot Corporation GmbH, Baden, Germany).

Key factors affecting dynamic electrical conductivity of carbon black-based elastomeric composites

A screening study using a Design of Experiment (DoE) approach was executed with two additional elastomers. They are functionalised with two different polar chemical groups: 25 mol% Epoxidised NR (ENR-25, Wurfbain Nordmann B.V. Zaandam, Netherlands) and low-cis amine-end-functionalised BR (Nipol® BR 1250H, coded as F-BR, Zeon Europe GmbH, Dusseldorf, Germany) [20]. Two additional conductive carbon black types were employed:

- Extra-Conductive Carbon Black (ECCB), tradename Ketjenblack EC-300J, 800 m^2/g and 330 mL/100g (Nouryon Specialty Chemicals, Deventer, the Netherlands);
- Ultra-Conductive Carbon Black (UCCB), tradename Ketjenblack EC-600JD, 1400 m^2/g and 500 mL/100g (Nouryon Specialty Chemicals, Deventer, the Netherlands).

For further investigations, the abovementioned NR TSR20 and BR1280 were employed. Additionally, another carbon black was used in this investigation. Its technical data regarding the BET and OAN values are given as follows:

- Conductive CB, Printex XE2B, 1000 m^2/g and 420 mL/100g (Orion Engineered Carbons GmbH, Cologne, Germany), coded as Printex.

Furthermore, to study the effect of rubber polarity on dynamic electrical conductivity of elastomeric composites, Nitrile Butadiene Rubber (NBR) with 41 wt% of ACryloNitrile (ACN) group (Nipol® 1041L coded as NBR41, Zeon Europe GmbH, Düsseldorf, Germany) was investigated.

Other compounding ingredients were of technical quality, including:

- Treated Distillate Aromatic Extracted (TDAE) oil (Vivatec 500, Hansen & Rosenthal KG, Hamburg, Germany);
- Tall oil (Sylvatal™ 25/30S, Arizona Chemical B.V., Almere, Netherlands);
- N-(1,3-dimethylbutyl)-N'-Phenyl-p-PhenyleneDiamine (6PPD) (Vulkanox 4020/LG, Lanxess Deutschland GmbH, Cologne, Germany);
- 2,2,4-TriMethyl-Quinoline (TMQ), (Vulkanox HS/LG, Lanxess Deutschland GmbH, Cologne, Germany);
- Stearic Acid, (Edenor ST1 GS, Emery Oleochemicals GmbH, Düsseldorf, Germany);
- Zinc Oxide (ZnO), (Merck & Co, Darmstadt, Germany);
- α-Sulphur (Eastman Chemical Corporation, Langenfeld, Germany);

5

- N-Tert-Butyl-Benzothiazole Sulfenamide (TBBS), (Rhenogran TBBS-80, Lanxess Deutschland GmbH, Cologne, Germany).

5.2.2. Composites preparation

The composites were prepared using a two-stages mixing procedure. A masterbatch was prepared in an internal mixer (Brabender Plasticorder 350s, Brabender GmbH & Co KG, Germany). A good mixing quality is essential for adequate dispersion and distribution of filler particles in elastomeric composites, which determines the final properties of the vulcanisates. Proper settings of mixing conditions, i.e. fill factor, temperature, rotor speed and mixing time result in an optimum filler dispersion and final performance of the composites. In the current study, an internal mixer with tangential rotors was used. For this rotor geometry, the optimal fill factor is suggested to be in the range of 0.70-0.80. Therefore, a value of 0.75 was selected. The starting mixing temperature was 60°C, and the mixing time was 10 min. For the rotor speed, a more rigorous mixing affects the dispersion of carbon black particles, breaking up carbon black agglomerates and distributing them homogenously. The rotor speed was taken into account by varying it from 80-120 rpm [5,22]. Results show a negligible influence of different rotor speeds on the electrical conductivity of the composites measured under dynamic conditions. Therefore, a rotor speed of 100 rpm was selected. The mixing time was 10 min for the initial investigations (preliminary experiments and DoE study) and then 6.2 min for the remaining investigations.

NR and BR were initially blended for 1 min. The NR used was masticated before the addition of BR in order to have a comparable viscosity and better blend compatibility. Carbon black was firstly divided into two portions, then pre-dispersed in TDAE oil and added to the mixer. Each portion of carbon black and TDAE oil was mixed for 3.5 and 2 min in case of total mixing time of 10 and 6.2 min, respectively. For the remaining time, the rest of the ingredients (6PPD, TMQ, ZnO and stearic acid) were incorporated and mixed.

NBR-based composites were mixed following the same procedure: Rubber mastication for 1 min, subsequent additions of the first and second portions of CB and tall oil mixed for 2 min for each portion. Finally, the remaining ingredients as TMQ, ZnO and stearic acid were mixed for 1.2 min.

All the masterbatches, NR, BR and NBR based, were discharged from the internal mixer and sheeted out on a two-roll mill for 2 min at 2 mm nip width of the rolls (Polymix 80 T, Schwabenthan-Maschinen GmbH & Co. KG, Berlin, Germany).

They were conditioned for 24 h before the incorporation of sulphur and TBBS in the second mixing stage on the two-roll mill at a low temperature of 50°C for 5 min mixing time to avoid premature crosslinking of the composites. For each experimental part, elastomer and filler types and amount were varied as shown in Table 1.

Table 1 Elastomeric composite formulations.

Ingredients	Amount (parts per hundred rubber: phr)			
	Part I: **Pre-experiments**	**Part II:** **DoE**	**Part III:** **Rubber polarity**	**Part IV:** **CB type and amount**
Rubbers	NR/BR 50/50	Variable	NBR41: 100	NR/BR 25/75
CB	N330: 60 CCB: 40	Variable [a]	Printex: Variable (8-22 phr)	Variable [a]
Process oil	N330: 12-30 CCB: 8-20	Half amount of CB		
6PPD	1.5			
TMQ	4.0			
Stearic acid	2.0			
ZnO	5.0			
α-Sulphur	1.5			
TBBS	1.8			

[a] Carbon black amounts variable according to the DoE screening.

Curing characteristics of the composites were analysed using a Rubber Process Analyser (RPA 2000, Alpha Technologies, Ohio, USA). Each measurement was done for 20 min at 160°C with a frequency of 1.667 Hz and an oscillating shear angle of 0.5°. The optimum curing times at 95% t_{c95} were taken as input for the curing process. The composites were vulcanised at 100 bar in a Wickert press WLP 1600 (Wickert Maschinenbau GmbH, Landau, Germany) to their t_{c95} at 160°C.

5.2.3. Composites characterisations

The *dynamic electrical conductivity* was characterised using an in-house developed setup described in Chapter 3.

As an indicator of the degree of filler-filler interaction, the decay in the storage shear moduli (G') from small to large deformations, known as *Payne effect* [23], was measured in an RPA before the incorporation of the curatives (i.e. *Payne Effect uncured*) and after curing (i.e. *Payne Effect cured*). The Payne effect of uncured composites was measured with varying strain in the range of 0.56 to 100%, a

temperature of 100°C and a frequency of 0.5 Hz. The Payne effect of cured composites was measured under the same conditions after curing them at 160°C in the RPA for 20 min.

Hardness and Mooney viscosity tests were carried out using vulcanised composites. *Hardness* was measured with a Digi test II durometer (Bareiss, Oberdishingen, Germany) according to ISO 48-4:2018. *Mooney viscosity ML(1+4)100°C* was measured using a Mooney viscometer MV200VS (Alpha Technologies, Gembloux, Belgium).

Atomic Force Microscopy (AFM) analysis was performed using Multimode 8 AFM (Bruker, Santa Barbara, CA, USA) with a Nanoscope V controller and a JV vertical engage scanner. Measurements of the composites were performed in a tapping mode using a cantilever with a nominal spring constant of around 42 N/m and a nominal tip apex radius of 8 nm (model NCH, NanoWorld, Switzerland). Composites vulcanised at 160°C to their t_{c95} were prepared by microtoming their surfaces at – 140°C with a cryo-ultramicrotome (Ultracut EM-FCS, Leica, Germany) using steel and glass knifes.

Broadband Dielectric Spectrometer (BDS) with an Alpha-A high performance frequency analyser of Novocontrol Technologies (Montabaur, Germany), was used to measure the dielectric constant and electrical conductivity of gum rubbers vulcanised to their optimum cure time t_{c95}. The 0.5 mm vulcanised composites were cut into a disk sample with a diameter of 15 mm and then mounted in the dielectric cell between two parallel gold-plated electrodes. Electrical conductivity and dielectric constant ε' (the real part of the complex dielectric constant ε*) were measured. A frequency sweep from 1 to 10^5 Hz at two different temperatures of 25 and 100°C were carried out.

5.2.4. Design of Experiments DoE – screening study

A 2^4 full factorial Design of Experiments (DoE) approach, with 4 factors and 2 levels with an additional central point, was used for the screening design study to identify the most important factor(s) that affects the dynamic electrical conductivity of elastomeric composites. The summary of the possible crucial factors, levels and responses is shown in Table 2. All the experiments were carried out randomly to avoid bias in the measurements. The software Minitab® (Minitab Ltd., Covetry, United Kingdom) was used to examine the obtained data.

Figure 1 shows the cube plots from the DoE analysis. The full factorial design with four factors is depicted by two blue cubes, relative to the lower and higher level of the factor D, i.e. the total surface area of CB. The three axes in the cubes indicate the rubber polarity, blend ratio and carbon black type. The basic DoE includes 2^4 experiments (corner points of the cubes in blue) plus three repetitions of the central point (in red), with a total of 19 runs. To efficiently estimate the effect of the factors on the response, the DoE analysis was further optimised by using a Central Composite Design CCD. Additional 6 axial points (in grey), 2 central points of the lower- and upper-level cubes (in green) and further 3 repetitions of red central points were added. This results in 30 experiments. A full quadratic design was selected for the present study to be fully aware of confounding effects. The response is the electrical conductivity measured under a dynamic deformation at 100°C, 100 Hz, 10% static strain and 1% dynamic strain [5].

Table 2   Summary of the factors and levels for the DoE screening study.

Factors	Levels: Values	Domains
A: Rubber polarity [a]	Lower: 0	Non-polar rubbers: NR/BR blend
	Central: 5	Blend of polar and non-polar rubber
	Upper: 10	Polar rubber: ENR-25/F-BR blend
B: Blend ratio (wt% NR)	Lower: 25	NR/BR and ENR-25/F-BR: 25/75
	Central: 50	ENR-25/F-BR and NR/F-BR: 50/50
	Upper: 75	NR/BR and ENR-25/F-BR: 75/25
C: CB type (m²/g) [b]	Lower: 200	CCB: BET 200 m²/g
	Central: 800	ECCB: BET 800 m²/g
	Upper: 1400	UCCB: BET 1400 m²/g
D: CB amount (m²) [c]	Lower: 4000	For CCB: 16 phr. For UCCB: 2.9 phr
	Central: 8000	For ECCB: 10 phr
	Upper: 12000	For CCB: 48 phr. For UCCB: 8.6 phr

[a] This factor was considered as a customised polarity scale ranging from 0 to 10.
[b] The type of conductive carbon blacks was differentiated by their specific surface areas (m²/g).
[c] To compare carbon blacks with different BET Specific Surface Areas SSA_{BET}, the same total surface area of carbon black particles dispersed in an elastomer was considered as factor D and it was estimated as the product of $SSA_{BET} \cdot amount\ CB\ (phr)$ [24].

Some approximations were made for the investigated factors A rubber polarity and D total surface area of carbon blacks. A customised scale was considered to indicate the polarity level of elastomers. This was done by taking into account the amount and the polarity of the functional groups (epoxy and amine) in the ENR-25 and F-BR rubbers, respectively. In this context, 0 was assigned to non-functionalised NR/BR blends, 10 to functionalised ENR-25/F-BR blends and 5 to blends consisting of non- and functionalised rubbers, like NR/F-BR and ENR-25/BR. Furthermore,

the approach of considering the total surface area of carbon blacks in composites was used. It was calculated as the product of the Specific Surface Area (SSA) of a carbon black multiplied by its amount in elastomeric composites. This assumption was considered to enable a relative comparison between the carbon blacks with different surface areas, especially a very high- and a very low-SSA carbon black. The accessible surface area of the carbon blacks dispersed in the matrix is unknown and supposed to be higher than these effective values, since their agglomerates are further broken-down during mixing.

Data were examined using a statistical analysis, called ANOVA (Analysis of Variance), to determine the significance of the investigated factors and their influential interactions. A pareto chart measures the statistical significance of the factors in the predictive mathematical model. The *t-value* limit is dictated by a two-tailed distribution depending on the stabilised confidence value and the degree of freedom of the design. It is a dimensionless statistical scale calculated by dividing the magnitude of the effect by the standard error, expressed by the following equation [25]:

$$t - value = \frac{|Effect|}{\sqrt{MS_{residual}\left(\frac{1}{n_{upper}} + \frac{1}{n_{lower}}\right)}} \tag{1}$$

where $MS_{residual}$ is the mean square (the ratio of sum of squares and the degree of freedom), n is the number of experiments in the upper and lower levels.
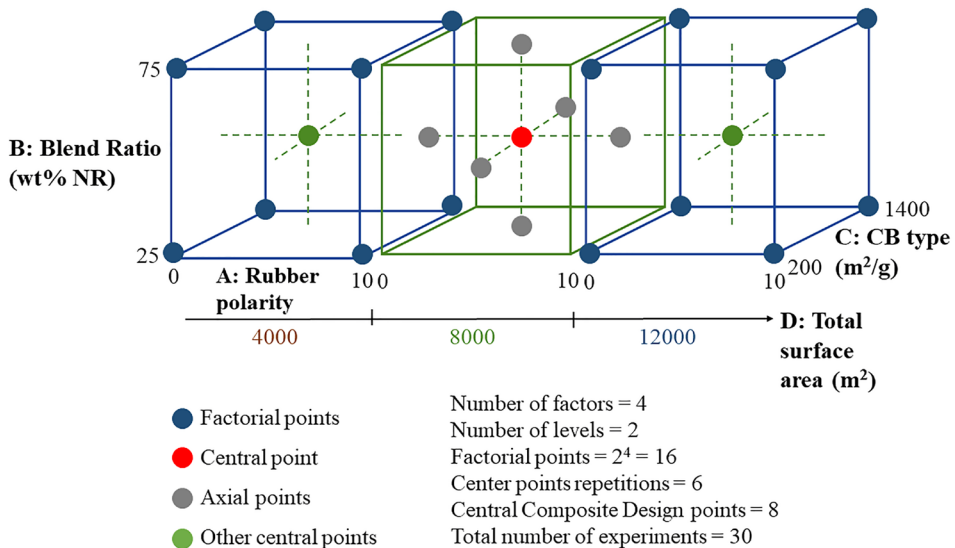

Figure 1 Cube plots of the full quadratic model with four factors and two levels design.

5.3.   Results and discussion

5.3.1.   Optimisation of the amount of process oil

Elastomeric composites filled with active fillers basically require the addition of a process oil to improve their processability which ultimately determines the final properties of the composites. For this optimisation, a 50/50 blend of NR/BR was filled with two carbon black grades, i.e. conventional, N-series carbon black and Conductive Carbon Black (CCB). Figure 2 shows the hardness and viscosity of the investigated elastomeric composites filled with carbon black N330 (at 60 phr) and CCB (at 40 phr), as a function of the amount of process oil TDAE. With increasing the amount of TDAE oil, the Mooney viscosities and hardness of the composites decrease.

5
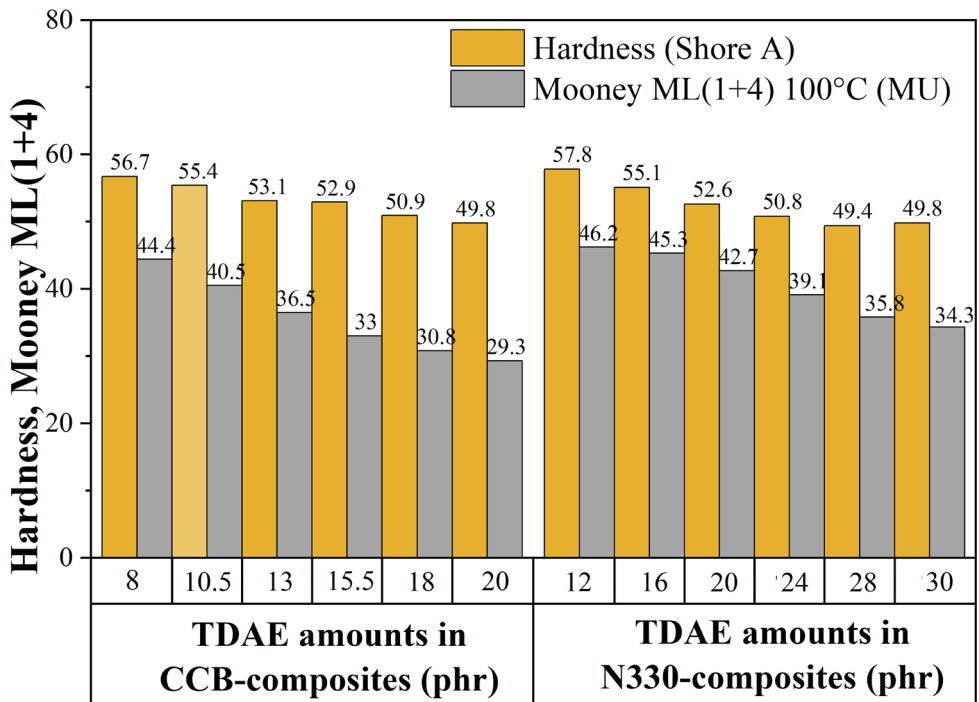
Figure 2   Effect of the process oil TDAE amounts on hardness and Mooney viscosity of the composites based on 50/50 NR/BR blends filled with CCB at 40 phr and N330 at 60 phr.

In general, process oils function as plasticisers, existing in a highly viscous liquid state that imparts a softening and lubricating effect to the polymer mixture, resulting in a lower modulus, hardness of the composites. According to the free volume theory, process oils with lower molecular weights create larger free volumes in the polymeric matrix [26,27]. This increases the mobility of polymeric chains and leads

to a increase or decrease in the glass transition temperature of the elastomeric composite. Furthermore, process oils also affect filler dispersion, especially in the case of active fillers. The low molecular weights of process oils make their molecules more mobile within the polymer matrix compared to the polymeric chains. In this way, if the process oil and filler are compatible, the oil molecules have a greater potential to be absorbed by the filler surface during dispersion of the filler in an internal mixer. This results in a better filler micro-dispersion, lowered composite viscosity, and so improved processability of the composites.
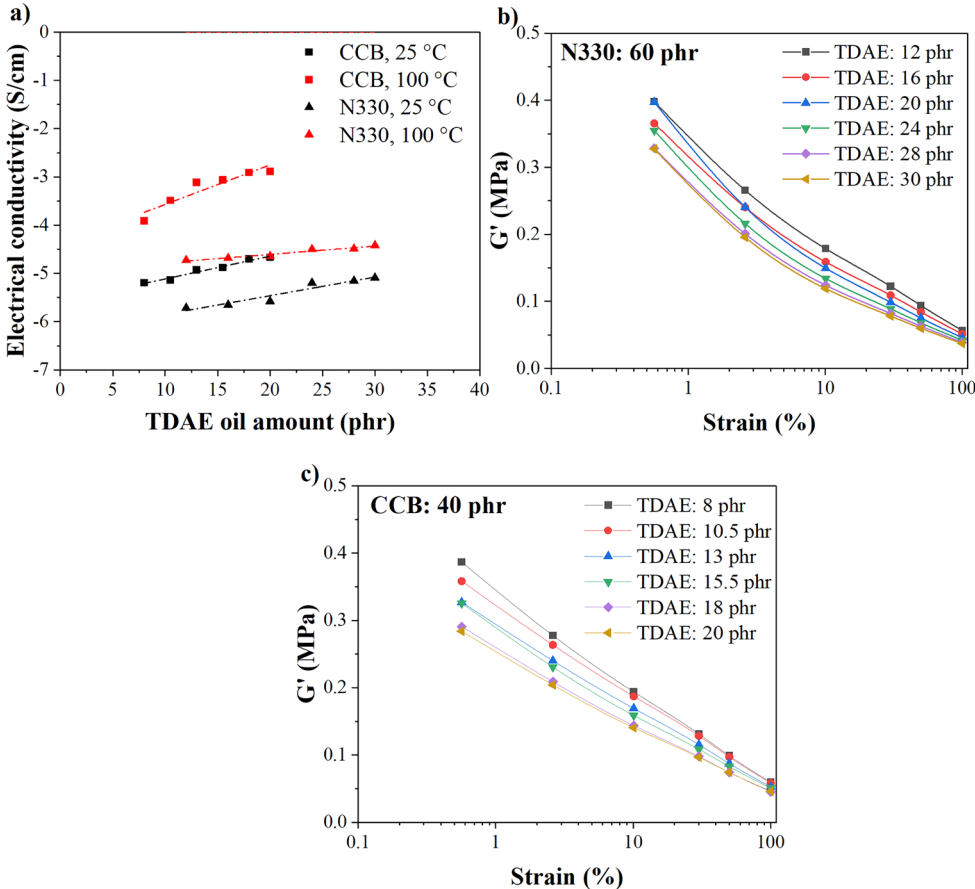
Figure 3 Effect of TDAE oil on: (a) Electrical conductivity measured at 25 and 100°C; Payne effect of 50/50 NR/BR blends filled with (b) 60 phr of N330 and (c) 40 phr of CCB.

In Figure 3, the dynamic electrical conductivity at 25 and 100°C as well as the Payne effect plots of the elastomeric composites with increasing TDAE oil amount are reported. As above mentioned, the addition of plasticizer in elastomeric composites increases the polymer chain mobility, improving the flow characteristic of the

composites and therefore, lowering the Mooney viscosity. In Figure 3 it is reported that adding a higher amount of plasticiser causes a slight increase in the electrical conductivity and a reduced Payne effect of the composites. This is attributed to an improved micro-dispersion of the carbon black particles. The plasticiser acts as dispersing agent and improves the compatibility between the elastomeric matrix and the carbon black. This promotes improved filler-filler interaction and better dispersion.

It is noteworthy that CCB gives a higher electrical conductivity than N330, even though the CCB was added in a smaller amount. It is well comprehended that the higher surface area and structure of an active filler should result in a more extensive filler network leading to shorter distances between filler particles, then increased electron tunnelling bands and so increased conductive paths within the system. CCB has a significantly higher surface area and structure than conventional CB N330, thus leading to superior conductivity in CCB-based composites. Based on the results of this preliminary experiment, to obtain adequate properties of the composites, the amount of TDAE process oil used in the following experimental parts was therefore selected at half the amount (50 wt%) of carbon black content, i.e. 20 phr and 30 phr of TDAE oil for CCB- and N330-based composites, respectively. This is because at these two amounts the micro-dispersion of carbon blacks as indicated by Payne effects and the electrical conductivity of the obtained composites become optimal.

5

5.3.2. DoE screening study

After having optimised the amount of process oil, a DoE for the screening study was carried out to identify the most influencing factor on dynamic electrical conductivity of the composites. The dynamic electrical conductivity values of the obtainable composites are reported in Table 3.Figure 4a shows the Pareto chart, and Figure 4b shows the normal plot of standardised effects with 95% of confidence ($\alpha = 5\%$).

The Pareto chart reveals that the total surface area of carbon black is the only statistically significant factor, as its absolute value is the only one crossing the reference line, the t-value limit as explained in Paragraph 2.4. The influential interactions between the total surface area and other factors (AD, BD and CD) are neither insignificant. The values of adjusted R^2 (i.e. the coefficient of determination, indicating how well the model fits the data adjusted according to the number of predictors) was 96.3%, indicating that the model fits significantly the data. In Figure 4b, the normal plot of the standardised effects shows their distribution fitting line in case of a standard deviation of 1.

Chapter 5

Table 3 Test runs for DoE screening study.

Run	A:Rubber polarity	B: Blend ratio (%NR)	C: CB types (m²/g)	D: Total surface area of CB (m²)	Response: Conductivity
1	10	50	800	8000	-8.83
2	5	50	800	4000	-8.82
3	5	75	800	8000	-8.52
4	5	50	1400	8000	-9.01
5	0	50	800	8000	-8.92
6	5	50	800	12000	-3.91
7	5	50	800	8000	-9.36
8	5	50	800	8000	-8.92
9	5	25	800	8000	-8.02
10	5	50	200	8000	-7.77
11	10	25	1400	4000	-9.38
12	0	25	200	12000	-4.13
13	0	75	1400	4000	-9.39
14	10	25	200	12000	-3.50
15	5	50	800	8000	-9.16
16	0	25	200	4000	-9.38
17	0	25	1400	4000	-9.38
18	5	50	800	8000	-8.90
19	0	75	1400	12000	-4.65
20	10	25	200	4000	-9.39
21	10	75	200	12000	-4.45
22	10	75	1400	4000	-9.27
23	0	75	200	12000	-3.73
24	0	25	1400	12000	-3.65
25	5	50	800	8000	-9.36
26	5	50	800	8000	-9.16
27	10	75	200	4000	-9.44
28	10	75	1400	12000	-4.46
29	10	25	1400	12000	-4.45
30	0	75	200	4000	-9.19

In Figure 4b, the normal plot of the standardised effects shows their distribution fitting line in case of a standard deviation of 1. This plot confirms that the linear and square terms (D and DD, respectively) of the total surface area of carbon blacks are statistically significant, as they are further away from 0. Additionally, the plots indicate that these terms have a positive standardised effect, meaning that, from low to high levels of this factor, the response increases.

a)

Pareto chart of the standardized effects
(α=0.05)

A – Rubber polarity
B – Blend ratio (NR/BR)
C – Carbon black type (m^2/g)
D – Total surface area (m^2)

$R^2=98.19\%$
$R^2(adj)= 96.26\%$
$R^2(pred)=89.76\%$

5

b)

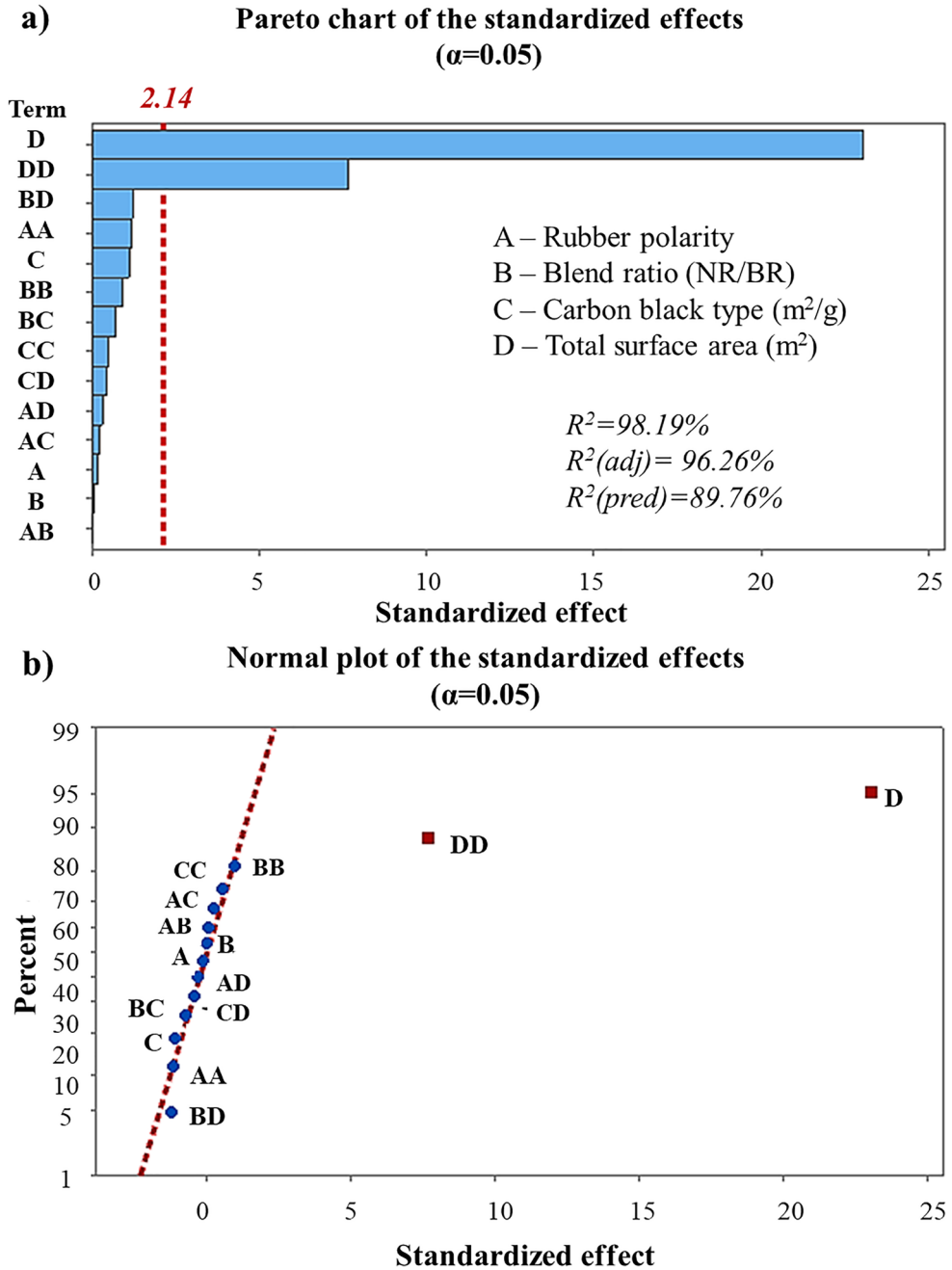## Normal plot of the standardized effects
(α=0.05)

Figure 4   (a) Pareto chart and (b) normal plot of standardised effects of the full factorial design.

For a better DoE interpretation, in Figure 5, the analysis of residuals is reported to determine its effectiveness. In the normal probability plot, see Figure 5a, the residuals are distributed on a straight line. There are no points lying away from the line, meaning that there are no outliers. In the residual versus fits, see Figure 5b, the points are randomly distributed on both sides of 0 with no recognisable pattern, confirming the absence of outliers and the presence of influential points in the model (i.e. the points far away in x-direction). The histogram shown in Figure 5c reflects that the residuals are distributed around 0. Furthermore, in the residual versus observation order plot in Figure 5d, the points are also randomly distributed, confirming the reliability of the measured response. Overall, it can be concluded that the DoE screening study meets its analysis assumptions. Therefore, it is possible to affirm that the dynamic electrical conductivity of elastomeric composites is not affected by rubber types, blend ratios and carbon black types.

In the following sections, the correlation between these factors and electrical conductivity is further analysed to understand the underlying reasons behind the DoE screening results.
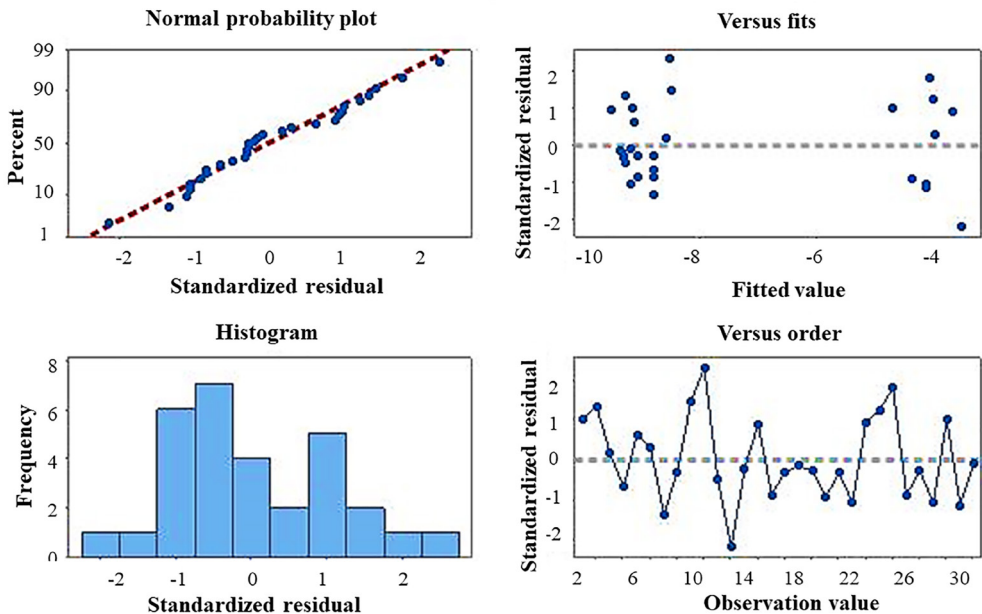

Figure 5   Residual plots of DoE: (a) Residual normal probability, (b) residual versus fitted value, (c) histogram of standardised residual and (d) residual versus observation order.

5.3.3.   Influence of rubber polarity

The DoE screening reveals that the factors rubber polarity and blend ratio are not statically significant for the variaton of the dynamic electrical conductivity of the composites. In the following paragraphs, these two factors are further investigated in order to understand and elucidate their effects in a better way. To study the effect of rubber polarity on dynamic electrical conductivity of the composites, a rubber with a rather high polarity, i.e. acryloNitrile Butadiene Rubber (NBR) was investigated and compared with the non-polar 25/75 NR/BR blend.

In this experimental part, Broadband Dielectric Spectroscopy (BDS) was used. It is a technique capable of measuring the response of polymeric materials under applied oscillating electrical field by determining the polarisation of charges (ions and electrons) in a material [27,28]. The response was characterised by measuring the complex dielectric constant ε^* and conductivity. The real part of dielectric constant ε', which is related to the permanent dipole reorientation, quantifies the dielectric polarisation of the material. The imaginary part ε'' is related to the energy dissipation in the material during the dipole reorientation. Besides the dielectric constant, during BDS analysis, the electrical conductivity with varying frequency is measured. The main difference between BDS and DMA with the electrical circuit setup used in the current study regards the range of conductivity measured. BDS quantifies the electrical conductivity of polymers in insulative, semi-conductive and conductive regions, as a response of the composites to an electric field. While, an in-house developed setup used in this work, a DMA combined with electrical devices, studies the response to mechanical deformation of the composites with only semi-conductive and conductive regions [5]. Thus, in this paragraph, to investigate the effect of rubber polarity on dynamic electrical conductivity, BDS measurement of gum elastomers at 25 and 100°C in the frequency range from 1 to 10^5 Hz was carried out.

Figure 6 shows the dielectric constant and the electrical conductivity as a function of frequency of the investigated materials. The dielectric constants of NR and BR at 25 and 100°C are comparable, while the dielectric constant at 100°C of NBR41 is remarkably higher than at 25°C, especially in the low frequency region. The increase of dielectric constant of NBR41 with temperature is due to the contribution of the charge carriers of its polar groups ACN to the polarisation. At higher temperatures, the dipoles have a higher thermal excitation energy, which rotate sufficiently fast to improve the polarisation and, in turn, increase the dielectric constant. This phenomenon is visible only at low frequencies, since in this range the ionic

polarisation intervenes, inducting a displacement of positive ions respect to negative ions. At high frequencies, the orientation polarization related to the structure of the material takes place. NBR41 also has a higher dielectric constant compared to NR and BR. At 25°C and 100 Hz, their values are 22.40, 3.09 and 3.25, respectively. This result confirms the strong polarisation of the ACN groups along the molecular chains of NBR.
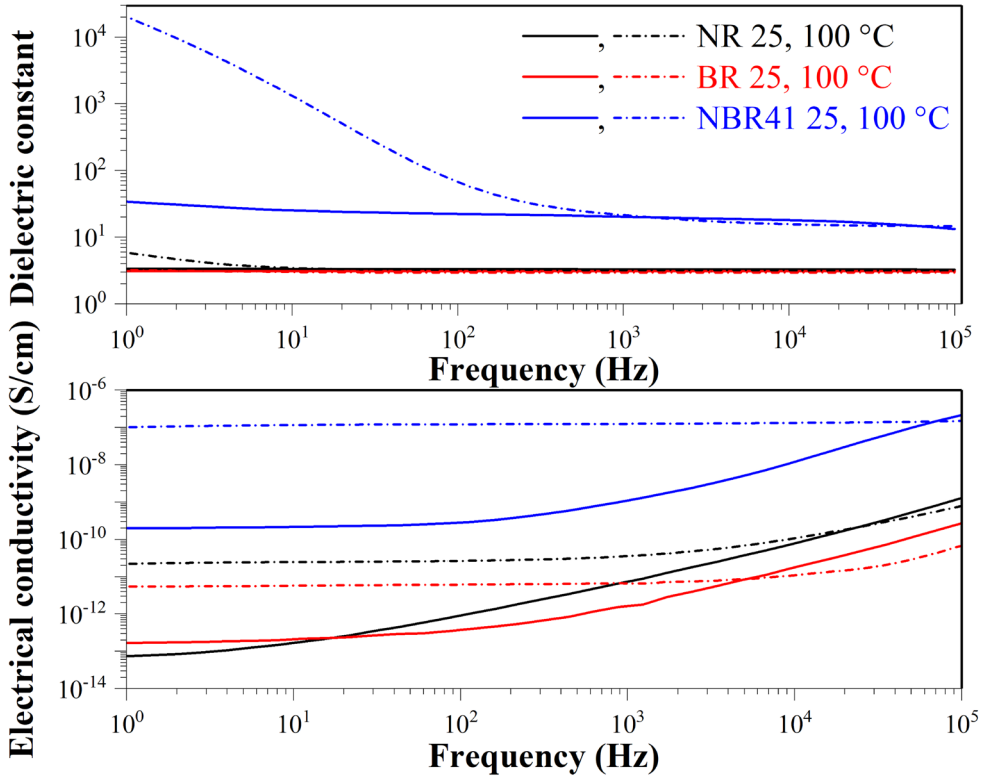

Figure 6   Electrical conductivity and dielectric constant as a function of frequency measured with BDS of the gum rubbers NR, BR and NBR41 at 25 and 100°C.

Figure 6 shows that the electrical conductivity at 25°C exhibits a plateau at low frequencies (namely DC conductivity) and a power-law dependency trend at high frequencies (namely AC conductivity). In polymers, the AC conductivity is expressed by the following power law equation [29-31]:

$$\sigma(\omega) = \sigma_{DC} + A\omega^{s(T)} \tag{2}$$

Where, $\sigma(\omega)$ is the measured AC conductivity in BDS, σ_{DC} is the DC conductivity, A is a temperature dependent constant representing the polarisability, ω is the

frequency and *s(T)* reflects the interaction term between the mobile ions and the surrounding environment. The AC conductivity increases with increasing frequency and temperature due to the electrical charges hopping mechanism across the materials in the presence of an electrical field. Therefore NR, BR and NBR have a higher electrical conductivity at 100°C compared to that at 25°C. Overall, the higher electrical conductivity of NBR41 when compared to NR and BR stays in agreement with the dielectric constant of NBR. This effect depends on the polarisable polar group in the rubbers e.g. ACN of NBR.

The progression of conductivity of composites filled with conductive filler follows a sigmoidal curve, known as the percolation plot [8,9]. Once the amount of conductive filler reaches a critical value – the percolation threshold – a sharp increase in conductivity occurs. This marks the transition from an insulator to a conductor. Figure 7 shows the electrical conductivity (i.e. measured at 100°C and 100 Hz) of the 25/75 NR/BR blend and NBR41 filled with an increasing volume fraction of conductive carbon black. In this plot, in the insulating region, the NBR41 composite has a higher electrical conductivity than the NR/BR composite, due to the strong polar nature of ACN groups. This stays in agreement with the results shown in Figure 6.
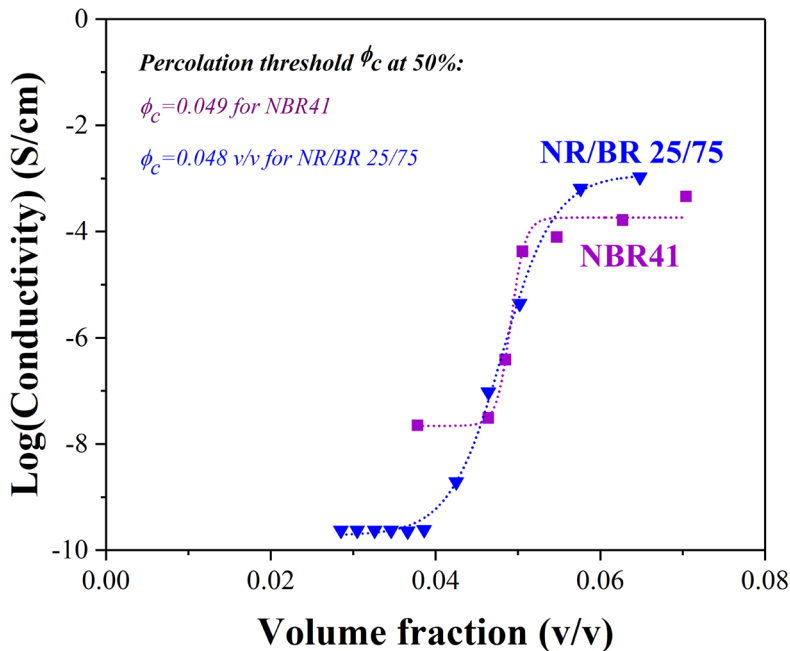
5

Figure 7   Electrical conductivity measured in DMA at 100°C and 100 Hz of 25/75 NR/BR blend and NBR41 as a function of the volume fraction of conductive carbon black Printex.

However, in the percolation region, the conductivity values of these composites are similar. This indicates a comparable percolation threshold of the two composite types. In the conducting region, it shows a small difference in conductivity. The NR/BR blend has a slightly higher electrical conductivity. This is possibly because CB is an apolar filler leading to a better compatibility with the non-polar rubbers. Although unfilled NBR41 has a higher electrical conductivity compared to gum NR/BR (Figure 6), when filled with the conductive filler, NBR41 shows a different trend. The electrical conductivity of NR/BR increases by around 7 orders of magnitude, while in the case of NBR41, it increases only by around 4 orders of magnitude. This reflects that, by using a strongly polar rubber, the carbon black network percolates and forms a continuous conductive path in a smaller degree. It is attributed to less compatibility between the polar rubber and the rather non-polar carbon black. Overall, investigating a broader range of rubber polarity, it is confirmed that the ultimate electrically conductivities of the rubbers having very different polarities do not differ considerably. From this point of view, this result confirms the outcome of the DoE screening as discussed in the previous section. However, increasing the polarity of the elastomeric matrix the conductivity of the composites in the insulating region increased due to the increased intrinsic electrical conductivity.

5.3.4. Influence of blend ratios

The effect of different blend ratios on the dynamic electrical conductivity measured at 100°C was investigated with 5 different proportions of NR/BR (i.e. 25/75, 40/60, 50/50, 60/40, 75/25 by weight) as well as NR- and BR-single elastomeric composites filled with 12000 m^2 of CCB (equal to 48 phr). From Figure 8, it is visible that the composites based on single elastomers and their blends have the same electrical conductivity. The results imply that the phase separation in the NR/BR blend does not seem to interfere the carbon black distribution and the conductive path, see the AFM images in Figure 8. The microscopic images show that carbon black particles are readily distinguished based on their brightest contrast due to the highest stiffness compared to the elastomeric phases. NR and BR are detected as light and dark domains, respectively, due to their difference in moduli. Furthermore, in all Figures, some light elliptical structures are present. It is reported that these are caused by the curing of the composite and they appear as white structures due to different crosslink densities [32].

Based on the AFM images, the blend of 25/75 NR/BR shows more bright rubber domains compared to the other two images, which is in line since there is a higher

proportion of BR in the blend. The carbon black particles are visualised more in the darker domains, in BR phase. However, it should not be concluded that the carbon black particles prefer the BR phase rather than NR phase. This is because the NR phase has a higher viscosity and is brighter than the BR phase, which might hinder the visualization of carbon black particles in NR domains. This results in a lower contrast between the particles and the NR phase. Hence, the concentration of filler in NR domains is still unclear. Basically, the carbon black distribution in polymer blends depends on the viscosity and polarity of the blended matrices and mixing conditions [33-35]. NR and BR have comparable polarities but are different in viscosity. During the mixing of blended polymers with different viscosities, shear forces are concentrated in the softer polymer phase(in this case, BR) and the filler particles are located preferably in the softer phase as well as the blend interphases [33-35].
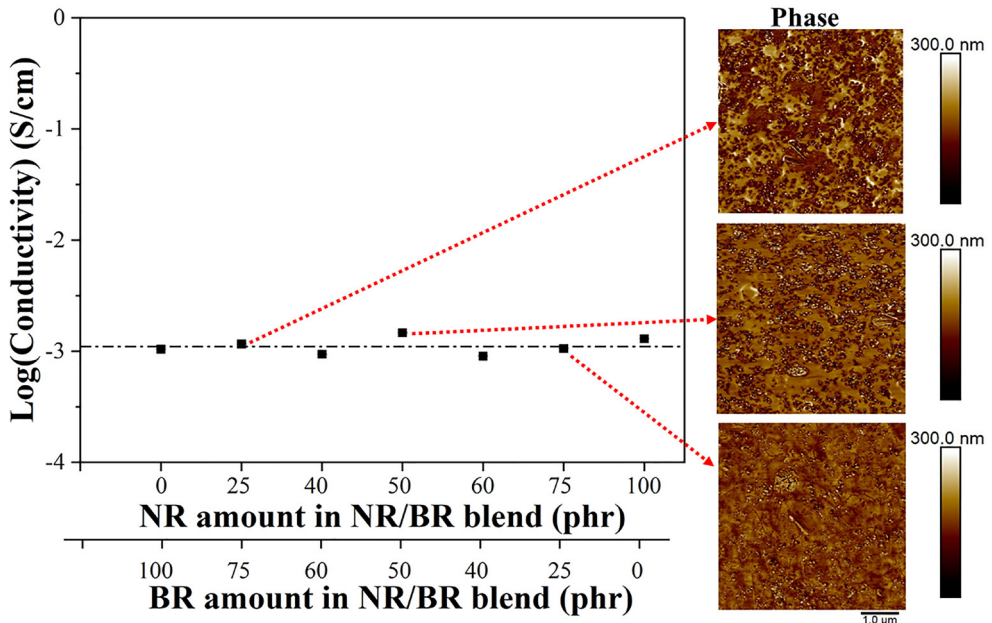
Figure 8 Electrical conductivity plot of NR/BR blends with different blend ratios filled with 12000 m² of CCB; and AFM images of the NR/BR blends with three blend ratios: (upper) 25/75, (middle) 50/50 and (lower) 75/25 by weight.

By the present AFM images, this elucidation cannot be supported. When considering the electrical conductivity of the composites (Figure 8), the results demonstrate that all composites possess a comparable electrical conductivity performance. Therefore, the phase separation, blend ratios and carbon black concentration in rubber phases do not show a clear impact on the conductive network formation of filler in the

blends. It is also noticeable that the carbon black particles have a similar size and distribution degree in the matrix, resulting in a comparable electrical conductivity of the blends.

Overall, from Figure 8, it is clear that various blend ratios do not affect the dynamic electrical conductivity of the elastomeric composites, which is in line with the results from the DoE screening. In the next paragraph, the last two factors are investigated: Carbon black type and amount. For this, the 25/75 NR/BR blend was selected due to its easy processability.

5.3.5. Effects of carbon black type and amount

The DoE study reveals that the total surface area of carbon blacks dispersed in the composites is the only significant factor influencing the dynamic electrical conductivity. There is a certain minimum level of the total surface area of carbon blacks that leads to the onset of conductivity in the composites, regardless of the type of carbon blacks. However, different types of carbon blacks render an optimum conductivity to elastomeric composites at different specific amounts, due to the variation in their specific surface areas and structures. Hence, conductive carbon blacks with various specific surface areas and structures are studied in this section.

Three parameters describe the percolation plot: The percolation threshold, the slope in the sigmoidal plot and the ultimate conductivity value. Several models have been proposed to determine the percolation threshold of the filled polymers [7]. In the present work, a sigmoidal-Boltzmann model is used to determine the percolation threshold, following:

$$Log\,(\sigma) = A_2 + \frac{A_1 - A_2}{1 + e^{\frac{\phi - \phi_c}{\Delta x}}} \tag{3}$$

where σ is the electrical conductivity; ϕ is the volume fraction of carbon black; A_1 and A_2 are the two asymptotic values of the logarithms of the electrical conductivity in the insulation and conduction regions, respectively; ϕ_c is the percolation threshold at a conductivity value ($A_1 + A_2/2$). Δx is the slope factor, i.e. the constant period of the independent variable determining the rise profile from A_1 to A_2: for a high Δx, the increase is slow while for low Δx, the increase is quick. According to this model, the fitting of conductivity of the 25/75 NR/BR blend filled with different conductive carbon blacks is shown in Figure 9. The data demonstrated in Table 4 are derived from the sigmoidal-Boltzmann model analysis. Increasing the specific surface area and the structure of carbon blacks, the percolation plots are shifted towards lower values of volume fraction.
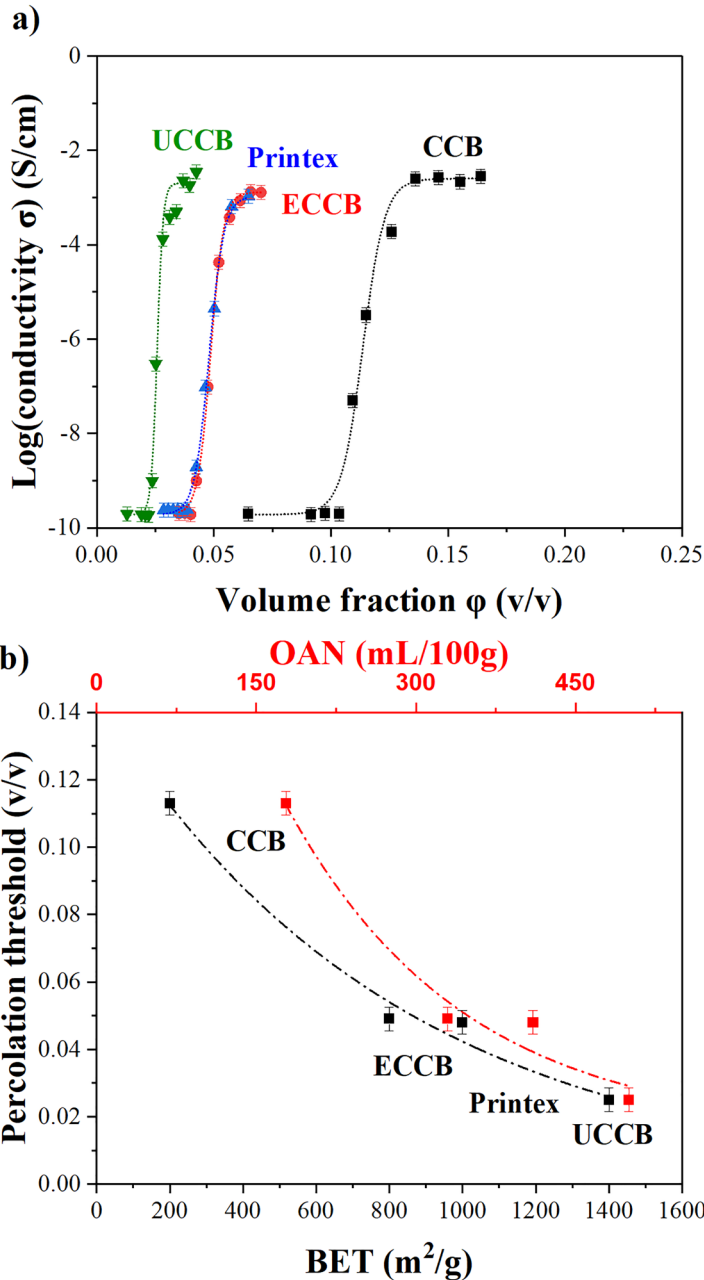
a)

b)

Figure 9   (a) Percolation plot with sigmoidal-Boltzmann model and (b) the determined percolation threshold as a function of surface area BET and structure OAN for different carbon black grades.

However, it should be remarked that Printex shows a marginally unexpected tendency, since it has a higher specific surface area and a higher structure than that

of ECCB. The percolation curve of Printex should be shifted towards a lower filler volume fraction. This issue might be attributed to a slightly poorer dispersibility of Printex in the composites as discussed later in the following paragraphs. The high values of *adj-R^2* indicate that the sigmoidal-Boltzmann model fits the data well, see Table 4. As above-mentioned, there are three parameters influencing the percolation plot and estimated by the sigmoidal-Boltzmann model estimate: electrical conductivity in insulating and conducting region, slope factor of the percolation plot and the percolation threshold. The values of the conductivity in the insulating region (see Figure 9a and A_1 values in Table 4) are similar for all carbon black types. This is obvious since the matrix is based on the same elastomer. The differences of conductivities in the conducting region (see Figure 9a and A_2 values in Table 4) of the four types of carbon blacks are negligibly small. This is attributed to the small difference in the filler network formation and the concentration of electron tunnelling bands generated in the matrix. This variation inevitably occurs due to the deviations in the dispersibility of the carbon blacks and in the mixing quality. The slope factor of the percolation plot Δx decreases by increasing the specific surface area and the structure of the carbon black. UCCB with the highest surface area and structure gives the fastest percolating tendency ($\Delta x = 0.001$) with the smallest volume fraction used to obtain the same level of percolation threshold compared to other types. CCB shows the highest volume fraction and slowest in forming the conductive network ($\Delta x = 0.005$). While ECCB and Printex are moderate for both parameters.

Table 4   Parameters of the sigmoidal-Boltzmann fitting according to classical percolation theory, based on the results in Figure 9a.

Parameters	CCB	ECCB	Printex	UCCB
A_1 (S/cm)	-9.72	-9.72	-9.72	-9.72
A_2 (S/cm)	-2.60	-2.89	-2.97	-2.70
ϕ_c (v/v)	0.114	0.049	0.048	0.025
Δx	0.005	0.003	0.003	0.001
Adj-R^2	98.9	99.8	99.8	98.9

The last important parameter to take into account is the percolation threshold ϕ_c at 50% in the percolation region. By increasing the surface area of the carbon blacks, the percolation threshold decreases from 0.114 v/v for carbon black CCB with a specific surface area of 200 m^2/g to 0.025 v/v for carbon black UCCB with a specific surface area of 1400 m^2/g. These percolation threshold values predicted with the

sigmoidal-Boltzmann equation are presented in Figure 9b as a function of the carbon black specific surface area BET and the structure defined by the OAN number. This figure illustrates the clear trends that follow the theory: The higher the surface area and the structure of conductive carbon blacks, the lower the percolation threshold. Higher structures increase the conductivity at lower carbon black loadings because more branches of carbon black aggregates are provided leading to an increased potential formation of conductive bands. Higher surface areas of carbon black also result in stronger interparticle forces and more filler-filler interactions at lower CB amounts. Furthermore, the specific surface area BET and the structure OAN of the carbon blacks considered in this study are linearly related. This is the reason for the same correlation found for these two parameters regarding the conductivity.

Figure 10a presents the sigmoidal trend of the electrical conductivity of various carbon black types as a function of Payne effects of uncured composites. The x-axis is the Payne effect as an estimation of the filler network and conductive paths. It means that there is a value of the Payne effect at which the carbon filler particles start to percolate forming a conductive network. This gives the possibility to predict the approximate percolation threshold, expressed as filler-filler interaction in the unit MPa. In Figure 10b, Payne effect values of the cured compounds are higher than the Payne effect of uncured compounds due to an increased elastic modulus since the crosslink formation restricts the polymeric chain motion. The curves present some differences compared to Figure 10a. Thus, the onsets of the percolation region for the four carbon black types are in a wider range and do not coincide. This is due to the fact that the curing of the composites affects the filler networks.
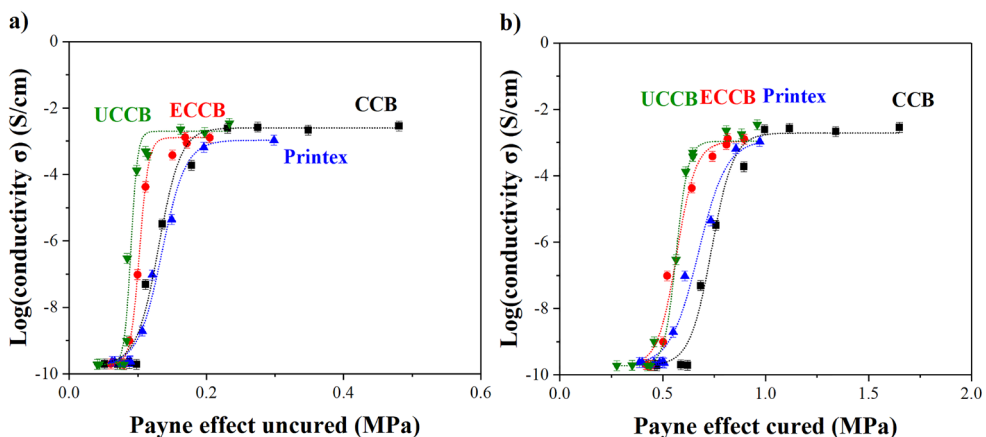
5

Figure 10 Conductivity as a function of the Payne effects of (a) uncured and (b) cured composites. The experimental data are fitted with sigmoidal-Boltzmann model.

Figure 11 and Table 5 report the percolation thresholds predicted using the sigmoidal-Boltzmann equation for the different carbon blacks. For the Payne effect uncured and cured, the percolation thresholds are not strongly dependent on the carbon black characteristics.
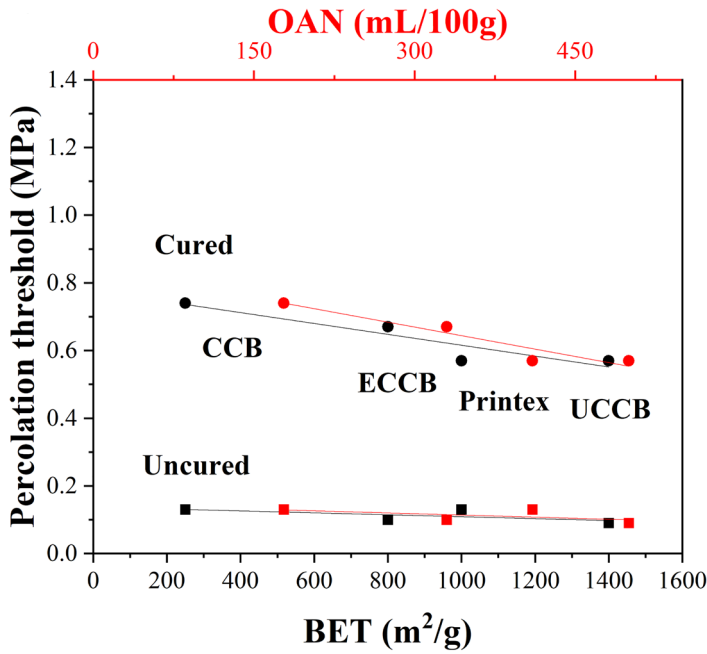

Figure 11 Percolation threshold in terms of Payne effects of uncured and cured composites as a function of specific surface area BET and structure OAN of the four carbon black types.

Table 5 Parameters of the sigmoidal-Boltzmann fitting according to the Payne effect (uncured and cured).

Parameters	CCB	ECCB	Printex	UCCB
Payne effect uncured				
A_1 (S/cm)	-9.72	-9.72	-9.72	-9.72
A_2 (S/cm)	-2.60	-2.89	-2.97	-2.70
ϕ_c (MPa)	0.13	0.10	0.13	0.09
Δx	0.016	0.007	0.017	0.005
Adj-R^2 (%)	98.1	99.6	98.9	96.4
Payne effect cured				
A_1 (S/cm)	-9.72	-9.72	-9.72	-9.72
A_2 (S/cm)	-2.60	-2.89	-2.97	-2.70
ϕ_c (MPa)	0.74	0.67	0.57	0.57
Δx	0.06	0.07	0.05	0.03
Adj-R^2 (%)	98.7	98.0	98.1	99.6

The result agrees with the DoE screening study. This phenomenon may be ascribed to the fact that the Payne effect is an actual measurement of the extent of filler network. This can function as a new method to predict the percolation threshold of the composites by simply measuring the Payne effect. From this study it results that an elastomeric composite is electrically conductive (i.e. electrical conductivity higher than 10^{-5} S/cm) when filled with an amount of conductive carbon black having the Payne effect uncured of ca. 0.08-0.15 MPa and the Payne effect cured of ca. 0.6-0.7 MPa. The higher the surface area and structure of a carbon black, the lower the percolation threshold in terms of Payne effect is.

Figure 12 presents the sigmoidal trend of the electrical conductivity of the composites containing different carbon black types with increasing total effective surface area of carbon blacks. In this case, the total effective surface area was calculated by considering the amount of CB, the total surface area (BET) and the effective volume fraction via the following equation:

$$Total\ effective\ surface\ area\ (m^2) = BET_{CB}\left(m^2/g\right) \cdot m_{CB}\ (g) \cdot \phi_{eff} \quad (4)$$

where ϕ_{eff} and m represent the effective volume fraction and the amount of carbon black. The concept of effective volume fraction of carbon black in elastomeric composites was firstly introduced by Medalia [36] and Kraus [37] and later elaborated by Wang et al. [38]. The value of the effective volume fraction is based on the presence of occluded rubber within the carbon black aggregates and agglomerates in the composites. This occluded rubber cannot be deformed under loading, thereby influencing the electrical and mechanical properties of the composites. Consequently, the occluded rubber increases the effective volume fraction of the filler. It was found that the relationship between the effective volume fraction and the volume fraction of carbon black is dependent on the structure OAN of the carbon black, as described by the following equation [36-37]:

$$\phi_{eff} = \phi\ \frac{0.0181 \cdot OAN + 1}{1.59} \quad (5)$$

This effective volume fraction is considered as a crucial factor influencing the volume fraction of the carbon black in elastomeric composites [36-37]. Therefore, this factor is taken into account when estimating the total effective surface area of carbon black particles distributed within the composites, as described in Equation 4.

When considering the total effective surface area as the x-axis, the percolation plot in Figure 12a is different from the previous ones based on the volume fraction of carbon blacks as shown in Figures 9a. As described, the total effective surface area is an assumed value of carbon black surface area that comes into contact with the

5

elastomeric matrix. In Figure 9, the percolation threshold is expressed in terms of volume fraction, that only involves the amount of the carbon black present in the elastomeric composites. This means that the percolation threshold does not take into account the actual filler-filler interactions in the elastomeric composites, which is the primary parameter influencing the electron tunnelling bands and conductive paths in the elastomeric matrix. It can be seen that the carbon blacks CCB and ECCB appear to exhibit similar total effective surface areas in the matrix at the given percolation point, despite their differences in surface area and structure. This means that the lower amount of carbon black with a higher surface area and structure can be used to reach the percolation point. This is logical since, to obtain a comparable electrical conductivity in a given polymer composite, there should be a certain level of accessible surface area of carbon black required in the matrix. This is why reducing further the surface area and increasing the structure of carbon blacks are meaningful in this technology, because the amount of carbon blacks can be reduced significantly. However, Printex shows a different value compared to the other two types of carbon black. This is in line with the explanation given in Figure 9a which suggests that it is due to its inferior dispersibility than other carbon blacks when prepared under a given mixing condition. The accessible surface area of carbon black depends on the filler dispersion. For Printex this value is higher due to a higher agglomeration.
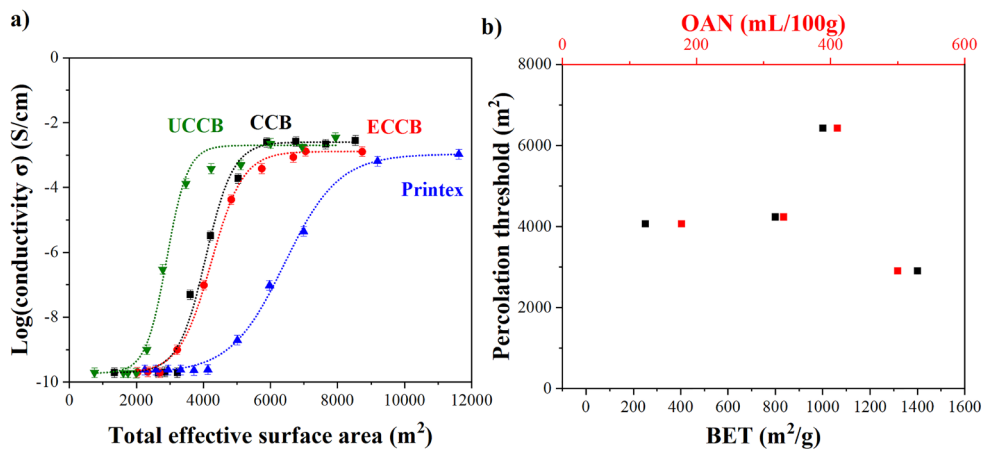

Figure 12   (a) Conductivity as a function of the total effective surface area with sigmoidal-Boltzmann model and (b) its percolation threshold as a function of BET and OAN of the four carbon black types.

Figure 12b, it is not possible to define a clear trend when correlating the values of percolation threshold in terms of total effective surface area and the BET surface

area and OAN structure of carbon blacks. Table 6 illustrates the explicit data that the carbon blacks CCB and ECCB have comparable values of percolation threshold. Whilst, Printex and UCCB have different values. Printex-based composites show a higher percolation threshold, probably due to the inferior dispersibility in the elastomeric matrix, as above-mentioned. This result again reflects that the mixing quality and the dispersibility of the conductive carbon blacks used should be optimum. UCCB-based composites show a lower percolation threshold. A possible explanation might be that the specific surface area and structure of this conductive carbon black are extremely high. With an optimum mixing quality, this UCCB can be dispersed appropriately and gives a comparable electrical conductivity at a significantly lower loading level compared to other grades.

Table 6   Parameters of the sigmoidal-Boltzmann fitting according to the total effective surface area.

Parameters	CCB	ECCB	Printex	UCCB
Total effective surface area				
A_1 (S/cm)	-9.72	-9.72	-9.72	-9.72
A_2 (S/cm)	-2.60	-2.89	-2.97	-2.70
ϕ_c (m^2)	4070	4234	6419	2304
Δx	410.3	472.5	805.5	313.0
Adj-R^2 (%)	98.8	99.8	99.8	99.8

5.4.   Conclusions

Key factors influencing the electrical conductivity of the elastomeric composites were investigated. The methodology of Design of Experiment (DoE) was used to investigate the influences of rubber polarity, blend ratio, conductive carbon black type and amount. The electrical conductivity was measured in dynamic compression deformations simulating tyre-rolling conditions. The total surface area of the filler is the only factor that significantly affects the percolation threshold and the ultimate dynamic electrical conductivity of the elastomeric composites. This means that the formation of a conductive path in an elastomeric matrix and the transfer of charge carriers between the gaps are independent on the rubber type and the blend ratios.

To understand the underlying reasons behind the DoE results, each factor was investigated in detail. It was shown that rubbers with different polarities (NR/BR and NBR) and blend ratios (NR/BR: 25/75, 40/60, 50/50, 60/40 and 75/25) have comparable electrical properties in the conducting region. The different polarity affects the electrical conductivity of the elastomeric composites in the insulating region, but not the ultimate electrical conductivity. Additionally by varying the blend

ratio, the ultimate electrical conductivity remains constant and comparable with the gum elastomeric composites.

To further analyse the effect of carbon black type and amount, percolation threshold values were determined by using the mathematical sigmoidal-Boltzmann model. This model enables a comparison of the percolation thresholds, slope of percolating regions and ultimate values of dynamic electrical conductivity of the composites. This study shows a correlation between the dynamic electrical conductivity with the Payne effect and the total effective surface area, resulting in a sigmoidal trend as well and implying the existence of a percolation threshold in terms of these two parameters. The correlation of dynamic electrical conductivity with Payne effect exists since both techniques are related to the micro-dispersion of fillers in an elastomeric matrix. The percolation threshold determined by Payne effect for both uncured and cured elastomeric composites is very similar for the four types of the conductive carbon blacks. This again confirms that the electrical conductivity depends mainly on the carbon black amount. Additionally, the measurement of the Payne effect gives an indication regarding the percolation region of the elastomeric composites studied.

5.5.   References

[1]   J. Kruželák, A. Kvasničáková, K. Hložeková, I. Hudec, Progress in polymers and polymer composites used as efficient materials for EMI shielding, Nanoscale Adv. 3 (2021) 123–172. https://doi.org/10.1039/D0NA00760A.

[2]   B. Guo, Z. Tang, L. Zhang, Transport performance in novel elastomer nanocomposites: Mechanism, design and control, Prog. Polym. Sci. 61 (2016) 29–66. https://doi.org/10.1016/J.PROGPOLYMSCI.2016.06.001.

[3]   M.C.V. Omelan, A. Diekmann, U. Giese, Development of soft electrical conductive PDMS/CNT-Composites with extremely low CNT Content, KGK Kautschuk Gummi Kunststoffe. 73 (2020) 22–30.

[4]   C. Mangone, W. Kaewsakul, M. Klein Gunnewiek, A.P.J. van Swaaij, L. Reuvekamp, J.W.M. Noordermeer, A. Blume, Design and performance of flexible polymeric piezoelectric energy harvesters for battery-less tyre sensors, Smart Mater. Struct. 31 (2022) 095034.

[5]   C. Mangone, W. Kaewsakul, A.P.J. van Swaaij, K. Bandzierz, M.K. Gunnewiek, A. Blume, Dynamic measurement setups for validating piezoelectric energy harvesters in driving conditions, Polym. Test. 119 (2023) 107932. https://doi.org/10.1016/J.POLYMERTESTING.2023.107932.

[6]   Z. Yang, S. Zhou, J. Zu, D. Inman, High-performance piezoelectric energy harvesters and their applications, Joule. 2 (2018) 642–697. https://doi.org/10.1016/j.joule.2018.03.011.

[7]   M. Klüppel, The Role of Disorder in Filler Reinforcement of Elastomers on Various Length Scales, Adv. Polym. Sci. 164 (2003) 1–86. https://doi.org/10.1007/B11054.

[8]   N. Probst, Conducting Carbon Black, Carbon Black. (2018) 271–288. https://doi.org/10.1201/9781315138763-8.

[9]   M.E. Spahr, R. Gilardi, D. Bonacchi, Carbon Black for Electrically Conductive Polymer Applications, (2017) 375–400. https://doi.org/10.1007/978-3-319-28117-9_32.

[10]   Y. Nakaramontri, S. Pichaiyut, S. Wisunthorn, C. Nakason, Hybrid carbon nanotubes and conductive carbon black in natural rubber composites to enhance electrical conductivity by reducing gaps separating carbon nanotube encapsulates, Eur. Polym. J. 90 (2017) 467–484. https://doi.org/10.1016/J.EURPOLYMJ.2017.03.029.

[11]   K. Yamaguchi, J.J.C. Busfield, A.G. Thomas, Electrical and mechanical behavior of filled elastome. I. The effect of strain, J. Polym. Sci. Part B Polym. Phys. 41 (2003) 2079–2089. https://doi.org/10.1002/POLB.10571.

[12]   J.J.C. Busfield, A.G. Thomas, K. Yamaguchi, Electrical and mechanical behavior of filled elastomers 2: The effect of swelling and temperature, J. Polym. Sci. Part B Polym. Phys. 42 (2004) 2161–2167. https://doi.org/10.1002/POLB.20085.

5

[13]   J.J.C. Busfield, A.G. Thomas, K. Yamaguchi, Electrical and mechanical behavior of filled rubber. III. Dynamic loading and the rate of recovery, J. Polym. Sci. Part B Polym. Phys. 43 (2005) 1649–1661. https://doi.org/10.1002/POLB.20452.

[14]   E.S. Bhagavatheswaran, S.R. Vaikuntam, K.W. Stöckelhuber, S. Wießner, G. Heinrich, A. Das, High-performance elastomeric strain sensors based on nanostructured carbon fillers for potential tire applications, Mater. Today Commun. 14 (2018) 240–248. https://doi.org/10.1016/J.MTCOMM.2018.01.013.

[15]   E.S. Bhagavatheswaran, Exploring the Piezoresistive Characteristics of Solution Styrene Butadiene Rubber composites under static and Dynamic Conditions - A Novel Route to Visualize Filler Network Behavior in Rubbers, PhD thesis, Technische Universität Dresden, 2019.

[16]   S. Wießner, E.S. Bhagavatheswaran, K.W. Stöckelhuber, G. Heinrich, A. Das, Piezoresistivity - A powerful tool to monitor the behaviour of filler networks in rubber, AIP Conf. Proc. 2289 (2020) 20065. https://doi.org/10.1063/5.0028322.

[17]   Indriasari, W. Kaewsakul, W.K. Dierkes, A. Blume, Defining Key Factors in Carbon Black-Filled NR/BR Compounds for Balancing Aircraft Tire Tread Properties, J. Compos. Sci. 2019, Vol. 3, Page 47. 3 (2019) 47. https://doi.org/10.3390/JCS3020047.

[18]   M. Salehi, J.W.M. Noordermeer, L.A.E.M. Reuvekamp, A. Blume, Parameter optimization for a laboratory friction tester to predict tire ABS braking distance using design of experiments, Mater. Des. 194 (2020) 108879. https://doi.org/10.1016/J.MATDES.2020.108879.

[19]   K.C. Nuñez Carrero, L.E. Alonso Pastor, M. Hernández Santana, J. María Pastor, Design of self-healing styrene-butadiene rubber compounds with ground tire rubber-based reinforcing additives by means of DoE methodology, Mater. Des. 221 (2022) 110909. https://doi.org/10.1016/J.MATDES.2022.110909.

[20]   R. Stubblefield, O. Piffard, Tire undertread, US 2019/0016178, 2016.

[21]   A. Limper, Mixing of rubber compounds, Mix. Rubber Compd. (2012) 1–239. https://doi.org/10.3139/9783446428652.

[22]   C. Mangone, W. Kaewsakul, M. Klein Gunnewiek, L. Reuvekamp, J.W.M. Noordermeer, A. Blume, Electrically conductive elastomers: Key factors and new insight in determining the percolation threshold, in: Ger. Int. Rubber Conf. DKT IRC 2021, Nuremberg, Germany, 2021.

[23]   Payne AR, Whittaker RE, Low strain dynamic properties of filled rubbers, Rubber Chem. Technol. 44 (1971) 440–478. https://doi.org/10.5254/1.3547375.

[24]   L. Guy, S. Daudey, P. Cochet, Y. Bomal, New Insights in the Dynamic Properties of Precipitated Silica Filled Rubber Using a New High Surface Silica, Kgk-Kautschuk Gummi Kunststoffe. 62 (2009) 383–391.

[25]   R. Jones, DOE Simplified: Practical Tools for Effective Experimentation. 17 (2001) 322–322. https://doi.org/10.1002/QRE.376.

[26]   B. Rodgers, Rubber compounding: chemistry and applications, CRC Press, 1-624.

https://doi.org/10.1201/b18931.

[27]   A. Rathi, M. Hernández, S.J. Garcia, W.K. Dierkes, J.W.M. Noordermeer, C. Bergmann, J. Trimbach, A. Blume, Identifying the effect of aromatic oil on the individual component dynamics of S-SBR/BR blends by broadband dielectric spectroscopy, J. Polym. Sci. Part B Polym. Phys. 56 (2018) 842–854. https://doi.org/https://doi.org/10.1002/polb.24599.

[28]   I. Popov, S. Cheng, A.P. Sokolov, Broadband Dielectric Spectroscopy and Its Application in Polymeric Materials, Macromol. Eng. (2022) 1–39. https://doi.org/10.1002/9783527815562.MME0059.

[29]   A. Ladhar, M. Arous, H. Kaddami, M. Raihane, A. Kallel, M.P.F. Graça, L.C. Costa, AC and DC electrical conductivity in natural rubber/nanofibrillated cellulose nanocomposites, J. Mol. Liq. 209 (2015) 272–279. https://doi.org/10.1016/J.MOLLIQ.2015.04.020.

[30]   N. Guskos, E.A. Anagnostakis, V. Likodimos, T. Bodziony, J. Typek, M. Maryniak, U. Narkiewicz, I. Kucharewicz, S. Waplak, Ferromagnetic resonance and ac conductivity of a polymer composite of Fe_3O_4 and Fe_3C nanoparticles dispersed in a graphite matrix, J. Appl. Phys. 97 (2005) 024304. https://doi.org/10.1063/1.1836855/930397.

[31]   G.C. Psarras, E. Manolakaki, G.M. Tsangaris, Dielectric dispersion and ac conductivity in—Iron particles loaded—polymer composites, Compos. Part A Appl. Sci. Manuf. 34 (2003) 1187–1198. https://doi.org/10.1016/J.COMPOSITESA.2003.08.002.

[32]   L.P.A.E.M. Reuvekamp, Reactive mixing of silica and rubber for tyres and engine mounts: influence of dispersion morphology on dynamic mechanical properties, PhD thesis, University of Twente, 2003.

[33]   M.E. Spahr, R. Rothon, Carbon Black as a Polymer Filler, in: Polym. Polym. Compos. A Ref. Ser., Springer, Berlin-Heidelberg, Germany, 2016: pp. 1–31. https://doi.org/10.1007/978-3-642-37179-0_36-2.

[34]   I.H. Jeon, H. Kim, S.G. Kim, Characterization of Rubber Micro-Morphology by Atomic Force Microscopy (AFM), Rubber Chem. Technol. 76 (2003) 1–11. https://doi.org/10.5254/1.3547733.

[35]   W.M. Hess, C.R. Herd, P.C. Vegvari, Characterization of Immiscible Elastomer Blends, Rubber Chem. Technol. 66 (1993) 329–375. https://doi.org/10.5254/1.3538316.

[36]   A.I. Medalia, Morphology of aggregates: VI. Effective volume of aggregates of carbon black from electron microscopy; Application to vehicle absorption and to die swell of filled rubber, J. Colloid Interface Sci. 32 (1970) 115–131. https://doi.org/10.1016/0021-9797(70)90108-6.

[37]   G. Kraus, A Carbon Black Structure-Concentration Equivalence Principle. Application to Stress-Strain Relationships of Filled Rubbers, Rubber Chem. Technol. 44 (1971) 199–213. https://doi.org/10.5254/1.3547354.

5

Chapter 6

Conductive and conventional carbon blacks for electrically conductive elastomers

Flexible active materials for powering tyre sensors are becoming increasingly relevant, leading to a growing interest in the development of conductive elastomers. Particularly, these conductive elastomers can be used as electrodes of piezoelectric materials, giving the capability to harvest electrical power. The present work aims to investigate the effect of carbon black type on dynamic electrical conductivity of elastomeric composites. The conductivity was measured using an in-house developed measurement setup based on a dynamic mechanical analyser. Elastomeric composites comprising Natural Rubber (NR) and Butadiene Rubber (BR) at a 25/75 blend ratio by weight filled with conventional and conductive carbon blacks having specific surface areas in the range of 78 and 1400 m^2/g were considered. Sigmoidal-Boltzmann model was applied to predict the percolation threshold of NR/BR composites. New insights were gained by correlating the dynamic electrical conductivity of NR/BR composites with the Payne effect, which serves as an indicator of the filler-filler interaction, and total effective surface area of the carbon blacks. Mechanical properties and Small-Angle X-ray Scattering (SAXS) of the elastomeric composites were also measured. Both measurements underlined the main differences between conventional and conductive carbon blacks.

6

6.1.   Introduction

Incorporating conductive carbon blacks into an insulating polymeric matrix increases its electrical conductivity due to a hopping and tunnelling phenomenon of charge carriers across the carbon black network [1-3]. The filler amount at which a conductive path is established is called the percolation threshold. From this state on, the gap distance between the filler aggregates is small enough for the electrons to be transported between different aggregates, forming electron tunnelling bands. The conductivity level of such composites varies from insulation (10^{-14} S/cm) to conduction (1 S/cm), depending on filler type and amount, filler dispersibility and elastomeric matrix [4].

Electrically conductive elastomers are widespread and being applied for flexible electronic components [5-7]. The application taken into account in this study is their integration into piezoelectric energy harvesters for tyres, capable of providing a battery-less system for autonomous operations and sensors [8-11]. For tyre application, this composites need to withstand the dynamic service conditions of the rolling tyres. In a previous research included in Chapter 3, the laboratory setups capable of measuring electrical conductivity of polymeric materials under tyre-rolling conditions were successfully designed and validated [10]. The dynamic mechanical deformation, occurring during tyre-rolling conditions, affects the physical contact and the tunnelling gap between carbon black particles, enhancing the electrical conductivity of the composites. In a follow-up study included in Chapter 4, elastomeric composites were used as an electrode of a piezoelectric energy harvester including a polyvinylidene difluoride as piezoelectric polymer [9]. This study gave a notable preliminary indication of the efficiency of an elastomer-based piezoelectric harvester and the importance of a flexible electrode.

Key factors for an increased dynamic electrical conductivity of elastomeric composites were investigated and reported in [12] and Chapter 5. As an outcome of a full factorial Design of Experiments (DoE) study, the carbon black amount in elastomeric composites, expressed via the total surface area, was the only significant factor. Blend ratios of rubbers with different polarity, i.e. Natural Rubber (NR), Butadiene Rubber (BR), Epoxidized Natural Rubber (ENR) and Functionalised Butadiene Rubber (F-BR) revealed to be statistically insignificant. In this study, only conductive carbon blacks with high specific surface areas and structures were considered. The sigmoidal-Boltzmann model represented a good methodology to understand the reasons underling the DoE results. This model gave a new approach

for correlating the dynamic electrical conductivity with the Payne effect as an indicator of filler-filler interactions and total effective surface area of carbon blacks.

The current study proposes to investigate different categories of carbon blacks: Conventional carbon blacks (N-series: N134, N330, N339, N326) and various conductive carbon blacks with higher specific surface area and structure than the conventional ones. A sigmoidal-Boltzmann model is employed to determine the percolation threshold and find the correlations with the carbon blacks' specific surface area and structure. While an high specific surface area of carbon blacks is connected to the primary particle size and stronger inter-particle forces, a higher structure of carbon black is connected to higher branched aggregates. Thus, the combined effect of both properties of carbon black contributes to the degree of the formation of conductive paths in elastomeric composites. The effects of these possible crucial factors are discussed and the conductivity behaviour of elastomeric composites is modelled. Mechanical properties and Small-Angle X-ray Scattering were also measured to further study the influence of carbon black types.

6.2.   Experimental

6.2.1.   Materials

Rubbers used were Natural Rubber and high-cis branched Butadiene Rubber were described in Chapter 5. The Carbon Black types employed are summarised in Table 1 with their values of specific surface area Brunauer-Emmet-Teller BET and Oil Adsorption Number OAN indicating the filler structure.

Table 1   Carbon black types, tradenames, suppliers, and properties.

CB category	Code	Tradename / Supplier	BET (m²/g)	OAN (mL/100g)
Conventional	N326	N326 / MAKROChem, Poland	78	72
	N339	N339 / MAKROChem, Poland	91	120
	N330	N330 / Cabot Corporation, Germany	78	88
	N134	N134 / Cabot Corporation, Germany	134	127
Conductive	CCB	Vulcan XC72 / Cabot Corporation, Germany	200	174
	ECCB	Ketjenblack EC-300J / Nouryon, the Netherlands	800	330
	Printex	Printex XE2B / Orion Engineered Carbons, Germany	1000	420
	UCCB	Ketjenblack EC-600JD / Nouryon, the Netherlands	1400	500

Other composites ingredients were of technical quality, described in Chapter 5.

6.2.2.   Composites preparations

All the composites were prepared using a two-stage mixing procedure. A masterbatch was prepared in an internal mixer (Brabender Plasti-Corder 350s, Brabender GmbH & Co KG, Germany) with a starting temperature of 60°C, 75% fill factor and a rotor speed of 100 rpm. Mixing time was 6.2 min. The elastomer and filler types and amounts were varied as shown in Table 2.

Table 2   Elastomeric composites formulations.

Ingredients	Amount (parts per hundred rubber, phr)
NR	25
BR	75
CB	Variable
Process oil	Half amount of CB
6PPD	1.5
TMQ	4.0
Stearic acid	2.0
ZnO	5.0
α-Sulphur	1.5
TBBS	1.8

NR and BR were initially blended in the internal mixer for 1 min. The NR was masticated before the addition of BR to have comparable viscosity and hence better blend compatibility. Carbon black was first divided into two portions, then pre-dispersed in TDAE oil and added to the mixer. Each portion of carbon black and TDAE oil was mixed for 2 min. For the remaining 1.2 min, the rest of the ingredients (6PPD, TMQ, ZnO and stearic acid) were added and mixed.

After discharging the masterbatches from the internal mixer, they were sheeted out on a two-roll mill for 2 min at a 2 mm nip width of the rolls (Polymix 80 T, Schwabenthan-Maschinen GmbH & Co. KG, Berlin, Germany). They were stored at an ambient temperature for 24 h before the incorporation of sulphur and TBBS in the second mixing stage on the two-roll mill at a low temperature of 50°C for 5 min mixing time to avoid premature crosslinking of the composites.

Curing characteristics of the composites were analysed using setups and conditions reported in Chapter 5.

6.2.3. Composites characterisations

The *dynamic electrical conductivity* was characterised using an in-house setup described in Chapter 3.

Payne effect uncured and cured were measured in the RPA according to the description in Chapter 5.

Tensile tests were performed using a Zwick tensile tester (model Z1.0/TH1S, ZwickRoell GmbH & Co. KG, Haan, Germany) with dumbbell specimens type 2 at a crosshead speed of 200 mm/min, according to ASTM D412.

Small Angle X-ray Scattering (SAXS) analyses were performed at the European Synchrotron Radiation Facility (ESRF) in Grenoble on beamline ID02 at wavelength $\lambda = 1$ Å using a test specimen to detector distance of 31m and 8m. 2D scattering images were recorded with an Eiger2X 4M pixel detector and normalised to azimuthally averaged scattering profiles $I(q)$ using standard procedures [14]. This resulted in an available scattering vector range q between 0.0002 and 0.025 A^{-1} [14]. The scattering vector q is related to the scattering angle θ by the following equation:

$$q = \frac{4\pi}{\lambda} \sin\left(\frac{\theta}{2}\right) \tag{1}$$

Composite test specimens (cured at their optimal t_{c95}) have been prepared with a thickness of 2 mm and were scanned across their cross-sectional area. The recorded data of these line scans were averaged and corrected for scattering backgrounds.

Scattering data can be analysed in different ways to obtain information on the hierarchical structure of carbon black in vulcanised elastomeric composites. This comprises primary particle in level 1, aggregates of primary particles in level 2, and agglomerates of aggregates in level 3. Beaucage et al. developed a unified model equation to characterise the filler network at each structural level i and estimate the size of primary particle R_{NP}, aggregates and agglomerates R_{agg} [15,16]. The model is derived as follows:

$$I(q) = \sum_{i=1} G_i exp\left(-\frac{q^2 R_{gi}}{3}\right) + (B_i \operatorname{erf} R_g/\sqrt{6})\, q_i^{-pi} \tag{2}$$

where i is the structural level, Rg is the radius of gyration, p is the power law exponent, *erf* is the error function. G is the Guinier pre-factor and B is the Porod coefficient, both depend on the properties of primary particle (i.e. carbon black). The radius of gyration specifies the size of each structural level in the hierarchy, while the power law exponent specifies the morphology of each structural level. The value

of q at which a slope change is visible corresponds to the gyration radius for that specific structural level.

To determine the radii of the structural levels more precisely, Kratky et al.'s approach was chosen [17-19]. With this approach the product $I(q)q^2$ is plotted as a function of q. In this plot the change in slope is recognised with a maximum. Therefore, an analysis of these peaks corresponding to the structural level of the hierarchy of carbon black networks gives information about the size of aggregates and about particle sizes as well. Thus, a Peak Analysis with OriginPro 2021b (OriginLab Corporation, Northampton, Massachusetts, USA) was carried out to determine the values of the radii. This was done using the following equation:

$$R_i = \frac{\pi}{q_{max,i}} \tag{3}$$

where i is the structural level, representing primary particle size R_{NP}, and aggregates and agglomerates size, R_{agg}.

6.3. Results and discussion

6.3.1. Electrical conductivity vs CB volume fraction

A previous study, reported in [12] and Chapter 5, revealed that the total surface area of carbon blacks in the selected elastomeric composites is the only significant factor influencing their electrical conductivity under dynamic conditions. Conductive carbon blacks with a specific surface area BET higher than 200 m^2/g and a structure OAN higher than 150 mL/100g exhibit a certain minimum level of Payne effect at which the onset of conductivity in the composites occurs. This work investigates conventional carbon blacks to assess the applicability of the modelling and theory developed in the previous paper for conductive blacks, reported in Chapter 5. Firstly, the percolation plot with conductivity as a function of volume fraction, according to the classical percolation theory, is considered. Secondly, in the following section the percolation threshold, expressed in terms of Payne effect and total effective surface area, is calculated for all the carbon black types.

The progression of conductivity of composites filled with carbon blacks follows a sigmoidal curve known as the percolation plot. Once the amount of carbon black reaches the percolation threshold, a sharp increase in conductivity occurs, marking the transition from an insulator to a conductor. In the Chapter 5 and in the present work, a sigmoidal-Boltzmann model is used to determine the percolation threshold, following:

$$Log\,(\sigma) = A_2 + \frac{A_1 - A_2}{1 + e^{\frac{\phi - \phi_c}{\Delta x}}} \tag{4}$$

where σ is the electrical conductivity; ϕ is the volume fraction of carbon black; A_1 and A_2 are the two asymptotic values of the logarithms of the electrical conductivity in the insulation and conduction regions, respectively; Δx is the slope of the curve; ϕ_c is the percolation threshold at a conductivity value $(A_1+A_2/2)$.

According to this model, Figure 1a shows the fitting of the conductivity of NR/BR blend at 25/75 as a function of the volume fraction of conventional and conductive carbon blacks. The parameters of the model are reported in Table 3. The sigmoidal-Boltzmann model fits the experimental data of both categories of carbon blacks very well. The values of the conductivity in the insulating region as well as in the conductivity region fall in the same orders of magnitude for all carbon black types, despite their different specific surface areas and structures. This confirms that conventional and conductive carbon blacks can form an optimum conductive filler network, providing an equal level of electrical conductivity. However, their physical properties regarding surface areas and structures differ, leading to different amounts of the individual carbon black required to create the optimal conductive filler network and electron tunnelling bands in the elastomeric composite.

6

The percolation threshold ϕ_c and rate Δx are the main parameters that differentiate the carbon black types. The determined percolation threshold expressed as volume fraction, predicted by the Boltzmann equation, is presented in Figure 1b as a function of specific surface area BET and structure OAN. It is visible that an increasing specific surface area of carbon blacks results in a sharp decrease in the percolation threshold.

The percolation threshold, according to the classical percolation theory (volume fraction), exhibits an exponential decline trend with increasing BET and OAN of the carbon blacks. This finding is in good agreement with the previous work, reported in Chapter 5 and [12]. Conventional carbon blacks have percolation thresholds comparable to each other due to similar specific surface area and structure. The exponential trend is strongly influenced by carbon blacks with high surface area and structure, where the minimum aggregate distance for electron hopping is reached. Higher surface areas imply stronger interparticle forces, and higher structures imply more branches of the carbon black aggregates.
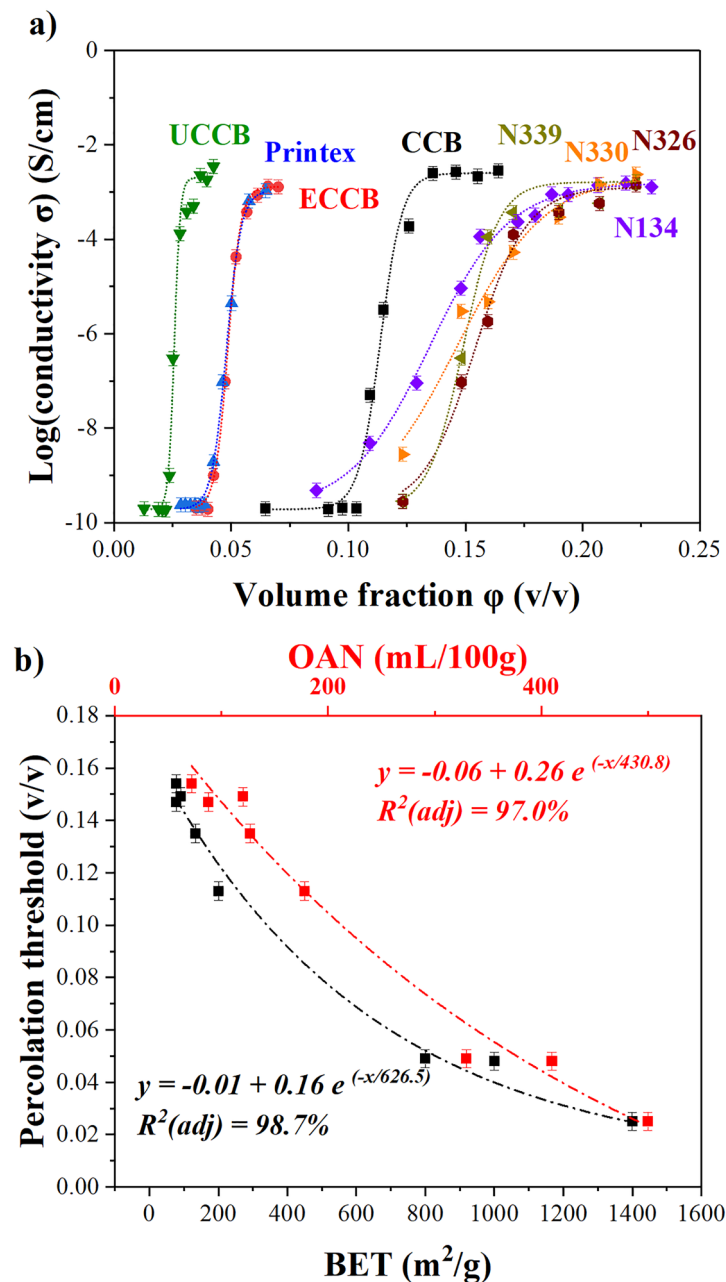
a)

b)

Figure 1 (a) Percolation plot with sigmoidal-Boltzmann model and (b) the determined percolation threshold as a function of BET and OAN of carbon blacks.

From Figure 1b, a predictive equation was obtained to calculate the percolation based on the specific surface area and structure of the carbon blacks. Table 3 reports

the percolation rates Δx for all CBs. Conductive carbon blacks have lower Δx values compared to conventional carbon blacks, ranging between 0.001 and 0.005. The lower the percolation rate Δx is, the faster is the formation of a continuous conductive network. This is due to their higher specific surface area and higher structure, providing an extended carbon black network. Among the category of conventional carbon blacks, the Δx values do not seem to be correlated to the values of the specific surface area and the structure. The percolation rates for this category follows this order: N339 < N326 < N134 < N330. The order of the percolation rates Δx is not in line with the specific surface area BET and structure OAN, following both the order: N134 > N339 > N330 > N326. The disagreement between the percolation rates and the surface areas and structures of the conventional carbon blacks is attributed to the competitive effect between these two factors: 1) dispersibility degree; and 2) active surface area of carbon blacks. N326 has the lowest BET and OAN. A low BET means it is basically the easiest to mix and disperse this CB in an elastomeric matrix due to weaker interparticle forces. The higher OAN leads to a higher branched structure of carbon black. In this case, the polymer can more easily penetrate inside the CB agglomerate, resulting in a better dispersion. It is assumable that the BET and the weaker interparticle forces are dominant, resulting in a faster percolation rate of N326 in the composite. When comparing N339 and N330, N339 has a higher structure with a similar surface area. Here, the effect of structure can be seen. The higher structure gives a faster percolation rate. This is also due to a better dispersibility caused by the branched structure of carbon black. More aggregate and agglomerate branches provide more potential to be broken down during mixing implying a better dispersion. With this better dispersion characteristic, N339 exhibits a faster percolation than N330. For N134 and N330, N134 has the smallest primary particle size and most branched structure, which seems to be the most difficult one to disperse in the composite.

6

Table 3   Parameters of the sigmoidal-Boltzmann fitting according to the classical percolation theory.

Parameters	N326	N330	N339	N134	CCB	ECCB	Printex	UCCB
A_1 (S/cm)	-9.72	-9.72	-9.72	-9.72	-9.72	-9.72	-9.72	-9.72
A_2 (S/cm)	-2.90	-2.65	-2.79	-2.81	-2.60	-2.89	-2.97	-2.70
Φ_c (v/v)	0.154	0.147	0.149	0.135	0.114	0.049	0.048	0.025
Δx	0.011	0.019	0.007	0.017	0.005	0.003	0.003	0.001
R^2 (adj)	98.8	97.8	98.2	99.4	98.9	99.8	99.8	98.9

6.3.2. Electrical conductivity and Payne effect correlation

Figure 2 reports the sigmoidal trends of electrical conductivity of conventional and conductive carbon blacks as a function of Payne effects of the uncured and the cured composites using the Boltzmann model. The Payne effect, as an estimation of filler network, shows a sigmoidal curve when plotted as x-axis with electrical conductivity as y-axis. Both plots of the conductivity as a function of Payne effects of uncured and cured composites show sigmoidal trends. The main difference of these two trends is the higher range of Payne effect of cured composites due to the formed crosslinks and so higher elastic modulus. Both fittings have a high value of R^2. In Table 4, the model parameters are reported. Also, in this case, like in Figures 1a and 1b, the percolation rates Δx of the sigmoidal trends and percolation thresholds (expressed in MPa) represent the main differences between the carbon black types. The percolation rates Δx of the percolation plot is generally strongly affected by the carbon black particle size, aggregate aspect ratio and dispersion. Conductive carbon blacks show lower Δx values compared to the conventional carbon blacks, which is consistent with the results in Table 3. This confirms the significant effect of interparticle forces and highly branched aggregates of the conductive carbon blacks on the percolation region, making these carbon blacks percolating faster. Among conductive carbon blacks, the percolation rates Δx decrease with increasing surface area and structure, aligning with the previous interpretation. For conventional carbon blacks, the observed trend in Table 3 follows the order: N339 ~ N326 < N134 ~ N330. As explained earlier, this trend is not in line with the specific surface area and structure of the conventional carbon blacks. The explanation was given in the previous section, attributing it to their different dispersibility in the elastomeric composite.

In Chapter 5, it was possible to determine a value for the percolation threshold based on Payne effects of the uncured and cured composites, which proved to be valid for all types of conductive carbon blacks [12]. For the category of conductive carbon blacks, the filler starts to percolate when filled with the required amount of conductive carbon black giving the Payne effect uncured of ca. 0.1-0.2 MPa and the Payne effect cured of ca. 0.6-0.7 MPa. From the results in Figure 2 and Table 4, it is not possible to confirm this trend for all carbon black types. Conventional carbon blacks exhibit a higher percolation threshold in terms of Payne effect compared to the conductive carbon blacks, because of their lower surface areas and structures. Conductive carbon blacks reach an ultimate conductivity level at a lower carbon black amount. On one hand, the higher specific surface areas of these fine-particles and stronger interparticle forces results in more contact points across the carbon

black network and the formation of continuous conductive path at a lower filler amount. Hence, elastomeric composites require a smaller amount of conductive carbon blacks to achieve the ultimate conductivity, and thus a lower Payne effect. On the other hand, increasing the structure of carbon blacks also increases the Payne effect values. Higher amounts of conventional carbon blacks are needed to reach the ultimate electrical conductivity. Consequently, conventional carbon blacks form larger aggregates and agglomerates in the elastomeric matrix, resulting in a higher value of Payne effect.
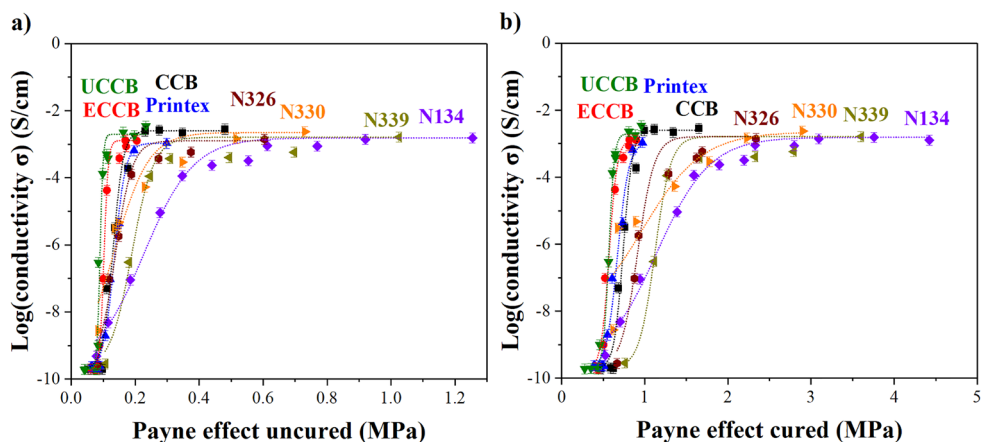

Figure 2 Conductivity as a function of Payne effect (a) uncured and (b) cured, with the sigmoidal-Boltzmann model.

However, particularly in Figure 2a, all the curves exhibit similar onsets in the percolation region based on the Payne effect, while such a similar onset is not visible in Figure 2b. Payne effect values of the cured elastomeric composites are higher due to the increased elastic modulus caused by crosslinks formation, which restricts polymeric mobility. In addition, it is common for active fillers that the filler clusters tend to reagglomerate in the initial stage and induction period of cure, known as the flocculation phenomenon, leading to larger agglomerates which also contribute to a higher moduli of the composites [20-22]. The onsets of the percolation threshold based on Payne effect uncured occur at similar Payne effect values, implying independence from carbon black types with different surface areas and structures. The onsets based on Payne effects of cured composites show a wider range, indicating an influence of carbon black type. This could be attributed to the interference of generated polymer network, crosslinks, bound rubber content and flocculation effect as discussed earlier.

Table 4 Parameters of the sigmoidal-Boltzmann fitting according to the Payne effects of uncured and cured composites.

Parameters	N326	N330	N339	N134	CCB	ECCB	Printex	UCCB
Payne effect uncured								
A_1 (S/cm)	-9.72	-9.72	-9.72	-9.72	-9.72	-9.72	-9.72	-9.72
A_2 (S/cm)	-2.90	-2.65	-2.79	-2.81	-2.60	-2.89	-2.97	-2.70
Φ_c (MPa)	0.14	0.13	0.19	0.23	0.13	0.10	0.13	0.09
Δx	0.03	0.05	0.03	0.08	0.02	0.01	0.02	0.01
R^2 (adj)	97.5	91.1	97.4	98.4	98.1	99.6	98.9	96.4
Payne effect cured								
A_1 (S/cm)	-9.72	-9.72	-9.72	-9.72	-9.72	-9.72	-9.72	-9.72
A_2 (S/cm)	-2.90	-2.65	-2.79	-2.81	-2.60	-2.89	-2.97	-2.70
Φ_c (MPa)	0.91	0.96	1.12	1.14	0.74	0.67	0.57	0.57
Δx	0.10	0.36	0.10	0.32	0.06	0.07	0.05	0.03
R^2 (adj)	95.2	90.0	97.4	98.9	98.7	98.0	98.1	99.6

For both cured and uncured composites, the percolation region, after the onset, is influenced by the interparticle distances of the filler. Each carbon black type presents a different sigmoidal S-shape because of the differences in their morphology and structure, and consequently in the different dispersibility in the composites. Conventional carbon blacks, compared to the conductive grades, have larger particle sizes, inferior interparticle forces and require a significantly higher amount to form a conductive network. The breakup of filler network contributes to the observed Payne effect variations. Higher filler contents of the conventional blacks increase the modulus G' due to higher filler volume fractions and the hydrodynamic effect. Ultimately, this category of carbon blacks exhibits a higher percolation rate in the percolation region, implying a higher amount needed for the formation of the conductive network. Therefore, there is no clear correlation between the percolation threshold in terms of Payne effects and the surface area and structure of the carbon blacks. Besides, two separate groups of the percolation curves can be observed for the conductive and conventional carbon blacks, primarily because of the differences in the dispersibility, active surface area, structure, and volume fraction of the two types of carbon blacks. This confirms that the conductive carbon blacks can provide effective conductivity with only a small quantity compared to the conventional ones.

Figure 3 shows the predicted percolation threshold in terms of Payne effect uncured and cured as a function of carbon black surface area and structure. These results clearly demonstrate the distinct groups between the conventional and the conductive carbon blacks. The specific surface area BET and structure OAN number of the

carbon blacks employed in this study exhibit a linear relationship. This indicates that these two parameters have similar correlation trends regarding their influence on conductivity. As aforementioned, the percolation threshold of the conductive carbon blacks is independent of their surface area and structure. The conventional carbon blacks show sharply increasing trends of percolation threshold with increasing surface area and structure.
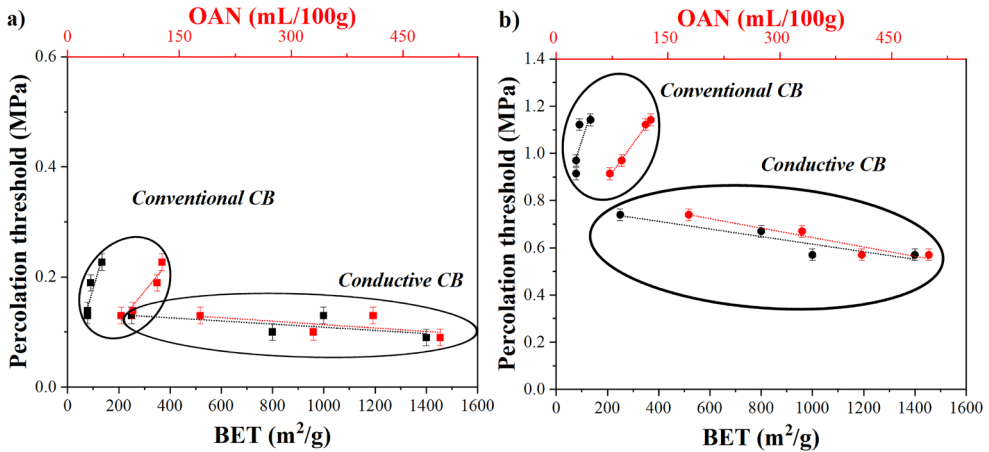

Figure 3 Determined percolation threshold based on Payne effect (a) uncured and (b) cured as a function of BET and OAN of the composites for carbon blacks.

6

6.3.3. Electrical conductivity and surface area correlation

To compare carbon blacks with different BET Specific Surface Areas SSA_{BET}, the same total effective surface area of carbon black particles dispersed in an elastomer was considered. It was calculated by considering the amount of CB and the effective volume fraction via the following equation:

$$Total\ effective\ surface\ area\ (m^2) =\ BET_{CB}\left(m^2/g\right) \cdot m_{CB}\ (g) \cdot \phi_{eff} \qquad (5)$$

where ϕ_{eff} and m are the effective volume fraction and the amount of carbon black. The concept of effective volume fraction of carbon black in elastomeric composites was firstly introduced by Medalia [23] and Kraus [24] and re-elaborated later by Wang et al. [25]. The value of the effective volume fraction is based on the concept of occluded rubber. Carbon black is present in elastomeric composites as aggregates and agglomerates. These aggregates and agglomerates include the occluded rubber that is shielded from any outside forces. Therefore, the occluded rubber is unable to deform under loading, influencing in turn electrical and mechanical properties of the composites. Therefore, the occluded rubber increases the effective volume fraction of the filler. It was found that the relationship between the effective volume fraction

and the volume fraction of the carbon black depends on the structure OAN of the carbon black, according to the following equation:

$$\phi_{eff} = \phi \; \frac{0.0181 \cdot OAN + 1}{1.59} \tag{6}$$

Consequently, this effective volume fraction results to be a factor that influences the volume fraction of the carbon black in the elastomeric composites.

Figure 4a presents the sigmoidal trends of the electrical conductivity with increasing total effective surface area of carbon blacks. Considering the total effective surface area as x-axis, the percolation plot is similar to the previous ones based on Payne effect data, as shown in Figures 2 and 3. This is because the total effective surface area indicates the total available carbon black surface area evaluated to be in contact with the elastomeric matrix in the composite. Thus, it is related to the entire filler network formed in the composite: The higher the specific surface area of the filler, the higher the filler-filler interactions and the lower the percolation threshold.

Figure 4b and Table 5 presents the percolation thresholds predicted by using the sigmoidal-Boltzmann equation as a function of BET and OAN of the carbon blacks. It is not possible to determine a trend correlating the values of percolation threshold in terms of total effective surface area and carbon blacks' properties. As described, the total effective surface area is an assumed value of available carbon black surface area to be in contact with the elastomeric matrix. For conventional carbon blacks N326, N330, N339 and N134, the critical values of total effective surface area increase with increasing specific surface area and structure of the fillers. The conductive carbon blacks, CCB and ECCB, appear to show similar values of total effective surface area resulting in a similar percolation threshold. However, Printex and UCCB have different values. Printex-based composites have an higher percolation threshold, probably due to the inferior dispersibility in the elastomeric matrix, as above-mentioned. UCCB-based composites have a lower percolation threshold. A possible explanation might be that for this carbon black, the specific surface area is very high and the amount in the composite is very low. The dispersion of the CBs with a relatively high specific surface area in elastomeric composite is increased only to a certain limit in the internal mixer. Note that the mixing quality is a crucial factor affecting the correlation, between the electrical conductivity and the total effective surface area and the outlier data point possibly for Printex might be due to its inferior dispersibility in the elastomeric matrix. Thus, it is worth remarking that carbon black grades require a sufficient dispersion level to reach the optimal possible performance.
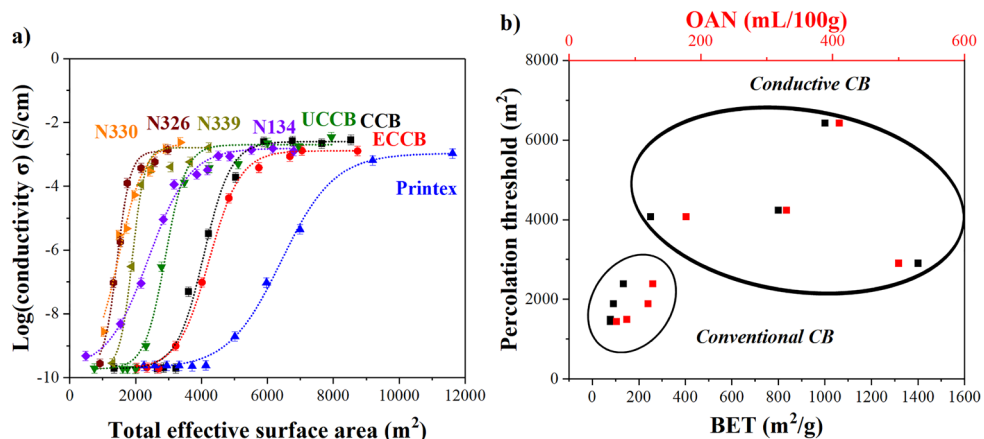
Figure 4   (a) Conductivity as a function of total effective surface area of carbon blacks with the sigmoidal-Boltzmann model, and (b) the determined percolation threshold as a function of BET and OAN for carbon blacks.

Table 5   Parameters of the sigmoidal-Boltzmann fitting according to the total effective surface area.

Parameters	N326	N330	N339	N134	CCB	ECCB	Printex	UCCB
A_1 (S/cm)	-9.72	-9.72	-9.72	-9.72	-9.72	-9.72	-9.72	-9.72
A_2 (S/cm)	-2.90	-2.65	-2.79	-2.81	-2.60	-2.89	-2.97	-2.70
Φ_c (m^2)	1440	1491	1890	2390	4070	4234	6419	2904
Δx	199.6	380.4	188.5	623.2	410.3	572.5	805.5	313.5
R^2 (adj)	98.7	96.7	98.1	99.4	98.6	99.8	99.7	99.0

6

6.3.4.   Mechanical properties of elastomeric composites

For tyre applications, elastomeric composites require specific properties and performance. This section presents the relationship between the mechanical properties of the investigated composites and the carbon blacks used.

Figures 5a and 5b show the tensile strength, reinforcement index M300/M100 and elongation at break, of the 25/75 NR/BR composites filled with carbon blacks at the amounts giving the same total surface area in the elastomeric composite, i.e. 7000 m^2. The conventional carbon blacks exhibit a stronger reinforcing effect than the conductive carbon blacks, as indicated by the higher tensile strengths and reinforcement indices. This is because at this given total surface area of the carbon blacks, the amounts of conductive carbon blacks are significantly smaller. As a result, the reinforcement of the composites is considerably reduced. In contrast to this, the conventional grades were added at relatively high volume fractions, at which the ultimate conductivity level has already been achieved.

Table 6 Carbon black amount (phr, volume fraction) of elastomeric composites at (I) equal total effective surface area of 7000 m^2 and at (II) the ultimate electrical conductivity.

CB types	(I) At the equal total surface area of 7000 m^2		(II) At the ultimate electrical conductivity	
	CB amount (phr)	CB volume fraction (v/v)	CB amount (phr)	CB volume fraction (v/v)
N326	85	0.230	85	0.230
N330	85	0.230	85	0.230
N339	75	0.210	75	0.210
N134	52	0.164	65	0.190
CCB	28	0.104	56	0.172
ECCB	9	0.038	18	0.072
Printex	7	0.031	14	0.058
UCCB	5	0.022	10	0.043

Table 6 confirms that conventional carbon blacks give the constant ultimate conductivity already at 7000 m^2, except for N134 as this carbon carbon black still requires a slightly higher amount to reach the optimum level. This implies that the filler network of conventional carbon blacks fully expands throughout the matrix, resulting in a greater extent of reinforcing interactions than that of the conductive carbon blacks (which have an under-expanded filler network). These reinforcing interactions contribute to the superior reinforcement of rubbers.

Figures 5c and 5d depict the composites with higher loadings of conductive and conventional carbon blacks. Even with only a small additional amount of ECCB, Printex and UCCB, the mechanical properties are significantly improved. This improvement can be attributed to their exceptionally high surface area and structure as discussed earlier. At this amount, conductive carbon black forms a conductive network allowing a good mechanical reinforcement as well. ECCB at 18 phr gives a comparable tensile strength to a reinforcing carbon black e.g. N330 at 85 phr. UCCB and Printex are required at considerably lower quantities, i.e. 10 and 14 phr, respectively, to achieve the ultimate conductivity. However, due to the relatively lower volume fractions of these two grades, the strength properties of the composites are inferior, based on less reinforcing rubber-filler interactions.
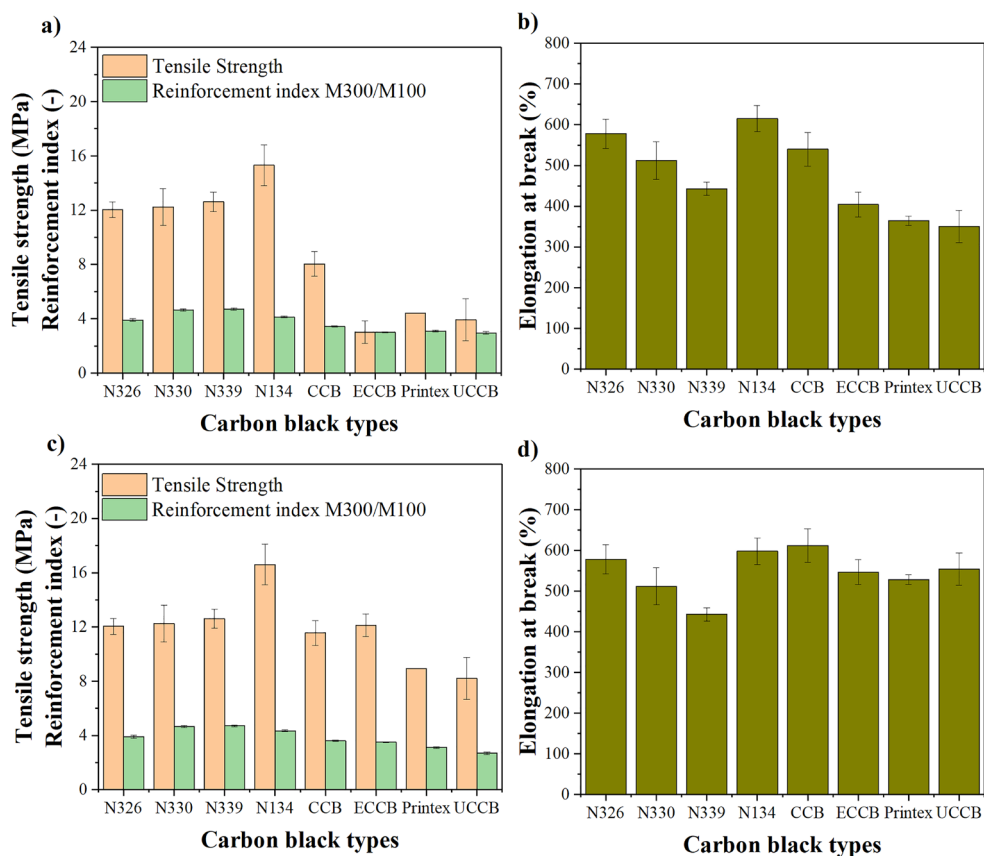
Figure 5 Tensile strength, reinforcement index and elongation at break of NR/BR blends at 25/75 filled with carbon blacks (a, b) at the same total effective surface area of 7000 m^2 and (c, d) at the ultimate of the conductive region.

6.3.5. SAXS measurement of elastomeric composites

SAXS measurement allows a structural analysis of elastomeric composites by measuring the intensities of an X-ray beam scattered by the composite. The filler network in elastomeric composites has a hierarchical structure with several characteristic length scales: Primary particles, aggregates composed of multiple primary particles and agglomerates formed by various aggregates. Figure 6a shows the scattered intensity $I(q)$ for the elastomeric composites filled with N134, CCB, ECCB and UCCB blacks as a function of wave vector q. Because the intensity $I(q)$ is proportional to the volume fraction of the scattered particle, $I(q)$ is normalised by the relative volume fraction of carbon black. The volume fractions of the investigated elastomeric composites are reported in Table 7. The curves show a clear trend with increasing filler amount in elastomeric composites. The intensity $I(q)/\phi_{CB}$

161

decreases with increasing volume fraction of the carbon blacks, since larger structural features are screened. In this plot, the scattering curve can be divided into three different structural levels identified by the slopes of the curves, according to the power law exponent in Figure 6.
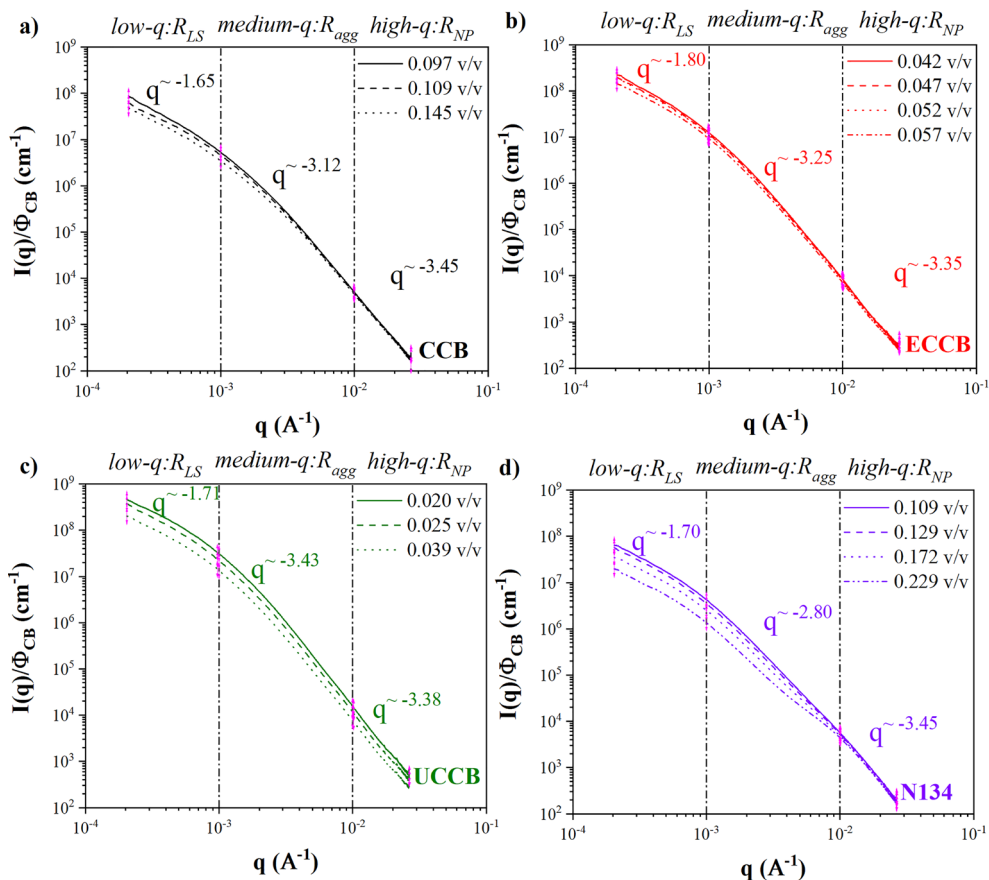

Figure 6 SAXS intensities as a function of wave vector q for (a) CCB, (b) ECCB, (c) UCCB and (d) N134 at different loading.

The high-q range (q higher than 10^{-2} A^{-1}) displays the surface scattering from the smallest hierarchical structure, the primary particle. In this region the power law exponent is -3.35 and -3.45, the slope represents the surface roughness of the primary particles. The higher the absolute value of the power law exponent is, the lower is the surface roughness of the carbon black. In this case, the investigated carbon black particles present an identical surface roughness. At around 10^{-2} A^{-1}, it is possible to notice a breakage in the slope, called Guinier knee [19]. This breakage is related to the radius of gyration of the primary particles. This medium-q range indicates the

scattering of the carbon black aggregates. The power law exponents of the elastomeric composites vary from -2.80 to -3.43. Also in this case, the exponents depend on the surface fractal dimensions of the aggregates. The higher the absolute value of this exponents becomes, the higher the surface fractal dimension is. With an increasing specific surface area of the carbon black, the exponent increases from -2.80 to -3.43. This is due to the fact that smaller carbon black primary particles are characterised by a much higher roughness for higher crystallite edges and a more pronounce surface energy [1]. Another breakage in slope, i.e. Guinier knee, is shown in this region, marking a change of slope at 10^{-3} A^{-1}. At the low-q range (q lower than 10^{-3} A^{-1}), the power law exponent represents the surface scattering from large scale structures. Thus, an agglomerate hierarchical structure of CB network is recognised. Different carbon black types present the same power law exponents and thus the same surface fractal dimensions at a large scale. The Guinier knee provides the possibility to measure the radius of the aggregates and primary particles. This concept is more explicit in the Kratky plot, obtained by plotting $q^2I(q)/\phi_{CB}$ versus q to analyse the CB structure quantitively [16,19]. Figure 7 shows the Kratky plots of the investigated composites. Here, it is possible to distinguish two peaks, between low and intermediate q and between intermediate and high q.

For the N134 CB type, these two peaks are more visible due to the lower surface area and the higher volume fraction of the filler in the composite. A further analysis of these two peaks gives information on the size of aggregates and particles as well. Thus, a Peak Analysis with OriginPro 2021b (OriginLab Corporation, Northampton, Massachusetts, USA) was carried out to determine the values of the radii according to Equation 3. The results are reported in Table 7. The primary particles of different carbon black grades in the composites measured by SAXS have a radius close to the supplier information. N134 grade has a particle size distribution between 15-18 nm and CCB around 14 nm, which are close to the calculated values in Table 7. ECCB and UCCB were in pellet form with 100 nm radius of aggregates; these values also match with the present finding. From the ratio of primary particle and aggregate radii of each carbon black type, the approximate number of particles per aggregate was calculated. The aggregates of conductive carbon blacks contain a higher number of particles per aggregate, implying a higher branched structure, shorter interparticle distances and a more extended filler network compared to the conventional counterparts.
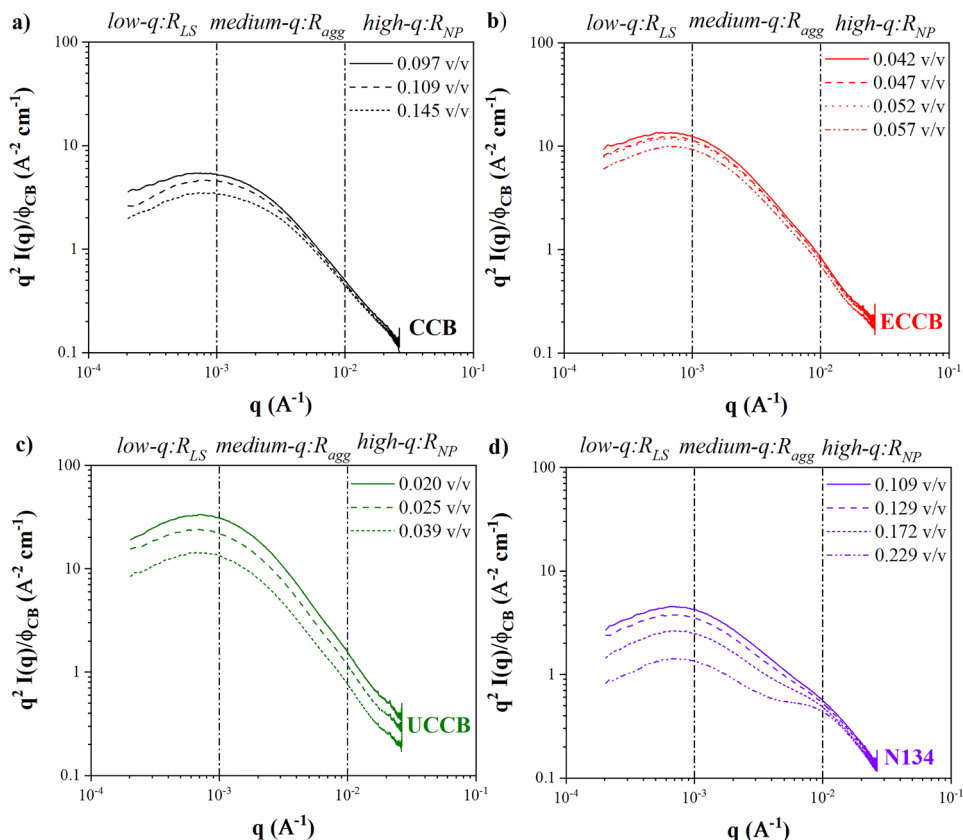
6

Figure 7 Kratky plot of the scattered intensities for peak analysis for (a) CCB, (b) ECCB, (c) UCCB and (d) N134.

One key conclusion can be drawn from these SAXS data. The hierarchical structure of the carbon blacks investigated in this work includes the primary particles with the size of 10-20 nm and the aggregates containing 5-10 primary particles (when considering the linear dimensions of the filler network). The particle and aggregate radii of the conductive carbon blacks reported in Table 7 are comparable for each investigated filler amount. However, the conventional carbon black N134 differs from the conductive carbon blacks CCB, ECCB and UCCB only in terms of surface fractal dimension and of the number of particles per aggregate. The different value of number of particles per aggregates for these two CB categories confirms the similar percolation threshold in terms of Payne effect for the conductive carbon blacks and its differences from the conventional carbon blacks.

Table 7 Parameters resulting from SAXS: Aggregates radius R_{agg}, primary particles radius R_{NP} and number of particles per aggregate N_{agg}.

CBs	Volume fraction ϕ [v/v]	R_{agg} [nm]	R_{NP} [nm]	N_{agg}	Graphical morphology of carbon blacks in elastomeric composites
N134	0.109	94.9	16.4	5.8	
	0.129	101.7	17.0	5.9	
	0.172	108.4	17.7	6.1	
	0.229	101.7	17.9	5.7	
CCB	0.097	100.1	13.1	7.6	
	0.109	95.5	10.4	9.1	
	0.145	94.4	12.5	7.6	
ECCB	0.042	90.4	12.3	7.3	
	0.047	95.8	13.2	7.3	
	0.052	94.1	13.4	7.1	
	0.057	107.5	15.2	7.1	
UCCB	0.020	103.1	10.9	9.5	
	0.025	102.7	10.4	9.9	
	0.039	106.1	11.3	9.4	

6.4.   Conclusions

Conventional and conductive carbon black categories were utilised as reinforcing fillers for elastomeric composites, and their electrical conductivity was investigated. The electrical conductivity was measured under dynamic deformations simulating tyre-rolling conditions. Initially, a percolation plot according to the classical percolation theory was constructed, taking into account the volume fraction of the filler in NR/BR blends at a 25/75 weight ratio. The percolation threshold values were determined using the mathematical sigmoidal-Boltzmann model. This model enabled a comparison of the percolation thresholds, slopes of percolating regions and ultimate values of dynamic electrical conductivity of the composites. The ultimate dynamic electrical conductivity was found to be the same for all types of carbon black. This confirms that, despite their different physical properties, all grades sufficiently form a conductive filler network that leads to comparable electron tunnelling bands inside the composites. The percolation rates and percolation thresholds were the primary variables in the percolation plots for all grades, as these two parameters depend on the specific surface area and structure of the carbon blacks.

This study reveals a sigmoidal trend in the correlation between dynamic electrical conductivity and the Payne effect. In the plot depicting electrical conductivity as a

6

function of Payne effect of the uncured composites, both conventional and conductive carbon blacks exhibit a similar onset of the percolation region. This implies that the conductivity at the onset of percolation region is independent of the carbon black type. The progression of conductivity within the percolation region, after the onset, is influenced by the dispersibility and active surface of carbon blacks. Thus, the percolation threshold based on Payne effect of uncured composites is in the range of 0.1 and 0.2 MPa. When plotting the conductivity as a function of Payne effect of cured composites, the onset of the percolation region for all carbon blacks does not coincide and exhibits a wider range compared to Payne effect of uncured composites. This discrepancy may be attributed to the effects of crosslinks and filler flocculation and reagglomeration. For the same reason, the percolation threshold based on Payne effect of cured composites for conventional and conductive blacks, after the onset, falls within a wider range of 0.6 and 1.1 MPa.

Moreover, based on the sigmoidal trends of conductivity with increasing total effective surface area of the carbon blacks, it is not possible to define a trend correlating the percolation threshold with the BET and OAN of carbon blacks. Conventional carbon blacks demonstrate an increasing percolation threshold with increasing specific surface area and structure, while conductive carbon blacks exhibit a similar value. This is because a certain dispersed surface area of carbon black is necessary to form a continuous conductive network in the elastomeric composites.

Conclusively, the SAXS measurements confirmed that the main differences between the two categories of carbon blacks lie in the surface fractal dimension of aggregates and the number of particles per aggregate which influence the filler network structure of various carbon black category types.

6.5. References

[1] M. Klüppel, The Role of Disorder in Filler Reinforcement of Elastomers on Various Length Scales, Adv. Polym. Sci. 164 (2003) 1–86. https://doi.org/10.1007/B11054.

[2] N. Probst, Conducting Carbon Black, Carbon Black. (2018) 271–288. https://doi.org/10.1201/9781315138763-8.

[3] M.E. Spahr, R. Gilardi, D. Bonacchi, Carbon Black for Electrically Conductive Polymer Applications, (2017) 375–400. https://doi.org/10.1007/978-3-319-28117-9_32.

[4] M.E. Spahr, R. Rothon, Carbon Black as a Polymer Filler, in: Polym. Polym. Compos. A Ref. Ser., Springer, Berlin-Heidelberg, Germany, 2016: pp. 1–31. https://doi.org/10.1007/978-3-642-37179-0_36-2.

[5] J. Kruželák, A. Kvasničáková, K. Hložeková, I. Hudec, Progress in polymers and polymer composites used as efficient materials for EMI shielding, Nanoscale Adv. 3 (2021) 123–172. https://doi.org/10.1039/D0NA00760A.

[6] B. Guo, Z. Tang, L. Zhang, Transport performance in novel elastomer nanocomposites: Mechanism, design and control, Prog. Polym. Sci. 61 (2016) 29–66. https://doi.org/10.1016/J.PROGPOLYMSCI.2016.06.001.

[7] M.C.V. Omelan, A. Diekmann, U. Giese, Development of soft electrical conductive PDMS/CNT-Composites with extremely low CNT Content, KGK Kautschuk Gummi Kunststoffe. 73 (2020) 22–30.

[8] Z. Yang, S. Zhou, J. Zu, D. Inman, High-performance piezoelectric energy harvesters and their applications, Joule. 2 (2018) 642–697. https://doi.org/10.1016/j.joule.2018.03.011.

[9] C. Mangone, W. Kaewsakul, M. Klein Gunnewiek, A.P.J. van Swaaij, L. Reuvekamp, J.W.M. Noordermeer, A. Blume, Design and performance of flexible polymeric piezoelectric energy harvesters for battery-less tyre sensors, Smart Mater. Struct. 31 (2022) 095034.

[10] C. Mangone, W. Kaewsakul, A.P.J. van Swaaij, K. Bandzierz, M.K. Gunnewiek, A. Blume, Dynamic measurement setups for validating piezoelectric energy harvesters in driving conditions, Polym. Test. 119 (2023) 107932. https://doi.org/10.1016/J.POLYMERTESTING.2023.107932.

[11] Y. Nakaramontri, S. Pichaiyut, S. Wisunthorn, C. Nakason, Hybrid carbon nanotubes and conductive carbon black in natural rubber composites to enhance electrical conductivity by reducing gaps separating carbon nanotube encapsulates, Eur. Polym. J. 90 (2017) 467–484. https://doi.org/10.1016/J.EURPOLYMJ.2017.03.029.

[12] C. Mangone, W. Kaewsakul, K. Bandzierz, M.K. Gunnewiek, A. Blume, Key factors affecting dynamic electrical conductivity of elastomeric compounds, Prep. (2023).

6

[13]   Payne AR, Whittaker RE, Low strain dynamic properties of filled rubbers, Rubber Chem. Technol. 44 (1971) 440–478. https://doi.org/10.5254/1.3547375.

[14]   T. Narayanan, M. Sztucki, T. Zinn, J. Kieffer, A. Homs-Puron, J. Gorini, P. Van Vaerenbergh, P. Boesecke, Performance of the time-resolved ultra-small-angle X-ray scattering beamline with the Extremely Brilliant Source, J. Appl. Crystallogr. 55 (2022) 98–111.
        https://doi.org/10.1107/S1600576721012693/JL5029SUP1.PDF.

[15]   G. Beaucage, H.K. Kammler, S.E. Pratsinis, Particle size distributions from small-angle scattering using global scattering functions, Urn:Issn:0021-8898. 37 (2004) 523–535. https://doi.org/10.1107/S0021889804008969.

[16]   G.P. Baeza, A.C. Genix, C. Degrandcourt, L. Petitjean, J. Gummel, M. Couty, J. Oberdisse, Multiscale filler structure in simplified industrial nanocomposite silica/SBR systems studied by SAXS and TEM, Macromolecules. 46 (2013) 317–329. https://doi.org/10.1021/ma302248p.

[17]   N. Gundlach, R. Hentschke, Modelling Filler Dispersion in Elastomers:Relating Filler Morphology to Interface Free Energiesvia SAXS and TEM Simulation Studies, Polymers. 28 (2018) 446. https://doi:10.3390/polym1004044.

[18]   F. De Geuser, A. Deschamps, Precipitate characterisation in metallic systems by small-angle X-ray or neutron scattering, Comptes Rendus Phys. 13 (2012) 246–256. https://doi.org/10.1016/J.CRHY.2011.12.008.

[19]   N. Warasitthinon, A.C. Genix, M. Sztucki, J. Oberdisse, C.G. Robertson, The Payne effect: Primarily polymer-related or filler-related phenomenon?, Rubber Chem. Technol. 92 (2019) 599–611.
        https://doi.org/10.5254/RCT.19.80441.

[20]   G.G.A. Böhm, M.N. Nguyen, Flocculation of carbon black in filled rubber compounds. I. Flocculation occurring in unvulcanized compounds during annealing at elevated temperatures, J. Appl. Polym. Sci. 55 (1995) 1041–1050. https://doi.org/10.1002/APP.1995.070550707.

[21]   G. M., N. L., Y. H. H., O. C. P., Flocculation in Carbon Black Filled Rubber Compounds, in: KGK Kautschuk Gummi Kunststoffe, 2002: pp. 596–604.

[22]   J. Kadlcak, L. Tunnicliffe, B. James, L. Jorge, C. Roman, K. Ivo, Evaluation of Carbon Black Flocculation in Natural Rubber Melts, in: RubberCon, 2014: pp. 1–9.

[23]   A.I. Medalia, Morphology of aggregates: VI. Effective volume of aggregates of carbon black from electron microscopy; Application to vehicle absorption and to die swell of filled rubber, J. Colloid Interface Sci. 32 (1970) 115–131. https://doi.org/10.1016/0021-9797(70)90108-6.

[24]   Kraus G, A Carbon Black Structure-Concentration Equivalence Principle. Application to Stress-Strain Relationships of Filled Rubbers, Rubber Chem. Technol. 44 (1971) 199–213. https://doi.org/10.5254/1.3547354.

[25]   M.J. Wang, S. Wolff, E.H. Tan, Filler-Elastomer Interactions. Part VIII. The Role of the Distance between Filler Aggregates in the Dynamic Properties of Filled Vulcanizates, Rubber Chem. Technol. 66 (1993) 178–195. https://doi.org/10.5254/1.3538305.z

6

Chapter 7

Flexible lead-free ferroelectric composites: processing parameters and effect of elastomer polarity

The interest in energy harvesting technology is steadily growing in the field of self-powered wireless sensors for smart tyres. The purpose of this study is to prepare a flexible piezoelectric composite having a potential to store the energy dissipated in tyres. In this work, the effect of elastomer polarity on piezoelectric coefficient of piezoelectric composites including lead-free $K_{0.5}Na_{0.5}NbO_3$ (KNN) ferroelectric ceramic in elastomeric matrix was investigated. The investigated elastomers were Epoxidised Natural Rubbers (ENRs) with 25 and 50 mol% of epoxide content, and acryloNitrile Butadiene Rubbers (NBRs) with 28, 41 and 50 wt% of acrylonitrile content. Processability, curing behaviour, contact poling process and piezoelectric properties of the elastomeric composites based on those different elastomers filled with 30 vol% of KNN were analysed. The morphology of KNN in the composites, analysed by Scanning Electron Microscope (SEM) and X-Ray Diffraction (XRD), confirmed the unchanged crystalline structure of KNN in the elastomeric composites. With an increasing elastomer polarity, the dielectric constant of the matrix increases, resulting in a higher piezoelectric constant. Additionally, the higher dielectric constant and electrical conductivity of the elastomer enhance also the efficient of the poling process. Apart from the improved electrical properties of the composites when increasing the elastomer's polarity, the overall properties and experimental evidence confirm the enhancement in interfacial interactions between KNN and the investigated polar elastomers.

7

Chapter 7

7.1.   Introduction

Piezoelectric materials have drawn tremendous attention in the field of smart sensors and renewable energy for their potential to generate electrical energy by material deformation under mechanical forces. They can be applied as sensors and energy harvesters [1-3]. Materials with non-centrosymmetric crystalline structures and with a lack of an inversion centre show a piezoelectric effect. When deformed, a dipole moment is formed in the structure of such a material, resulting in one-positively and one-negatively charged sides. By applying electrodes on both sides on the material under deformation, a flow of electrical current is generated, and thus the material functions as an energy harvester [4-7]. With this attractive feature, piezoelectric materials can power sensors, ensuring autonomous operations of the systems. One of the most profitable stakeholders of this mechanism is the automotive industry [1,2,8,9]. An increasing number of sensors are being integrated into tyres to monitor real-time performance of the tyres. During driving the vehicles, tyres are continuously subjected to dynamic deformations as well as vibrations and excitations due to tyre-road contact interactions. Hence, this tyre-running operation is considered as a good condition for activating piezoelectric materials.

There are two different categories of piezoelectric materials: Polymers and ceramics. In Chapter 4, an energy harvester comprising the piezoelectric polymer PolyVinyliDene diFluoride (PVDF) and an elastomeric electrode in a sandwich-like structure was developed [10,11]. Chemical adhesion between the two components ensured a flexible and stable harvester able to generate 28 mW in a lab-scale by using a setup simulating the rolling tyre conditions [12]. These studies showed promising results towards the use of a piezoelectric polymer for tyre applications. However, PVDF as a thermoplastic polymer can represent an inconvenience for real-tyre applications in terms of flexibility and durability. The current research proposes the search for an alternative piezoelectric material for tyre applications. Piezoelectric ceramic is not favourable for this due to its brittleness [13,14]. Piezoelectric composites have been researched and analysed for their advantages of combining the mechanical flexibility of a polymer matrix and the high piezoelectric properties of a ceramic filler [5,15].

Piezoelectric composites include a piezoelectric ceramic particulate in a polymeric matrix. Their properties can be tailored according to the requirements of the desired application by selecting the proper polymer matrix, the filler type and varying the volume fraction of polymer and filler [16,17]. A piezoelectric ceramic can have a single crystal or a polycrystalline structure. The first type, the single crystal ceramic,

shows a spontaneous polarisation throughout the composite, aligning in the same direction under deformation. Polycrystalline ceramics are characterised by grains with dipole moments randomly oriented. These piezoelectric composites are classified as ferroelectric materials as their spontaneous polarisations can be oriented in a certain direction by applying a high electrical field and thus aligning the dipole moments [18-20]. This process is called poling process, and the direction of which the dipoles are aligned is the poling direction. The poling process depends on the polymer properties. Particularly, the electrical field applied during the poling process acting on ferroelectric particles is influenced by the dielectric constant and the electrical conductivity of the polymer matrix [18-20]. On one hand, the dielectric constant of the polymer matrix represents its ability to store electric charges during exposure to an electric field. Thus, a higher dielectric constant normally implies a better polarisation. However, an increase in the dielectric constant may indicate an increase in the dielectric loss, resulting in an energy dissipation in the form of heat and thus reducing the strength of the electrical field applied on the ferroelectric ceramic. On the other hand, the electrical conductivity represents the ability of the polymer to conduct electric current. Generally, a low electrical conductivity is desired to avoid any electrical field dissipation. The poling time strongly depends on these two properties of the polymeric matrix. It can vary from 20 hours to few hours, according to the electrical properties of the polymer matrix. It is important to control the poling parameters to achieve the desired poling efficiency, as well as the desired piezoelectric coefficients.

7

Another important aspect to consider for piezoelectric composites is their operational temperature. Each polycrystalline ferroelectric ceramic is characterised by a temperature, known as Curie temperature, below which the material presents a non-centrosymmetric structure and can be polarised. Piezoelectric ceramic and composites are known to have a Curie temperature higher than 200°C. This factor makes ceramic-based composites much more favourable for the tyre application compared to the piezoelectric polymers having a Curie temperature of around 100-140°C [21,22]. This is due to the fact that the manufacturing temperature of tyres is in the range of 160 to 180°C.

Various works have been emphasising the high performance of Lead Zirconate Titanate with the chemical symbol $PbZr_xTi_{1-x}O_3$ and known as PZT [1]. The magnitude of the piezoelectric effect is described by the piezoelectric coefficient d_{ij}. It corresponds to the polarisation generated per unit of an external applied force. Its two indices i and j indicate the polarisation direction and the direction of applied

mechanical deformation, respectively. This ceramic reaches the value for the piezoelectric coefficient d_{33} in the range of 200-800 pC/N with its Curie temperature in the range of 200-360°C [23-26]. However, the substance Pb is classified by European Community REACH regulation 1907/2006/EEC as Substance of Very High Concern (SVHC). Therefore, lead-free alternatives have been investigated and developed. Among those, $K_xNa_{1-x}NbO_3$ (KNN) has attracted a high interest for its high piezoelectric coefficient, high Curie temperature and its potentially adequate dispersibility in the polymeric composites [27-29].

There are several works investigating the use of different types of ceramics in polymeric matrices like polyurethane [30,31], epoxy [31-33], polyimide [34], etc. In all these works, the piezoelectric coefficient of the composites reached the values of 25-30 pC/N. Besides the properties of the ceramics, the matrix properties like viscosity, microstructures, as well as its compatibility with the filler are crucial for piezoelectric composites. The polymeric matrix plays a vital role in the piezoelectric efficiency of composites. Stuber et al. [31,35] studied different types of ferroelectric ceramics: $BaTiO_3$ (BT), $K_{0.5}Na_{0.5}Li_{0.03}NbO_3$ (KNLN) and $PbZrTiO_3$ (PZT) in polymers such as polyurethane, epoxy resin and PolyDiMethylSiloxane (PDMS). The main conclusion from this work was that the conductivity of the matrix affects the poling process. After only 10 minutes of poling, the composites were fully polarised and reached a high value of the piezoelectric coefficient. Studies on modelling the behaviour of composites at varying volume fractions of ceramic confirmed that the dielectric constant of the matrix also plays an important role [36,37].

Few investigations have been done on natural and synthetic elastomers. Promsawat et al. [38] prepared piezoelectric composites based on Natural Rubber (NR) and varying amount of polycrystalline $Pb(Mg_{0.65}Nb_{2/3})_{0.65}Ti0_{.35}0_3$ (PMNT) from 60 to 150 phr. Composites were mixed in an internal mixer. After having cured them at their optimal curing times, a contact poling was applied with an electrical field of 2.5 kV/mm for 30 min at 60°C. This work showed that the contact poling of these elastomeric composites results in an increase in the output voltage from 1 to 2 V. Other authors prepared the same composites, results showed that NR filled with 100 phr of PMNT reached only 0.00021 pC/N [39]. Up to now, a piezoelectric composite including a synthetic and natural rubber has not optimally been developed.

Therefore, this study aims to investigate the piezoelectric composites based on elastomers with different polarity levels, i.e. Epoxidised Natural Rubber (ENR) and Nitrile Butadiene Rubber (NBR) filled with ferroelectric ceramic $K_{0.5}Na_{0.5}NbO_3$

(KNN). The effects of the elastomer properties on the piezoelectric performance were examined. The processability, poling process, the piezoelectric, dielectric, and mechanical properties of the composites were analysed. The morphology of KNN in the elastomeric composites were analysed by using SEM-EDX and XRD.

7.2. Experimental

7.2.1. Materials

The elastomers used were: Epoxidised Natural Rubbers (ENRs) with 25 and 50 mol% of epoxide content (ENR-25, Wurfbain Nordmann B.V., Zaandam, the Netherlands, and ENR-50, Muang Mai Guthrie Public Co. Ltd., Phuket, Thailand); and acryloNitrile Butadiene Rubbers (NBRs) with 28, 41 and 50 wt% of acrylonitrile groups (NBR-28, NBR-41 and NBR-50, Zeon Europe GmbH, Düsseldorf, Germany). Physical and chemical properties of the elastomers are reported in Table 1. As ferroelectric ceramic, $K_{0.5}Na_{0.5}NbO_3$ (KNN) from American Elements (Los Angeles, California) was used. The particle size of KNN was in the range of 1-10 µm.

Other compounding ingredients were of technical quality:
- Tall oil (Sylvatal^{TM} 25/30S, Arizona Chemical B.V., Almere, Netherlands);
- Stearic acid (Edenor ST1 GS, Emery Oleochemicals GmbH, Düsseldorf, Germany)
- Zinc Oxide (ZnO), (Merck & Co, Darmstadt, Germany)
- α-Sulphur (Eastman Chemical Corporation, Langenfeld, Germany)
- N-Tert-Butyl-Benzothiazole Sulfenamide (TBBS), (Rhenogran TBBS-80, Lanxess Deutschland GmbH, Cologne, Germany).

7

Table 1   Physical and chemical properties of the elastomers ENRs and NBRs.

Elastomers	Epoxide/Nitrile content	Mooney viscosity, ML (1+4) 100°C (MU)
ENR-25	25 mol% epoxide	81.4
ENR-50	50 mol% epoxide	80.0
NBR-28	28 wt% acrylonitrile	50.0
NBR-41	41 wt% acrylonitrile	62.5
NBR-50	50 wt% acrylonitrile	77.5

7.2.2. Sample preparation

All the composites were prepared using a two-stage mixing procedure. A masterbatch was prepared in an internal mixer (Brabender Plastograph EC Plus,

Brabender GmbH & Co KG, Germany), with a starting temperature of 60°C and a fill factor of 75%. The rotor speed and mixing time were 100 rpm and 6.2 min, respectively. The general formulations of the composites are reported in Table 2.

Table 2   Elastomeric composite formulations.

Ingredients	Amount (phr)
Rubber	100
KNN	Variable
Tall oil	6
Stearic acid	2
ZnO	5
α-Sulphur	1.5
TBBS	1.8

Rubber was initially masticated for 1 min. KNN was firstly divided in two portions, and then pre-dispersed in tall oil and added to the mixer after the rubber mastication. Each portion of KNN-premixed tall oil was mixed for 2 min. For the remaining 1.2 min, ZnO and stearic acid were added and mixed. All the masterbatches were discharged from the internal mixer and sheeted out on a two-roll mill for 2 min at 1 mm nip width of the rolls (Polymix 80 T, Schwabenthan-Maschinen GmbH & Co. KG, Berlin, Germany). Then, the masterbatches were conditioned at ambient temperature for 24 h before the incorporation of sulphur and TBBS in the second mixing stage was done on the roll mill at a low temperature of 50°C for 5 min.

The curing characteristics of the composites were analysed using a Rubber Process Analyser (RPA 2000, Alpha Technologies, Ohio, USA). Each measurement was carried out for 20 min at 170°C, a frequency of 1.667 Hz and an oscillating shear angle of 0.5°. The composites were cured at 100 bar in a Wickert press WLP 1600 (Wickert Maschinenbau GmbH, Landau, Germany) to their t_{c90} at 170°C.

7.2.3.   Sample characterisations

KNN particles were analysed using a Scanning Electron Microscopy (SEM) conducted by Zeiss Merlin HR-SEM (Oberkochen, Germany). KNN particles were firstly dispersed in ethanol with a sonicator and then analysed by HR-SEM.

To homogenise the KNN particles, a grinding process was carried out. 10 g of KNN powder was mixed in 30 g of stainless-steel balls with 1 mm diameter and 30 g of stainless-steel balls with 3 mm diameter. This was mixed for 48 h in a ball miller with a rotation speed of 200 rpm. The KNN particles were analysed after this grinding process using the HR-SEM.

After having mixed and vulcanised the KNN-based composites, X-Ray Diffraction (XRD) and SEM - Energy-Dispersive X-ray spectroscopy (SEM-EDX) were carried out for elastomeric composites including ENR-25, NBR-28 and NBR-50 filled with 30 vol% KNN. For a clear investigation of the morphology of these elastomeric composites, all the composites were fractured in liquid nitrogen without coating.

The crystallographic properties of ENR-25, NBR-25, NBR-41 and NBR-50 filled with 30 vol% KNN were analysed using an X-Ray Diffraction (XRD) with a high-resolution Bruker D8 Discover XRD (Leiderdorp, the Netherlands), Cu-Kα_1 radiation (wavelength of 1.54 Å) and an Eiger2 R 500K area detector. Samples were 1 mm thick. The θ–2θ scans were performed with a step size of 0.01° and a counting time of 1 s per step. Three measurements were done for each composite.

Afterwards, a contact poling process was applied to the vulcanised elastomeric composites in cylindrical shape of 20 mm diameter and 1 mm thickness. Gold electrodes were sputtered through a shadow mask on both sides of the cylindrical composites with a sputter coater (QuorumQ300T, East Sussex, UK). The poling took place in a silicone oil bath at a temperature of 25°C for variable times from 2 to 120 min and varying electric fields from 1 to 12 kV/mm. A silicone oil bath was used for its high dielectric strength, preventing arcing at the surface of the specimen, and its high thermal properties, implying a good temperature-controlled system. An electrical field was generated by a DC high voltage amplifier (Heinzinger, PNC 30000, Rosenheim, Germany). The composites were conditioned for at least 24 h before further measurements.

7

In this study, d_{33} was measured, as the composite was deformed in the same direction as the applied electric field. The d_{33} of poled composites was measured using PM300 Berlincourt type piezometer (Piezotest, London, United Kingdom) with a static force of 0.6 N and a sinusoidal deformation of 0.25 N at 110 Hz.

Conductivity and the dielectric constant of gum rubbers and elastomeric composites were measured using a Broadband Dielectric Spectrometer BDS with an Alpha-A high performance frequency analyser produced by Novocontrol Technologies (Montabaur, Germany). Composites specimens were in cylindrical shape with a dimension of 0.5 mm thickness and 15 mm diameter. Frequency sweeps from 10^{-1}-10^4 Hz at 25°C were carried out.

Tensile tests were performed using a Zwick tensile tester (model Z1.0/TH1S, ZwickRoell GmbH & Co. KG, Haan, Germany) with dumbbell-shaped specimens (type 2) at a crosshead speed of 200 mm/min according to ASTM D412.

7.3.   Results and discussion

7.3.1.   KNN morphology

Figure 1 shows the SEM micrographs of KNN particles at different magnifications. The filler particles have a wide particle size distribution, that is in the range of 0.2-2 µm. Due to the irregular shape of KNN, it was not possible to accurately calculate the exact dimensions of the particles. However, it is possible to distinguish two main portions: One with particle sizes around 0.2-0.4 µm and another one with 1-2 µm.
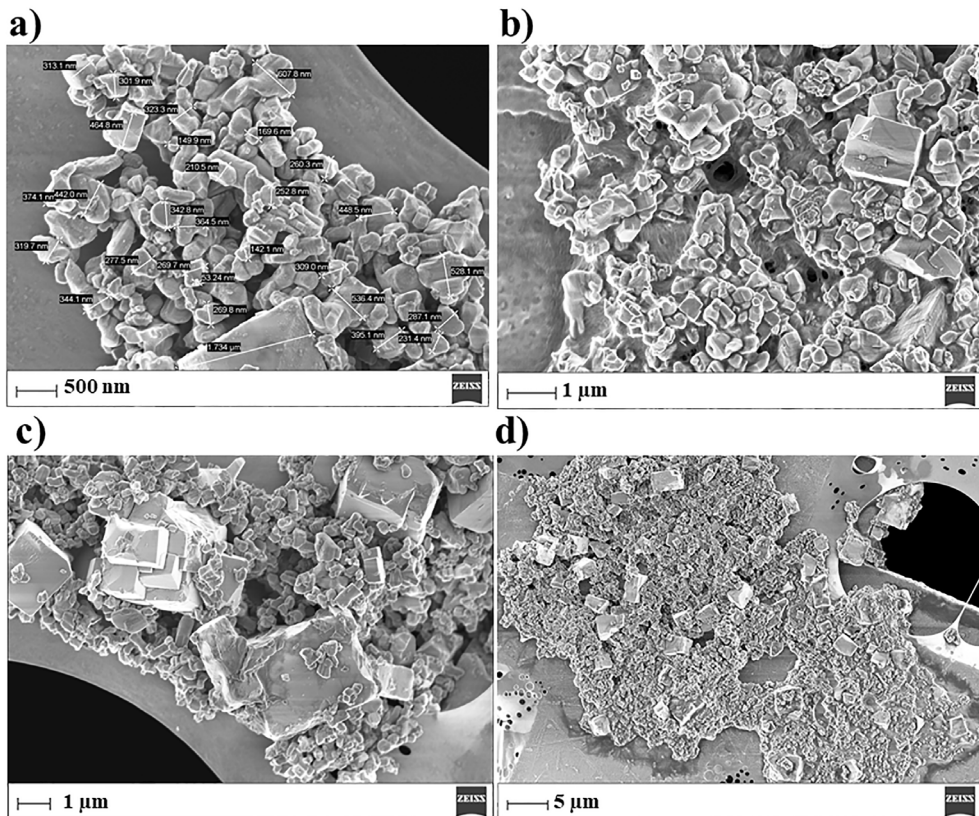

Figure 1   SEM micrographs of KNN particles at magnifications.

Figure 2a and b reports the SEM micrographs and the piezoelectric coefficients of NBR-50 filled with 10 vol% of ground KNN. After the grinding process, the KNN particle size was reduced. NBR-50 filled with 10 vol% of both ground and non-ground KNN particles was mixed in an internal mixer and polarised under optimal poling conditions.

a)

b)
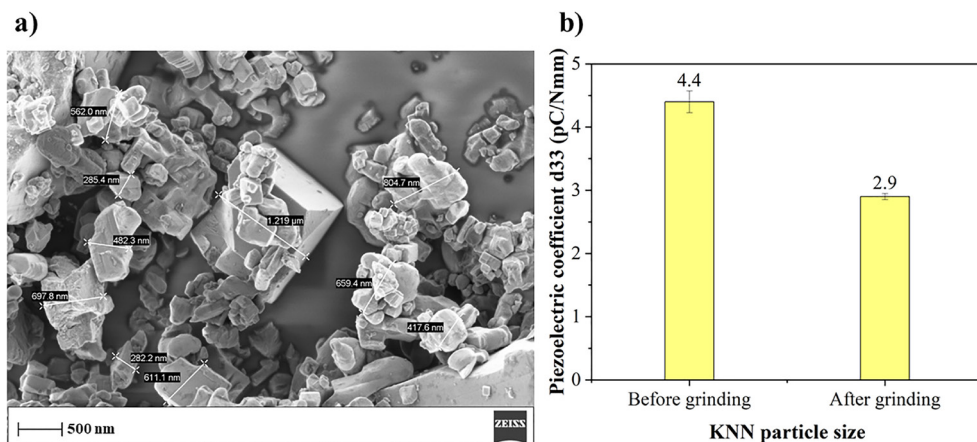
Figure 2   (a) SEM micrographs of KNN particles after grinding at magnifications of 50000x; (b) Piezoelectric coefficient of NBR-50 filled with 10 vol% of ground and non-ground KNN.

According to the literature, the larger particle sizes of KNN contribute to a higher piezoelectric activity and the smaller particle sizes contribute to an increased dielectric constant of the composites. The piezoelectric coefficient d_{33} decreases with a decreasing particle size due to a decreasing poling process efficiency [40,41]. The piezoelectric composites need to be polarised by applying a high electrical field which results in a net dipole moment. Larger particles are characterised by a lower interaction with polymeric chains, implying a higher interaction among the particles themselves, and so a higher electronic transmission during the poling. Thus, the particle size is directly connected to the poling efficiency: The larger the particle size is, the better the poling process becomes. Particles with a smaller size but higher surface area have a higher tendency to increase the dielectric constant of the composites due to the high polarity. Overall, the higher dielectric constants of composites still influence the optimum piezoelectric properties, as described later by Yamada's model (see Equation 1). However, the influence of the surface area is less significant for the poling efficiency compared to the effect of larger particle sizes. Hence, the effect of the larger particle sizes is the key factor contributing to the increased piezoelectric coefficient.

7.3.2.   Morphology of KNN-based elastomeric composites

X-ray diffraction patterns of different elastomer types (ENR-25, NBR-28, NBR-41 and NBR-50) are presented in Figure 3. Each pattern is normalised to the highest intensity peak. It is confirmed that KNN has an orthorhombic crystal symmetry, known as perovskite. This phase is indexed as KNN ($K_{0.5}Na_{0.5}NbO_3$ ICSD collection code: 186333, reported by the analyser software). In the plots, the peaks of the crystal

facets are shown. Between 20 and 30 degrees, small peaks are present in all elastomeric composites probably due to the presence of a secondary phase. In conclusions, the crystal structure of KNN can be found in all elastomeric composites meaning that it resists the production process of the elastomeric composites.
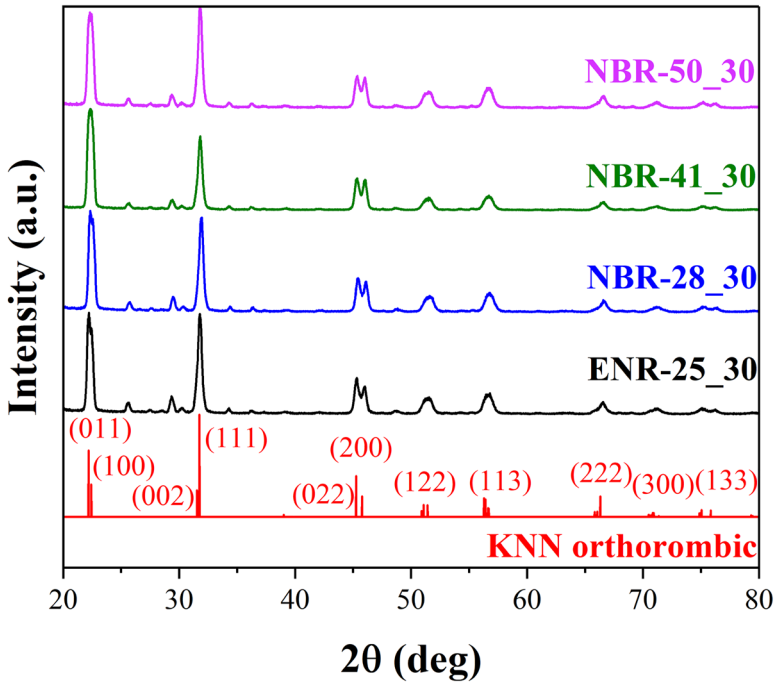

Figure 3   X-ray diffraction pattern of elastomeric composites including ENR-25, NBR-28, NBR-41, NBR-50 filled with 30 vol% of KNN.

SEM and SEM-EDX were then carried out to analyse the morphology of the elastomeric composites and the KNN dispersion in the elastomer matrices. Figure 4 shows the SEM images of the three selected elastomeric composites: ENR-25 (Figure 4a), NBR-28 (Figure 4b) and NBR-50 (Figure 4c) filled with 30 vol% of KNN. In these images, the particle size distribution of KNN fits to the SEM images of the pure KNN particles in Figure 1. In all three elastomer matrices, it is possible to distinguish two main portions of KNN: One with particle sizes around 0.2-0.4 µm and another one with 1-2 µm. Moreover, all three elastomer matrices have similar

KNN dispersion degrees. This may imply similar interfacial interactions between KNN and the elastomers. This aspect is further evaluated by the EDX technique.
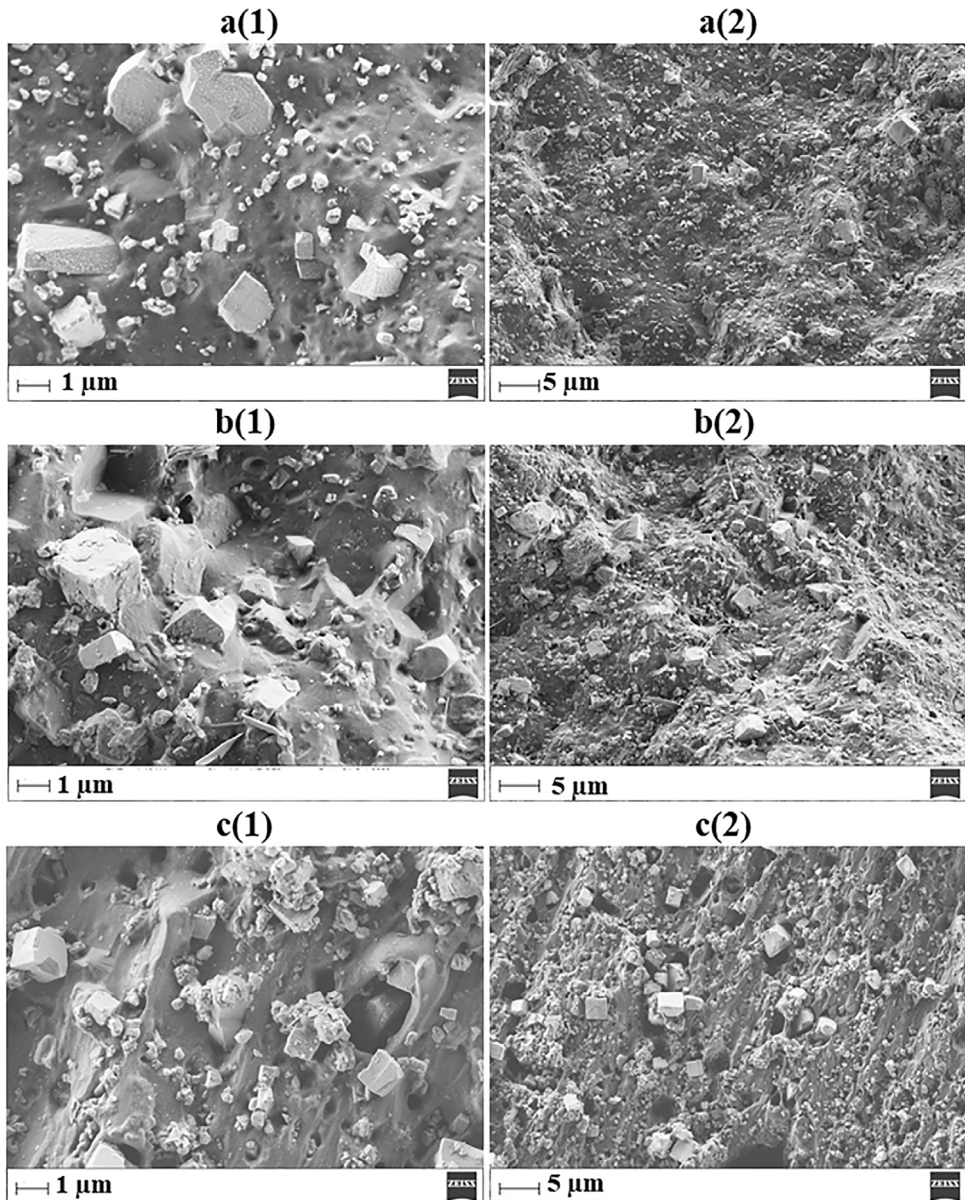
Figure 4   SEM images of (a) ENR-25, (b) NBR-28 and (c) NBR-50 filled with 30 vol% of KNN at magnifications.
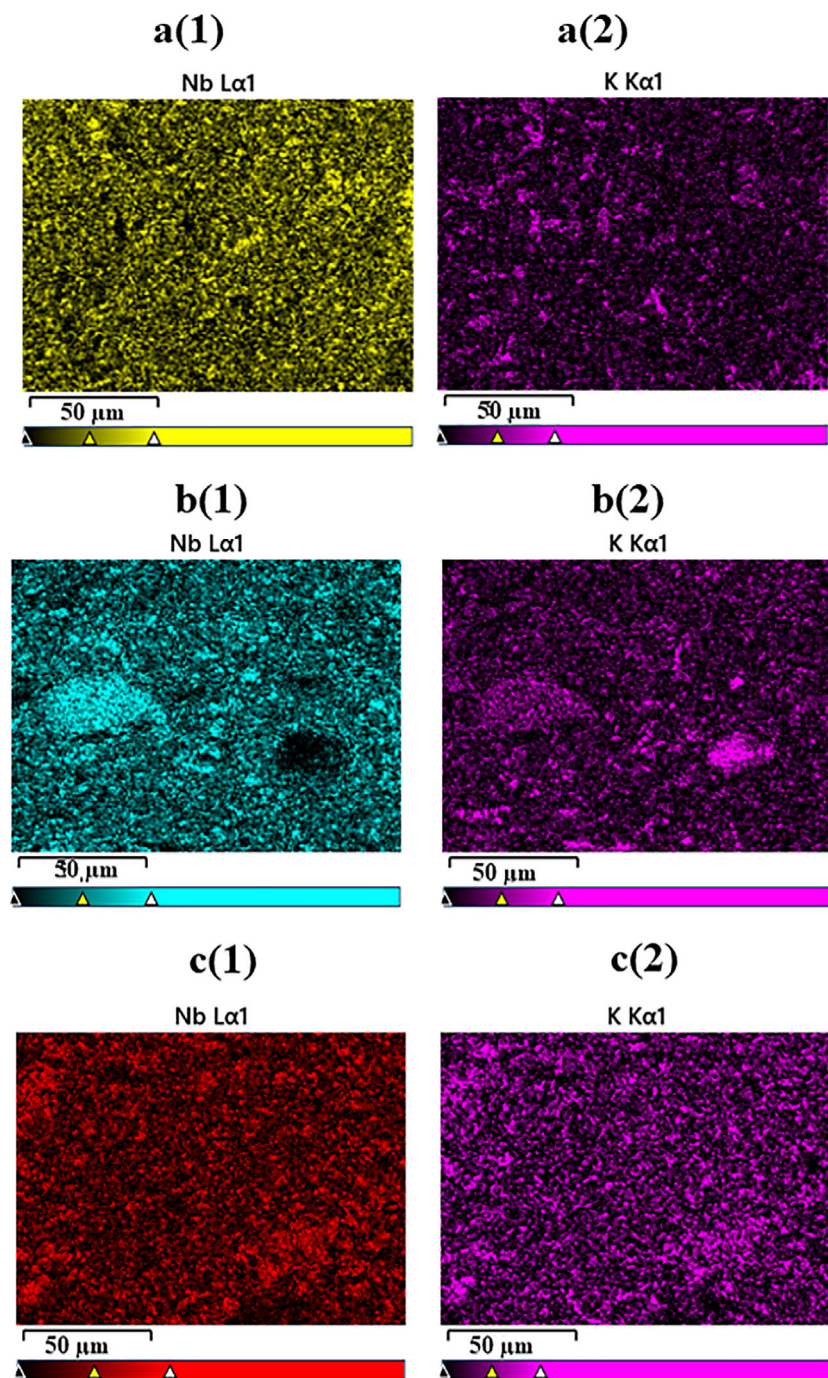
Figure 5   SEM-EDX maps illustrating the distributions of (1) Nb Lα and (2) K Kα in (a) ENR-25, (b) NBR-28 and (c) NBR-50 filled with 30 vol% of KNN.

Figure 5 shows the distributions of niobium Nb (column 1 of Figure 5), and potassium K (column 2 of Figure 5) of KNN particles, which were examined with SEM-EDX to measure the intensity of the Lα as well as Kα line across the elastomeric composites. L and K are the outermost shell of the respective atoms (Nb and K) from which the electron is ejected due to the X-rays.

It is possible to visualise the good dispersion level of Nb and K particularly for ENR-25 and NBR-50. A higher agglomeration tendency is visible in NBR-28. This can be potentially attributed to the lower viscosity of NBR-28. With increasing the acrylonitrile groups in NBR, the dispersion is improved which might be attributed to the better compatibility due to the polarity matching between NBR-50 and KNN.

In the following sections, other properties of the elastomeric composites, i.e. the viscosity and their mechanical properties, are discussed to confirm the compatibility between the KNN and the elastomers.

7.3.3. Processability and curing behaviour

The mixing footprints showing the mixing torque and temperature curves of the composites based on ENRs and NBRs with 30 vol% of KNN are presented in Figure 6.
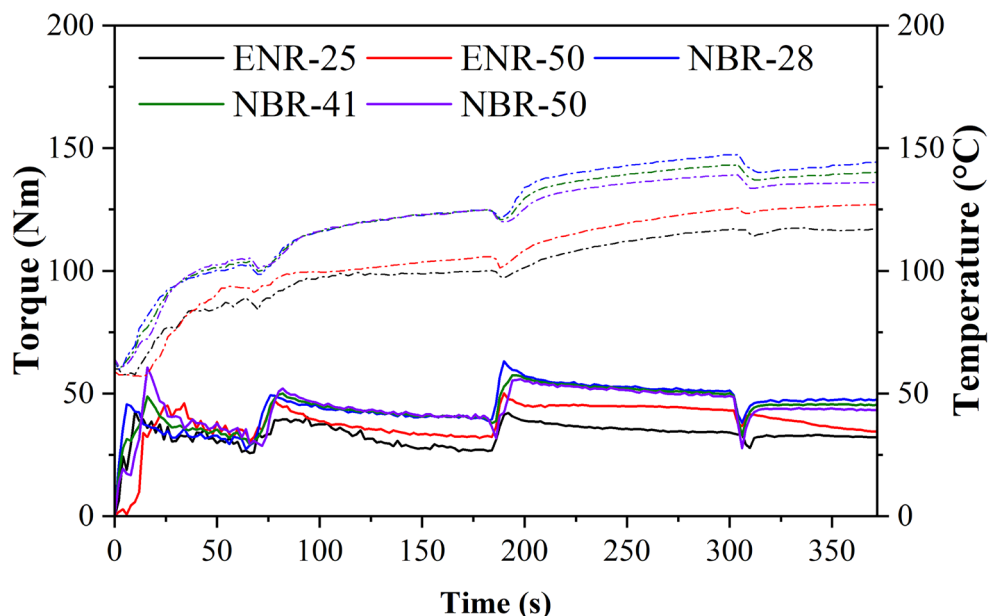
Figure 6   Masterbatch mixing torque (solid line) and temperature (dashed line) of ENRs and NBRs composites with 30 vol% of KNN.

During the rubber mastication in the first minute, all mixing torques show similar trends for all elastomer types. After rubber mastication, KNN and the plasticiser were added to the internal mixer in two portions. The initial rise of the torque is referred to the incorporation stage of KNN in the elastomer, followed by a progressively lowered torque due to deagglomeration and further dispersion of the filler particles. The heat generation from this mixing process results in the elevated mixing temperatures.

In comparison to the NBR-based composites, the ENR composites show a lower final mixing torque and batch temperature to disperse KNN particles, despite the higher viscosities of raw ENRs compared to raw NBRs. This might be due to the better compatibility between ENRs and KNN than ENRs and NBRs. This result is in line with the SEM-EDX images (Figure 5) illustrating the better dispersion of the ENR-25 composite compared to NBR-28. However, with increasing amount of polar functional groups, the elastomeric composites show the following trend: ENR-50 has a higher final mixing torque and batch temperature than ENR-25, while NBR-based composites show a slightly lower final mixing torque and batch temperature. For NBR, the rise of the acrylonitrile groups increases the polarity and its compatibility with the polar KNN, leading to slightly lower shear forces during compounding and, in turn, slightly lowered final mixing torque. Therefore, the mixing compatibility between KNN and NBR with a higher ACN content is dominant over the starting viscosity of the elastomers. For ENRs, the molecular chains of ENR-50 tend to self-crosslink since the epoxide groups are prone to be opened at elevated temperature [43-45]. The opened structure of an epoxide ring on the ENR main chain consists of a hydroxyl group and one active proton. The hydroxyl group generates hydrogen bonds between the ENR molecular chains, leading to the higher intermolecular interactions in the ENRs. This is more pronounced with an increasing epoxide level. As a result, the viscosity during mixing of ENR-50 is higher than of ENR-25, leading to increased shear forces and the higher final mixing torque and batch temperature for the ENR-50-based composite compared to the ENR-25 counterpart.

Figure 7 shows the rheocurves of gum and filled composites with 30 vol% of KNN. The main parameters derived from the cure curves are: Minimum torque (M_L), torque difference (ΔM), scorch time (t_{s2}) and cure time (t_{c90}).

The minimum torque M_L is an indication of the composite viscosity at the set cure temperature: The M_L influences the processability of the composites. The elastomeric composites filled with 30 vol% of KNN show higher values of minimum

torques than that of the gum rubber composites due to the hydrodynamic effect of the added filler particles. With an increase in the polar functional groups in all elastomeric composites, the M_L decreases. When the polarity of the elastomers increases, the better elastomer-KNN compatibility results in a better flowability of the mixtures. This explanation also supports the better dispersion of KNN in NBRs with an increasing polarity level. The molecular weight and the Mooney viscosity of ENRs is slightly reduced with an increasing epoxide content since the strong acid used for their epoxidation process and the ring opening of the epoxide groups cause chain scissions of ENR molecules. Consequently, the raw ENR-50 has a lower molecular weight and Mooney viscosity than ENR-25, ENR-50 provides a slightly lower viscosity in the initial curing stage (M_L).
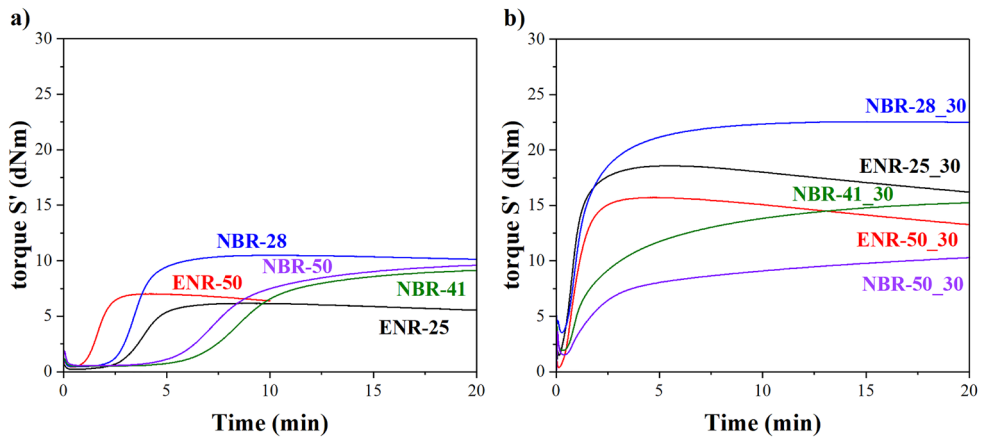
Figure 7   Curing characteristics of (a) gum rubbers and (b) filled elastomeric composites with 30 vol% of KNN.

The stiffness of the elastomeric composites can be related to the difference between M_H and M_L, that is influenced by the crosslink density and the filler network. It can be seen from Figure 7a that with an increasing polarity of the gum rubber the torque difference M_H-M_L decreases, except for ENR-50. This can be explained by the fact that the increment of the functionalities in the two elastomers, the carbon-carbon double bonds in their molecular chains decrease, resulting in a decrease in the active crosslinking sites, and so decreased crosslink density of the composites. The different behaviour of ENR-50 gum rubber may be due to the opened structure of ENRs causing self-crosslinks giving an extra polymer network in the materials.

The increase in the torque difference with decrasing elastomer polarity is also valid for the composites, as shown in Figure 7b. By comparing the cure curves of filled and gum rubbers, it seems that the filler-filler interactions from the polar KNN

185

particles also have an effect in this case [46]. Increasing the polarity of the elastomers in elastomeric composites results in a significant decrease in the cure torque difference. This can be linked to the better compatibility between a higher polar elastomer and the polar KNN particles as discussed earlier. This leads to smaller clusters and better dispersion of KNN in the matrices.

The cure rate of elastomeric composites determines the kinetics of the crosslinking of the elastomeric chains. For gum rubbers, the cure rate decreases with increasing acrylonitrile content in NBR, while it increases with increasing epoxide content in ENR. For ENR, curing by sulphur is faster and more efficient than for unmodified NR because the epoxide groups act as reactive sites facilitating the crosslinking formation [43,47]. For NBR, increasing the acrylonitrile content results in a lower extent of crosslinking sites, and thus a slower curing rate. The filled elastomeric composites are characterised by a higher cure rate compared to gum rubbers. This is because some fillers e.g. KNN are commonly identified to provide a catalytic effect on the kinetics of curing due to an increased heat conductivity in the elastomeric composite [48,49].

7.3.4. Poling study

Piezoelectric composites show piezoelectric properties when the spontaneous polarisation is oriented by applying a high electrical field in a process called poling. The piezoelectric performance of these composites is highly influenced by the degree of poling of the ceramic particles in the elastomeric matrix. The poling field acting on the piezoelectric particles is influenced by the dielectric constant of the matrix. This is because the higher dielectric constant of the matrix increases the effective electric field that the particles experience. Thus, tuning of the optimal poling conditions of the KNN-based elastomeric composites were investigated. A poling study was conducted for the composites with 30 vol% of KNN. In Table 3, the investigated range of poling parameters (temperature, electric field, and time) are reported. To optimise the poling parameters, the piezoelectric coefficients d_{33} were measured after the poling.
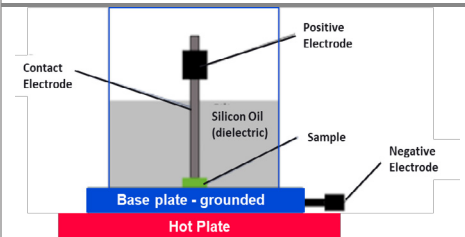
The optimal poling temperature depends on three factors: The Curie temperature of the ferroelectric ceramic KNN, the temperature at which the electrical conductivity of the polymeric matrix increases, and the degradation temperature of the elastomers [31,50]. The Curie temperature of KNN is around 300°C [50], and the safe processing temperature of elastomers is up to 180°C depending on the exposure time. The only limitation for using poling temperatures up to 180°C is the electrical

conductivity of the elastomer. At temperatures above 25°C, an excessively high current flows through a composite resulting in a reduction of the effective electrical field of the ceramic particles [31,50]. This is due to the strong polarisation of the polar chemical groups of NBR and ENR. Thus, the poling temperature was selected at room temperature.

The electrical field was varied in the range of 1 and 10 kV/mm. For both elastomer types, the piezoelectric coefficient increases in the range of 1 and 5 kV/mm and remains constant above this value. This means that the maximum possible d_{33} is achieved for these composites. Thus, with increasing the conductivity of the matrix, the required voltage to fully pole the piezoelectric composite is reduced, and this results in fully polarised piezoelectric composites. This is also in good agreement with the literature [31]. For the same reason, the composites require a poling time of 5 min to reach the saturation. This time is relatively short compared to the values reported in literature, ranging from 30 min to 2 h [31,36,37,51-54]. The high dielectric constant of the elastomeric matrix facilitates the alignment of the dipoles in the piezoelectric composites, as in these rubbers more electrical charges can be stored during the exposure to anelectrical field.

Table 3   Poling conditions for NBRs and ENRs filled with 30 vol% of KNN.

Contact poling setup		Poling conditions	Investigated range	Optimal value
		Temperature (°C)	25-100	25
		Electrical field (kV/mm)	1-10	5
		Time (min)	1-20	5

7.3.5.   Piezoelectric properties

The dielectric constant ε and the piezoelectric coefficient d_{33} were measured and reported in Figures 8a and b as a function of the elastomer type. With increasing amount of polar groups in the elastomers the dielectric constant as well as the piezoelectric coefficient increase. The dielectric constant of ENRs filled with 30 vol% of KNN increases from 20.8 to 48.8 for ENRs with 25 and 50 mol% of epoxide content, respectively. While, for NBRs with 28 and 50 mol% of acrylonitrile content, the dielectric constant increases from 45.9 to 52.9, respectively. The increase of the dielectric constant of composites reflects the synergistic effect of the strong

polarisation of the epoxide and acrylonitrile groups and the high-volume fraction of the the filler KNN.

The piezoelectric coefficient d_{33} (Figure 8b) follows the same trend as the dielectric constant in Figure 8b. For ENR-25 and ENR-50, the d_{33} values increase from 4.6 to 11.6 pC/N. While, for NBR-28 to NBR-50, the d_{33} values increase from 6.9 to 12.5 pC/N. The influencing factors on this parameter are the piezoelectric coefficient and the dielectric constant of the ceramic, dielectric constant of the polymer matrix, as well as the poling process. These composites have the same type and amount of ferroelectric ceramic, and the poling study was carried out to maximise its effectiveness for all composites. Thus, the only remaining influencing factor is the dielectric constant of the matrix.
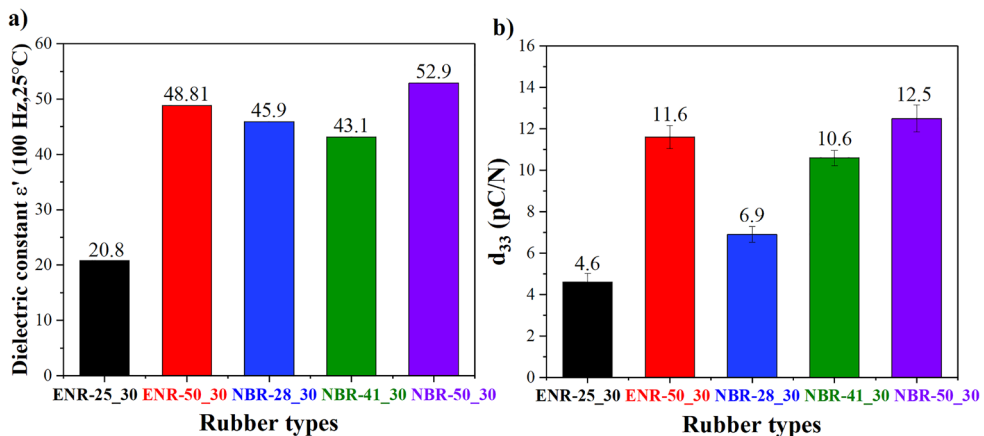
Figure 8   (a) Dielectric constant ε and (b) piezoelectric coefficient d_{33} of ENR-25, ENR-50, NBR-28, NBR-41, NBR-50 filled with 30 vol% of KNN.

Particularly, the piezoelectric coefficient of the composites depends on the difference of the dielectric constant of the matrix and the filler (see Yamada's model, equation 1). The dielectric constant of the matrix directly affects the electrical field acting on the ferroelectric ceramic during the poling process. The higher the dielectric constant of the matrix, the smaller is the mismatch between the dielectric constant of the matrix and the piezoelectric ceramic and the better is the polarisation of the ferroelectric ceramic, leading to a higher piezoelectric coefficient of the composites.

In Figure 9a, the dielectric constant at varied frequencies of gum rubbers and their respective composites filled with 30 vol% of KNN is reported. For gum ENR, the dielectric constant increases with increasing amount of polar groups in the entire

frequency range. This is due to the fact that the dielectric constant of the composites
depends on the orientational polarisation of the polar groups in their structure, as
well as on the interfacial polarisation occurring at the boundaries of the building
blocks of the monomer units in the polymer chains. The gum NBR shows a
decreasing dielectric constant with higher acrylonitrile group content for a frequency
lower than 1 Hz. This is because in this range the dominant polarisation mechanism
is the interfacial polarisation. At this frequency range, the polarisability and charges
mobility in NBR increases with higher ACN contents. Thus, the ability of the
material to counteract the applied electric field is enhanced and the dielectric
constant decreases with increasing amount of acrylonitrile groups. At frequencies
higher than 1 Hz, the orientational polarisation is dominant, that is related to the
alignment of polar groups exposed to an electrical field. The higher the polar group
content is, the higher is the contribution to an orientational polarisation and the
higher is the dielectric constant. Gum ENR shows an increased dielectric constant
with increasing amount of epoxide groups in the whole frequency range, thus in the
interfacial and orientational polarisation regions. This may be attributed to the
different molecular structure and composition of ENR and NBR. NBR is produced
from the copolymerization of butadiene and acrylonitrile monomer while ENR is
synthesized by a later introduction of epoxide groups to the polymeric chain of NR.
The interfacial polarisation is much higher for NBR compared to ENR due to the
presence of the two building blocks.

Although the dielectric constants as a function of frequency of the gum rubbers show
different trends, they have a comparable value when filled with 30 vol% of KNN
(Figure 9b), particularly at a frequency higher than 10 Hz, i.e. orientational
polarisation region. This is particularly valid for ENR-50, NBR-28, NBR-41 and
NBR-50. When filled with ferroelectric ceramic, the dielectric constant of the
composites is determined by the interactions between the ceramic and the matrix.
The dielectric constant of the composites is higher than the dielectric constant of the
gum rubber because the ceramic particles are fully incorporated in the elastomer,
showing high polymer-filler interactions. In the case of these elastomeric
composites, with increasing polarity level in NBRs and ENRs, the dielectric constant
increases. This is because the rubber-filler interactions play a dominant role in the
composite polarisation. The similar dielectric constants of the composites based on
ENR-50, NBR-28, NBR-41 and NBR-50 and 30 vol% of KNN is due to the adequate
rubber-filler interactions as well as a similar dielectric constant of the gum rubbers.
For the same reason, ENR-30 filled with 30 vol% has the lowest dielectric constant

7

of all elastomeric composites, due to the low polar group content and therefore low rubber-filler compatibility.
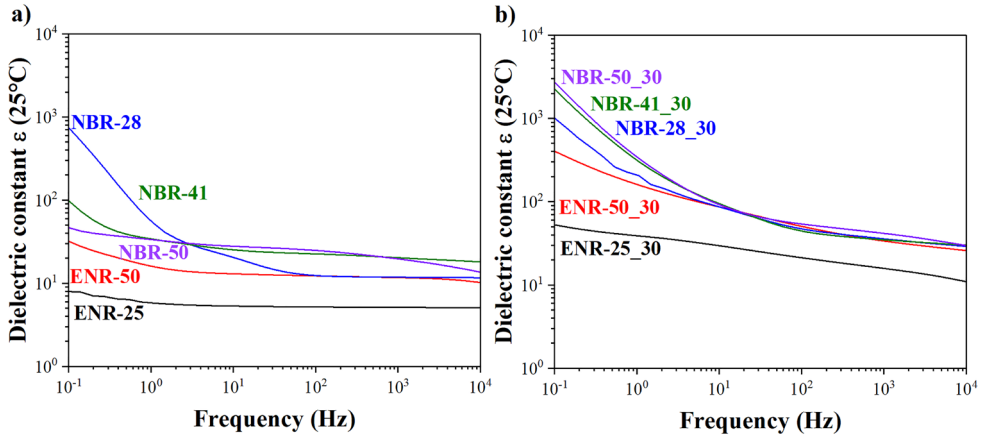

Figure 9 Dielectric constant of (a) gum rubbers and (b) filled with 30 vol% of KNN.

Several models have been considered so far in literature to predict the piezoelectric coefficient d_{33}. The most used one is the Yamada model with the following equation:

$$d_{33,r} = \frac{\alpha \varphi n \varepsilon_r}{n\varepsilon_r + (\varepsilon_f - \varepsilon_r)} d_{33,f} \tag{1}$$

where α is the poling efficiency, φ is the volume fraction of the ceramic particles in the composite, n is the shape factor of KNN. ε and d_{33} are the dielectric constant as well as the piezoelectric coefficient, and the indices f and r refer to the filler and the composite. This model confirms the strong influence of the dielectric constant of the matrix and the ceramic and their mismatch on the piezoelectric properties. As seen in Figurea 8 and 9, a higher dielectric constant implies a stronger polarisation of the KNN ceramic and thus a higher piezoelectric constant. The higher the dielectric constant of the matrix, the smaller is the difference $(\varepsilon_f - \varepsilon_r)$, and the higher are the piezoelectric properties. A smaller mismatch of dielectric constants of filler and matrix implies a more uniform poling electrical field, even at the interface avoiding the charge accumularion and lost of this electrical field. The poling efficiency α was considered as 100%, as the elastomeric composites were fully polarised during the poling process. The shape factor n of KNN was calculated from the SEM image depicted in Figure 1, by using the software ImageJ (Java image processing program developed in Laboratory for Optical and Computational Instrumentation, Madison, USA). The averages aspect ratio was 1.25 ± 0.09. For Yamada's model, n is considered as 3 for spherical particles, and higher than 3 for ellipsoidal particles. For

this study, a value of 4 for the low aspect ratio was considered. The piezoelectric coefficient and the dielectric constant of KNN particles are as follows: 80 pC/N and 250 [29].

In Table 4, the experimental values and the theoretical prediction of the piezoelectric coefficients are reported. The experimental values are close to the theoretical ones, except for ENR-50_30. For this elastomeric composite, the experimental value is slightly higher than the value predicted by Yamada's model probably due to filler-rubber compatibility, resulting in a higher dielectric constant and piezoelectric coefficient.

Table 4 Piezoelectric coefficient d_{33} for NBRs and ENRs filled with 30 vol% of KNN measured and predicted with the Yamada model.

Composites	Piezoelectric coefficient, d_{33} (pC/N)	
	Experimental value	**Yamada model**
ENR-25_30	4.6 ± 0.4	4.3
ENR-50_30	11.6 ± 0.6	7.0
NBR-28_30	6.9 ± 0.3	8.1
NBR-41_30	10.6 ± 0.4	11.5
NBR-50_30	12.5 ± 0.6	12.1

Earlier works [35,55] showed that the conductivity of a polymeric matrix does not have a direct effect on the piezoelectric coefficient, but on the poling efficiency. An increasing conductivity of the matrix decreases the electrical field required to polarise the composites. Ideally, there is also a threshold value of the conductivity for these composites, above which the dielectric loss of composites is high, and in turn the electrical field for the poling process required to polarise the elastomeric composites is low.

In Figures 10a and b, the electrical conductivity of gum rubbers and elastomeric composites measured by BDS is reported. In this study, as a DC electrical field is applied during the poling process, a DC conductivity of composites needs to be determined to further understand the polarisation of the poling process. In the BDS plot (Figure 10), the conductivity decreases with decreasing frequency. The electrical conductivity exhibits a plateau at low frequencies (named DC conductivity) and a power-law dependency at high frequencies (named AC conductivity). In polymers, the AC conductivity is expressed by the following power-law equation [52,55]:

7

$$\sigma(\omega) = \sigma_{DC} + A\omega^{s(T)} \tag{2}$$

where, $\sigma(\omega)$ is the measured AC conductivity in BDS, σ_{DC} is the DC conductivity, A is a temperature-dependent constant representing the polarisability of the polymer, ω is the frequency and $s(T)$ reflects the interaction term between the mobile ions and the surrounding environment. The power law exponents depend on temperature, and the type and amount of filler in the composites, and typically fall between 0 and 1. They are usually obtained from the slope of Log-Log plots derived from Equation (2).

Gum rubbers and elastomeric composites in Figures 10a and b present an increasing electrical conductivity as a function of frequency due to the abovementioned power-law equation and existence of DC conductivity at low frequency and AC conductivity at high frequency. The increasing electrical conductivity as a function of frequency is due to the activation of electrical dipoles within the polymeric chain. Gum rubbers show a DC conductivity in the frequency range between 0.1 and 50 Hz and an AC conductivity in the frequency range above 50 Hz. The DC conductivity of the gum ENRs increases with increasing polar epoxide content due to the electrical charges hopping mechanism across the materials in the presence of an electrical field. The DC conductivity of the gum NBRs decreases with increasing amount of polar acrylonitrile groups. At low frequency, due to the increasing polar acrylonitrile groups in gum NBRs, with increasing electrical field the mobility of the charge carriers at the interface increases, limiting the charge carriers mobility throughout the decreasing the conductivity of these gum NBRs rubbers. This is correlated to the high dielectric constant of NBRs below 1 Hz, as shown in Figure 9a. The high DC conductivity and low dielectric constant at low frequency range is directly correlated to the piezoelectric properties reported in Figure 8b.

For all gum rubbers, the AC conductivity increases with increasing amount of polar groups in agreement with the barrier hopping model [55].

Elastomeric composites filled with 30 vol% of KNN show a DC conductivity in the frequency range between 0.1 and 2 Hz and an AC conductivity above 2 Hz. When filled with the ferroelectric ceramic KNN, the AC and DC conductivity depends on the charge carriers hopping across the KNN particles and the amount of polar groups of the elastomers. With increasing epoxide content, ENR shows a higher DC and AC conductivity due to a higher dielectric constant (Figure 9b) and higher interactions between the polar KNN and the elastomer. With increasing acrylonitrile content,

NBR shows a slightly decreased DC conductivity at low frequency and a slightly increased AC conductivity at high frequency. This is due to the lowered dielectric constant of gum rubber at low frequency and increased dielectric constant at higher frequency, as shown in Figure 9a.

NBR-28, NBR-41 and NBR-50 filled with 30 vol% of KNN show a higher DC electrical conductivity and AC conductivity than all ENRs due to the high intrinsic DC and AC electrical conductivity of gum rubbers.

Despite this high-electrical conductivity, all composites were polarised successfully. However, some small deviations of the experimental data compared to the theoretical values predicted by the Yamada's model can be due to the lowered poling efficiency for the highly electrically conductive elastomers.
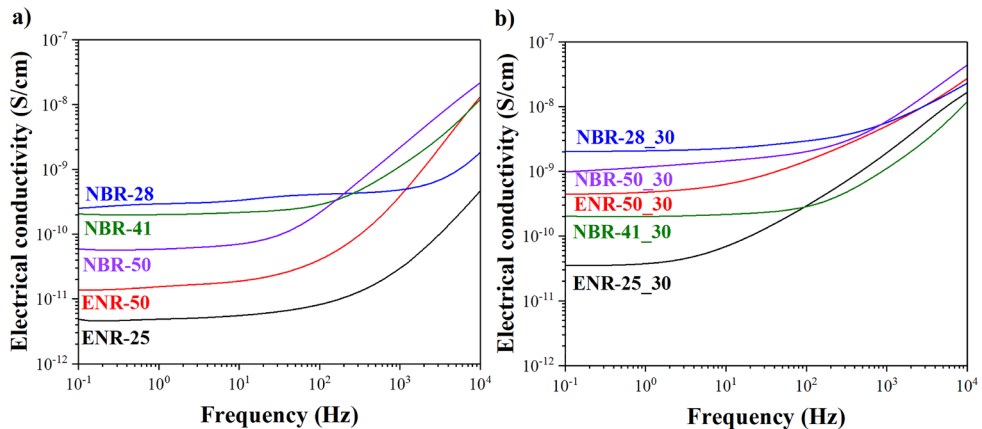
Figure 10   Electrical conductivity of (a) gum rubbers and (b) filled with 30 vol% of KNN.

7.3.6. Mechanical properties

The mechanical characteristics of the gum rubbers and elastomeric composites are shown in Figure 11. The addition of a reinforcing filler in an elastomer generally improves the stress-strain properties. However, fillers with particle sizes higher than 1 µm act as a diluent in elastomers and are non-reinforcing. As shown in Figure 1, the particle size of KNN used in this study is in the range of 0.2-2 µm. Thus, KNN is classified as a non-reinforcing filler. Therefore, in Figure 11, the non-reinforcing effect of KNN in ENR and NBR composites is noticeable. Nevertheless, the compatibility effect between ENRs and NBRs with KNN can be reflected by these mechanical properties. For ENR-25 and ENR-50 filled with 30 vol%, compared to gum rubber, the moduli at 100% and 300% strain increase, implying stiffer materials. This stiffening leads to a lower tensile strength and elongation at break of ENR-

based composites. Comparing ENR-25 and ENR-50 filled with 30 vol% of KNN, the tensile strength and the elongation at break slightly increase. This is ascribed to the effect of improved rubber-filler interactions.
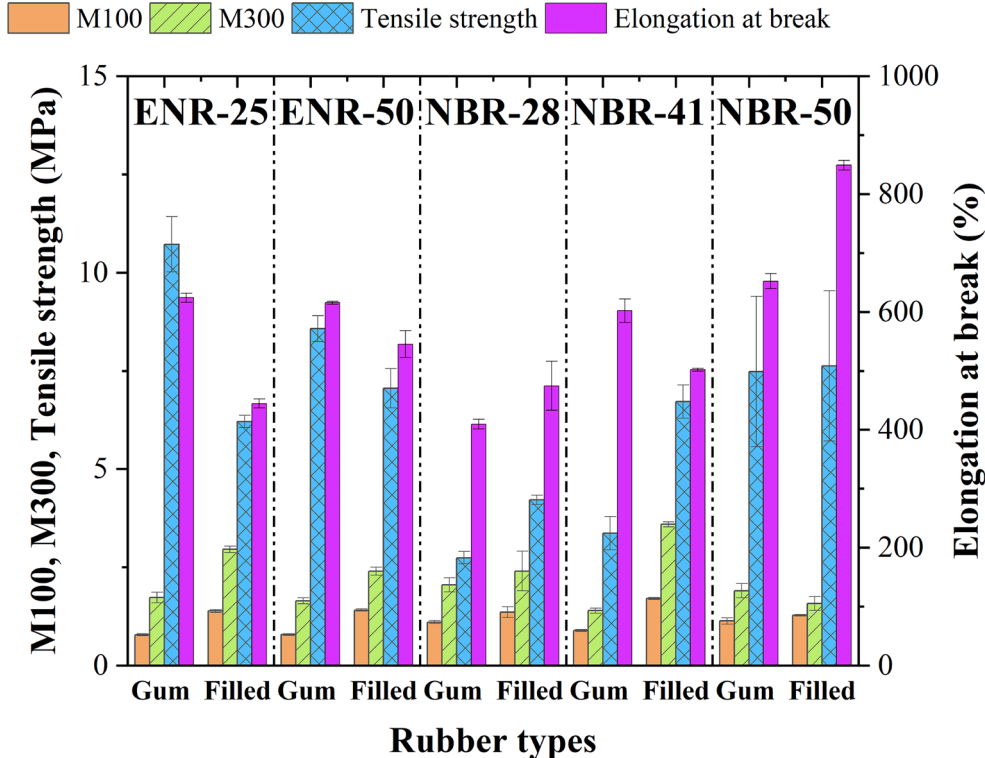

Figure 11 Stress-strain properties: Moduli at 100% and 300% (M100, M300), tensile strength and elongation at break of rubbers unfilled and filled with 30 vol% of KNN.

For NBRs, as compared between filled and gum rubbers, the moduli increase for NBR-28, NBR-41, and 50 wt% of acrylonitrile content, the moduli are similar. This is due to the hydrodynamic effect of added filler.

The variations in tensile strength and elongation at break are potentially due to the stiffness influenced by the polymer network density and crosslink types as well as the interactions between the rubber and the filler. For ENRs filled with 30 vol% of KNN, the tensile strength and the elongation at break are lower than the gum ENRs due to a highly stiff material. For NBR-based composites, when filled with 30 vol% of KNN, the elongation at break increased for all composites, while the tensile strengths are increased for NBR-28 and NBR-50 while it is decreased for NBR-41. For NBR-28 and NBR-50 based composites, the combined effect of network density, crosslinking types and rubber-filler interactions result in the increase in the two

properties. NBR-41 shows a similar behaviour as ENRs that can be caused by the same reasons.

7.4. Conclusions

Piezoelectric composites consisting of modified natural rubbers and NBRs as matrices and the ceramic KNN as ferroelectric particles were investigated. Firstly, the effect of different elastomers on the piezoelectric properties of composites was studied. Epoxidised Natural Rubber (ENR) with two levels of epoxidation (25 and 50 mol%) and Nitrile Butadiene Rubber (NBR) with three levels of acrylonitrile content (28, 41 and 50 wt%) were used. The polarity of both elastomer types affects the mixing, the poling process, and the piezoelectric properties. The higher the polarity of the elastomer, the higher is the efficiency of the poling process and, therefore, the higher is the piezoelectric coefficient. Elastomers with a higher polarity like ENR-50 and NBR-50, when filled with 30 vol% of KNN, reach values of the piezoelectric coefficient of around 12 pC/N. The mechanical properties were also measured. KNN acts as a non-reinforcing filler due to its large particle size. Nonetheless, it gives improved interfacial interactions with polar elastomers through polar-polar interaction. Therefore, the tensile properties, in particular the moduli of the composites are improved.

7

7.5.   References

[1]   I.A.H. Al-Najati, K.W. Chan, S.Y. Pung, Tire strain piezoelectric energy harvesters: a systematic review, Int. J. Power Electron. Drive Syst. 13 (2022) 444–459. https://doi.org/10.11591/IJPEDS.V13.I1.PP444-459.

[2]   M. Germer, U. Marschner, A. Richter, Energy Harvesting for Tire Pressure Monitoring Systems from a Mechanical Energy Point of View, IEEE Internet Things J. 9 (2022) 7700-7714. https://doi.org/10.1109/JIOT.2022.3152547.

[3]   J. Ghazanfarian, M.M. Mohammadi, K. Uchino, Piezoelectric Energy Harvesting: A Systematic Review of Reviews, Actuators. 10 (2021) 312. https://doi.org/10.3390/ACT10120312.

[4]   L. Liu, X. Guo, W. Liu, C. Lee, Recent progress in the energy harvesting technology-from self-powered sensors to self-sustained iot, and new applications, Nanomaterials. 11 (2021) 2975. https://doi.org/10.3390/nano11112975.

[5]   J.F. Tressler, L. Qin, K. Uchino, 7.21 Piezoelectric Composite Sensors, Compr. Compos. Mater. II. 5 (2018) 408–419. https://doi.org/10.1016/B978-0-12-803581-8.03937-0.

[6]   K. Maity, D. Mandal, Piezoelectric polymers and composites for multifunctional materials, Adv. Light. Multifunct. Mater. (2021) 239–282. https://doi.org/10.1016/B978-0-12-818501-8.00001-9.

[7]   J. Yvonnet, Piezoelectricity, Solid Mech. Its Appl. 258 (2019) 91–102. https://doi.org/10.1007/978-3-030-18383-7_5.

[8]   K.H. Mak, S. McWilliam, A.A. Popov, Piezoelectric energy harvesting for tyre pressure measurement applications, Proc. Inst. Mech. Eng. Part D J. Automob. Eng. 227 (2013) 842–852. https://doi.org/10.1177/0954407012463849.

[9]   Z. Yang, S. Zhou, J. Zu, D. Inman, High-performance piezoelectric energy harvesters and their applications, Joule. 2 (2018) 642–697. https://doi.org/10.1016/j.joule.2018.03.011.

[10]   C. Mangone, M. Klein Gunnewiek, L. Reuvekamp, W. Kaewsakul, A. Blume, Method for chemically adhering a diene rubber to a piezoelectric polymer, WO/2021/052951, 2021.

[11]   C. Mangone, W. Kaewsakul, M. Klein Gunnewiek, A.P.J. van Swaaij, L. Reuvekamp, J.W.M. Noordermeer, A. Blume, Design and performance of flexible polymeric piezoelectric energy harvesters for battery-less tyre sensors, Smart Mater. Struct. (2022) 095034.

[12]   C. Mangone, W. Kaewsakul, A.P.J. van Swaaij, K. Bandzierz, M.K. Gunnewiek, A. Blume, Dynamic measurement setups for validating piezoelectric energy harvesters in driving conditions, Polym. Test. 119 (2023) 107932. https://doi.org/10.1016/J.POLYMERTESTING.2023.107932.

[13]   S. Bauer, F. Bauer, Piezoelectric polymers and their applications, in: Springer Ser. Mater. Sci., Springer Verlag, 2008: pp. 157–177.

[14] Y. Saito, H. Takao, T. Tani, T. Nonoyama, K. Takatori, T. Homma, T. Nagaya, M. Nakamura, Lead-free piezoceramics, Nature. 432 (2004) 84–87. https://doi.org/10.1038/nature03028.

[15] A.O. Sanches, J.A. Malmonge, W.K. Sakamoto, Piezoelectric composites: Fabrication, characterization, and its application as sensor, Recent Adv. Complex Funct. Mater. From Des. to Appl. (2017) 195–215. https://doi.org/10.1007/978-3-319-53898-3_8.

[16] H. Khanbareh, V.Y. Topolov, C.R. Bowen, Piezo-active composites: Classification and effective physical properties, Springer Ser. Mater. Sci. 283 (2019) 1–23. https://doi.org/10.1007/978-3-030-19204-4_1.

[17] P. Eltouby, I. Shyha, C. Li, J. Khaliq, Factors affecting the piezoelectric performance of ceramic-polymer composites: A comprehensive review, Ceram. Int. 47 (2021) 17813–17825. https://doi.org/10.1016/J.CERAMINT.2021.03.126.

[18] C.R. Bowen, H.A. Kim, P.M. Weaver, S. Dunn, Piezoelectric and ferroelectric materials and structures for energy harvesting applications, Energy Environ. Sci. 7 (2014) 25–44. https://doi.org/10.1039/C3EE42454E.

[19] Ferroelectric Materials for Energy Applications, Ferroelectr. Mater. Energy Appl. (2018). https://doi.org/10.1002/9783527807505.

[20] J. Rödel, K.G. Webber, R. Dittmer, W. Jo, M. Kimura, D. Damjanovic, Transferring lead-free piezoelectric ceramics into application, J. Eur. Ceram. Soc. 35 (2015) 1659–1681. https://doi.org/10.1016/j.jeurceramsoc.2014.12.013.

[21] T. Rojac, M. Makarovic, J. Walker, H. Ursic, D. Damjanovic, T. Kos, Piezoelectric response of BiFeO3 ceramics at elevated temperatures, Appl. Phys. Lett. 109 (2016) 042964. https://doi.org/10.1063/1.4960103.

[22] S. Mishra, L. Unnikrishnan, S.K. Nayak, S. Mohanty, Advances in Piezoelectric Polymer Composites for Energy Harvesting Applications: A Systematic Review, Macromol. Mater. Eng. 304 (2019) 1800463. https://doi.org/10.1002/MAME.201800463.

[23] J.H. Yoo, J.D. Han, H.J. Yoo, S.G. Ok, J.S. Ok, PTC properties of PE/CB composites for energy saving heating elements, Ferroelectrics. 515 (2017) 75–82. https://doi.org/10.1080/00150193.2017.1360111.

[24] E. Sun, W. Cao, Relaxor-based ferroelectric single crystals: growth, domain engineering, characterization and applications, Prog. Mater. Sci. 65 (2014) 124. https://doi.org/10.1016/J.PMATSCI.2014.03.006.

[25] G. Helke, K. Lubitz, Piezoelectric PZT Ceramics, Springer Ser. Mater. Sci. 114 (2008) 89–130. https://doi.org/10.1007/978-3-540-68683-5_4/COVER.

[26] E.G. Fesenko, A.Y. Dantsiger, L.A. Resnitchenko, M.F. Kupriyanov, Composition-Structure-Properties Dependences In Solid Solutions On The Basis Of Lead-Zirconate-Titanate And Sodium Niobate, Ferroelectrics. 41 (1982) 137–142. https://doi.org/10.1080/00150198208210616.

7

[27] T.R. Shrout, S.J. Zhang, Lead-free piezoelectric ceramics:Alternatives for PZT?, Electroceramics. 19 (2007) 111–124.https://doi.org/10.1007/S10832-007-9047-0.

[28] Y. Saito, H. Takao, High performance lead-free piezoelectric ceramics in the (K,Na)NbO 3 -LiTaO 3 solid solution system, Ferroelectrics. 338 (2006) 17–32. https://doi.org/10.1080/00150190600732512.

[29] D.B. Deutz, N.T. Mascarenhas, S. van der Zwaag, W.A. Groen, Enhancing energy harvesting potential of (K,Na,Li)NbO3-epoxy composites via Li substitution, J. Am. Ceram. Soc. 100 (2017) 1108–1117. https://doi.org/10.1111/jace.14698.

[30] R. Mitkus, L. Piechowiak, M. Sinapius, Characterization of UV Light Curable Piezoelectric 0-0-3 Composites Filled with Lead-Free Ceramics and Conductive Nanoparticles, J. Compos. Sci. 7 (2023) 89. https://doi.org/10.3390/JCS7020089/S1.

[31] V.L. Stuber, T.R. Mahon, S. Van Der Zwaag, P. Groen, The effect of the intrinsic electrical matrix conductivity on the piezoelectric charge constant of piezoelectric composites, Mater. Res. Express. 7 (2019) 015703. https://doi.org/10.1088/2053-1591/AB5BB3.

[32] D.B. Deutz, N.T. Mascarenhas, J.B.J. Schelen, D.M. de Leeuw, S. van der Zwaag, P. Groen, Flexible piezoelectric touch sensor by alignment of lead-free alkaline niobate microcubes in PDMS, Adv. Funct. Mater. 27 (2017) 1–7. https://doi.org/10.1002/adfm.201700728.

[33] H. Khanbareh, S. Van Der Zwaag, W.A. Groen, Effect of dielectrophoretic structuring on piezoelectric and pyroelectric properties of lead titanate-epoxy composites, Smart Mater. Struct. 23 (2014) 105030. https://doi.org/10.1088/0964-1726/23/10/105030.

[34] D.Y. Hyeon, G.J. Lee, S.H. Lee, J.J. Park, S. Kim, M.K. Lee, K. Il Park, High-temperature workable flexible piezoelectric energy harvester comprising thermally stable (K,Na)NbO3-based ceramic and polyimide composites, Compos. Part B Eng. 234 (2022) 109671. https://doi.org/10.1016/J.COMPOSITESB.2022.109671.

[35] V.L. Stuber, D.B. Deutz, J. Bennett, D. Cannel, D.M. de Leeuw, S. van der Zwaag, P. Groen, Flexible Lead-Free Piezoelectric Composite Materials for Energy Harvesting Applications, Energy Technol. 7 (2019) 177–185. https://doi.org/10.1002/ENTE.201800419.

[36] J.E.Q. Quinsaat, T. de Wild, F.A. Nüesch, D. Damjanovic, R. Krämer, G. Schürch, D. Häfliger, F. Clemens, T. Sebastian, M. Dascalu, D.M. Opris, Stretchable piezoelectric elastic composites for sensors and energy generators, Compos. Part B Eng. 198 (2020) 108211. https://doi.org/10.1016/J.COMPOSITESB.2020.108211.

[37] I. Babu, G. de With, Enhanced electromechanical properties of piezoelectric thin flexible films, Compos. Sci. Technol. 104 (2014) 74–80. https://doi.org/10.1016/J.COMPSCITECH.2014.08.022.

[38] M. Promsawat, K.U. Boonsri, S. Samadoloh, N. Promsawat, E. Kalkornsurapranee, Effects of Poling on Electrical Properties of Flexible Piezoelectric Composites with Natural Rubber Matrix, IOP Conf. Ser. Mater. Sci. Eng. 553 (2019) 012008. https://doi.org/10.1088/1757-899X/553/1/012008.

[39] S. Samadoloh, N. Promsawat, E. Kalkornsurapranee, S. Pojprapai, M. Promsawat, Fabrication and characterization of flexible piezoelectric composites with natural rubber matrix, Integrated Ferroelectrics, 195 (2018) 30-38. https://doi.org/10.1080/10584587.2019.1570041.

[40] Y. Zhang, Z. Liu, F. Ding, W. Zhang, Effect of piezoelectric ceramic particles size gradation on piezoelectric properties of 0–3 cement-based piezoelectric composites, Smart Mater. Struct. 27 (2018) 085029. https://doi.org/10.1088/1361-665X/AAD0BE.

[41] S. Hunpratub, T. Yamwong, S. Srilomsak, S. Maensiri, P. Chindaprasirt, Effect of particle size on the dielectric and piezoelectric properties of 0–3BCTZO/cement composites, Ceram. Int. 40 (2014) 1209–1213. https://doi.org/10.1016/J.CERAMINT.2013.05.118.

[42] S. Bairagi, S.W. Ali, Effects of surface modification on electrical properties of KNN nanorod-incorporated PVDF composites, J. Mater. Sci. 54 (2019) 11462–11484. https://doi.org/10.1007/S10853-019-03719-X/METRICS.

[43] L.H. Gan, S.C. Ng, Kinetic studies of the performic acid epoxidation of natural rubber latex stabilized by cationic surfactant, Eur. Polym. J. 22 (1986) 573–576. https://doi.org/10.1016/0014-3057(86)90186-2.

[44] W. Kaewsakul, K. Sahakaro, W.K. Dierkes, J.W.M. Noordermeer, Cooperative effects of epoxide functional groups on natural rubber and silane coupling agents on reinforcing efficiency of silica, Rubber Chem. Technol. 87 (2014) 291–310. https://doi.org/10.5254/RCT.13.86990.

[45] W. Kaewsakul, Silica-Reinforced Natural Rubber for Low Rolling Resistance, Energy-Saving Tires, PhD thesis, University of Twente, 2013.

[46] H.D. Luginsland, J. Fröhlich, A. Wehmeier, Influence of Different Silanes on the Reinforcement of Silica-Filled Rubber Compounds, Rubber Chem. Technol. 75 (2002) 563–579. https://doi.org/10.5254/1.3544984.

[47] I.R. Gelling, N.J. Morrison, Sulfur Vulcanization and Oxidative Aging of Epoxidized Natural Rubber, Rubber Chem. Technol. 58 (1985) 243–257. https://doi.org/10.5254/1.3536063.

[48] S.M. Hosseini, M. Razzaghi-Kashani, Catalytic and networking effects of carbon black on the kinetics and conversion of sulfur vulcanization in styrene butadiene rubber, Soft Matter. 14 (2018) 9194–9208. https://doi.org/10.1039/C8SM01953C.

[49] C.G. Robertson, N.J. Hardman, Nature of Carbon Black Reinforcement of Rubber: Perspective on the Original Polymer Nanocomposite, Polym. 2021, Vol. 13, Page 538. 13 (2021) 538. https://doi.org/10.3390/POLYM13040538.

7

[50]   D.B. Deutz, N.T. Mascarenhas, J.B.J. Schelen, D.M. de Leeuw, S. van der Zwaag, P. Groen, Flexible Piezoelectric Touch Sensor by Alignment of Lead-Free Alkaline Niobate Microcubes in PDMS, Adv. Funct. Mater. 27 (2017) 1700728. https://doi.org/10.1002/ADFM.201700728.

[51]   D.A. Van Den Ende, B.F. Bory, W.A. Groen, S. Van Der Zwaag, Improving the d33 and g33 properties of 0-3 piezoelectric composites by dielectrophoresis, J. Appl. Phys. 107 (2010) 24107. https://doi.org/10.1063/1.3291131.

[52]   A. Tuluk, T. Mahon, S. van der Zwaag, P. Groen, Estimating the true piezoelectric properties of BiFeO3 from measurements on BiFeO3-PVDF terpolymer composites, J. Alloys Compd. 868 (2021) 159186. https://doi.org/10.1016/J.JALLCOM.2021.159186.

[53]   H. Khanbareh, S. Van Der Zwaag, W.A. Groen, Piezoelectric and pyroelectric properties of conductive polyethylene oxide-lead titanate composites, Smart Mater. Struct. 24 (2015). https://doi.org/10.1088/0964-1726/24/4/045020.

[54]   A. Tuluk, S. Joshi, T. Mahon, S. Van Der Zwaag, Tuning piezoproperties of BiFeO3ceramic by cobalt and titanium dual doping, J. Appl. Phys. 131 (2022) 214104. https://doi.org/10.1063/5.0091768/2836958.

[55]   V.L. Stuber, T.R. Mahon, S. Van Der Zwaag, P. Groen, The effect of the intrinsic electrical matrix conductivity on the piezoelectric charge constant of piezoelectric composites, Mater. Res. Express. 7 (2019) 15703. https://doi.org/10.1088/2053-1591/AB5BB3.

Flexible lead-free ferroelectric composites: processing parameters and effect of elastomer polarity

7

Chapter 8

Effect of the loading level of ferroelectric ceramic on properties of elastomeric composites

The interest in energy harvesting technology is steadily growing in the field of self-powered sensors for smart tyres. The purpose of this study is to develop a flexible ferroelectric material capable of capturing the energy dissipated in tyres. In this work, varying amounts of lead-free $K_{0.5}Na_{0.5}NbO_3$ (KNN) ferroelectric ceramic were mixed with rubbers characterised by different polarities, dielectric constants, and electrical conductivities. The rubbers used were Epoxidised Natural Rubber (ENR) with 25 and 50 mol% of epoxide contents, and acryloNitrile Butadiene Rubber (NBR) with 28 and 50 wt% of acrylonitrile contents. The processability, curing behaviour, contact poling process and piezoelectric properties of the ferroelectric composites based on the different rubbers filled with varied amounts of KNN in the range of 10 to 50 vol% were analysed. With increasing KNN amount and increasing rubber polarity, the dielectric constant of the matrix increases, resulting in a higher piezoelectric constant. A poling study was conducted using elastomeric composites vulcanised at different thicknesses, i.e. 0.3, 0.5 and 1 mm. It was observed that thinner samples exhibited a higher piezoelectric coefficient due to better poling efficiency.

8

Chapter 8

8.1.   Introduction

Piezoelectric polymeric composites have drawn tremendous attention in the field of smart sensors and renewable energy for their potential to generate electrical energy through material deformation under mechanical forces. They can be applied as e.g. sensors and energy harvesters [1-3]. Piezoelectric polymeric composites consist of a piezoelectric ceramic embedded in a polymeric matrix. One of their main advantages is the ability to tailor properties according to the specific application requirements by selecting the appropriate polymer matrix, filler type and content [4,5]. Applying a high electrical field to piezoelectric composites containing a polycrystalline ceramic aligns the dipole moments to a certain direction, resulting in positively and negatively charged sides [6-8]. This process is called the poling process, and the direction in which the dipoles align is the poling direction.

The deformation of a piezoelectric composite induces the accumulation of positive and negative electrical charges on the opposite sides of its structure. By applying electrodes on both sides of the piezoelectric material, a flow of electrical current is generated, allowing the material to function as an energy harvester [9-12]. With this attractive feature, a piezoelectric composite can power sensors, ensuring an autonomous operation of systems. An industy that benefits already from this technology is the automotive industry [1,2,13,14]. An increasing number of sensors are being integrated into tyres to monitor the real-time performance. During vehicle's operation, tyres are continuously subjected to dynamic deformations, vibrations, and excitations due to the tyre-road contact interactions. Hence, this tyre-running operation is considered to be an ideal condition for activating piezoelectric materials.

In Chapter 4, an energy harvester comprising the piezoelectric polymer PolyVinyliDene diFluoride (PVDF) and an elastomeric electrode in a sandwich structure was developed [15,16]. A chemical adhesion between the two components ensured a flexible and stable harvester capable of generating 28 mW in lab-scale experiments simulating the rolling tyre conditions [17]. These previous studies showed promising results towards the application of piezoelectric polymers in tyres. However, PVDF, being a thermoplastic polymer, may pose challenges in terms of flexibility and durability for real tyre applications. This research aims to find an alternative piezoelectric material suitable for tyre applications. A piezoelectric ceramic is not a favourable option due to its brittleness, which leads to a too early mechanical failure under dynamic deformations [18,19]. Therefore, piezoelectric polymeric composites have been analysed for their ability to combine the mechanical

flexibility of a polymer matrix with the high piezoelectric coefficient of a ceramic filler [10,20].

In a study presented in Chapter 7, piezoelectric composites based on different rubber types, i.e. Epoxidised Natural Rubber (ENR) and acryloNitrile Butadiene Rubber (NBR), and a fixed amount of the ferroelectric ceramic $K_{0.5}Na_{0.5}NbO_3$ (KNN) at 30 vol% were prepared and investigated. The rubbers were selected based on their polar functional groups: ENR with two levels of epoxidation (25 and 50 mol%) and NBR with three levels of acrylonitrile content (28, 41 and 50 wt%). The results of this study showed that the processability, contact poling process, and piezoelectric, dielectric and mechanical properties of the composites improved with the polarity of the matrix. The higher the polarity of the rubber, the better the compatibility with KNN and the better the dispersion of KNN in the rubber matrix. Moreover, a higher polarity of the rubber resulted in a higher dielectric constant of the matrices and, in turn, a shorter poling process (i.e. 5 min) and resulting piezoelectric coefficients of around 12 pC/N for ENR-50 and NBR-50 with 30 vol% of KNN. This selection of high polar rubber, i.e. ENR-50 and NBR-50, resulted to be the best option. Based on this outcome in Chapter 7, the current study aims to investigate the effect of various amounts of KNN in piezoelectric composites comprising ENR-25, ENR-50, NBR-28 and NBR-50 to evaluate whether the electrical and mechanical properties can be enhanced. Processability, contact poling study, piezoelectric, dielectric, and mechanical properties of the composites were analysed. Additionally, a chemical model study to further understand the interaction between KNN and the rubbers was also carried out.

8.2. Experimental

8.2.1. Materials

The same ingredients described in Chapter 7 were used in this study.
Additionally, for the chemical model study, the following materials were used:
1,2-Epoxidodecanes (Mark Life Science N.V., Amsterdam, the Netherland); Nitriledodecane (Mark Life Science N.V., Amsterdam, the Netherland); TetraHydroFuran (THF, VWR, Amsterdam, the Netherlands).

8.2.2. Chemical model study

The chemical model was performed in an ampoule of 20 mL, with the two types of dodecanes serving as solvents and 10 vol% of KNN added as filler. The ampoule was flushed with N_2 before and after material addition in order to prevent any side

8

reactions in the air. Three ampoules per each type of dodecanes were placed in a mechanical agitator device and stirred magnetically at room temperature for 1 h. Another set of three ampoules per each type of dodecanes was carried out at 150°C, placed in an oil-bath and magnetically stirred for 1 h. The reaction temperature was selected according to the temperature reached by the elastomeric composites during the mixing. After the reaction, the ampoules were dipped in cold water to immediately stop the reaction. The resulting KNN particles from each ampoule were then filtered from the reaction mixture, washed with TetraHydroFuran (THF), dried in an oven at 70°C for 24 h and then analysed.

ThermoGravimetric Analysis (TGA 550, TA Instruments, New Castle, Delaware, USA) and Fourier Transform Infrared spectroscopy (FT-IR, Perkin Elmer Spectrum, Milan, Italy) measurements were performed on KNN treated with epoxy- and nitrile-dodecanes at room temperature and at 150°C to assess the interaction between KNN and the functional groups of the dodecanes. For TGA analysis, ca. 10 mg of KNN particles were analysed in the temperature range of 30 to 620°C, with a heating rate of 10°C/min under a nitrogen atmosphere. FT-IR measurements were carried out with 10 mg of KNN particles finely ground with 90 g of KBr in a mortar. A further analysis was performed using a Diffuse Reflectance Infrared Fourier Transform Spectroscopy DRIFTS mode in the region from 4000 to 400 cm^{-1} with a resolution of 4 cm^{-1} and 64 individual scans. Each collected spectrum was measured in ambient air, using pure KBr as a background spectrum.

8.2.3.   Sample preparation

All the composites were prepared using a equipments and two-stage mixing procedure described in Chapter 7. The curing characteristics of the composites were analysed according to the description in Chapter 7.

8.2.4.   Sample characterisations

A contact poling process was applied to the elastomeric composites in a form of a cylinder of a 20 mm diameter and a 0.5 mm thickness. A detailed description of this procedure is explained in Chapter 7.

The piezoelectric coefficient d_{33}[pC/N] was measured according to the description given in Chapter 7.

The conductivity and dielectric constant of the gum rubbers and the elastomeric composites were measured using a Broadband Dielectric Spectrometer BDS with an

Alpha-A high performance frequency analyser produced by Novocontrol Technologies (Montabaur, Germany) with the conditions described in Chapter 7.

Tensile tests were performed using equipment and conditions reported in Chapter 7.

8.3. Results and Discussion

8.3.1. Chemical model study

A chemical model study was carried out on KNN particles in order to confirm its possible interfacial interactions between acrylonitrile groups of NBR and epoxide groups of ENR. Chemical methods like Nuclear Magnetic Resonance NMR, Liquid Chromatrography LC, Gas Chromatography GC and Mass Spectroscopy MS are difficult to apply to elastomeric vulcanisates. Therefore, low molecular weight model compounds like dodecanes can be employed to elucidate the mechanism and kinetics of the elastomeric chain with the fillers. In this study, two dodecanes with epoxide groups and acrylonitrile groups were utilised as model substances for ENR and NBR, respectively. Their interaction with the KNN filler was investigated.

In Figure 1a, the TGA of the KNN untreated and treated with epoxy- and nitrile-dodecanes is shown. For pure KNN, the first weight drop occurs at 50-120°C due to the water adsorption by the polar KNN. The second weight drop of pure KNN is above 500°C due to the that KNN degradation. For all the treated KNNs, whether at room temperature or at 150°C, the first weight drop is directly observed at 350°C due to the degradation of the polymer itself. In this case, there is no water evaporation due to the thermal treatment of the KNN particles. For these samples, the second weight loss occurs above 500°C, in line with pure KNN. The total weight loss of the sample treated at 150°C is slightly lower than that of pure KNN as well as that of the sample treated at room temperature. This can be because of thermal treatment as well as the interfacial connection between KNN with the epoxy and acrylonitrile groups at this high temperature, resulting in the higher loss of the attached hydrocarbon dodecanes modified with polar groups, compared to the ones at low temperature. Overall, it is possible to conclude that the weight losses of these treated samples are relatively small, less than one percent compared to pure KNN. This means that the interactions between the KNN and the epoxy and acrylonitrile functionalities are more likely ionic or dipole-dipole interactions rather than a covalent chemical bond. The evidence that there is no covalent bond between the KNN and the polar groups epoxy and acrylonitrile is confirmed by the FT-IR plots in Figure 1b. The only differences from pure KNN and treated KNN are the peaks at 2800-2900 cm^{-1}. Those are the peaks of the pure epoxy- and nitrile-dodecanes due

to C-H stretching vibration. This confirms the presence of the polymer on the KNN surface due to ionic or dipole-dipole interactions between KNN and the polar groups.
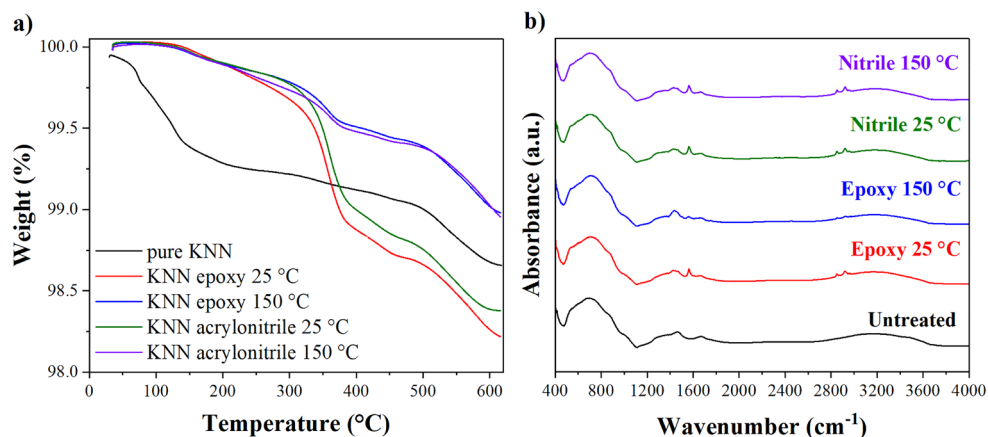

Figure 1   (a) TGA plots and (b) FT-IR spectra of KNN untreated and treated with epoxy- and acrylonitrile-dodecanes at 25 and at 150°C.

In the crystal structure of KNN, Niobium Nb is coordinated via covalent bonds with 6 oxygen atoms, forming an octahedra, and the cations sodium Na^+ and potassium K^+ are positioned in the corner of the unit cell, forming an ionic bond with the 12 surrounding oxygen atoms. The Nitrogen N of acrylonitrile groups of NBR as well as the oxygen O of the epoxide groups of ENR are electronegative and have free pairs of electrons. When KNN is mixed with these two rubbers (or the related dodecanes as model substances), Na^+ and K^+ are attracted by the electrons of the N and O due to the electrostatic forces, forming an ionic interaction. These interactions can create a relatively stable configuration, which is able to influence the vulcanisation and mechanical properties of these elastomeric composites. The entity of this influence depends on the mixing conditions and the ion concentration. Hence, in the following paragraph an elucidation of this phenomenon is explained. In Figure 2, the proposed interactions between the KNN and the rubbers NBR and ENR are shown.

In TGA in Figure 1a, the curves of the untreated and treated KNN confirm the absorption of water on the surface of KNN. Water can potentially form a dipole-dipole interaction with the Nitrogen N of the acrylonitrile group and the oxygen of the epoxide group via the hydrogen atoms. This interaction is very unlikely for happening due to the release of water during the mixing at a temperature above 100°C.
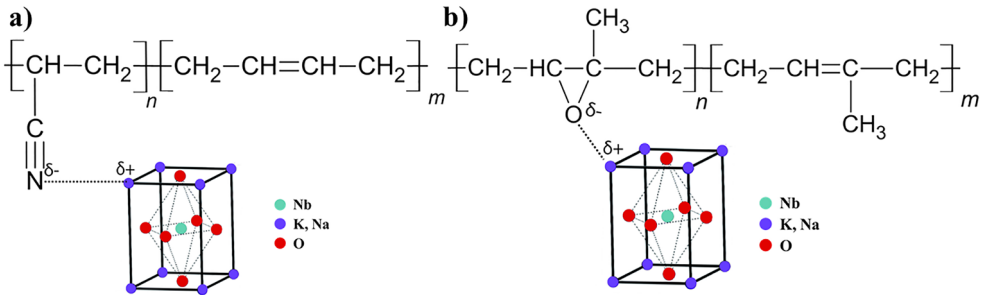
Figure 2   Proposed chemical interaction between KNN with (a) NBR and (b) ENR.

8.3.2.   Processability

The mixing fingerprints showing the mixing torques and temperatures of the composites based on ENRs (ENR-25 and ENR-50) and NBRs (NBR-28 and NBR-50) with 10-40 vol% of KNN are presented in Figure 3.
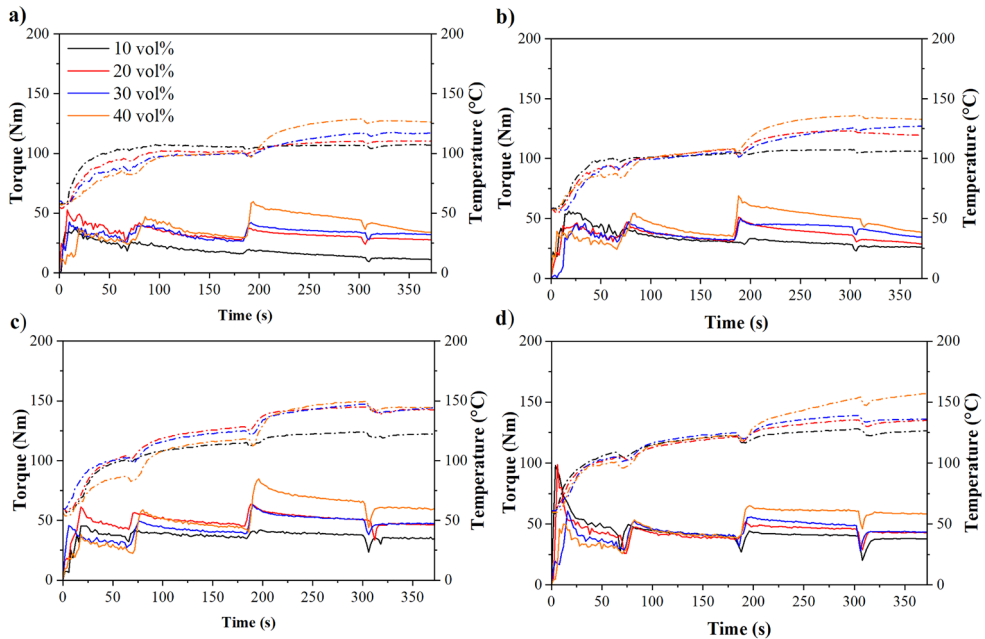

Figure 3   Mixing torques (solid lines) and temperatures (dotted lines) of elastomeric composites based on (a) ENR-25, (b) ENR-50, (c) NBR-28 and (d) NBR-50 and KNN amounts from 10 to 40 vol%.

During the first minute, the mixing torques decrease due to the rubber mastication and consequently reduced viscosity. After that, KNN and the plasticiser were added to the internal mixer in two portions. The initial rise in the torque is referred to the dosing of KNN filler into the rubber, followed by a progressively lowered torque

due to an ongoing filler incorporation into the elastomer matrix and improving KNN dispersion. The addition of higher volume fractions of KNN increases the mixing torque and masterbatch viscosity, primarily due to the hydrodynamic effect. The higher viscosity of the masterbatch results in greater shearing forces and heat generation during this mixing process, and thus a higher mixing temperature. This effect is particularly visible after the addition of the second portion of KNN and plasticiser, i.e. at around 180 s. When adding the first portion of KNN and plasticiser, the masterbatches with lower KNN amounts show higher temperatures, because the mixing chamber was initially filled with higher amounts of rubber, leading to higher fill factors, and hence higher shearing forces in the chamber. Generally, elastomeric composites slightly differ depending on the rubber type. However, it is possible to confirm the results of a previous publication [21]: ENRs composites show lower mixing torques while dispersing KNN particles, although raw ENRs have an initial higher viscosities than raw NBRs. This reflects the better compatibility between ENRs and KNN.
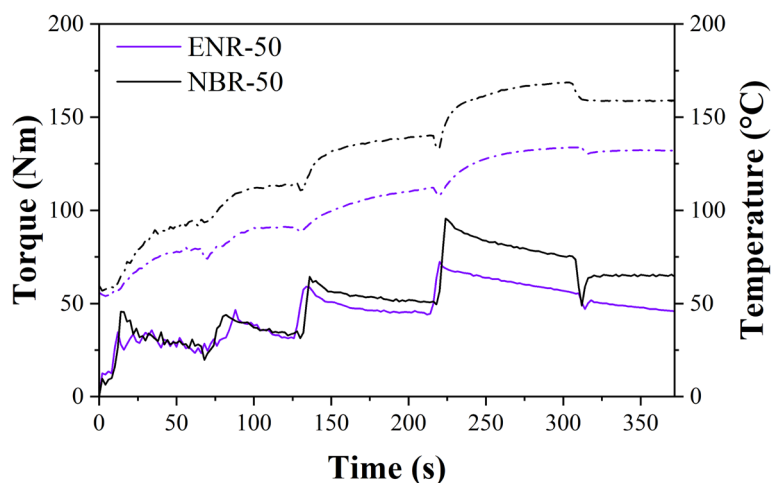
Figure 4   Mixing torques (solid lines) and mixing temperatures (dotted lines) of elastomeric composites comprising ENR-50 and NBR-50 filled with 50 vol% of KNN.

ENR-50 and NBR-50 were also filled with 50 vol% of KNN; the mixing torque and temperature are reported in Figure 4. Due to the high KNN amount, the mixing procedures for these composites were different. After the rubber mastication, KNN and the plasticiser were pre-mixed and divided into three portions. Each portion was added to the mixer and mixed for 1 min for the first portion and 1.5 min for the following two portions. The trend follows the results of Figure 3. Additionally, in Figure 4, the ENR-50 composite exhibits a lower mixing torque and temperature

compared to the NBR-50 one, due to better KNN-ENR compatibility, as above-mentioned.

8.3.3. Curing behaviour

Figure 5 shows the rheocurves of elastomeric composites based on ENR-25 and NBR-28 filled with 10 to 40 vol% KNN amounts and ENR-50 and NBR-50 filled with 10 to 50 vol% of KNN. The main parameters derived from the cure curves are: Minimum torque (M_L), torque difference (M_H - M_L) and optimum curing time (t_{c90}).
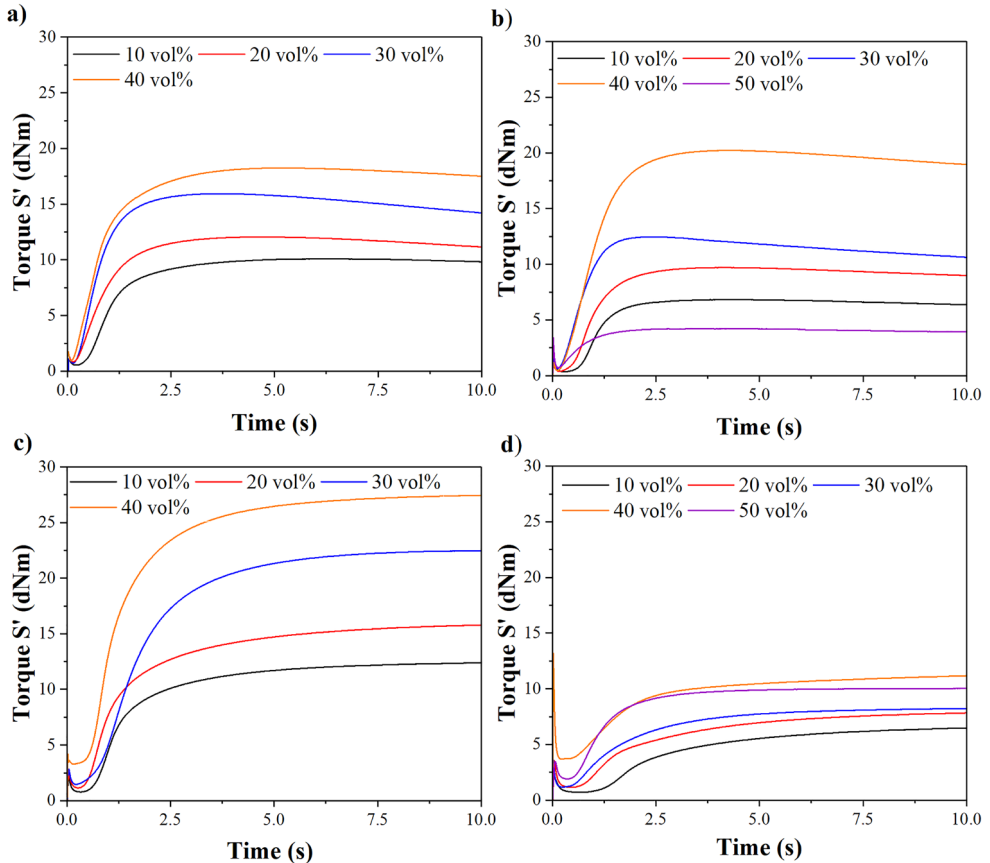

Figure 5   Curing characteristics of elastomeric composites including (a) ENR-25, (b) ENR-50, (c) NBR-28 and (d) NBR-50 with 10-50 vol% of KNN.

The minimum torque M_L is an indication of the composite viscosity at the set cure temperature. The minimum torque increases with increasing filler amount for all rubber types, due to the hydrodynamic effect caused by the added filler particles.

However, it is noticeable that NBR-50 filled with 50 vol% of KNN presents a lower minimum torque compared to the one at 40 vol% KNN. This is because this composite was mixed with a different procedure due to its high-volume fraction of KNN. It was prepared with three mixing steps, instead of two mixing steps for other composites, as shown in Figure 4. More steps of mixing can lead to more chain scissions of the rubber, better dispersion of the filler and so reduced viscosity.

The torque difference (M_H - M_L) primarily indicates the stiffness of the elastomeric composites influenced by the crosslink density, filler-filler and filler-rubber interactions. Moreover, this parameter also indicates the stiffness of the elastomeric composites influenced by these interactions.

With increasing amount of KNN in the composites, the filler-filler and the rubber-filler interactions increases (as seen in chemical model study), playing a significant role in enhancing the torque difference. In this case, the ENR-50 and NBR-50 composites with 50 vol% of KNN show different values of the torque difference due to the different mixing procedure as previously mentioned. When compared to NBR-50 filled with 50 vol% of KNN, ENR-50 with 50 vol% of KNN shows a lower torque difference. Two factors contribute to this phenomenon. Firstly, the crosslink density decreases since the reactive crosslinking sites decrease with increasing functionality level. Secondly, ENR-50 has a better compatibility with KNN compared to NBR-50, as shown in the Chapter 7 [21] and in chemical model study in Figure 2. This leads to smaller clusters and better dispersion of KNN, and therefore lower torque difference of the ENR-50 composite.

By comparing ENR-25 (Figure 5a) with ENR-50 (Figure 5b) and NBR-28 (Figure 5c) with NBR-50 (Figure 5d) filled with 10-40 vol% of KNN (i.e. same mixing procedure), it is possible to observe the effect of rubber polarity on the rheocurves. With increasing polar group content in ENRs and NBRs, the torque difference decreases. This can be linked to the diminished filler-filler interaction and better compatibility between a more polar elastomer and KNN particles as discussed earlier in the Chapter 7 [21,22].

The cure rate of the elastomeric composites determines the kinetics of the sulphur crosslinking reaction of elastomer chains in the composites: the higher the slope, the faster the cure rate. Increasing the KNN amount in the composites leads to an increase in the cure rate due to the increased heat conductivity by KNN in the elastomeric composites as well as better rubber-filler interactions [23,24], boosting the crosslinking reaction.

8.3.4.   Poling study

As reported Chapter 7 [21], the poling study was conducted for composites only filled with 30 vol% of KNN. Based on the measured piezoelectric constants d_{33} after the poling process, the optimal poling conditions of KNN-based elastomeric composites were selected.

The selected poling temperature was 25°C. Temperatures above 25°C result in an excessive current flow through the composite, reducing the effective electrical field experienced by the ceramic particles. This is due to the strong polarisation of the polar chemical groups of NBR and ENR. Owing to the strong polarity of the rubbers selected for this study, a high dielectric constant as well as a high intrinsic electrical conductivity were obtained. Applying an electric field of 5 kV/mm for 5 min resulted in the full polarisation of the piezoelectric elastomeric composites. More details and explanations for selecting these conditions are reported in Chapter 7 [21].
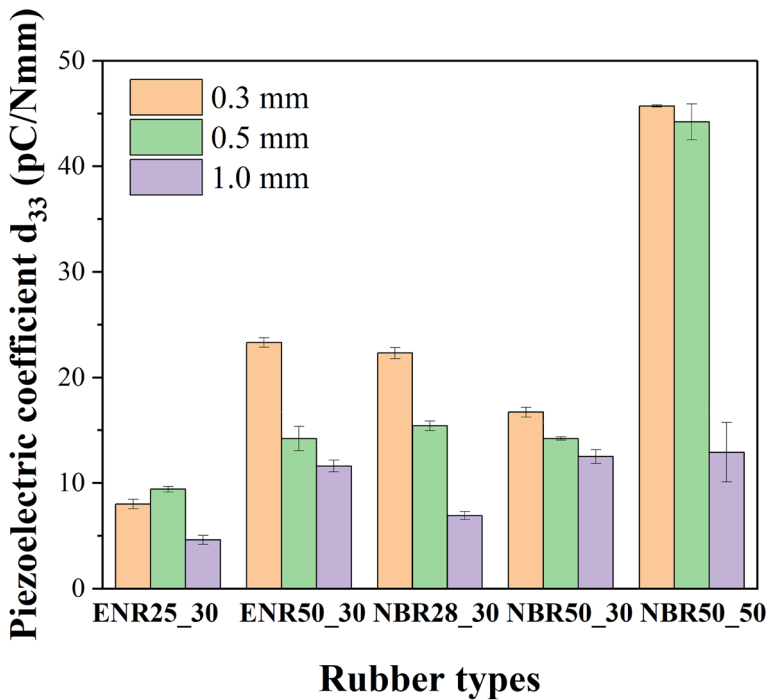
Figure 6   Piezoelectric coefficients of poled elastomeric composites including ENRs and NBRs with three different thicknesses: 0.3 mm (orange), 0.5 mm (green) and 1 mm (violet). Note that the composites NBR50_50, 1 mm thick, was poled at 2 kV/mm as poling electrical field, while the all the other composites at 5 kV/mm.

Figure 6 shows the piezoelectric coefficients of ENR-25, ENR-50, NBR-28 filled with 30 vol% of KNN and NBR-50 filled with 30 and 50 vol%. All composites were

vulcanised and polarised at three different thicknesses, i.e. 0.3, 0.5 and 1 mm. The thinner the elastomeric composites are, the higher becomes the piezoelectric coefficient. This is related to the dielectric constant and the electrical conductivity of the elastomers used in this study. For all elastomeric composites filled with 30 vol%, the difference in the piezoelectric coefficient for varied thicknesses is small. This is due to the synergistic effect of strong polarisation of the epoxide and acrylonitrile groups. When NBR-50 is filled with 50 vol%, the piezoelectric coefficient drastically decreases when increasing the sample thickness from 0.3 and 0.5 mm to 1 mm. This is due to the increased electrical conductivity of the composites when filled with such high amount of KNN (as explained below in Figure 8). Increasing the thickness of the material, it is difficult to polarise a conductive material. The interactions with KNN and the acrylonitrile group increase the dielectric constant as well as the electrical conductivity of the composites. Hence, the effective electric field that the KNN particles are subjected is much lower and, in turn, the piezoelectric coefficient is lower at higher thickness.

In composites, the ferroelectric ceramic requires a certain value of electrical field for a complete alignment. For NBR-50 filled with 50 vol% of KNN, it was only possible to apply an electrical field of 1-2 kV/mm to 1 mm thick samples. Higher electrical fields over this range create a short circuit in the composites. Although the time was varied from 5 min to 2 and 3 h, the piezoelectric coefficient remains low, as visible from Figure 6. When decreasing the thickness of NBR-50 with 50 vol% of KNN to 0.3 and 0.5 mm, an electrical field of 4-5 kV/mm was applied, resulting in a full polarisation of the composites. Although at 0.3 and 0.5 mm the samples exhibit similarly high piezoelectric properties, however, with the 0.5 mm thickness, the sample is easier to handle. This is mainly valid for the preparation and analysis of the KNN-based piezoelectric energy harvesters. Thus, the 0.5 mm thick sample was chosen for the next investigations.

8.3.5. Piezoelectric properties

To predict the piezoelectric coefficient d_{33} Yamada model was used:

$$d_{33,r} = \frac{\alpha \varphi n \varepsilon_r}{n \varepsilon_r + (\varepsilon_f - \varepsilon_r)} d_{33,f} \qquad (1)$$

where α is the poling efficiency, φ is the volume fraction of ceramic particles in the composite, n is the shape factor of KNN. ε and d_{33} are the dielectric constant and piezoelectric coefficient, respectively, and the indices f and r are relative to the filler and the composite. The poling efficiency α was considered as unity. The shape factor n of KNN was calculated from the SEM image reported in Chapter 7 [21]. A value

of 4 was considered. The measurement of the dielectric constant of the pure rubber ε_r was reported in [21] and in Chapter 7. At 100 Hz the dielectric constants of gum ENR-25, ENR-50, NBR-28 and NBR-50 were 5.2, 9.8, 12.25 and 24.6, respectively. The piezoelectric coefficient and the dielectric constant of KNN particles are as follows: 80 pC/N and 250, respectively [25,26].
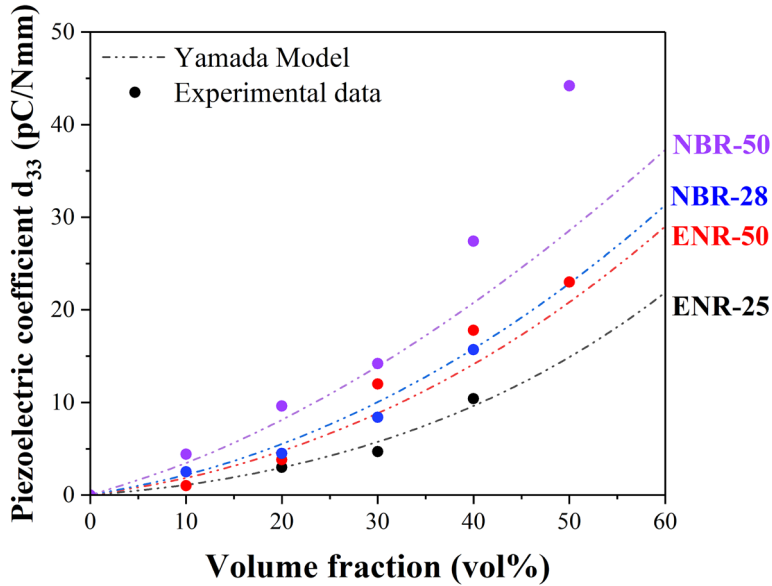

Figure 7   Piezoelectric coefficient of ENR-25 (black), ENR-50 (red), NBR-28 (blue) and NBR-50 (violet) as a function of KNN amount.

The piezoelectric coefficients of ENR and NBR-based elastomeric composites as a function of KNN volume fraction are reported in Figure 7. It includes both experimental and theoretical data predicted by using Yamada's model. One notable observation is that the piezoelectric coefficients predicted by Yamada's model are close to the experimental values for composites based on ENR-25 and NBR-28. For ENR-50, the piezoelectric constants are underestimated by Yamada's model. This mismatch results in much higher values for NBR-50. This result is also true for NBR filled with 40 and 50 vol% of KNN. This difference can be attributed to the increasing influence of rubber-filler interactions with increased rubber polarity as this parameter would contribute to higher piezoelectric performance of the composite. This parameter is not taken into account by the model. Therefore, the experimental values of highly polar NBR and ENR filled with high volume fractions of KNN results in underestimated values predicted by Yamada's model.

8

Among the elastomers studied, NBR-50 exhibits the highest values of the piezoelectric coefficient, followed by NBR-28, ENR-50 and ENR-25. This trend is due to the increased dielectric constant of the elastomeric matrix, that follows the same order: ENR-25 < ENR-50 < NBR-28 < NBR-50. The dielectric constant of the elastomeric matrix directly improve the poling process and the effective electric field acting on the KNN particles during the poling process. The higher the dielectric constant, the better is the polarisation of the piezoelectric ceramic. This leads to a higher piezoelectric coefficient. Figure 7 shows that the dielectric constant seems to be the determinating factor, compared to the impact of different compatibility levels between KNN and the rubber. Additionally, this remains valid even at high volume fraction of KNN.
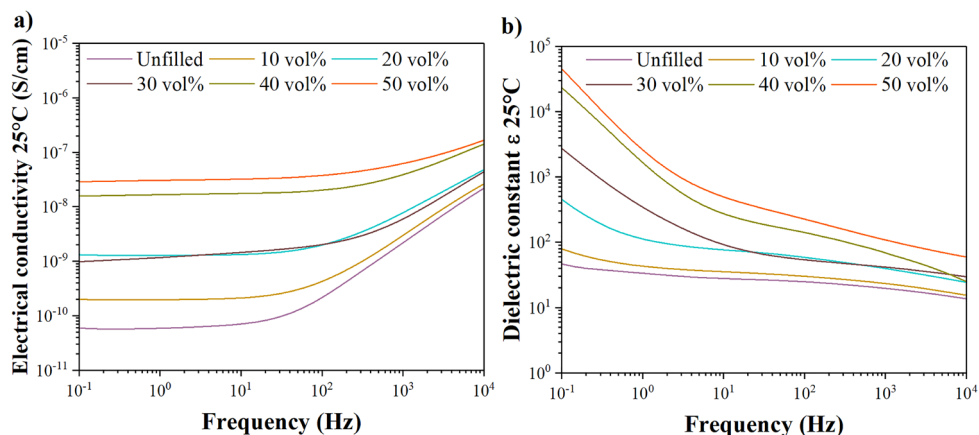
Figure 8   (a) Electrical conductivity and dielectric constant of NBR-50 unfilled and filled with increasing amount of KNN.

To further understand the higher piezoelectric coefficient of NBR-50 than the values predicted by Yamada's model, the electrical conductivity and dielectric constant were measured as a function of frequency with the Broadband Dielectric Spectroscopy (BDS). The electrical conductivity of NBR-50 unfilled and filled with increasing volume fractions of KNN is reported in Figure 8a. The conductivity decreases with decreasing frequency and reaches a plateau at low frequencies. The electrical conductivity exhibiting a plateau at low frequencies is known as Direct Current (DC) conductivity and follows a power-law dependency trend at high frequencies, known as Alternating Current (AC) conductivity. In polymers, the AC conductivity is expressed by the following power law equation:

$$\sigma(\omega) = \sigma_{DC} + A\omega^{s(T)} \tag{2}$$

where, $\sigma(\omega)$ is the measured AC conductivity by BDS, σ_{DC} is the DC conductivity, A is a temperature dependent constant representing the polarisability, ω is the

frequency, and *s(T)* is the power law exponent reflecting the interaction term between the mobile ions and the surrounding environment. The power law exponents depend on temperature, and the type and amount of filler in the composites [27]. It typically is between 0 and 1. They are usually obtained from the slope of Log-Log plots derived from Equation (2) [27].

Both AC and DC conductivities increase with an increasing volume fraction of KNN. This is due to the electrical charges hopping mechanism across the network of ferroelectric polar KNN and the polar groups of the elastomers (epoxide groups of ENR and acrylonitrile groups of NBR). This trend is in agreement with the findings from the poling study shown in Figure 6. The DC electrical conductivity of NBR-50 filled with 50 vol% of KNN is ca. 10^{-7} S/cm, belonging to the semi-conductor level. During the poling process, this elastomeric composite transfers the applied electric field outside the circuit, thereby reducing the effective electrical field to which the ferroelectric ceramics are subjected. Therefore, the thickness of the sample can be adjusted to control the effective electrical field.

In Figure 8b, the dielectric constant at varied frequencies of unfilled NBR-50 and its elastomeric composites with increasing KNN volume fraction is reported. The dielectric constant increases with an increasing addition of KNN. Generally, the dielectric constant of polymers depends on the orientation polarisation of polar groups in their structure, as well as on the interfacial polarisation occurring at the boundaries of the building blocks of the monomer units in the polymer chains. However, when filled with ferroelectric ceramic, the dielectric constant of the composites is predominated by the interactions between the elastomeric matrix and the filler [28]. In polymeric composites, at the molecular level, there is a reduction in polymeric chain mobility in proximity of the filler surface due to the filler aggregation and agglomeration. This results in a reduced density of polymeric chains near the filler, making them different from the bulk polymeric chains. Consequently, the interfacial region between the filler and the polymer affects the charge carriers' transportation when the composite is subjected to an electrical field, thereby impacting the dielectric constant of the composites. The addition of a filler with a high dielectric constant also leads to a higher interfacial polarisation, known as the Maxwell-Wagner-Sillars effect [29,30]. Finally, in Figure 8b, with increasing the KNN amount, the dielectric constant of the composites increases, because the ceramic particles become closer to each other and exhibit higher interfacial polarisation under externally applied electrical fields.

8

8.3.6. Mechanical properties

The change in the mechanical characteristics of elastomeric composites with increasing amount of KNN are shown in Figures 9 and 10. The addition of reinforcing fillers in elastomers generally improves the stress-strain properties. Although KNN has a particle size larger than 1 μm, the ionic or dipole-dipole interactions between ENR or NBR and KNN can affect the mechanical properties of these composites.

rubber with the higher concentrations of functional groups are lower, leading to softer elastomeric composites.
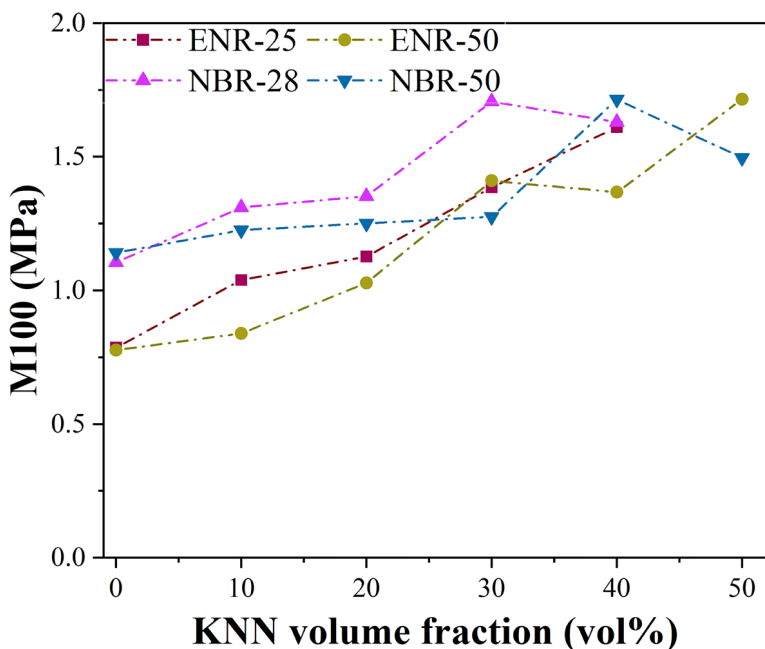
Figure 9   Stress-strain modulus at 100% (M100) of elastomeric composites with varying amounts of KNN.

For all ENRs and NBRs, the modulus at 100% strain M100 increases with increasing filler content. This is mainly due to the influence of the hydrodynamic effect of the added filler. In both rubber types, the modulus at 100% strain decreases with increasing epoxide content in ENR and acrylonitrile content in NBR. This can be explained by the same reasons given to the decreased stiffness, maximum torque and torque difference with increasing rubber polarity as shown in Figure 5. As the polar functional groups increase, the double bonds serving as crosslinking sites in ENRs and NBRs decrease. Consequently, it is expected that the crosslink densities of the

rubber with the higher concentrations of functional groups are lower, leading to softer elastomeric composites.

The tensile strength and elongation at break of the composites are presented in Figures 10a and 10b. These properties show different trends for the NBR and ENR-based composites. For both NBRs, the tensile strength and the elongation at break increase from unfilled to a filled compound with 10 vol%.
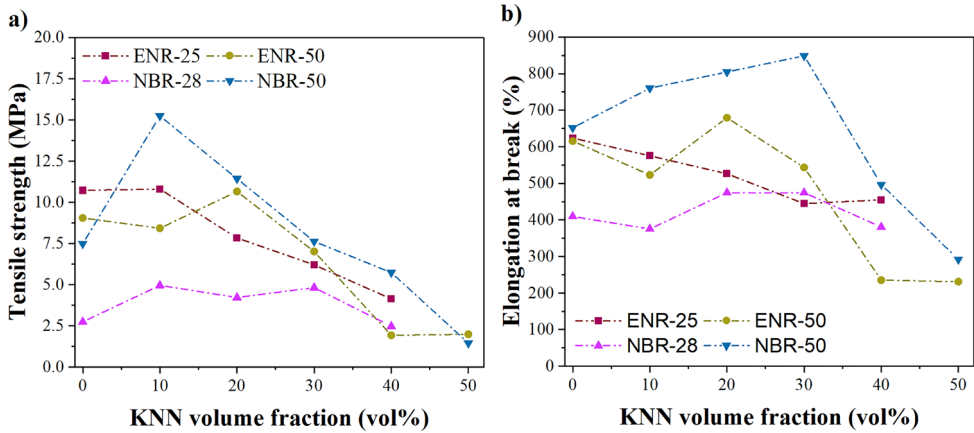

Figure 10 Stress-strain properties: (a) Tensile strength and (b) elongation at break of elastomeric composites with varying amounts of KNN.

The tensile strength values of NBR-28 filled with higher KNN amounts in the range of 10 to 30 vol% show further increased values compared to the unfilled rubber, while a decreased trend above 30 vol%. For NBR-50, the tensile strength decreases above 10 vol% of KNN. These trends are similar for the elongation at break values for both NBR rubbers (Figure 10b), but the changes occur at different KNN volume fractions. The elongation at break of NBR-28 and NBR-50 increases when adding KNN up to 30 vol% and after that drops. For both ENRs, the tensile strength and elongation at break directly decrease from unfilled to the filled compound. ENR-25 shows a decreasing tensile strength and elongation at break with increasing KNN volume fraction above 10 vol%, while for ENR-50 the tensile strength and the elongation at break decrease above 20 vol%.

The differences in tensile strength and elongation at break of the elastomeric composites are due to the stiffness related to an expected change in the polymer network density and the polymer-filler interactions. It is likely that, for ENR-25, the lower epoxide content lead to an insufficient compatibility between KNN and the rubber resulting in weak rubber-filler interaction and causes the continuous decrease

8

in tensile strength and elongation at break with increasing KNN quantity. For NBR-28 no drastic changes are visible. Whilst, for NBR-50 and ENR-50 based composites, the balance between changed mixing conditions, varying crosslink density and stronger interactions with KNN contributes to a high levels of the tensile strength and elongation at break at certain KNN amounts.

8.4.   Conclusions

Piezoelectric composites consisting of modified natural rubbers and synthetic elastomers as matrices and ferroelectric ceramic KNN as ferroelectric particles were investigated. A chemical model study was firstly carried out, considering KNN mixed in epoxy- and nitrile-dodecanes. From this, it results that the cations Na^+ and K^+ of KNN can create ionic or dipole-dipole interactions with the Nitrogen of acrylonitrile group and the Oxygen of epoxide group. This can result in relatively strong rubber-filler interactions of ionic nature, although the higher particle size of KNN.

In the ferroelectric composites, the increasing amount of KNN, between 10 and 50 vol% in the elastomeric composite affects the processing, poling process, and most importantly the piezoelectric properties. The value of this thickness of the composite was selected according to its better poling efficiency. Due to the most efficient poling process and handling, elastomeric composites with 0.5 mm thickness were prepared, polarised, and analysed. With an increasing KNN amount, the piezoelectric coefficient increases. Elastomers with a higher polarity, ENR-50 and NBR-50, when filled with 50 vol% of KNN, reach high values of piezoelectric coefficient, i.e. 20 and 45 pC/N, respectively. The difference in piezoelectric coefficient values is mainly due to the difference in their dielectric constants. The mechanical properties were also measured.

8.5. References

[1] I.A.H. Al-Najati, K.W. Chan, S.Y. Pung, Tire strain piezoelectric energy harvesters: a systematic review, Int. J. Power Electron. Drive Syst. 13 (2022) 444–459. https://doi.org/10.11591/IJPEDS.V13.I1.PP444-459.

[2] M. Germer, U. Marschner, A. Richter, Energy Harvesting for Tire Pressure Monitoring Systems from a Mechanical Energy Point of View, IEEE Internet Things J. 9 (2022) 7700-7714. https://doi.org/10.1109/JIOT.2022.3152547.

[3] J. Ghazanfarian, M.M. Mohammadi, K. Uchino, Piezoelectric Energy Harvesting: A Systematic Review of Reviews, Actuators. 10 (2021) 312. https://doi.org/10.3390/ACT10120312.

[4] H. Khanbareh, V.Y. Topolov, C.R. Bowen, Piezo-active composites: Classification and effective physical properties, Springer Ser. Mater. Sci. 283 (2019) 1–23. https://doi.org/10.1007/978-3-030-19204-4_1.

[5] P. Eltouby, I. Shyha, C. Li, J. Khaliq, Factors affecting the piezoelectric performance of ceramic-polymer composites: A comprehensive review, Ceram. Int. 47 (2021) 17813–17825. https://doi.org/10.1016/J.CERAMINT.2021.03.126.

[6] C.R. Bowen, H.A. Kim, P.M. Weaver, S. Dunn, Piezoelectric and ferroelectric materials and structures for energy harvesting applications, Energy Environ. Sci. 7 (2014) 25–44. https://doi.org/10.1039/C3EE42454E.

[7] Ferroelectric Materials for Energy Applications, Ferroelectr. Mater. Energy Appl. (2018). https://doi.org/10.1002/9783527807505.

[8] J. Rödel, K.G. Webber, R. Dittmer, W. Jo, M. Kimura, D. Damjanovic, Transferring lead-free piezoelectric ceramics into application, J. Eur. Ceram. Soc. 35 (2015) 1659–1681. https://doi.org/10.1016/j.jeurceramsoc.2014.12.013.

[9] L. Liu, X. Guo, W. Liu, C. Lee, Recent progress in the energy harvesting technology-from self-powered sensors to self-sustained iot, and new applications, Nanomaterials. 11 (2021) 2975. https://doi.org/10.3390/nano11112975.

[10] J.F. Tressler, L. Qin, K. Uchino, 7.21 Piezoelectric Composite Sensors, Compr. Compos. Mater. II. (2018) 408–419.
https://doi.org/10.1016/B978-0-12-803581-8.03937-0.

[11] K. Maity, D. Mandal, Piezoelectric polymers and composites for multifunctional materials, Adv. Light. Multifunct. Mater. (2021) 239–282.
https://doi.org/10.1016/B978-0-12-818501-8.00001-9.

[12] J. Yvonnet, Piezoelectricity, Solid Mech. Its Appl. 258 (2019) 91–102. https://doi.org/10.1007/978-3-030-18383-7_5.

[13] K.H. Mak, S. McWilliam, A.A. Popov, Piezoelectric energy harvesting for tyre pressure measurement applications, Proc. Inst. Mech. Eng. Part D J. Automob. Eng. 227 (2013) 842–852. https://doi.org/10.1177/0954407012463849.

[14] Z. Yang, S. Zhou, J. Zu, D. Inman, High-performance piezoelectric energy harvesters and their applications, Joule. 2 (2018) 642–697.
https://doi.org/10.1016/j.joule.2018.03.011.

8

[15]   C. Mangone, M. Klein Gunnewiek, L. Reuvekamp, W. Kaewsakul, A. Blume, Method for chemically adhering a diene rubber to a piezoelectric polymer, WO/2021/052951, 2021.

[16]   C. Mangone, W. Kaewsakul, M. Klein Gunnewiek, A.P.J. van Swaaij, L. Reuvekamp, J.W.M. Noordermeer, A. Blume, Design and performance of flexible polymeric piezoelectric energy harvesters for battery-less tyre sensors, Smart Mater. Struct. (2022) 095034.

[17]   C. Mangone, W. Kaewsakul, A.P.J. van Swaaij, K. Bandzierz, M.K. Gunnewiek, A. Blume, Dynamic measurement setups for validating piezoelectric energy harvesters in driving conditions, Polym. Test. 119 (2023) 107932. https://doi.org/10.1016/J.POLYMERTESTING.2023.107932.

[18]   S. Bauer, F. Bauer, Piezoelectric polymers and their applications, in: Springer Ser. Mater. Sci., Springer Verlag, 2008: pp. 157–177. https://doi.org/10.1007/978-3-540-68683-5_6.

[19]   Y. Saito, H. Takao, T. Tani, T. Nonoyama, K. Takatori, T. Homma, T. Nagaya, M. Nakamura, Lead-free piezoceramics, Nature. 432 (2004) 84–87. https://doi.org/10.1038/nature03028.

[20]   A.O. Sanches, J.A. Malmonge, W.K. Sakamoto, Piezoelectric composites: Fabrication, characterization, and its application as sensor, Recent Adv. Complex Funct. Mater. From Des. to Appl. (2017) 195–215.

[21]   C. Mangone, W. Kaewsakul, A. Tuluk, M.D. Nguyen, K. Bandzierz, A. Blume, Flexible lead-free piezoelectric composites: processing parameters and effect of elastomer polarity, Prep. (2023).

[22]   S. Sattayanurak, K. Sahakaro, W. Kaewsakul, W.K. Dierkes, L.A.E.M. Reuvekamp, A. Blume, J.W.M. Noordermeer, Enhancing performance of silica-reinforced natural rubber tyre tread compounds by applying organiclay as secondary filler, Rubber Chem. Technol. 94 (2021) 121–144. https://doi.org/10.5254/RCT.20.80373.

[23]   S.M. Hosseini, M. Razzaghi-Kashani, Catalytic and networking effects of carbon black on the kinetics and conversion of sulfur vulcanization in styrene butadiene rubber, Soft Matter. 14 (2018) 9194–9208. https://doi.org/10.1039/C8SM01953C.

[24]   C.G. Robertson, N.J. Hardman, Nature of Carbon Black Reinforcement of Rubber: Perspective on the Original Polymer Nanocomposite, Polym. 2021, 13 (2021) 538. https://doi.org/10.3390/POLYM13040538.

[25]   N.K. James, D.B. Deutz, R.K. Bose, S. van der Zwaag, P. Groen, High piezoelectric voltage coefficient in structured lead-free (K,Na,Li)NbO3particulate—epoxy composites, J. Am. Ceram. Soc. 99 (2016) 3957–3963. https://doi.org/10.1111/jace.14428.

[26]   D.B. Deutz, N.T. Mascarenhas, S. van der Zwaag, W.A. Groen, Poling piezoelectric (K,Na,Li)NbO3-polydimethylsiloxane composites, 515 (2017) 68–74. https://doi.org/10.1080/00150193.2017.1360110.

[27]   A.K. Jonscher, The 'universal' dielectric response, Nat. 1977 2675613. 267 (1977) 673–679. https://doi.org/10.1038/267673a0.

[28]   I. Popov, S. Cheng, A.P. Sokolov, Broadband Dielectric Spectroscopy and Its Application in Polymeric Materials, Macromol. Eng. (2022) 1–39. https://doi.org/10.1002/9783527815562.MME0059.

[29]   R. Wang, C. Xie, S. Luo, B. Gou, H. Xu, L. Zeng, The influence mechanism of nanoparticles on the dielectric properties of epoxy resin, RSC Adv. 9 (2019) 19648–19656. https://doi.org/10.1039/C9RA02889G.

[30]   M. Iwamoto, Maxwell–Wagner Effect, Encycl. Nanotechnol. (2015) 1–13. https://doi.org/10.1007/978-94-007-6178-0_5-2.

8

Chapter 9

Advancing elastomeric composites for piezoelectric energy harvesters

Elastomeric piezoelectric energy harvesters for battery-less tyre sensors have been developed. They include two components: a piezoelectric composite and an electrically conductive elastomer as an electrode. The composite was made out of a polar elastomer, i.e. Epoxidised Natural Rubber (ENR) and acryloNitrile Butadiene Rubber (NBR), filled with polycrystalline ferroelectric ceramic $K_{0.5}Na_{0.5}NbO_3$ (KNN). The poling process of the piezoelectric composite wa carried out when co-cured with elastomeric electrodes as well as gold sputtered electrode. The chemical adhesion of the two components, i.e. piezoelectric composite and conductive elastomer, is important for the poling process and the piezoelectric properties. Compared to the gold electrode, the newly developed piezoelectric elastomeric harvesters were effectively poled within shorter time by applying a lower electrical field. The piezoelectric coefficients of ENR with 50 mol% of epoxy groups (i.e. ENR-50) and of NBR with 50 wt% of acrylonitrile groups (i.e. NBR-50) filled with 50 vol% of KNN were doubled in comparison to the gold-electroded composites, due to the chemical adhesion between the piezoelectric composite and the conductive elastomer. The output voltage and the output power of the piezoelectric energy harvesters were measured using a Dynamic Mechanical Analysis (DMA) by simulating tyre-rolling conditions. ENR-50 was selected for a further study due to the better chemical adhesion with the conductive elastomer. The harvester including ENR-50 with 50 wt% of KNN was estimated to generate 0.14 $\mu W/cm^2$. An area of 200 cm^2 of this harvester is sufficient to successfully power a tyre sensor.

9

Chapter 9

9.1.   Introduction

Over the last decades, piezoelectric energy harvesters have received increasing attention for providing sustainable energy, that can be used in smart sensors [1-4]. Piezoelectric energy harvester includes two components: a piezoelectric material itself and an electrode. Piezoelectric materials can generate electrical energy during deformation. These materials are characterised by a non-centrosymmetric structure, that results in two opposite charged sides: positively and negatively. By applying an electrode on both sides of the piezoelectric material under deformation, a flow of electrical current is enabled. This current can then be stored in a capacitor for self-powered sensors [5,6].

Among piezoelectric materials, the category of ferroelectric materials is most studied due to their high efficiency [7,8]. They are characterised by a spontaneous electric polarisation that can be oriented in a certain direction and remains permanent after having applied an electrical field. Piezoelectric ceramics have a polycrystalline structure, characterised by grains randomly oriented [11,12]. The category of this polycrystalline ceramic is also classified as ferroelectric because it presents piezoelectric properties only by aligning the grains in the same direction.

This study focuses on the development of a piezoelectric material for tyres. During running the vehicles, tyres are continuously subjected to dynamic deformations as well as vibrations and excitations [13,14]. This represents an attractive feature for piezoelectric materials. The repetitious deformation of the piezoelectric material, when installed as part of a tyre in an appropriate position, provides a potential to continuously produce electricity, that can then be stored in a capacitor of a sensor. An example of a sensor used in tyres is the Tyre Pressure Monitoring System (TPMS). The use of this device is growing due to the regulations established in Europe, USA and Asia [15]. This sensor, monitoring the tyre pressure, can indicate whether the running tyres are under or over-inflated. A variety of designs have been proposed to ensure a self-powered TPMS by using an energy harvester [14,16-20]. However, a piezoelectric material able to withstand the tyre-rolling conditions and generate enough electricity to power a sensor is not yet fully established.

Both categories of piezoelectric materials, polymers and ceramics, can be characterised by their flexibility and durability [13,14,20-27]. In this study, piezoelectric composites are taken into account, including a polycrystalline ferroelectric ceramic dispersed in a polymeric matrix. The type of the matrix and the ceramic as well as their ratio can be tailored according to the requirements of a

certain application [28-31]. In Chapter 7, piezoelectric composites including a highly polar elastomer, i.e. Epoxidised Natural Rubber (ENR) and acryloNitrile Butadiene Rubber (NBR), and the ceramic $K_{0.5}Na_{0.5}NbO_3$ were prepared [32]. It was proven that the use of elastomers with a high electrical conductivity shortens the poling process time (from 20 to 5 min) and decreases the electrical field from 10 to 5 kV/mm. Piezoelectric composites with a distinct piezoelectric coefficient of 45 pC/N were developed. For this poling process, specimens were sputtered with gold, and this metal was used as an electrode. Up to now, only metal electrodes have been applied to ferroelectric materials for their polarisation [33-39]. A metal electrode is susceptible to fracture and hence unable to be the optimal electrode for an energy harvester mounted in tyres. Additionally, the metal was always physically attached to the surface of the ferroelectric material. In Chapter 4, it was also proven that the chemical adhesion between the piezoelectric polymer PVDF and a conductive material, done after the poling process of PVDF, brings a substantially high output power [26].

This research aims to use a flexible electrode during the poling process of piezoelectric composites, replacing the gold-sputtered material. Piezoelectric composites including ENRs and NBRs filled with KNN particles were considered. As flexible electrode, an electrically conductive elastomer was selected due to its elastic nature and compatibility with tyre compounds. Generally, elastomers are insulating materials due to their hydrocarbon-based polymeric chains. Introducing conductive carbon black particles in the elastomeric matrix increases its electrical conductivity for the formation of a continuous conductive network [40-42]. Therefore, as the flexible electrode, a blend of Natural Rubber (NR) and Butadiene Rubber (BR) filled with 6 vol% of a high surface area and high structure carbon black was selected. These two components were chemically adhered by co-curing and the role of the chemical adhesion on the poling process was studied. The piezoelectric performance of the piezoelectric energy harvesters was investigated and discussed in this work.

9

9.2.   Experimental

9.2.1.   Materials

The raw materials were described in Chapter 7.

The electrically conductive composites included Natural Rubber (NR grade Technical Specified Rubber TSR20, Wurfbain Nordmann B.V., Zaandam, Netherlands) and high-cis branched Butadiene Rubber (BR grade 1280, LG Chem

Europe GmbH, Eschborn, Germany). The filler employed in this stage was Extra-Conductive Carbon Black (ECCB), tradename Ketjenblack EC-300J (Nouryon Specialty Chemicals, Deventer, the Netherlands). This carbon black has a specific Braunauer-Emmet-Teller (BET) surface area (ASTM D-6556) of 800 m^2/g and an Oil Adsorption Number (OAN) indicating the filler structure (ASTM D-2414) of 330 mL/100g.

Other compounding ingredients were of technical quality as described in Chapter 7.

9.2.2. Sample preparation

9.2.2.1. Piezoelectric composites

All the composites were prepared using the equipments and a two-stage mixing procedure reported in Chapter 7.

9.2.2.2. Electrically conductive composites

The formulations of the investigated electrically conductive composites are reported in Table 1. All the composites were prepared using the equipment and a two-stage mixing procedure reported in Chapter 6.

Table 1   Formulations of the conductive composites.

Ingredients	Amount (phr)
NR	25
BR	75
ECCB	15
TDAE	7.5
6PPD	1.5
TMQ	4.0
Stearic Acid	2
ZnO	5
α-Sulphur	1.5
TBBS	1.8

9.2.2.3. Preparation of piezoelectric energy harvester

The curing characteristics of the composites were analysed as described in Chapter 7.

The piezoelectric and conductive composites were assembled in a sandwich-like configuration by using a Wickert press WLP 1600 (Wickert Maschinenbau GmbH, Landau, Germany) at 170°C and 100 bar. This step was done in tensile sheets made

of structural steel. They included a 0.5 mm-thick steel sheets (for the piezoelectric composite) placed in between two 0.1 mm-thick sheets (for the elastomeric conductive composite). The resulting energy harvester had a total thickness of 0.7 mm. For the ENR-25, ENR-50 and NBR-28-based harvesters, cylinders of 20 mm diameter were then cut with a proper cutter. For NBR-50, cylinders of 5 mm were cut due to the inhomogeneous adhesion between the two components.

9.2.3. Sample characterisations

After having vulcanised the two components, contact poling was applied to the elastomeric composites in cylindrical shape of 20 mm diameter and 0.7 mm thickness. Moreover, the piezoelectric composites were also vulcanised in cylindrical shape of 20 mm diameter and 0.5 mm thickness and gold electrodes were sputtered through a shadow mask on both sides of the cylindrical composites with a sputter coater (QuorumQ300T, East Sussex, UK). Details of the poling process were reported in Chapter 7.

The piezoelectric coefficient d_{33} according to the description reported in Chapter 7 was analyzed.

The output voltage and output power generated by the piezoelectric patch and the electrical conductivity were monitored using in-house developed setups. They consisted of Dynamic Mechanical Analysis DMA Eplexor 9 (Netzsch Gabo Instruments GmbH, Ahlden, Germany). Details of these setups are explained in Chapters 3 and 4 [26,27].

9.3.   Results and Discussion

9.3.1.   Conductive properties of elastomeric composites

Electrically conductive elastomers were used as electrode for the piezoelectric composites based on KNN-filled elastomers (i.e. ENRs and NBRs). In case of elastomers, incorporating carbon black in an insulating elastomer increases its electrical conductivity due to a hopping and tunnelling phenomena of charge carriers across the carbon black network [42,43]. The carbon black surface area, structure and amount are crucial for the electrical conduction mechanism [44]. In Figure 1, the electrical conductivity of the NR/BR blends filled with increasing amounts of ECCB is shown. The conductivity was measured under dynamic conditions at 10% of static strain and 2% of dynamic strain [44]. The depicted plot is known as a percolation plot, as it represents the transition of the material from an insulator with low conductivity (10^{-10} S/cm) to a conductor (10^{-2} S/cm). In this study, NR/BR filled

9

with 6 vol% of ECCB was used as the electrode for the developed energy harvester, as this is the minimum amount of carbon black rendering the optimum conductivity.
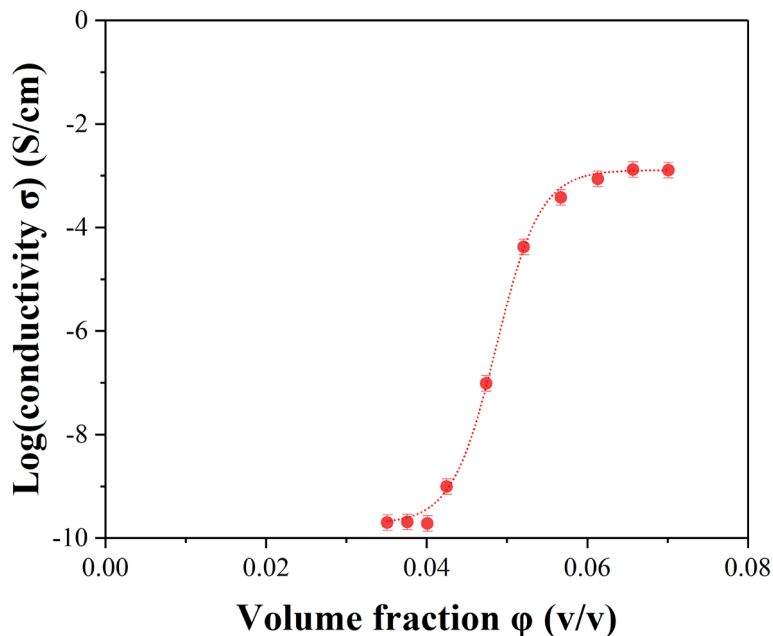

Figure 1   Percolation plot of NR/BR blends filled with increasing amounts of ECCB.

The electrical conductivity of the elastomeric composites with 6 vol% of ECCB was measured under static conditions as well, before starting the dynamic measurements. This resulted in a conductivity higher than 10^{-5} S/cm, which is already in the conductive region. It is reported in the literature that the electrical conductivity of a polymer filled with conductive fillers increases exponentially when an electrical field is applied [45,46]. Particularly, when the filler amount exceeds the percolation threshold, the electric-field-assisted tunnelling occurs across the conductive network. Thus, larger numbers of charge carriers pass through the conductive filler particle interphase. Depending on the filler amount, it exists a threshold value for the electrical field above which the conductivity of the composites increases drastically, i.e. 4 and 5 orders of magnitude, increasing the electrical field from 1 to 10 kV/mm [45,46].

9.3.2.   Poling study

Piezoelectric composites exhibit piezoelectric properties when the spontaneous polarisation is appropriately oriented by applying a high electrical field in a process called poling. The piezoelectric performance of these composites is highly

influenced by the degree of poling of the ceramic particles in an elastomeric matrix. In Chapter 7, it was proven that the poling field acting on the piezoelectric particles is influenced by the dielectric constant and conductivity of the matrix [32]. This is because these two parameters influence the effective electric field to which the ferroelectric ceramic particles are subjected. For the same reason, another potential parameter that influences the poling process is the chemical adhesion between the piezoelectric material and the electrode. In chaper 4, the piezoelectric polymer PVDF was chemically adhered with an electrically conductive elastomer [26]. This piezoelectric energy harvester was able to generate a high amount of power (of around 28 µW/cm^2 at 100°C and 100 Hz), thanks to the activation sites on the PVDF surface created with this chemical adhesion. The electrical current flows in a more efficient manner, compared to the gold electrodes. In Chapter 4, the chemical adhesion was done after the poling process of PVDF. The current research aims to investigate the effect of the chemical adhesion between the piezoelectric material and the electrode on the poling process.

In this study, the piezoelectric composite, including the rubbers ENR and NBR filled with KNN, were co-vulcanised with the conductive elastomer. The piezoelectric composites including ENR-25, ENR-50 and NBR-25 were vulcanised as cylinder with a diameter of 20 mm. However, NBR-50 filled with KNN had a lower compatibility with the conductive elastomer due to a large difference of the polarity of these harvester components. Therefore, for NBR-50 an elastomeric composite in cylindrical shape with a smaller diameter, i.e. 5 mm, was made. To investigate the effect of the different electrodes on the performance of the piezoelectric composites, the gold and elastomeric composite were compared. The poling study was carried out for all composites with varied amounts of KNN, in the range of 10-50 vol%. In Table 2 the investigated range of poling parameters (i.e. temperature, electric field, and time) are reported with their optimal values for a gold and elastomeric electrode. The optimal poling parameters correspond to the highest obtained values of the piezoelectric coefficient d_{33} of the piezoelectric harvesters.

9

The study reported in Chapter 7 revealed that the electrical conductivity and dielectric constant of the ENR and NBR rubbers are too high for carrying out the poling process at a higher temperature than 25°C [32] due to the strong polarisation of the polar chemical groups of the NBR and ENR rubbers. The electrical field was varied in the range of 1 and 6 kV/mm. When gold electrode is used, the piezoelectric composites are characterised by a piezoelectric coefficient that increases in the range of 1-5 kV/mm and remained constant above this upper limit. Thus, at 5 kV/mm and

after 5 min, the KNN particles in the composites are fully polarised. When the conductive elastomer is used as an electrode, a much lower electrical field is needed to polarise KNN particles. By applying 1 kV/mm for only 3 min, the composites reach the highest piezoelectric coefficient. Above this electrical field and time, the coefficient remains constant, confirming also in this case the full polarisation of KNN particles. This is valid for all rubber types. This means that the good chemical adhesion between the electrode and the piezoelectric material increases the poling efficiency. Although the lower conductivity of the conductive elastomer, compared to gold electrode, a much lower electrical field and shorter time during poling process is needed. The higher number of activation sites on the surface of the piezoelectric material due to its good adhesion with the electrode implies a more efficient transfer of DC electrical field and, thus, a shorter and more efficient poling process.

Table 2   Effective poling conditions for piezoelectric energy harvester with NBR and ENR filled with 30 vol% KNN.

Poling conditions	Investigated range	Optimal value – gold electrode	Optimal value – elastomer electrode
Temperature (°C)	25	25	25
Electrical field (kV/mm)	1-10	5	1
Time (min)	5-30	5	3

9.3.3. Piezoelectric coefficient

The piezoelectric coefficients d_{33} of ENR-25, ENR-50, NBR-28 and NBR-50 filled with varying amounts of KNN combined with elastomeric and gold electrodes are reported in Figure 2.

Overall, using a conductive elastomer chemically adhered to a piezoelectric material, results in a better performance of the piezoelectric composites compared to gold electrode. This is more emphasised at a higher volume fraction of KNN. For ENR-25 and NBR-28 filled with 40 vol% of KNN, the piezoelectric coefficient increases from 10.4 to 16.6 pC/Nmm and from 16 to 46 pC/Nmm, respectively, when using the elastomeric electrode. For ENR-50 and NBR-50, filled with 50 vol% of KNN, the piezoelectric coefficients increase drastically, when using the elastomer electrode. The increase of the piezoelectric properties reflects the combined effect of more activation sites in the interphase of the piezoelectric material and electrode, as well as a more efficient poling process.

Additionally, the plot confirms the previously reported trend: The higher the rubber polarity, the higher is the dielectric constant and hence, the higher is the piezoelectric coefficient [32]. NBR-50 shows the best piezoelectric performance. However, these composites are characterised by higher error bars, particularly at volume fractions between 30 and 50 vol%. This is because the high polarity of the rubber combined with the high amount of the polar KNN filler makes it lesser compatible with the non-polar NR/BR of the electrode.
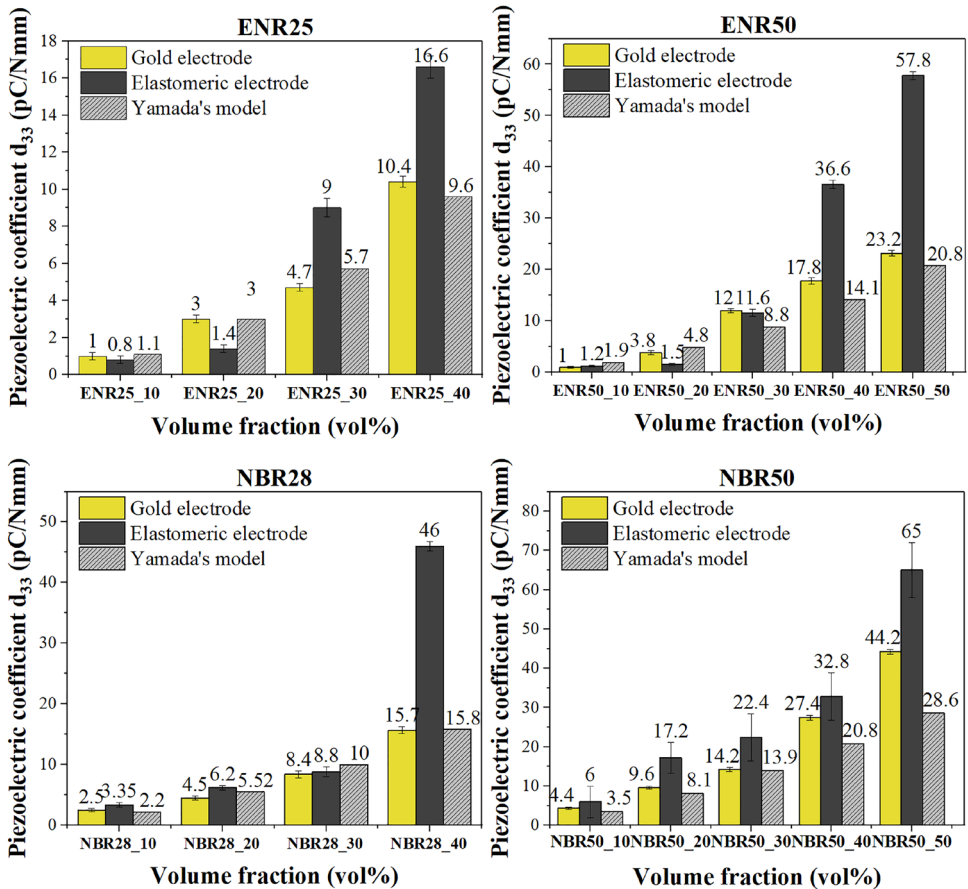
Figure 2   Piezoelectric coefficient d_{33} measured and theoretically predicted with Yamada's model of (a) ENR-25, (b) ENR-50, (c) NBR-28 and (d) NBR-50 filled with varied KNN amounts with gold and elastomeric electrodes.

In the graphs, the piezoelectric coefficients predicted by Yamada's model as described in Chapter 7 are shown additionally. The theoretical values of Yamada's model are close to the piezoelectric coefficient values measured by using gold electrodes. However, at a KNN volume fraction of 40-50 vol%, the experimental

data are underestimated. At this volume fraction, KNN ceramic particles form larger agglomerates inside the composites and it is more difficult to estimate the value of the shape factor of each single particle and as well as of the agglomerate.

The experimental values of the piezoelectric coefficient of the composites with elastomeric electrodes are much higher than the ones predicted by Yamada's model. This is because the Yamada's model and all the other models presented in the literature do not include the potential presence of a chemical bond between these two components. This is a very important finding and represents a new way for achieving a higher performance of piezoelectric elastomeric materials.

9.3.4. Output voltage of piezoelectric energy harvesters

After having applied a contact poling on the harvesters with gold and elastomer-electrodes, the output voltage was measured in a DMA by varying frequency from 0.01 to 100 Hz at room temperature, and by varying temperature from 25 to 100°C at 100 Hz. The values of dynamic and static strains, as well as temperature and frequency were selected based on the assumption of a specific car by considering its weight and tyre series [26,27]. The applied load on each tyre was estimated for the selected car and the analysis conditions were simulated by DMA, i.e. 10% of static strain and 2% of dynamic strain [26,27].

Figure 3 shows the output voltage derived from the harvesters as a function of frequency at room temperature. For these measurements, the rubbers ENR-25, ENR-50 and NBR-28 filled with the highest KNN amount (i.e. 40 and 50 vol%) were considered. The NBR-50-based piezoelectric composite is not reported here due to its non-homogeneous adhesion with the conductive elastomer; it showed too high error bars and was considered as not repeatable.

Figure 3 indicates that the output voltage increases with increasing frequency due to the mechanical excitations from the DMA to the materials and, in turn, a more frequent dipole activation of the piezoelectric material. The chemical adhesion between the piezoelectric composite and the electrode plays an essential role. Piezoelectric composites with an elastomeric electrode generate a higher current compared to the gold electrode, as more electrical charges can be transferred from the piezoelectric materials to the electrode. Gold particles were spattered on the surface of piezoelectric composites. Hence, this process made the gold electrode also lesser uniform than the elastomeric composites and shows cracking under the exposure to a high electrical field.
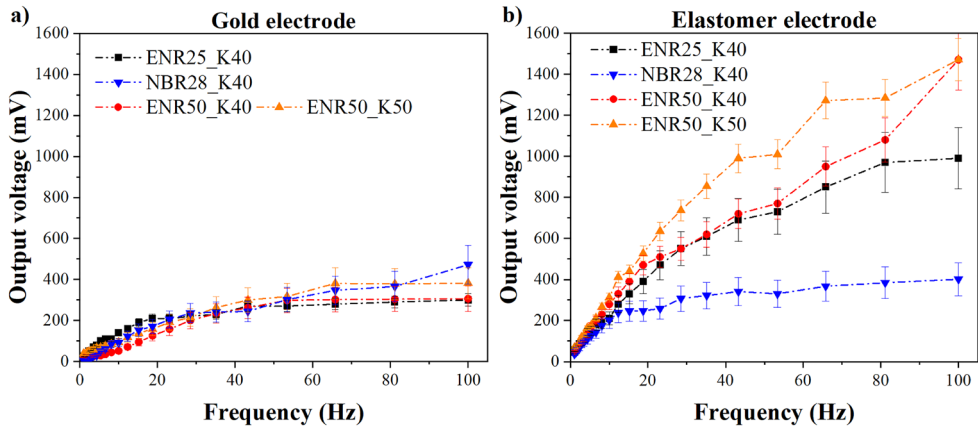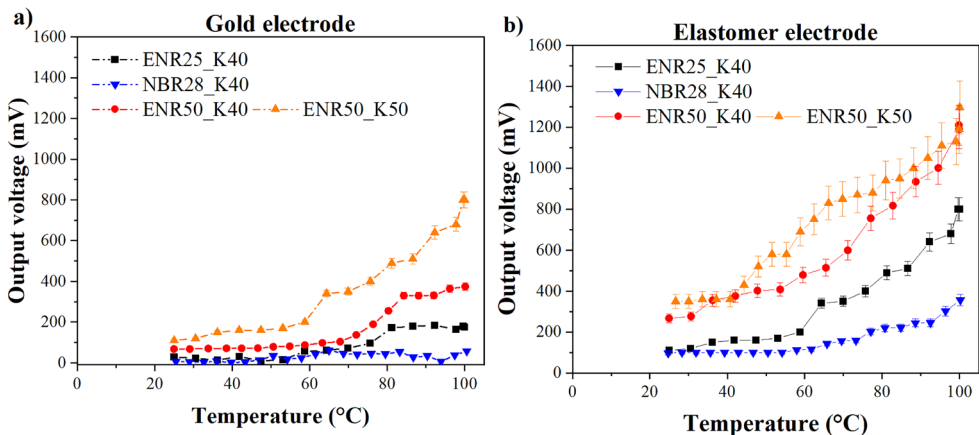
Figure 3 Output voltage as a function of frequency at 25°C of ENRs and NBRs filled with 40 and 50 vol% of KNN electroded with gold and conductive elastomers.

By increasing the temperature from 25 to 100°C (Figure 4), the generated voltage rises significantly. This means that the piezoelectric performance of the harvesters is widely affected by the temperature. This phenomenon can be explained by multiple aspects. Firstly, with increasing temperature, the electrical conductivity of the elastomer is increased. Elevated temperatures accelerate the charge carriers hopping across the conductive network [26,41,47]. Secondly, the elevated temperatures accelerate also the mobility of the dipoles within the structure of the piezoelectric composites. This joint effect confirms again the significant role of the chemical adhesion between the two components, as the increased conductivity of the elastomer is affecting the output voltage of the harvester.

Figure 4 Output voltage as a function of temperature at 100 Hz of ENRs and NBRs filled with 40 and 50 vol% of KNN electroded with gold and conductive elastomers.

9

Figures 3 and 4 confirm the trend previously reported in Figure 2: The output voltage is higher for the rubber matrix with a higher dielectric constant. Moreover, frequency and temperature in the current study have proportionally a similar effect on the output voltage of elastomer-electroded harvesters. This conclusion is based on the observation that, in Figures 3b and 4b, the output voltages at 100 Hz and 100°C are equally at 1300 mV.

9.3.5. Output power of piezoelectric energy harvesters

From the output voltage generated during a DMA measurement, the power was calculated according to Equation 1. This was done to estimate if the gained energy is high enough to power a tire sensor. In Figure 5, the output power generated by the harvesters composed of the piezoelectric composites (i.e. ENRs and NBR-28 filled with KNN) and the electrically conductive elastomer composite (i.e. NR/BR filled with 6 vol% of ECCB) is presented. The piezoelectric harvester generates a higher power with increasing frequency and temperature. As described in Chapter 4 [26], the values of the output power of the harvester were calculated according to the actual rolling conditions of a tyre simulated in lab scale. The static and the dynamic strains of these measurements were chosen based on a reference car tyre. It is also known that during the car driving, the tyre temperature can reach up to 80°C. Further, the tyre-road interactions can contribute to vibrations reaching 100 Hz inside the tyre. Therefore, if the harvester is mounted as a part of a tyre, the output power produced can be around 0.14 $\mu W/cm^2$.
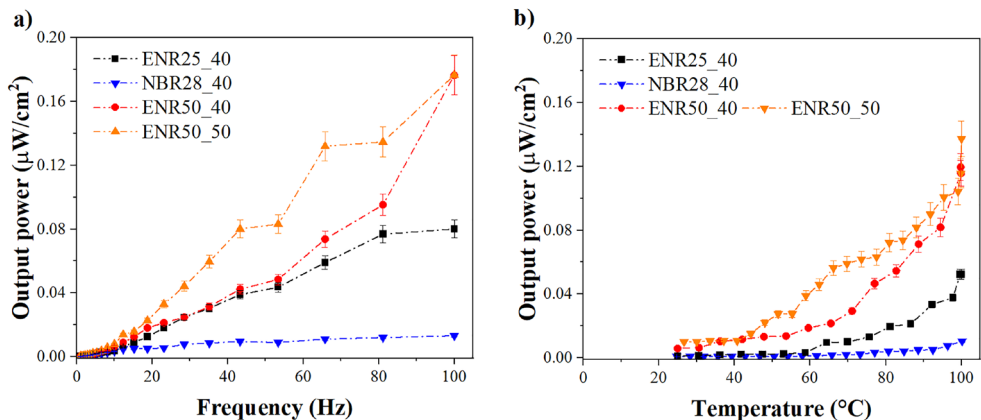

Figure 5   Output power of the energy harvesters including ENRs and NBRs filled with 40 and 50 vol% of KNN and conductive elastomers as a function of (a) frequency at room temperature and (b) temperature at 100 Hz.

One of the most commonly used tyre sensors is the Tyre Pressure Monitoring System (TPMS), which is installed in tyres to monitor the tyre pressure for evaluating fuel consumption efficiency and safety aspects of the running tyres. This sensor requires 28 µW when measuring the pressure every 15 min [14,26]. As a result, to ensure sufficient energy for continuously supplying the TPMS sensor, the area of the piezoelectric energy harvester should be ca. 200 cm^2.

9.4.   Conclusions

Piezoelectric energy harvesters comprising piezoelectric composites and an electrically conductive elastomer were evolved. The piezoelectric composites were based on different polar rubbers, i.e. Epoxidised Natural Rubber (ENR) and acryloNitrile Butadiene Rubber (NBR), filled with increasing amounts of KNN. The electrically conductive elastomer consists of a blend of Natural Rubber (NR) and Butadiene Rubber (BR) filled with 6 vol% of a high surface area and high structure carbon black. Both main components were co-vulcanised at 170°C and the effect of interfacial adhesion on the poling process and the output voltage was studied.

Contact poling of these harvesters showed a higher efficiency compared to the gold electrode harvesters. When using the gold as an electrode, the optimised poling electrical field and time were 5 kV/mm and 5 min, respectively. While, with the elastomeric electrode, those parameters were 3 kV/mm and 3 min, respectively. The piezoelectric coefficient of the harvesters, particularly when increasing KNN amount, increases considerably.

The output voltage and power were also monitored in a Dynamic Mechanical Analyser DMA by selecting the proper values of strains, frequency, and temperature to simulate the rolling tyre conditions. The output voltage and power increased with increasing frequency and temperature, with both types of electrodes. However, in the case of the elastomeric electrode, these two parameters reached a higher absolute value. This is a joint effect of the chemical adhesion between the piezoelectric and conductive components, which increases the electrical conductivity and the acceleration of charge carriers/dipoles mobility.

Under the assumption of a reference passenger car, a piezoelectric energy harvester based on a composite of ENR-50 with 50 vol% of KNN and an electrically conductive elastomer with an area of 200 cm^2 was estimated to sufficiently power a tyre sensor.

9

9.5.   References

[1]   L. Liu, X. Guo, W. Liu, C. Lee, Recent progress in the energy harvesting technology-from self-powered sensors to self-sustained IoT, and new applications, Nanomaterials. 11 (2021) 2975. https://doi.org/10.3390/nano11112975.

[2]   H. Elahi, K. Munir, M. Eugeni, S. Atek, P. Gaudenzi, Energy harvesting towards self-powered iot devices, Energies. 13 (2020) 5528. https://doi.org/10.3390/EN13215528.

[3]   Y. Wu, Y. Ma, H. Zheng, S. Ramakrishna, Piezoelectric materials for flexible and wearable electronics: A review, Mater. Des. 211 (2021) 110164. https://doi.org/10.1016/J.MATDES.2021.110164.

[4]   M. Safaei, H.A. Sodano, S.R. Anton, A review of energy harvesting using piezoelectric materials: State-of-the-art a decade later (2008-2018), Smart Mater. Struct. 28 (2019) 113001. https://doi.org/10.1088/1361-665X/AB36E4.

[5]   D.K. Khatua, S.J. Kim, Perspective on the development of high performance flexible piezoelectric energy harvesters, J. Mater. Chem. C. 10 (2022) 2905–2924. https://doi.org/10.1039/D1TC06089A.

[6]   F. Khameneifar, S. Arzanpour, M. Moallem, A piezoelectric energy harvester for rotary motion applications: Design and experiments, IEEE/ASME Trans. Mechatronics. 18 (2013) 1527–1534. https://doi.org/10.1109/TMECH.2012.2205266.

[7]   J. Rödel, K.G. Webber, R. Dittmer, W. Jo, M. Kimura, D. Damjanovic, Transferring lead-free piezoelectric ceramics into application, J. Eur. Ceram. Soc. 35 (2015) 1659–1681. https://doi.org/10.1016/j.jeurceramsoc.2014.12.013.

[8]   H. Khanbareh, V.Y. Topolov, C.R. Bowen, Piezo-active composites: Classification and effective physical properties, Springer Ser. Mater. Sci. 283 (2019) 1–23. https://doi.org/10.1007/978-3-030-19204-4_1.

[9]   A.K. Batra, A. Alomari, A.K. Chilvery, A. Bandyopadhyay, K. Grover, Piezoelectric Power Harvesting Devices: An Overview, Adv. Sci. Eng. Med. 8 (2016) 1–12. https://doi.org/10.1166/ASEM.2016.1819.

[10]   S.K. Karan, S. Maiti, J.H. Lee, Y.K. Mishra, B.B. Khatua, J.K. Kim, S. Das Mahapatra, P.C. Mohapatra, A.I. Aria, G. Christie, Y.K. Mishra, S. Hofmann, V.K. Thakur, S.R. Anton, H.A. Sodano, J. Wu, M. Stewart, M.G. Cain, C. Chen, X. Wang, Y. Wang, D.D. Yang, F. Yao, W. Zhang, B. Wang, G.A. Sewvandi, D.D. Yang, D. Hu, Recent Development of Lead-Free Piezoelectrics, Adv. Lead-Free Piezoelectric Mater. 30 (2018) 37–64. https://doi.org/10.1007/978-981-10-8998-5/COVER.

[11]   Y. Saito, H. Takao, T. Tani, T. Nonoyama, K. Takatori, T. Homma, T. Nagaya, M. Nakamura, Lead-free piezoceramics, Nature. 432 (2004) 84–87. https://doi.org/10.1038/nature03028.

[12]   T.R. Shrout, S.J. Zhang, Lead-free piezoelectric ceramics: Alternatives for PZT?, J. Electroceramics. 19 (2007) 111–124. https://doi.org/10.1007/S10832-007-9047-0.

[13]   Z. Yang, S. Zhou, J. Zu, D. Inman, High-performance piezoelectric energy harvesters and their applications, Joule. 2 (2018) 642–697. https://doi.org/10.1016/j.joule.2018.03.011.

[14]   C.R. Bowen, M.H. Arafa, Energy harvesting technologies for tire pressure monitoring systems, Adv. Energy Mater. 5 (2015) 1–17. https://doi.org/10.1002/aenm.201401787.

[15]   R. Matsuzaki, A. Todoroki, Wireless monitoring of automobile tires for intelligent tires, Sensors. 8 (2008) 8123–8138.https://doi.org/10.3390/s8128123.

[16]   A.E. Kubba, K. Jiang, A comprehensive study on technologies of tyre monitoring systems and possible energy solutions, Sensors. 14 (2014) 10306–10345. https://doi.org/10.3390/s140610306.

[17]   M. Löhndorf, T. Kvisterøy, E. Westby, E. Halvorsen, Evaluation of Energy Harvesting Concepts for Tire Pressure Monitoring Systems, Int. Work. Micro Nanotechnol. Power Gener. Energy Convers. Appl. (2007) 331–334.

[18]   M. Germer, U. Marschner, A. Richter, Energy Harvesting for Tire Pressure Monitoring Systems from a Mechanical Energy Point of View, IEEE Internet Things J. 9 (2022) 7700-7714. https://doi.org/10.1109/JIOT.2022.3152547.

[19]   B. Wu, Y. Fang, L. Deng, Summary of energy collection application in vehicle tire pressure monitoring system, ACM Int. Conf. Proceeding Ser. 19 (2019) 1–6. https://doi.org/10.1145/3351917.3351918.

[20]   A. Toghi Eshghi, S. Lee, H. Lee, Y.-C. Kim, Parameter study and optimization for piezoelectric energy harvester for TPMS considering speed variation, Smart Mater. Nondestruct. Eval. Energy Syst. 9806 (2016) 1–19. https://doi.org/10.1117/12.2219567.

[21]   I.A.H. Al-Najati, K.W. Chan, S.Y. Pung, Tire strain piezoelectric energy harvesters: a systematic review, Int. J. Power Electron. Drive Syst. 13 (2022) 444–459. https://doi.org/10.11591/IJPEDS.V13.I1.PP444-459.

[22]   M. Keck, A new approach of a piezoelectric vibration-based power generator to supply next generation tire sensor systems, in: Proc. IEEE Sensors, IEEE, Atlanta, USA, 2007: pp. 1299–1302. https://doi.org/10.1109/ICSENS.2007.4388648.

[23]   Q. Zheng, H. Tu, A. Agee, Y. Xu, Vibration energy harvesting device based on asymmetric air-spaced cantilevers for tire pressure monitoring system, in: Proc. Power MEMS, PowerMEMS, Washington, USA, 2009: pp. 403–406.

[24]   K.H. Mak, S. McWilliam, A.A. Popov, Piezoelectric energy harvesting for tyre pressure measurement applications, Proc. Inst. Mech. Eng. Part D J. Automob. Eng. 227 (2013) 842–852. https://doi.org/10.1177/0954407012463849.

9

[25] D.A. Van Den Ende, H.J. Van De Wiel, W.A. Groen, S. Van Der Zwaag, Direct strain energy harvesting in automobile tires using piezoelectric PZT-polymer composites, Smart Mater. Struct. 21 (2012) 1–11. https://doi.org/10.1088/0964-1726/21/1/015011.

[26] C. Mangone, W. Kaewsakul, M. Klein Gunnewiek, A.P.J. van Swaaij, L. Reuvekamp, J.W.M. Noordermeer, A. Blume, Design and performance of flexible polymeric piezoelectric energy harvesters for battery-less tyre sensors, Smart Mater. Struct. 31 (2022) 095034.

[27] C. Mangone, W. Kaewsakul, A.P.J. van Swaaij, K. Bandzierz, M.K. Gunnewiek, A. Blume, Dynamic measurement setups for validating piezoelectric energy harvesters in driving conditions, Polym. Test. 119 (2023) 107932. https://doi.org/10.1016/J.POLYMERTESTING.2023.107932.

[28] J. Yvonnet, Piezoelectricity, Solid Mech. Its Appl. 258 (2019) 91–102. https://doi.org/10.1007/978-3-030-18383-7_5.

[29] R.E. Newnham, D.P. Skinner, L.E. Cross, Connectivity and piezoelectric-pyroelectric composites, Mater. Res. Bull. 13 (1978) 525–536. https://doi.org/10.1016/0025-5408(78)90161-7.

[30] A.O. Sanches, J.A. Malmonge, W.K. Sakamoto, Piezoelectric composites: Fabrication, characterization, and its application as sensor, Recent Adv. Complex Funct. Mater. From Des. to Appl. (2017) 195–215. https://doi.org/10.1007/978-3-319-53898-3_8/FIGURES/14.

[31] K. Uchino, Piezoelectric composite materials, Adv. Piezoelectric Mater. Sci. Technol. (2010) 318–346. https://doi.org/10.1533/9781845699758.1.318.

[32] C. Mangone, W. Kaewsakul, A. Tuluk, M.D. Nguyen, K. Bandzierz, A. Blume, Flexible lead-free piezoelectric composites: processing parameters and effect of elastomer polarity, Prep. (2023).

[33] J.E.Q. Quinsaat, T. de Wild, F.A. Nüesch, D. Damjanovic, R. Krämer, G. Schürch, D. Häfliger, F. Clemens, T. Sebastian, M. Dascalu, D.M. Opris, Stretchable piezoelectric elastic composites for sensors and energy generators, Compos. Part B Eng. 198 (2020) 108211. https://doi.org/10.1016/J.COMPOSITESB.2020.108211.

[34] A. Tuluk, S. Joshi, T. Mahon, S. Van Der Zwaag, Tuning piezoproperties of BiFeO3ceramic by cobalt and titanium dual doping, J. Appl. Phys. 131 (2022) 214104. https://doi.org/10.1063/5.0091768/2836958.

[35] I. Babu, G. de With, Enhanced electromechanical properties of piezoelectric thin flexible films, Compos. Sci. Technol. 104 (2014) 74–80. https://doi.org/10.1016/J.COMPSCITECH.2014.08.022.

[36] V.L. Stuber, T.R. Mahon, S. Van Der Zwaag, P. Groen, The effect of the intrinsic electrical matrix conductivity on the piezoelectric charge constant of piezoelectric composites, Mater. Res. Express. 7 (2019) 15703. https://doi.org/10.1088/2053-1591/AB5BB3.

[37]   H. Khanbareh, S. Van Der Zwaag, W.A. Groen, Piezoelectric and pyroelectric properties of conductive polyethylene oxide-lead titanate composites, Smart Mater. Struct. 24 (2015). https://doi.org/10.1088/0964-1726/24/4/045020.

[38]   D.B. Deutz, N.T. Mascarenhas, S. van der Zwaag, W.A. Groen, Poling piezoelectric (K,Na,Li)NbO3-polydimethylsiloxane composites, 515 (2017) 68–74. https://doi.org/10.1080/00150193.2017.1360110.

[39]   W. Wang, Z. Chen, Z. Zhou, Y. Li, R. Liang, Enhancing Electromechanical Properties of PZT-Based Piezoelectric Ceramics by High-Temperature Poling for High-Power Applications, ACS Appl. Mater. Interfaces. (2023). https://doi.org/10.1021/acsami.2c19802.

[40]   J.B. Donnet, R.C. Bansal, M.J. Wang, Carbon Black: Science and Technology, Second Edition, Routledge, Boca Raton, USA, 2018. https://doi.org/10.1201/9781315138763.

[41]   M.E. Spahr, R. Gilardi, D. Bonacchi, Carbon Black for Electrically Conductive Polymer Applications, (2017) 375–400. https://doi.org/10.1007/978-3-319-28117-9_32.

[42]   M. Klüppel, The Role of Disorder in Filler Reinforcement of Elastomers on Various Length Scales, Adv. Polym. Sci. 164 (2003) 1–86. https://doi.org/10.1007/B11054.

[43]   N. Probst, Conducting Carbon Black, Carbon Black. (2018) 271–288. https://doi.org/10.1201/9781315138763-8.

[44]   C. Mangone, W. Kaewsakul, K. Bandzierz, M.K. Gunnewiek, A. Blume, Key factors affecting dynamic electrical conductivity of elastomeric compounds, Prep. (2023).

[45]   B.X. Du, Z.L. Li, Z.R. Yang, Field-dependent conductivity and space charge behavior of silicone rubber/SiC composites, IEEE Trans. Dielectr. Electr. Insul. 23 (2016) 3108–3116. https://doi.org/10.1109/TDEI.2016.7736876.

[46]   A. Can-Ortiz, L. Laudebat, Z. Valdez-Nava, S. Diaham, Nonlinear Electrical Conduction in Polymer Composites for Field Grading in High-Voltage Applications: A Review, Polym. 2021, 13 (2021) 1370. https://doi.org/10.3390/POLYM13091370.

[47]   J.G. Meier, M. Klüppel, Carbon black networking in elastomers monitored by dynamic mechanical and dielectric spectroscopy, Macromol. Mater. Eng. 293 (2008) 12–38. https://doi.org/10.1002/mame.200700228.

9

Chapter 10

Summary

Samenvatting

10

Nowadays, tyre sensors are becoming increasingly important for ensuring safe driving and efficient tyre performance. Legislation aimed at reducing fuel consumption and CO_2 emissions, along with the recognition of the importance of maintaining proper tyre pressure, has contributed significantly to the widespread use of a Tyre Pressure Monitoring System (TPMS). A TPMS monitors the tyre pressure and alerts the driver if any of the tyres are under- or over-inflated.

Piezoelectricity is an interesting phenomenon that holds the potential to enable autonomous operation of tyre sensors. Piezoelectric materials can generate electrical energy when subjected to deformation. A piezoelectric energy harvester consists of two components: a piezoelectric material itself and an electrode. Piezoelectric materials are characterised by a net dipole moment, resulting in two oppositely charged sides. By applying an electrode on both sides of the piezoelectric material during deformation, a flow of electrical current is enabled. This current can then be stored in a capacitor to supply self-powered sensors. During vehicle operation, tyres are continuously subjected to dynamic deformations, vibrations and excitations. The repetitious deformation of the piezoelectric material, when integrated into a tyre, provides the potential to continuously produce electricity, that can be stored in a capacitor of a sensor. Despite extensive research in this field, a piezoelectric device suitable for mounting in tyres to power sensors has not yet been established.

This study focuses on the development of a piezoelectric material specifically designed for tyres. There are two categories of piezoelectric materials: ceramics and polymers. On the one hand, ceramics generally offer higher piezoelectric coefficients, but they are rigid, brittle, and relatively heavy. On the other hand, piezoelectric polymers offer better flexibility but possess lower piezoelectric coefficients, resulting in inferior electricity generation compared to piezoelectric ceramics. Given the promising characteristics and limitations of piezoelectric materials, the objective of the current study is to identify an adequate material capable of generating sufficient energy to power tyre sensors.

The experimental outcomes of this research project can be summarised as follows:

In *Chapter 3*, an analytical setup was developed to experimentally validate the energy harvesters for their use in tyres. The setup was designed to measure the harvested electrical energy under simulated driving conditions. The dynamic properties and the output voltage of the harvesters were monitored using Dynamic Mechanical Analysis (DMA) under sinusoidal conditions. A PEH for tyre applications was prepared in a sandwich configuration, consisting of a piezoelectric material, i.e. PolyVinyliDene diFluoride (PVDF) film, inserted between two layers

of elastic electrodes, i.e. elastomers filled with a conductive carbon black filler. This development gave a promising method for analysing the electro-mechanical properties of conductive and piezoelectric materials and optimising their performance under simulated tyre-rolling conditions.

In *Chapter 4*, a flexible piezoelectric energy harvesting patch in a sandwich-like configuration was designed. This harvester was fabricated by inserting a piezoelectric PVDF film between two layers of conductive elastomer filled with carbon black and Single-Wall Carbon NanoTubes (SWCNT). The development started with improving the conductivity of the elastomer by adding 6 wt% of SWCNT masterbatch. The adhesion between the interfaces was enhanced through surface modification of the PVDF film by introducing oxygen functional groups via a plasma treatment and further modification with 3-thiocyanatopropyltriethxoy silane. The successful surface modification of the PVDF film was affirmed by X-ray photoelectron spectroscopy, T-peel and fatigue tests. The harvester was estimated to generate sufficient power to operate a reference tyre sensor, producing 28 μW/cm^2.

Chapters 5 and *6* are focused on the electrically conductive materials, specifically on the electrodes of the piezoelectric energy harvesters discussed in the previous chapters. *Chapter 5* aimed to identify the most influential factors affecting the dynamic electrical conductivity of elastomeric composites. Conductive carbon blacks with specific surface areas in the range of 200 to 1400 m^2/g were used. The results from a full factorial Design of Experiment study indicated that the rubber types with different polarities, rubber blend ratios, and carbon black types appeared to be statistically insignificant. The carbon black amount expressed in terms of total surface area was the only significant factor. The Sigmoidal-Boltzmann model was applied to predict the percolation threshold of Natural Rubber (NR) and Butadiene Rubber (BR) blends filled with conductive carbon blacks. In *Chapter 6,* a comparison was made between conventional and conductive carbon blacks with specific surface areas in the range of 78 to 1400 m^2/g filled in NR/BR 25/75 blends. The Sigmoidal-Boltzmann model was applied to predict the percolation threshold of the NR/BR composites. A newly developed correlation between the dynamic electrical conductivity of NR/BR composites, the Payne effect, and the total effective surface area of the carbon blacks gave new insights into the different conducting mechanisms of these two carbon black grades.

Chapters 7 and *8* are focused on the other component of the piezoelectric energy harvesters, the piezoelectric material. In these chapters, elastomeric piezoelectric composites based on Epoxidised Natural Rubbers (ENR) and acryloNitrile

10

Butadiene Rubbers (NBR) filled with a ferroelectric ceramic $K_{0.5}Na_{0.5}NbO_3$ (KNN) were investigated. In ***Chapter 7,*** different elastomer types with varying polarity were considered, including ENR with 25 and 50 mol% of epoxide content, and NBR with 28, 41 and 50 wt% of acrylonitrile content. The processability, curing behaviour, contact poling process, and piezoelectric properties of the elastomeric composites filled with 30 vol% of KNN were analysed. An increase in elastomer polarity resulted in a higher dielectric constant of the matrix, leading to a higher piezoelectric coefficient. The overall properties and experimental evidence confirmed the enhancement in interfacial interactions between KNN and the investigated polar elastomers. In ***Chapter 8***, varying amounts (10-50 vol%) of KNN were mixed with ENR and NBR. Poling studies were conducted using elastomeric composites vulcanised at different thicknesses, i.e. 0.3, 0.5 and 1 mm. Thinner samples exhibited higher piezoelectric coefficients due to a better poling efficiency. With increasing KNN amount and increasing rubber polarity, the dielectric constant of the matrix increased as well, resulting in a higher piezoelectric coefficient. Although the particle size of KNN is large , the mechanical properties were increased due to strong ionic interactions between the polar functional groups of the rubber and KNN.

In ***Chapter 9***, elastomeric piezoelectric energy harvesters were developed, utilising the piezoelectric composites (discussed in Chapters 7 and 8) and an electrically conductive elastomer (developed in Chapters 5 and 6) as an electrode. Compared to the gold electrode, the newly developed piezoelectric elastomeric harvesters were found to be effectively poled within a shorter time and at a lower electrical field, thanks to the chemical adhesion between the components. The piezoelectric coefficients of ENR with 50 mol% of epoxide groups and of NBR with 50 wt% of acrylonitrile groups filled with 50 vol% of KNN were doubled in comparison to the gold-electroded composites. ENR-50 was selected for a further study due to its good chemical adhesion with the conductive elastomer. The harvester based on ENR-50 with 50 wt% of KNN 0.14 µW/cm^2 under rolling tyre conditions. An area of 200 cm^2 of this harvester seems to be sufficient to successfully power a tyre sensor.

In this study different types of piezoelecric energy harvesters in sandwich-like configuration were designed. Two categories of piezoelectric materials were investigated: the polymer PVDF and the piezoelectric composites including KNN dispersed in polar elastomers as ENR and NBR. Electrically conductive elastomeric composites were considered as flexible electrode. The piezoelectric energy harvesters designed in the whole study should be suitable for tyre application as they show a sufficiently high energy generation, flexibility and compability with tyre compounds.

Samenvatting

Bandensensoren worden tegenwoordig steeds belangrijker om veilig rijden en efficiënte bandenprestaties te garanderen. Wetgeving gericht op het verminderen van brandstofverbruik en CO_2-uitstoot, samen met de erkenning van het belang van het handhaven van de juiste bandenspanning, heeft aanzienlijk bijgedragen aan het wijdverbreide gebruik van een Tyre Pressure Monitoring System (TPMS). Een TPMS controleert de bandenspanning en waarschuwt de bestuurder als een van de banden een te lage of te hoge spanning heeft.

Piëzo-elektriciteit is een interessant fenomeen dat de autonome werking van bandensensoren mogelijk kan maken. Piëzo-elektrische materialen kunnen elektrische energie opwekken wanneer ze vervormd worden. Een piëzo-elektrische energie oogster bestaat uit twee componenten: een piëzo-elektrisch materiaal zelf en een elektrode. Piëzo-elektrische materialen worden gekenmerkt door een netto dipoolmoment, wat resulteert in twee tegengesteld geladen zijden. Door tijdens de vervorming aan beide zijden van het piëzo-elektrisch materiaal een elektrode aan te brengen, wordt een elektrische stroom mogelijk gemaakt. Deze stroom kan vervolgens worden opgeslagen in een condensator om sensoren van eigen stroom te voorzien. Tijdens het gebruik van een voertuig worden banden voortdurend blootgesteld aan dynamische vervormingen, trillingen en schokken. De herhaalde vervorming van het piëzo-elektrisch materiaal, wanneer geïntegreerd in een band, biedt het potentieel om continu elektriciteit te produceren, die kan worden opgeslagen in een condensator van een sensor. Ondanks uitgebreid onderzoek op dit gebied is er nog geen piëzo-elektrisch apparaat dat geschikt is voor montage in banden om sensoren van stroom te voorzien.

Dit onderzoek richt zich op de ontwikkeling van een piëzo-elektrisch materiaal dat speciaal is ontworpen voor banden. Er zijn twee categorieën piëzo-elektrische materialen: keramiek en polymeren. Aan de ene kant bieden keramische materialen over het algemeen hogere piëzo-elektrische coëfficiënten, maar zijn stijf, bros en relatief zwaar. Anderzijds bieden piëzo-elektrische polymeren meer flexibiliteit, maar hebben ze lagere piëzo-elektrische coëfficiënten, waardoor ze minder elektriciteit opwekken dan piëzo-elektrisch keramiek. Gezien de veelbelovende eigenschappen en beperkingen van piëzo-elektrische materialen is het doel van het huidige onderzoek om een geschikt materiaal te vinden dat voldoende energie kan opwekken om bandensensoren van stroom te voorzien.

De experimentele resultaten van dit onderzoeksproject kunnen als volgt worden samengevat:

10

In *Hoofdstuk 3* werd een analytische opstelling ontwikkeld om de energieoogsters experimenteel te valideren voor gebruik in banden. De opstelling werd ontworpen om de geoogste elektrische energie te meten onder gesimuleerde rijomstandigheden. De dynamische eigenschappen en de opgewekte spanning van de oogstmachines werden gecontroleerd met behulp van Dynamische Mechanische Analyse (DMA) onder sinusvormige omstandigheden. Een piëzo-elektrische energie oogster voor bandentoepassingen werd voorbereid in een sandwichconfiguratie, bestaande uit een piëzo-elektrisch materiaal, d.w.z. PolyVinyliDene diFluoride (PVDF) film, ingevoegd tussen twee lagen elastische elektroden, d.w.z. elastomeren gevuld met een geleidende koolstofzwarte vulstof. Deze ontwikkeling leverde een veelbelovende methode op voor het analyseren van de elektromechanische eigenschappen van geleidende en piëzo-elektrische materialen en het optimaliseren van hun prestaties onder gesimuleerde rolomstandigheden van de band.

In *Hoofdstuk 4* werd een flexibele piëzo-elektrische patch in een sandwich-achtige configuratie ontworpen. Deze oogster werd gemaakt door een piëzo-elektrisch PVDF-folie tussen twee lagen geleidend elastomeer gevuld met roet en Single-Wall Carbon NanoTubes (SWCNT) te plaatsen. De ontwikkeling begon met het verbeteren van de geleidbaarheid van het elastomeer door 6 wt% SWCNT-masterbatch toe te voegen. De hechting tussen de interfaces werd verbeterd door oppervlaktemodificatie van de PVDF-film door het introduceren van functionele groepen met zuurstof via een plasmabehandeling en verdere modificatie met 3-thiocyanatopropyltriethoxy silaan. De succesvolle oppervlaktemodificatie van de PVDF-film werd bevestigd door X-ray photoelectron spectroscopy (XPS), T-peltesten- en vermoeiingstesten. De energie oogstende patch genereerde naar schatting voldoende vermogen om een referentie sensor te laten werken en produceerde 28 μW/cm^2.

Hoofdstukken 5 en 6 op de elektrisch geleidende materialen, van de piëzo-elektrische energie-oogsters die in de voorgaande hoofdstukken.

De *Hoofdstukken 5 en 6* zijn gericht op de elektrisch geleidende materialen, specifiek op de elektroden van de piëzo-elektrische energie oogsters die in de voorgaande hoofdstukken zijn besproken. *Hoofdstuk 5* was gericht op het identificeren van de meest invloedrijke factoren die de dynamische elektrische geleidbaarheid van elastomere composieten beïnvloeden. Er werden geleidende roeten gebruikt met specifieke oppervlakken in het bereik van 200 tot 1400 m^2/g. De resultaten van een volledig factorieel experimenteel ontwerpstudie (Design of Experiment) gaven aan dat de rubbersoorten met verschillende polariteiten, rubber

meng verhoudingen en roet types statistisch niet significant bleken te zijn. De hoeveelheid roet uitgedrukt in totaal oppervlak was de enige significante factor. Het Sigmoidal-Boltzmann model werd toegepast om de percolatie drempel te voorspellen van natuurrubber (NR) en butadieenrubber (BR) mengsels gevuld met geleidende carbonblacks. In *Hoofdstuk 6* werd een vergelijking gemaakt tussen conventionele en geleidende roeten met specifieke oppervlakken in het bereik van 78 tot 1400 m^2/g gevuld in NR/BR 25/75 mengsels. Het Sigmoidal-Boltzmann model werd toegepast om de percolatie drempel van de NR/BR composieten te voorspellen. Een nieuw ontwikkelde correlatie tussen de dynamische elektrische geleidbaarheid van NR/BR-composieten, het Payne-effect en het totale effectieve oppervlak van de roeten gaf nieuwe inzichten in de verschillende geleidingsmechanismen van deze twee roet soorten.

De *Hoofdstukken 7 en 8* richten zich op de andere componenten van de piëzo-elektrische energie oogsters, het piëzo-elektrisch materiaal. In deze hoofdstukken werden piëzo-elektrische composieten op basis van elastomeren, namelijk geëpoxideerde natuurrubbers (ENR) en acryloNitril-butadieenrubbers (NBR), gevuld met een ferro-elektrisch keramiek $K_{0.5}Na_{0.5}NbO_3$ (KNN) onderzocht. In *Hoofdstuk 7* werden verschillende elastomeren met verschillende polariteit onderzocht, waaronder ENR met een epoxide gehalte van 25 en 50 mol%, en NBR met een acrylonitril gehalte van 28, 41 en 50 wt%. De verwerkbaarheid, het uithardingsgedrag, het polen van de composieten, en de piëzo-elektrische eigenschappen van de elastomeer composieten gevuld met 30 vol% KNN werden geanalyseerd. Een toename in elastomeer polariteit resulteerde in een hogere diëlektrische constante van de matrix, wat leidde tot een hogere piëzo-elektrische coëfficiënt. De algemene eigenschappen en het experimentele bewijs bevestigden de verbetering van de interacties tussen KNN en de onderzochte polaire elastomeren. In *Hoofdstuk 8* werden variërende hoeveelheden (10-50 vol%) KNN gemengd met ENR en NBR. Studies naar het polen van de materialen werden uitgevoerd met gevulkaniseerd elastomeer composieten met verschillende diktes, d.w.z. 0,3, 0,5 en 1 mm. Dunnere monsters vertoonden hogere piëzo-elektrische coëfficiënten door een betere efficiëntie van het polen. Met een toenemende KNN hoeveelheid en toenemende rubber polariteit nam ook de diëlektrische constante van de matrix toe, wat resulteerde in een hogere piëzo-elektrische coëfficiënt. Hoewel de deeltjesgrootte van KNN groot is, de mechanische eigenschappen verhoogt door sterke ionische interacties tussen de polaire functionele groepen van het rubber en KNN.

10

In *Hoofdstuk 9* werden elastomere piëzo-elektrische energie oogsters ontwikkeld, die gebruikmaken van de piëzo-elektrische composieten (besproken in *Hoofdstuk 7 en 8*) en een elektrisch geleidend elastomeer (ontwikkeld in *Hoofdstuk 5 en 6*) als elektrode. Vergeleken met een gouden elektrode bleken de nieuw ontwikkelde piëzo-elektrische oogsters van elastomeren effectief gepoold te kunnen worden binnen een kortere tijd en bij een lager elektrisch veld, dankzij de chemische adhesie tussen de componenten. De piëzo-elektrische coëfficiënten van ENR met 50 mol% epoxide groepen en van NBR met 50 wt% acrylonitril groepen gevuld met 50 vol% KNN werden verdubbeld in vergelijking met de composieten met gouden elektroden. ENR-50 werd geselecteerd voor verder onderzoek vanwege de goede chemische hechting met het geleidende elastomeer. De energie oogsters op basis van ENR-50 met 50 vol% KNN genereerde naar schatting 0.14 $\mu W/cm^2$ onder rolbandomstandigheden. Een oppervlak van 200 cm^2 van deze oogster lijkt voldoende om een banden sensor van stroom te voorzien.

In dit onderzoek werden verschillende types piëzo-elektrische energie oogsters in een sandwich configuratie ontworpen. Twee categorieën piëzo-elektrische materialen werden onderzocht: het polymeer PVDF en piëzo-elektrische composieten met KNN gedispergeerd in polaire elastomeren zoals ENR en NBR. Composieten van elektrisch geleidende elastomeren werden beschouwd als flexibele elektrode. De in deze studie ontworpen piëzo-elektrische energie oogsters zijn geschikt voor toepassingen in banden omdat ze voldoende energie opwekken, flexibel zijn en compatibel zijn met de banden samenstelling.

Thesis

1. C. Mangone, From motion to power: Designing an innovative piezoelectric based energy generating system for tyres, PDEng thesis, University of Twente, 2019.

Journal articles

2. C. Mangone, W. Kaewsakul, M. Klein Gunnewiek, L.A.E.M. Reuvekamp, J.W.N. Noordermeer, A. Blume, Design and performance of flexible polymeric piezoelectric energy harvesters for battery-less tyre sensors, Smart Mater. Struct. 31 (2022) 095034.
3. C. Mangone, W. Kaewsakul, A.P.J. van Swaaij, K. Bandzierz, M. Klein Gunnewiek, A. Blume, Dynamic measurement setups for validating piezoelectric energy harvesters in driving conditions, Polym. Test. 119 (2023) 107932.
4. C. Mangone, W. Kaewsakul, K. Bandzierz, M. Klein Gunnewiek, A. Blume, Key factors affecting dynamic electrical conductivity of carbon black-based elastomeric composites, *In preparation*.
5. C. Mangone, W. Kaewsakul, K. Bandzierz, M. Klein Gunnewiek, M. Sztucki, A. Blume, Conductive and conventional carbon blacks for electrically conductive elastomers, *In preparation*.
6. C. Mangone, W. Kaewsakul, A. Tuluk, K. Bandzierz, A. Blume, Flexible lead-free ferroelectric composites: processing parameters and effect of elastomer polarity, *In preparation*.

Conference contributions

7. C. Mangone, W. Kaewsakul, M. Klein Gunnewiek, L.A.E.M. Reuvekamp, W.K. Dierkes, A. Blume, Conductive elastomers: Parameters affecting properties and conductivity, Tire Technology Conference 2019, 5-7 Mar, Hannover, Germany.
8. C. Mangone, W. Kaewsakul, M. Klein Gunnewiek, L.A.E.M. Reuvekamp, J. Noordermeer, A. Blume, Electrically conductive elastomers: Key factors and new insight in determining the percolation threshold, Deutsche Kautschuk-Gesellschaft – International Rubber Conference DKT IRC 2021, 27-29 Jul, Nuremberg, Germany.
9. C. Mangone, W. Kaewsakul, A.P.J. van Swaaij, K. Bandzierz, M. Klein Gunnewiek, A. Blume, New insight views of piezoelectric energy harvesters in tyres, International Elastomer Conference 2022, 10-13 Oct, Knoxville, Tennessee.
10. C. Mangone, W. Kaewsakul, K. Bandzierz, A. Blume, Enabling interfacial adhesion between conductive rubber and piezoelectric polymer for energy harvesting applications, International Rubber Conference IRC RubberCon 2023, 9-11 May, Edinburgh, UK.

Patents

11. C. Mangone, M. Klein Gunnewiek, L. Reuvekamp, Tyre comprising a piezoelectric device, 2021.
12. C. Mangone, M. Klein Gunnewiek, L. Reuvekamp, W. Kaewsakul, A. Blume, Method for chemically adhering a diene rubber to a piezoelectric polymer, 2021.

11

Dries for supporting me in developing the analytical setup in the first period of my EngD and for the constant daily help in the lab. You are a great technician! I had the honour to work with **Prof. Dr. Ir. Jacques Noordermeer**. Dear **Jacques**, I am grateful for the opportunity to learn from you through discussion and insightful feedback.

I would like to acknowledge the NOVel Aerospace Material of Delft University of Technology for allowing me to visit and work in your lab. I learned a lot about piezoelectric and dielectric materials by working with the whole team.

I would also like to thank the graduation committee members for taking the time to review my thesis and provide feedback.

During these six years, many colleagues accompanied me in the long working days. **Marzieh**, **Neven**, **Ayush** and **Zuzanna**, I have enjoyed sharing the office with you during my EngD. You made fantastic the beginning of this journey. **Jan-Willem**, we couldn't be office mates for too long due to your set temperature of 16°C, but I liked your openness and directness. **Marcin**, your contagious laugh and your Ferrero Giotto made my PhD life more enjoyable. **Zuzanna**, you have been more than just an office mate or a colleague. You have been truly an indispensable friend. With some laughs and some tears, we finished together the EngD. Although our paths separated afterwards, you have been of great support to me in these years. Thank you very much for that! **Priyanka**, we were in the same office probably in the most stressful period of the PhD: the writing period. Nevertheless, I enjoyed very much our chat and you have always managed to calm me down. Thanks to all **other ETE colleagues** for the coffee breaks, small talks in the morning and drinking in the afternoon. Special thanks to my new colleagues in **Apollo Tyres Global R&D**. **Nico**, **Lehani**, **Steven**, **Nandhini** and (again) **Zuzanna**, thanks for all your support in the past year.

In the past years, I have met wonderful friends. **Adam**, **Martin**, **Tatjana**, **Constantinos** and **Johanna**, thanks for all the laughs and jokes we shared (and many others to go!). **Rosa**, **Marzieh**, and **Paloma**, thanks for all the dancing nights, friendship and fun. **Antonella** e **Vanessa**, sono felice di avervi incontrato. Il vostro sorriso e la vostra solaritá mi ha sempre supportato.

Un ringraziamento infinito va **alla mia famiglia**. Senza di voi non sarei la persona che sono oggi. Il vostro sostegno é stato essenziale per raggiungere questo traguardo. Grazie per avermi sempre sostenuto e soprattutto capito. **Raffaella e Michele**, si dice che gli amici sono i fratelli che ti scegli. Per me voi siete la mia famiglia acquisita. Abbiamo condiviso molte avventure all'universitá, avventure che ci rendono ancora

11

Acknowledgements

amici tutt'oggi, nonostante la lontananza. Grazie mille per avermi accompagnata e supportata anche in questo percorso. **Alessia, Luca** e **Alessandro**, vi ringrazio di cuore per le cene durante il lockdown e quelle risate che hanno sempre alleviato tutte le mancanze. Senza di voi, la vita qui in Olanda non sarebbe stata la stessa.

Dulcis in fundo, I would like to express my profound gratitude to **Chris**. Dear **Chris**, thank you for all the support and for never leaving me alone, particularly during the stressful moments. Grazie per sostenermi, sempre e comunque, con le tue dolci parole, la tua musica col piano immaginario, la tua forza e il tuo essere brillante.
And behind a great son, there is always a great mother. Thank you **Joan** for all the lovely and encouraging messages during this year. You supported me like a mother would do for her son/daughter. Thanks a lot, and next time let's get a gin tonic in a proper glass.

This journey to this point has been one of both challenge and fulfillment. To each and every single one of you who gave me unwavering support, who had an encouraging word in one of my dark moments, or who simply gave me a hug, thank you. This thesis is not just my work, but it is a mosaic of all your support. Cheers to every single one of you, and here's to our next new adventures.

Carmela